AIMING FOR THE TOP CORNER:

Measuring top-quark pair production in association with additional jets in highly boosted events using the ATLAS detector

Jonathan Jamieson

School of Physics and Astronomy
College of Science and Engineering
University of Glasgow
March 28, 2022

A dissertation submitted to the University of Glasgow
for the degree of Doctor of Philosophy

Abstract

Since beginning operations in 2010 the Large Hadron Collider (LHC) has consistently pushed the boundaries of high energy physics and provided a wealth of proton-proton collision events. Due to the high centre of mass energies achieved, and the QCD nature of proton-proton collisions, the LHC is particularly suited to the production of top-quarks, resulting in the apt nickname of 'top factory'. This thesis outlines the process of making state-of-the-art precision measurements of the top-quark pair production cross-section in events with a high energy top-quark and additional radiation, using data recorded by the ATLAS detector at the LHC from 2015 to 2018. Focus is put on comparing measured values with different QCD predictions showcasing how suited current theories are to estimating complex, multi-scale, and above leading-order processes. Both single and double-differential cross-section measurements as functions of various event kinematic properties are presented with results derived from proton-proton collisions, at a centre-of-mass energy of 13 TeV. Additionally a single differential measurement is used to set limits on new physics using an effective field theory framework.

Acknowledgements

There are a great many people who deserve thanks for helping me over the past four years and without whom this thesis would not exist. In fact there are many more than can be thanked here so I apologise in advance for those not included, rest assured your support was appreciated.

Firstly I would like to thank my supervisor Mark Owen who's infuriating habit of always being right was, all things considered, a blessing. Having his unwavering support and guidance has been vital throughout my PhD and learning from his approach to problems and attention to detail has undoubtably made me a better physicist. A special thanks must also go to Federica Fabbri who has been a constant source of knowledge, encouragement, and panic-inducing Skype messages. Her energy to answer any and all questions, no matter how naive, her kind words, and her collaborative work ethic have been nothing short of inspirational. I would also like to extend thanks to my second supervisor Craig Buttar who has always been open and willing to help should any problems arise, and has made me feel welcome within the Glasgow ATLAS group.

Thanks must also go to my collaborators in Germany, Kevin S, and Johannes E, who have contributed directly to the work outlined in this thesis as well as providing their expertise and guidance and have been a joy to work with.

I would also like to thank Tony, Aidan, Christoph, Sarah, Jay, Mike, Lauren, Chloe, Dan[2], and everyone in the Glasgow group past and present who have answered my questions, made me feel welcome, and kept me company in the pub on Fridays. I should also thank Gordon and Sam for their tireless work keeping my jobs from crashing, and Jill and Valerie who have kept me right over the years and ensured my travel was always smooth and worry free. Special thanks should also be given to Andy Buckley who provided the original LaTeX template for the document you are reading.

I should also thank all of those I had the pleasure to share an office with, whether in Glasgow or at CERN. A special thanks to my officemates prior to starting my PhD: Dwayne, Donatas, Will, and Morag, who's encouragement pushed me to seek out further research in the first place.

Thanks should also go to Neil and Dana who have been in the trenches with me from day one, acting as a sounding board for my terrible ideas, and a source of support and solidarity when the going got rough. As have the rest of my fellow cohort: Aaron, Adam, Bruno, Candice, David, Ethan, Greg, Laurynas, Lucas, Maty, Melissa, Savannah, Tom, and many other great people I met at CERN or while networking over a beer or three.

I wish also to thank my friends in Glasgow and beyond who have helped support me through the years, in particular my long-standing flatmate John, who's years of friendship and many drunken chats about life and physics more than make up for his sub-par rocket league skills. Thanks also to Alexia, Tom, Gordon, Cormac, Lucy, Ram, and Nat who's friendship has been invaluable through the difficulties of lockdown.

Lastly I want to thank my family, who have always been there for me with nothing but love, support, and encouraging words like: "your thesis is the most boring thing I've ever read". Thanks mum.

I couldn't have done this without you all, so in a way you're all to blame.

Dedicated to the late Julia Smith, I miss you big G.

Declaration

The research presented in this thesis is the result from my own work within the Experimental Particle Physics group in the School of Physics and Astronomy at the University of Glasgow and has not been submitted for another qualification to this or any other university.

The work was performed as part of the ATLAS collaboration at the LHC and thus makes use of tools and expertise developed over years of close collaboration between thousands of individuals, as well as data recorded by the ATLAS experiment. During my research I contributed directly to the collaboration through several ATLAS control room shifts and by helping maintain and improve communal software through a year-long position as Jet/$E_{\mathrm{T}}^{\mathrm{miss}}$ liaison for the Top working group.

The contents of Part I of this thesis (Chapters 1 – 6) give an introduction to the theory, detector, and experimental techniques relevant to the proceeding chapters and so do not cover work done solely by myself. The exception to this is Section 4.2 which outlines my contributions to the ATLAS muon trigger monitoring as part of my qualification task. Part II (Chapters 7 – 12) presents the boosted differential top-anti-top cross-section measurement published by ATLAS in 2022 [1], for which I was the lead analyst. The work builds on many of the tools and techniques developed in previous measurements. The studies outlined in these chapters are my own work apart from:

- Preparation of data sample and generation of simulated MC events (Section 7.1).
- Estimates of the multijet background (Section 7.3.1), and associated uncertainties (Section 9.3.1).

- Introduction of a new selection requirement used to reduce contamination from single-top backgrounds (Section 7.4.1 and Section 9.3.2).
- Development and validation of the unfolding framework (Sections 8.3 – 8.5)
- The interpretation of results in terms of effective field theory (EFT), including assessing the EFT sensitivity of different observables (Section 8.1.3) and extracting limits on two EFT operators (Chapter 11).

Jonathan Jamieson

Contents

"Careful. We don't want to learn from this."

— Bill Watterson

Part I.

Top-quark theory and experimental measurement with the ATLAS detector

Chapter 1.

Introduction

"In the beginning there was nothing, which exploded"
— Terry Pratchett, Lords and Ladies

It has been my experience, though likely coloured by circumstance, that of the various academic pursuits one could devote their time to, the physics of fundamental particles at high energies is consistently the most shocking, beautiful, and horrendously complicated.[1] Maybe it is not surprising then that the field attracts more than a few brave souls, with experiments at the Large Hadron Collider (LHC) being some of the largest scientific collaborations ever assembled. Within these collaborations thousands of scientists work to further our knowledge of the fundamental interactions that give the universe some semblance of order. This thesis presents the work I have contributed towards this immense collective understanding over the past four years. The main focus of which has been on the physics of the top quark, a fundamental particle whose large mass compared to other fundamental particles remains an outstanding question within the Standard Model. A key avenue to understanding the top-quark lies in making high precision measurements of various properties, including the cross-section of top-anti-top ($t\bar{t}$) production. The main bulk of this thesis covers such a precision measurement, focussing on high energy events in which one top-quark has a large transverse momentum (p_{T}), using data recorded by the ATLAS detector.

[1] At-least that's my excuse for spending so much of the last four years feeling utterly confused.

To ensure this work is given adequate context the following is split into several chapters with each falling under one of two broad headings. In Part I the theory and experimental framework adopted at the ATLAS detector is outlined starting in Chapter 2 with an introduction to the theory of the top-quark and its position within the Standard Model of particle physics. This is followed by an overview of the ATLAS detector and relevant parts of the LHC accelerator complex in Chapter 3, followed in Chapter 4 by a more detailed description of the ATLAS muon trigger system and a summary of the improvements I made to the real-time monitoring of trigger efficiencies. The next two chapters then set up the building blocks for performing a physics analysis, firstly Chapter 5 describes how signals recorded by the detector hardware are reconstructed into calibrated physics objects, before Part I is concluded in Chapter 6 with an overview of the Monte-Carlo methods used to create simulations of particle-physics events. Part II details the $t\bar{t}$ cross-section analysis which makes up the main experimental work of this thesis. This begins in Chapter 7 with an overview of the analysis strategy, followed in Chapter 8 by an outline of the observables used in the measurement and the method to correct data for detector effects (unfolding). Chapter 9 provides an overview of how various sources of uncertainty are treated in the analysis and details a novel method employed to reduce the impact of jet-related uncertainties. Chapter 10 summarises the results of the analysis and draws comparisons to current and previous related measurements. Lastly, Chapter 11 outlines a study exploring the sensitivity of the measured results to physics beyond the Standard Model. A summary of the discussed topics is provided in Chapter 12 along with considerations for future work.

Chapter 2.

The top-quark in the Standard Model

"Facts are meaningless. You can use facts to prove anything that's even remotely true."

— Homer Simpson, The Simpsons S9, E8 - Lisa the Sceptic

This chapter aims to introduce the underlying theoretical framework relevant to the analysis presented in this thesis. This begins with a general introduction to the Standard Model, how the top-quark fits into this picture and how our understanding can be informed through collider experiments. This is then followed by a discussion of the top-quark within effective theories extending beyond the Standard Model.

2.1. The Standard Model

The Standard Model (SM) of particle physics is the current best description of the building blocks of the observable universe. It describes all known elementary particles using the mathematical underpinning of quantum field theory (QFT) to explain interactions between them via three of the four known fundamental forces; electromagnetism, the weak nuclear force, and the strong force. Above a certain energy threshold the electromagnetic (EM) and weak forces can be unified into a combined electroweak (EW) interaction. A robust description of gravity in the quantum realm has not yet been formulated and as such the gravitational force is not included in the Standard Model.

The Standard Model Lagrangian ($\mathcal{L}_{\text{SM}}$) is invariant under several local (gauge) transformations. These symmetries necessitate the introduction of additional gauge

fields through which the above fundamental forces are introduced to the theory. These can be summarised by the $SU(3)_C \otimes SU(2)_L \otimes U(1)_Y$ symmetry. Here $SU(3)_C$ represents the strong interaction with the conserved current being colour charge (C), while $SU(2)_L \otimes U(1)_Y$ represents the unified electroweak interaction with weak isospin (L) and the hypercharge (Y) as the conserved quantities.

Particles in the SM come in two varieties: fermions with $\frac{1}{2}$ integer spin, and bosons which have integer spin. Fundamental (point-like) fermions are postulated to form all of the stable matter in the universe[1] and come in two forms: quarks - which interact via the strong force due to the presence of colour charge and leptons - which have no colour charge and thus interact only via electroweak interactions. Conversely the fundamental bosons are responsible for mediating interactions between fermions, with the gauge bosons originating from the above mentioned symmetries. Separately the scalar Higgs boson emerges as a requirement for the process of spontaneous electroweak symmetry breaking [2, 3], giving rise to the W- and Z-boson masses. The associated scalar field is responsible for the observed masses of the fermions via Yukawa couplings between the fermions and Higgs boson. These couplings are proportional to the mass of the fermion and thus more massive particles couple more strongly to the Higgs boson. The size of the Yukawa couplings, and hence the masses of the fermions, are not predicted by the SM and must be measured experimentally.

All matter particles have a corresponding anti-particle with the same quantum numbers but opposite charge. The gluon (g), photon (γ), Z-boson, and the Higgs boson are invariant under charge conjugation and so are each their own anti-particles, while the two W-bosons are each other's antiparticle. Despite neutrinos not possessing EM or colour charge, anti-neutrinos do exist in the SM and are distinct from regular neutrinos as they possess opposite chirality. Throughout this thesis the same names and symbols will be used for both particles and anti-particles unless a distinction between them is specifically required. Figure 2.1 summarises all seventeen elementary particles within the Standard Model showing their masses, electric charge and spin quantum numbers, taken from the Particle Data Group [4]. Additional colour bands indicate which fermions take part in interactions mediated by each gauge boson. The set of twelve fermions are further split into three generations with each successive generation containing two quarks, a charged lepton, and a neutrino with the same quantum numbers as the previous generation but orders of magnitude larger masses.

[1] A notable weakness of the SM is its inability to account for the origin of dark matter which is estimated to make up the bulk of the observable mass in the universe.

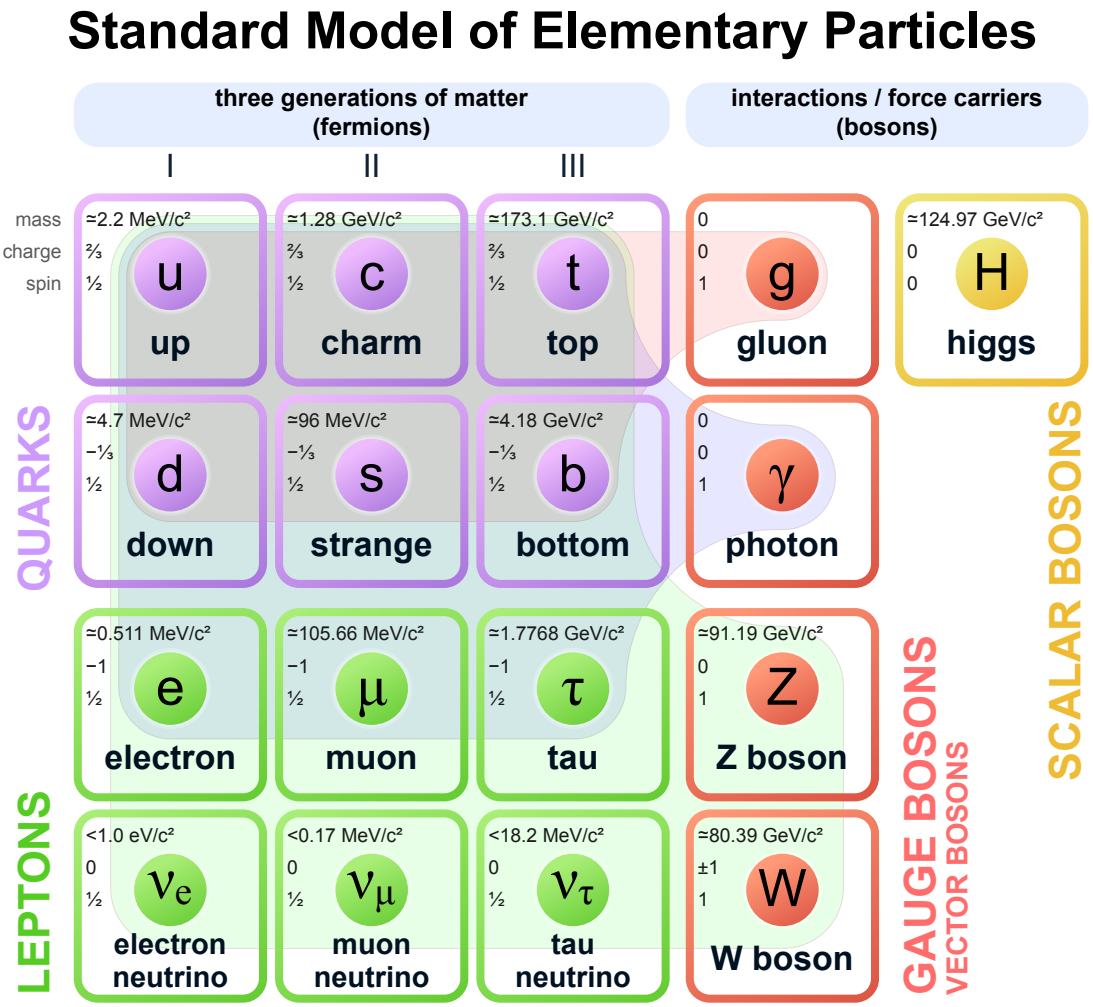

Figure 2.1: Fundamental particles within the Standard Model of particle physics. Mass, charge and spin values taken from the Particle Data Group [4], original image courtesy of [5], modified to enhance visualisation of the force groups.

All quarks in the SM carry colour charge and so can interact via the strong force with interactions described by quantum chromodynamics (QCD). The gluon is the massless force carrier for the strong interaction and is itself colour charged allowing for gluons to self-interact. Gluon self-interaction also leads to the principle of confinement in which coloured particles cannot exist in an isolated state and instead bind together to from colour-neutral hadrons, in a process known as *hadronisation*. The most common of these are mesons, formed of a quark, anti-quark pair, and baryons, formed of three quarks.

2.2. The top quark

The discovery of the top-quark in 1995 by the DØ and CDF collaborations at the Tevatron [6, 7] ended a two decade long search for the sixth quark flavour after its initial prediction in 1973 [8]. The long wait for experimental discovery compared to its third generation counterpart is a direct result of its uniquely large mass. The top-quark has the largest mass of all fundamental particles in the SM with a combination of the most recent experimental results giving a value of: $172.76 \pm 0.30\,\text{GeV}$ quoted by the Particle Data Group [4] using results from ATLAS, CMS, and Tevatron measurements. The high mass leads directly to numerous other useful properties, namely a very short lifetime and a strong coupling to the Higgs boson. The top quark finds itself uniquely positioned within the Standard Model as a result.

As the only quark with a mass greater than the W-boson the top-quark is capable of decaying via a flavour changing weak decay to an on-shell W-boson and a down-type quark. These decays are moderated by the CKM matrix [8, 9], which determines the mixing between quark flavours. The elements of this matrix have been evaluated experimentally [4] with $|V_{tb}|$ found to be significantly larger than both $|V_{td}|$ and $|V_{ts}|$, where the subscripts refer to the relevant quark flavours, meaning the decay $t \to Wb$ is expected to be highly dominant. Alternatively rare decays into an up-type quark and a neutral gauge boson or the Higgs boson are also possible. Such flavour changing neutral current decays are forbidden at tree-level in the SM but are possible at higher orders via processes involving a W-boson loop, such as in Figure 2.2. However in the SM these are heavily suppressed by the GIM mechanism [10] as well as a consequence of the strong hierarchy of CKM elements. As a result top quarks are expected to decay almost exclusively to a W-boson and a b-quark in the Standard Model.

A combined result of this single decay mode and the high mass of the top-quark, is an average lifetime of only $\sim 5 \times 10^{-25}$ s [4], which is significantly shorter than the timescale of the quark hadronisation process of $\sim 3 \times 10^{-24}$ s [11]. The top-quark thus does not undergo hadronisation allowing for the unique opportunity to study the properties of bare quarks.

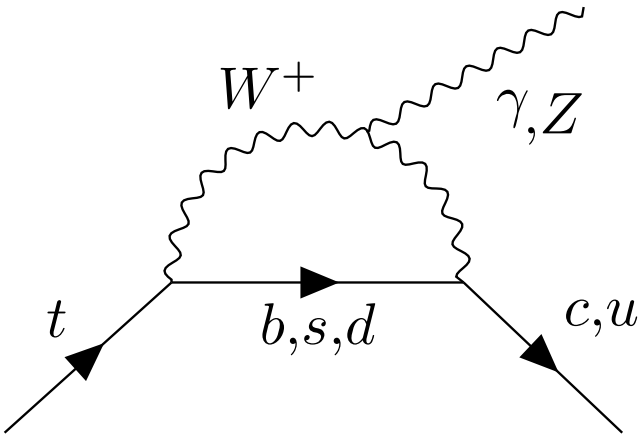

Figure 2.2: Feynman diagram of a possible flavour changing neutral current top-quark decay in the Standard Model.

2.3. Top-quark pair production at hadron colliders

At hadron colliders, like the LHC, top-quarks are predominantly produced as top-anti-top ($t\bar{t}$) pairs via the strong force. Electroweak initiated production of single top-quarks is also possible but less common within pp collisions. Figure 2.3 shows the leading-order Feynman diagrams for $t\bar{t}$ production which at the LHC is dominated by gluon-gluon fusion (90%), as in Figures 2.3a–c, with the remaining 10% of events produced via quark, anti-quark annihilation as in Figure 2.3d. Due to the dominant $t \to Wb$ decay mode, $t\bar{t}$ production events are classified by the decay products of the two W-bosons. Each can decay either into a lepton and associated neutrino ($\ell\nu$), or hadronically into a quark, anti-quark pair ($q\bar{q}'$) resulting in three distinct channels for $t\bar{t}$: All-hadronic, lepton+jets and di-lepton. Figure 2.4 shows the branching fractions for the three channels, with values again taken from the Particle Data Group [4].

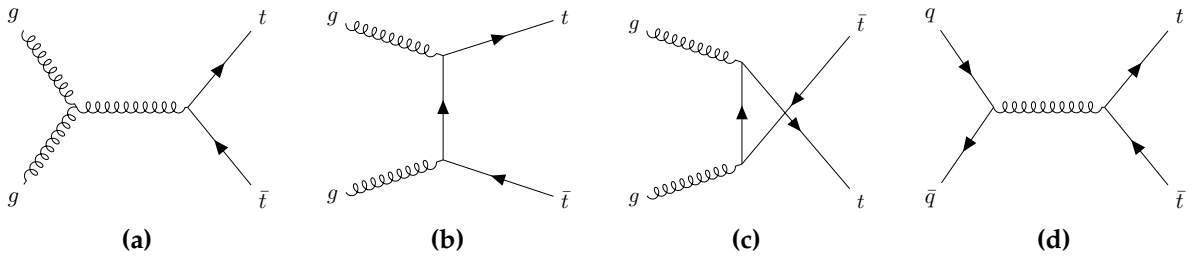

Figure 2.3: Leading order Feynman diagrams for top-quark pair production.

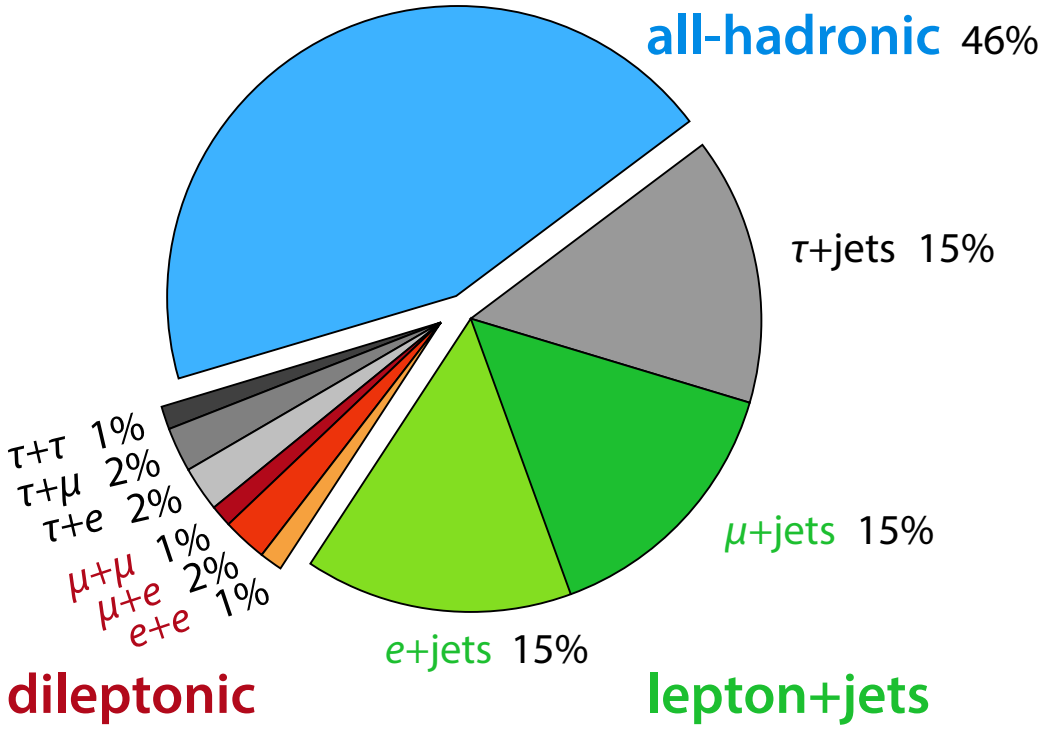

Figure 2.4: Branching fractions of the possible $t\bar{t}$ final states assuming 100% $t \to Wb$ decays and lepton universality [12]. At hadron collider experiments the lepton+jets and di-lepton channels often refer to e/μ states only.

2.3.1. Top anti-top production cross-section

The cross-section (σ) of any SM process is a measure of how likely it is to occur at a given energy. This can be calculated theoretically by summing over the matrix elements of all potential diagrams, like those in Figure 2.3 for leading order $t\bar{t}$ production. The number of diagrams is effectively infinite as it is possible to add any number of additional low momentum real emissions, such as in Figure 2.5a and any number of virtual gluon loops as in Figure 2.5b. However each additional QCD vertex contributes an extra factor of the strong coupling (α_S). The partonic cross-section can then be written in a simplified manner as a power series in α_S:

$$\hat{\sigma}_{ij\to t\bar{t}+X} = \underbrace{H^{(0)}}_{\text{LO}} + \underbrace{\alpha_S H^{(1)}}_{\text{NLO}} + \underbrace{\alpha_S^2 H^{(2)}}_{\text{NNLO}} + ..., \tag{2.1}$$

where ij refers to the interacting partons rather than the parent protons, $t\bar{t}+X$ denotes events with any number/type of additional emissions, and the $H^{(i)}$ denote hard-scatter diagrams whose amplitudes are all proportional to α_S^2. At high energies, such as those probed at the LHC, the strength of the α_S coupling is less than 1 thus diagrams with more vertices will have a reduced impact. The matrix element can then be calculated up to a specific order in α_S using perturbation theory. Calculations like this are commonly labelled with the highest calculated power of α_S as leading order (LO), next-to-leading order (NLO), next-to-next-to-leading order (NNLO) etc. State-of-the-art fixed-order calculations for $t\bar{t}$ production are performed up to NNLO in QCD [13–16]. These can be supplemented with NLO electroweak corrections [17], as well as calculations up to next-to-next-to-leading logarithm (NNLL) in re-summed soft gluon terms [16, 18, 19].

In practice expanding to higher orders in perturbation theory quickly becomes complex to calculate. Measuring the same cross-section at a collider experiment thus provides one of the simplest and yet most powerful tests of the Standard Model. In the context of collider physics the interaction cross-section can be calculated from the number of measured events. For example the $t\bar{t}$ production cross section at the LHC can be written as:

$$\sigma_{t\bar{t}} = \frac{N_{t\bar{t}}}{\mathcal{L}_{int}}, \tag{2.2}$$

where $N_{t\bar{t}}$ is the total number of $t\bar{t}$ events measured at a certain collision energy and $\mathcal{L}_{int}$ is the integrated luminosity. This is a measure of the total number of particle pairs

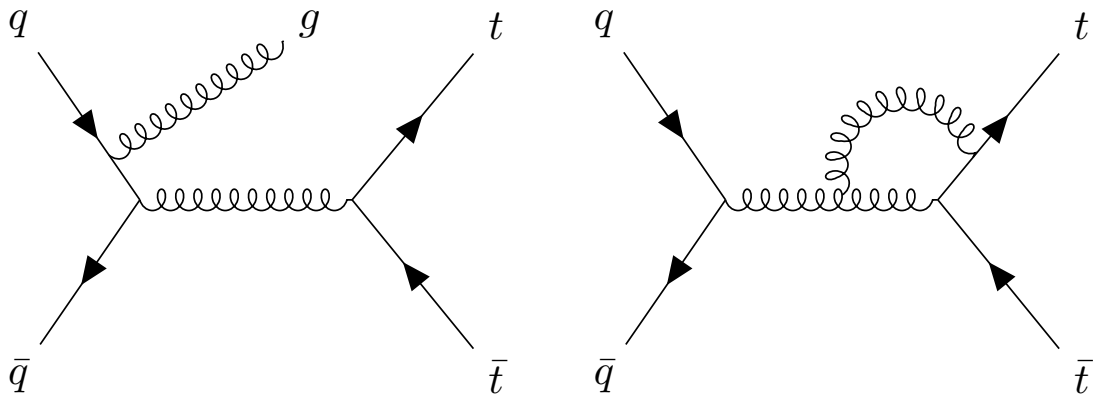

Figure 2.5: Example Feynman diagrams for $t\bar{t}$ production at above leading order with (a) an additional real gluon emission, (b) a virtual gluon loop.

with the potential to interact that have passed though the collision point over a set time and is dependent on parameters of the colliding beams as described in Section 3.1.

2.4. Beyond the Standard Model

The Standard Model is an incredibly impressive theory, and one of the most successful of all time, however it is not perfect. Despite correctly accounting for much of the observed universe there are several fundamental questions left unanswered, such as:

1. How does one properly incorporate gravity into the current model?
2. What is the source of the dark matter and dark energy observed by astronomers?
3. What is the source of the observed matter/anti-matter asymmetry in the universe?
4. Why is the top-quark so massive compared to the other fermions?
5. Why is the mass of the Higgs boson lower than expected when accounting for quantum top-loop corrections? [2]
6. What is the origin of the non-zero neutrino masses observed in oscillation experiments [4]?

[2] This is commonly referred to as the hierarchy problem and requires careful fine-tuning of SM parameters in order to cancel quadratic divergences in the Higgs mass terms. The need for such fine tuning is an indication that a more fundamental underlying theory is missing.

Answers to many of these questions and others often require the introduction of new particles, not predicted by the Standard Model. However the SM has been thoroughly tested at low energies up to the TeV scale, with no observation of new particles. Much of the search for new physics has moved towards higher energies as a result, in many cases above energies which can be probed directly by the LHC. There are no plans for significant increases to the energy reach of any current, or proposed, collider experiments in the near future. However the indirect effects of physics occurring at high energy scales can, in many cases, be observed at lower energies as slight deviations from the SM. As the heaviest fundamental particle the top-quark is likely to play an important role in searching for such high energy effects motivating making high precision top-quark measurements such as those outlined in this thesis.

2.4.1. The Standard Model effective field theory

There are several categories of beyond the Standard Model (BSM) theories, such as supersymmetry [20] and composite Higgs models [21], which directly address some of the questions above by introducing specific extensions to the SM. However a more general, model-independent, approach is possible by re-interpreting the Standard Model as one part of a larger effective field theory (EFT) [22–25]. An EFT is an effective low-energy approximation of a more fundamental theory with a higher natural energy scale (Λ). A Standard Model effective field theory (SMEFT) is easily constructed by expanding the SM Lagrangian by adding higher-order terms which describe the effects of the high-energy theory on observables at lower energies. These terms are naturally suppressed by powers of Λ and can be written in terms of an EFT operator multiplied by a Wilson-coefficient which dictates the strength of the operator's contribution. The new Lagrangian can be written as:

$$\begin{aligned} \mathcal{L}_{\text{SMEFT}} &= \mathcal{L}_{\text{SM}} + \mathcal{L}_{\text{eff}}(\Lambda), \\ \mathcal{L}_{\text{SMEFT}} &= \mathcal{L}_{\text{SM}} + \sum_{D} \sum_{i} \frac{C_i^D}{\Lambda^{D-4}} \hat{O}_i^D, \end{aligned} \tag{2.3}$$

where C_i^D is the Wilson-coefficient corresponding to the EFT operator $\hat{O}_i^D$, of mass dimension D. The collection of EFT operators are built using the same fields and gauge symmetries as the SM and must be of dimension above that of the Standard Model. In practice operators with odd dimensions violate baryon or lepton number conservation and thus the leading set of EFT operators typically considered are of

dimension six. Even at this lowest dimension there are a large number of possible operators (2499 in the commonly used Warsaw basis [26]). The impact of each operator arises either through modifications to existing SM vertices or by introducing new couplings that allow for additional diagrams. As a result only a small number are expected to significantly affect a given SM process.

2.4.2. EFT effects on top-quark pair production

In leading-order top-quark pair production diagrams, such as those shown in Figure 2.3, there are three different couplings from which EFT effects can enter. The first is the pure gluon vertex in Figure 2.3a. These vertices are less interesting with regards to $t\bar{t}$ measurements as they do not include the top-quark directly and are better constrained in multi-jet final states rather than $t\bar{t}$ production [27]. The vertices of heavy quarks and gluons are more interesting as they directly effect the coupling between the top-quark and the gluon, with EFT contributions introduced through the chromo-magnetic dipole operator (O_{tG}). The third possibility for EFT effects to enter into $t\bar{t}$ production is with the introduction of a non-SM vertex between two light-quarks and two heavy quarks. For the four-quark coupling there are a number of operators in the Warsaw basis which can have an effect, however $O_{tq}^{(8)}$ is expected to have the joint-largest impact on the $t\bar{t}$ production cross-section [28–30], and is the representative four-quark operator used in the EFT study in Chapter 11. The effective four-quark coupling and the modified heavy-quark gluon coupling are shown in Figure 2.6.

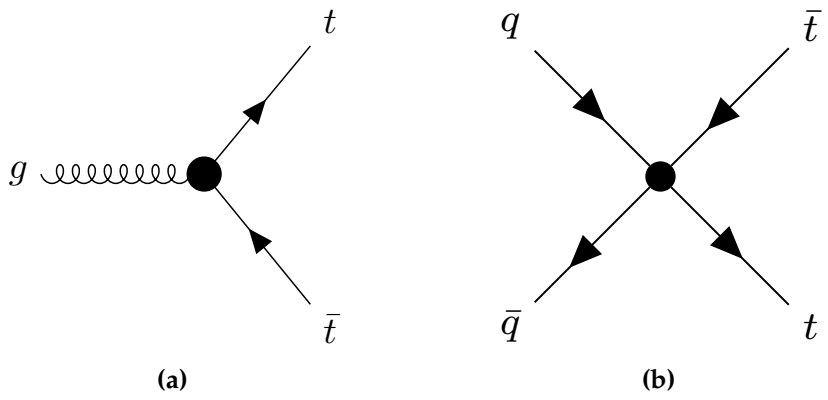

Figure 2.6: Vertices affected by EFT contributions that are relevant for leading-order $t\bar{t}$ production. The black dots show the couplings affected by (a) O_{tG} and (b) $O_{tq}^{(8)}$.

Due to the much larger fraction of gluon initiated $t\bar{t}$ production at the LHC the absolute effect of $O_{tq}^{(8)}$ on the $t\bar{t}$ cross-section is expected to be considerably lower than that from O_{tG}. However the relative probability for a parton to carry a larger fraction of the parent proton's momentum is much larger for valence-quarks than it is for gluons. As a result the fraction of $q\bar{q}$ initiated states is increased for events which contain a high energy top-quark and thus the effects of $O_{tq}^{(8)}$ are also expected to increase with energy. The impacts of four-quark operators on the kinematics of final-state particles are additionally expected to scale with energy in a stronger way than O_{tG} [31]. This difference in behaviour at high energies allows the effects of these two operators to be disentangled using only a single differential $t\bar{t}$ cross-section measurement, as demonstrated in Chapter 11.

Chapter 3.

The LHC and ATLAS

"If we hit that bullseye the rest of the dominoes will fall like a house of cards. Checkmate!"

— Capt. Zapp Brannigan, Futurama S1, E12 - When Aliens Attack

The Large Hadron Collider (LHC) [32] at CERN is the largest and most powerful particle accelerator ever built. It has been instrumental in many of the most important particle physics results in the past 12 years, including the discovery of the Higgs boson in 2012 [33, 34]. Located almost 100 metres below ground, straddling the French-Swiss border on the outskirts of Geneva, the LHC is the most recent addition to the larger CERN accelerator complex, shown in Figure 3.1. The LHC uses a combination of superconducting magnets and radio frequency cavities to accelerate two counter-circulating beams of proton[1] bunches to almost the speed of light. These bunches are then collided at four points around the ring's circumference at which the principal LHC experiments are housed. These include two specialised detectors; LHCb [35] - designed primarily around the study of heavy flavour physics and interactions involving B-mesons, and ALICE [36] - whose physics programme is based on heavy ion interactions. There are also two large general-purpose experiments; ATLAS [37] and CMS [38], which use full coverage detectors to make precision measurements of a wide range of Standard Model processes, as well as searching for evidence of new physics. The discussion that follows will focus primarily on the ATLAS experiment which, importantly for the analysis discussed in Part II of this thesis, is well suited to the measurement of top, anti-top quark pairs at high energies.

[1] or heavy ion (Pb, Au, and Xe)

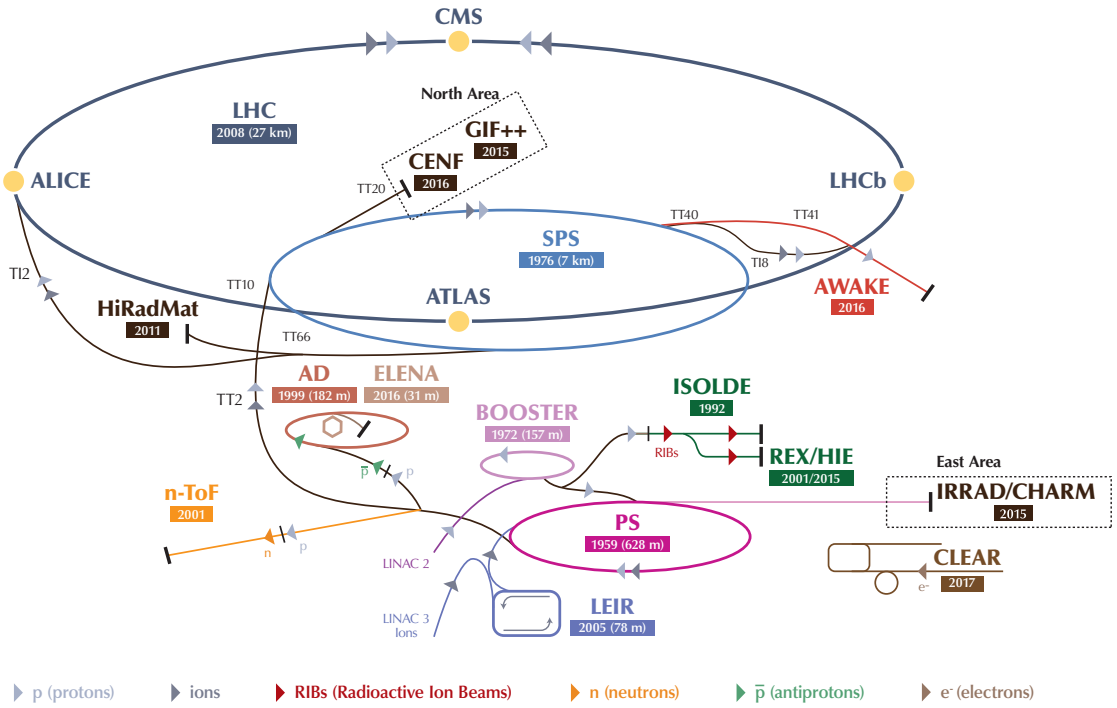

Figure 3.1: Schematic of the CERN accelerator complex as it was in 2018 with the LHC ring shown at the top [39]. Incremental acceleration stages used to provide high energy proton beams for the LHC are shown, starting from LINAC 2, going through the PS booster (BOOSTER), the PS, and SPS before finally entering the LHC ring at injection points TI2 and TI8.

3.1. The Large Hadron Collider

The success of the LHC project is owed in part to the ability to repurpose much of the existing accelerator infrastructure at the CERN site. The LHC ring itself is housed within the ∼27 km tunnel dug in the 1980s for the Large Electron Positron collider (LEP) experiment [40]. The high energy proton beams that eventually circulate this tunnel start their journey in a series of smaller accelerators built on the vestiges of previous experiments.

The different proton acceleration stages are outlined in Figure 3.1 starting from simple hydrogen gas which is ionised to produce H^- ions. These ions are then accelerated to 50 MeV in the LINAC 2 linear accelerator before being stripped of their two electrons and fed into the Proton Synchrotron Booster (PSBOOSTER). The booster accelerates the resulting protons up to 1.4 GeV before injecting them into the Proton Synchrotron (PS), which accelerates the injected protons to 26 GeV before passing them on to the Super Proton Synchrotron (SPS). The SPS is the final link in the chain,

accelerating protons to an energy of 450 GeV before feeding them into the LHC ring at two injection sites producing counter-circulating beams. The two proton beams continue to circulate within the LHC becoming accelerated to a current maximum energy of 6.5 TeV. Timed injections between the PS, SPS, and LHC result in beams with a bunched structure which by the end of data taking in 2018 consisted of 2556 proton bunches each containing $\sim 1.2 \times 10^{11}$ protons with a 25 ns spacing between bunches. In 2020 LINAC 2 was replaced with LINAC 4, which has a higher maximum operational energy of 160 MeV. This also allows for increased energy thresholds further downstream and is a vital step in achieving future high luminosity collisions.

During each acceleration stage a combination of radio frequency cavities, and bending and focussing electromagnets are used to accelerate the protons and maintain the desired beam structure. Powerful magnetic fields are needed to contain the beam radius, for which large superconducting magnets, cooled used liquid helium, are used. In total 1232 dipole magnets, each roughly 15 metres long, span a majority of the LHC circumference providing linear magnetic fields of opposing orientation across the two counter-circulating beams. In both cases the fields are perpendicular to the beam direction and result in a Lorentz force pointing into the centre of the ring. A schematic showing the internal structure and magnetic flux of the dipole magnets is shown in Figure 3.2. A further 392 main quadrupole magnets are used in pairs to periodically focus the beams in planes perpendicular to the direction of travel, ensuring the beams stay tightly collimated as they circulate. Several more quadrupoles as well as higher order sextupole, octupole, and decapole magnets are also needed to make further small corrections to the beam width, to counteract the spread of the proton bunches along the beam axis over time.

3.1.1. Instantaneous and integrated luminosity

For any particle collider it is necessary to quantify the magnitude of successful collisions produced. The primary operating parameter used at the LHC is the instantaneous luminosity ($\mathcal{L}$) [43]. This denotes the total number of particle pairs with the potential to interact that can be moved though a set area in a set period of time:

$$\mathcal{L} = \frac{N_{pp}}{cm^2 \times s} \tag{3.1}$$

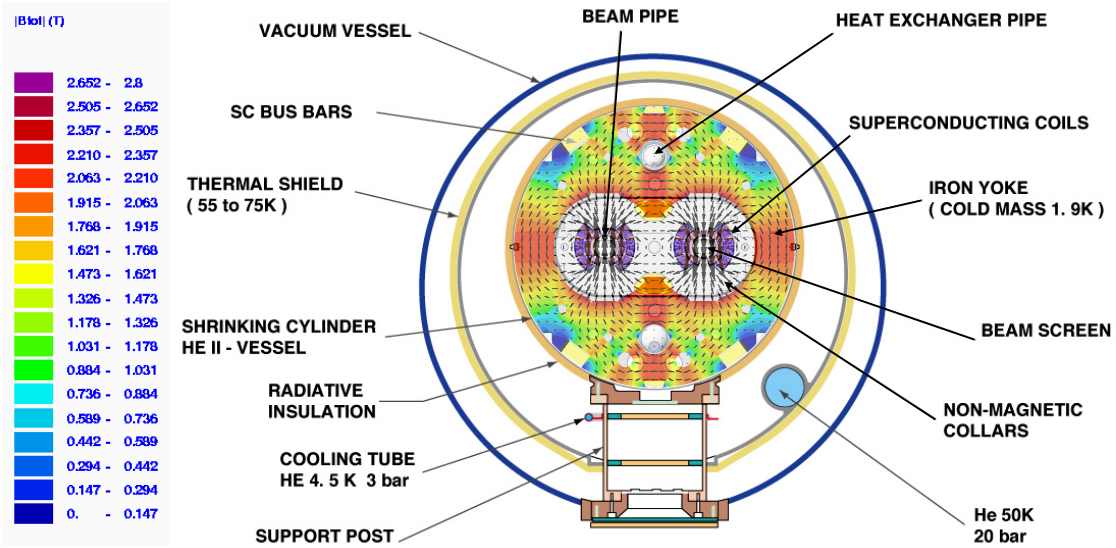

Figure 3.2: Transverse slice showing the internal structure of the LHC dipole magnet and cryostat systems [41]. A plot of the magnetic flux over the x-y plane of an example dipole is overlaid [42].

While not particularly intuitive this has the significant advantage of depending only on the size and structure of the colliding bunches. Assuming bunched proton beams with equal gaussian profiles the instantaneous luminosity is given by:

$$\mathcal{L}(t) = \frac{N_1 N_2 N_b}{b_s 4\pi\sigma_x\sigma_y}, \tag{3.2}$$

where N_1 and N_2 are the number of protons per bunch in each beam, N_b is the total number of bunches per beam, b_s is the spacing of bunches in each beam in units of time, and σ_x and σ_y are the horizontal and vertical dimensions of the bunches [44]. The total size of a recorded dataset can be represented by integrating the instantaneous luminosity over time to give the integrated luminosity. This is generally measured in inverse femtobarns (fb^{-1}) where a barn (b) is a unit of distance equal to $10^{-24}\,\text{cm}^2$. The integrated luminosity combined with the interaction cross-section introduced in Section 2.2 gives the total number of observed events of a particular interaction:

$$\mathcal{L}_{int} \cdot \sigma_{t\bar{t}} = \text{number of } t\bar{t} \text{ events} \tag{3.3}$$

3.1.2. LHC operation

To date there have been two major operating periods of the LHC, bookended by multi-year periods where the machine is shut-down for maintenance and upgrades. Run-1 covers the period between 2009 and 2013 in which protons were collided at centre of mass energies of 900 GeV, 7 TeV, and 8 TeV. This was followed by the first long shutdown during which the beam energy was increased. Run-2 covers operation from 2015 to 2018 during which time 156 fb^{-1} of pp collision data was produced at a centre of mass energy of 13 TeV. From this 139 fb^{-1} of useable physics data was recorded by the ATLAS detector [45]. During operating periods the LHC can not operate continuously as collisions remove some of the protons in the bunches. Data is thus recorded in individual *runs*, usually lasting several hours. When the proton intensity gets too low at the end of a run the beams are dumped and the machine is refilled.

The expected peak luminosity for the LHC before operation was $10^{34}\,\text{cm}^{-2}\,\text{s}^{-1}$, however with optimisations to the bunch structure and collision rate over time this was increased to the current peak value of $2.1 \times 10^{34}\,\text{cm}^{-2}\,\text{s}^{-1}$ recorded in 2018. Increasing the instantaneous luminosity also increases the number of pp interactions that occur per bunch crossing, known as pileup (μ). Over the course of Run-2 ATLAS recorded data with an average pileup of $\langle\mu\rangle = 33.7$, significantly higher than the expected value of $\langle\mu\rangle = 23$ used when considering the design of the detector [46]. This is problematic as excessive pileup collisions make it more difficult to accurately reconstruct the hard-scatter interactions of interest.

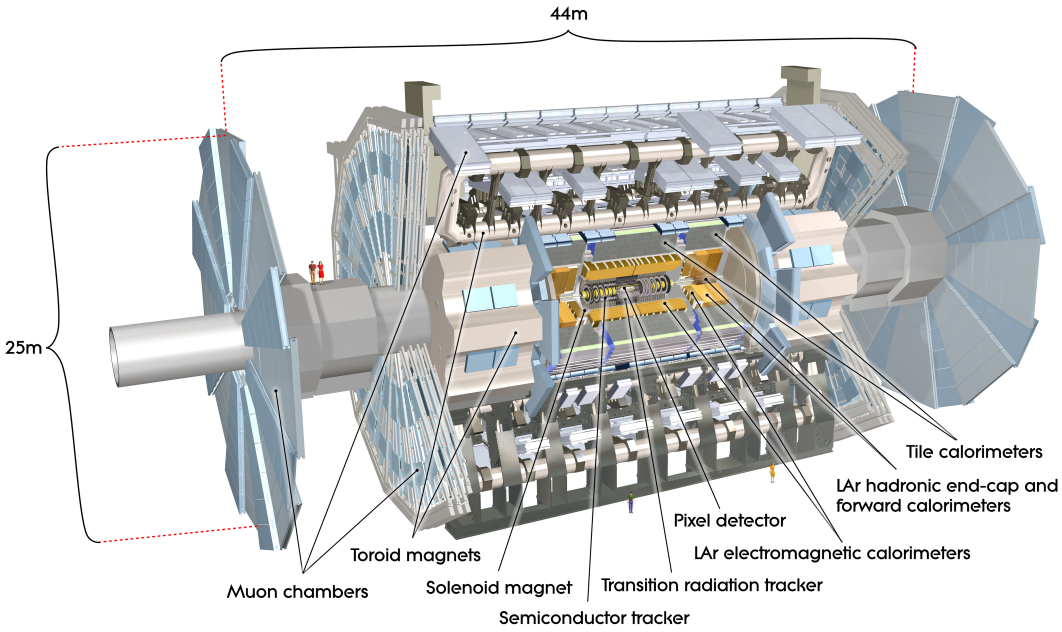

Figure 3.3: Schematic showing the scale and internal structure of the ATLAS detector [47].

3.2. ATLAS Detector

The ATLAS detector, shown schematically in Figure 3.3, is a multipurpose detector providing almost 4π solid angle coverage around a central interaction point (IP). The detector hardware consists of four main sub-detectors; an inner tracker, electromagnetic and hadronic calorimeters, and a composite muon spectrometer. Additionally a system of superconducting magnets are used to aid in identification and momentum measurements of charged particles. The different detector technologies are arranged concentrically around the beam pipe and interspersed with the magnets, with the most sensitive and radiation-hard technologies used closer to the interaction point and lower-granularity detection mediums placed further out. This multi-detector design allows for the detection of all known Standard Model particles apart from neutrinos, which escape the detector volume but are able to be reconstructed by calculating signatures of missing transverse momentum. Figure 3.4 showcases how different particle types are identified by the energy signatures they leave within the various sub-detectors. The following sections cover each of the main detector technologies in turn, starting with the innermost layers and moving outwards.

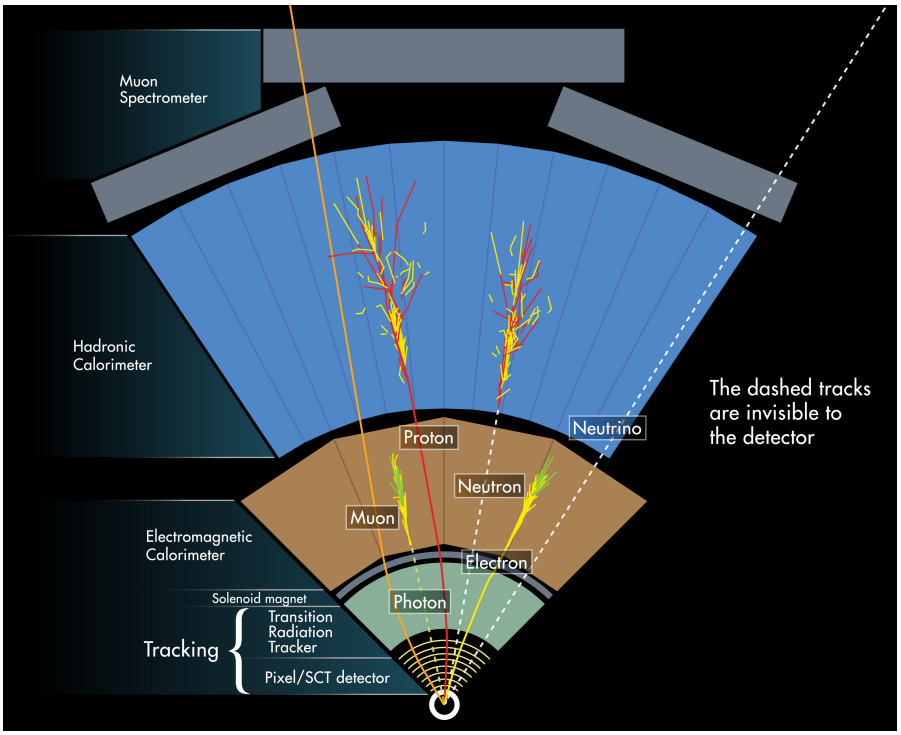

Figure 3.4: Simplified cross-section through the ATLAS detector barrel demonstrating how different types of particle interact within the various sub-detectors [48]. The different energy signatures left by each particle allows them to be identified.

ATLAS coordinate system

ATLAS uses a right-handed coordinate system with its origin at the nominal interaction point in the centre of the detector, to maintain consistency I will use the same convention throughout this thesis. In this system the z-axis points along the beam pipe, the x-axis points from the IP to the centre of the LHC ring, and the y-axis points upward. Cylindrical coordinates (r,ϕ) are used in the transverse plane, with ϕ being the azimuthal angle around the beam pipe. The polar angle θ, which spans the z-axis, is not Lorentz invariant and is thus often replaced with rapidity: $y = 0.5 \ln\left(\frac{E+p_z}{E-p_z}\right)$, where E is the total particle energy and p_z is the particle momentum along the z-direction. Differences in rapidity are Lorentz invariant. An alternative third quantity, the pseudorapidity, is defined in terms of the polar angle as: $\eta = -\ln\left(\tan(\theta/2)\right)$ and for massless, or high energy particles, is a very good approximation for y. The angular separation between particles is normally defined using the pseudorapidity as $\Delta R = \sqrt{(\Delta\phi)^2 + (\Delta\eta)^2}$.

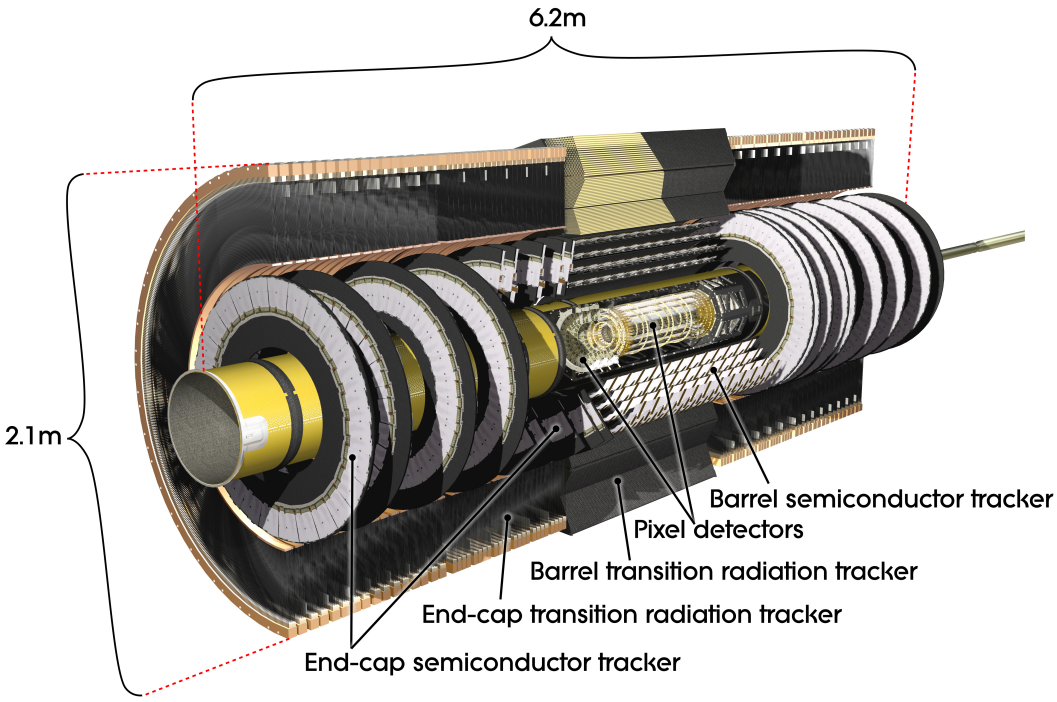

Figure 3.5: Schematic of the ATLAS inner detector barrel and endcap regions, showing the relative scale of the various layers [52]. The central solenoid is not shown.

3.2.1. Inner detector

The ATLAS inner detector (ID) [49, 50] is the closest sub-detector to the nominal interaction point and is designed to provide highly granular tracking information for charged particles as well as identification of interaction vertices. Three different detector technologies are used, spread out in distinct cylindrical layers, encircling the beam pipe, these are the Pixel detector, Semiconductor Tracker (SCT), and Transition Radiation Tracker (TRT). The ID is immersed in a constant 2 T magnetic field provided by the central solenoid which completely surrounds the active sub-detector regions. This allows for charge identification and accurate momentum measurements from the tracks of charged particle. The structure of the ATLAS inner detector is shown in Figure 3.5, though this does not show the surrounding central solenoid which has a diameter of 2.3m and a length of 5.3m [51].

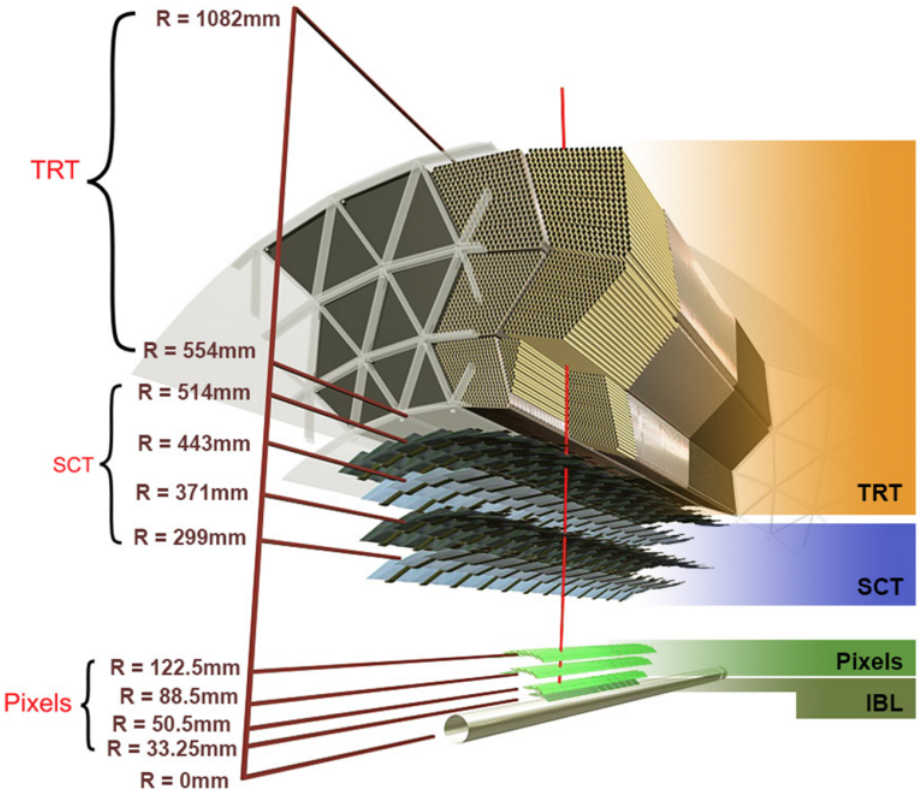

Figure 3.6: Exploded view showing the internal layers of the ATLAS inner detector barrel [53]. Charged particle trajectories are bent by a 2 T magnetic field produced by the surrounding solenoidal magnet system and produce hits in the different detector layers allowing tracks to be fit.

Pixel detector

The different layers within the ID barrel are shown in more detail in figure 3.6. The innermost layer is comprised of the Pixel detector [54] and an additional insertable *b*-layer (IBL) [55] placed directly next to the beam pipe. Both of these use semiconductor pixel technology to provide tracking information. Semiconductor tracking works in almost the same way as the CMOS sensor used in most consumer cameras: A charged particle passes through a doped silicon substrate producing excited electron-hole pairs, a charge placed across the sensor then collects the free electrons at the anode and registers a hit.

In pixel systems the active silicon sensors are fashioned into small rectangular pixels which are each individually bonded to shared readout electronics. The IBL is the closest detector sub-system to the beam line. It was added in 2013 during the first long shutdown of the LHC with the aim to prolong and improve the tracking

and b-quark identification performance of the ATLAS detector in regions with high expected radiation damage. The IBL covers a pseudorapidity range of $|\eta| < 3$ and due to its proximity to the interaction point does not have separate barrel and endcap regions. The remaining pixel detector consists of a 3-layer barrel and 2×3 endcap disks covering a pseudorapidity range of $|\eta| < 2.5$. Identical sensors are used in both the barrel and endcaps which are slightly larger than those in the IBL.

Semiconductor tracker

The semiconductor tracker or SCT [56] is next out from the beam line, like the pixel this is composed of active silicon sensors, though this time fashioned into larger strips. This design significantly reduces the manufacturing complexity at the expense of reduced granularity. The SCT is made up of four layers in the barrel and 2×9 endcap disks. Like the pixel detector the active regions of the SCT cover a range of $|\eta| < 2.5$ around the interaction point.

Transition radiation tracker

Together the pixel and SCT provide precision tracking information that is then supplemented with spatial hit information from the Transition Radiation Tracker [57] located further downstream from the interaction point. Rather than silicon the TRT uses a design consisting of gas-filled tubes (or straws) with a single positively charged anode wire running down the centre. When charged particles pass through the straw they ionise the gas mixture releasing electrons which travel down the wire and are recorded as a hit in readout electronics placed at either end.

The straws each have a diameter of 4 mm and are filled with a gas mixture consisting of 70% Xenon, 27% CO_2, and 3% Oxygen. In the barrel straws are stacked parallel to the beam-line while in the 2×2 endcap disks they are stacked perpendicularly in radial planes. The spacial resolution of the TRT is considerably lower than for the precision trackers, however this is mitigated by processing a much larger number of individual hits. Additionally the track lengths within the TRT are longer which enhances the accuracy of momentum measurements.

In addition to spatial and momentum measurements the TRT also helps aid electron identification as the space between straws in both the barrel and endcaps is filled

with a "radiator" material of mixed refractive index. The resulting transition radiation emitted by charged particles passing through this medium can be detected and is strongest for electrons due to their low mass [58]. The presence of transition radiation can thus be used as an additional signal in electron identification.

3.2.2. Calorimeters

The next layer out from the inner detector is the ATLAS calorimeter system [59]. The calorimeters are designed to absorb and measure the total energy of all incoming charged and neutral particles, except for muons and neutrinos which are expected to traverse the calorimeters without depositing all of their energy. This is achieved by interweaving high density "absorber" material with "active" detector regions. Incident particles interact with material in the absorber, losing momentum and creating showers of particles, the energy of which is measured by the active elements. The calorimeter is split into three sub-systems; the liquid argon (LAr) electromagnetic calorimeter (ECAL), the Tile barrel and LAr end-cap hadronic calorimeters (HCAL), and the LAr forward calorimeter (FCAL). The layout of the calorimeter system is shown in Figure 3.7.

LAr electromagnetic calorimeter

The liquid argon electromagnetic calorimeter [60] is the calorimeter sub-system closest to the ID and is designed primarily to detect electrons and photons with high granularity. Lead plates are used as the absorber material while the sensitive region contains liquid argon which is ionised by the shower particles, producing a measurable current. The ECAL consists of a three layer barrel and two end-caps, each consisting of an outer and inner wheel. Combined the ECAL has a sensitive range of $|\eta| < 3.2$, with perfect ϕ coverage due to the accordion structure used. An additional LAr based pre-sampler detector is included between the ID and ECAL in the region $|\eta| < 1.8$ in order to correct for the energy lost by electrons and photons in between the two systems.

Tile and LAr hadronic calorimeters

The hadronic calorimeter system is placed further out from the ECAL and is designed to measure the remaining energy of hadrons that are not fully absorbed by the EM

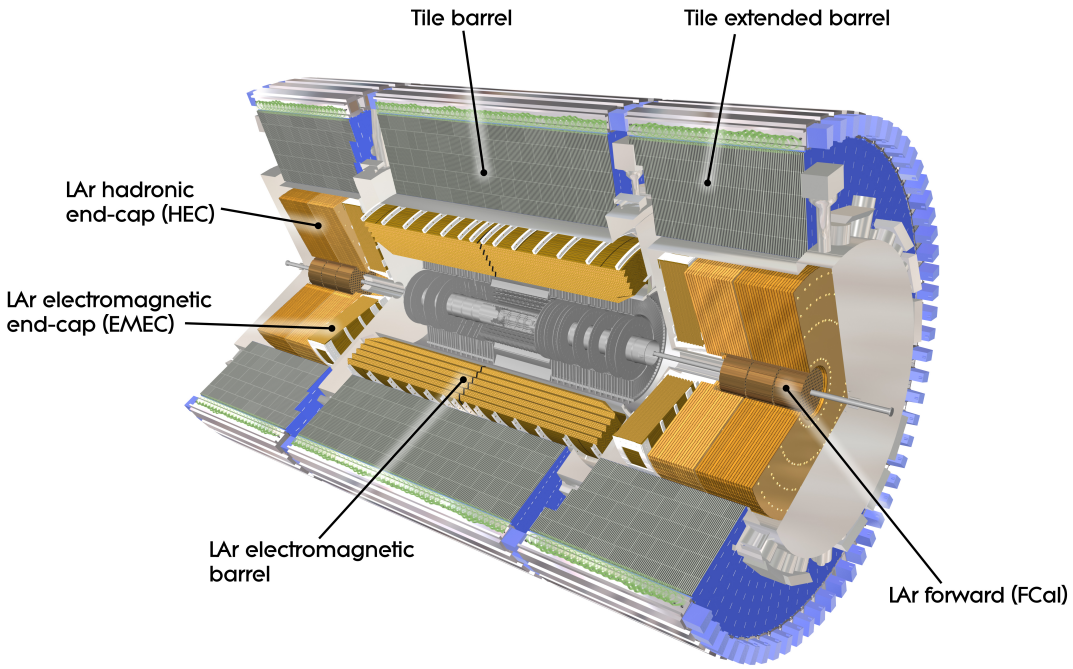

Figure 3.7: Schematic of the ATLAS calorimeter system showing the differing Tile and liquid argon technologies as well as the barrel and endcap layout [52].

layers. The active regions of the HCAL use both Tile [61] and LAr [60] technologies with poorer granularity than the ECAL. The HCAL regions are physically larger however ensuring there is adequate material depth to minimise punch through in which very high energy particles pass through the calorimeter without being fully absorbed. The three-layered barrel consists of steel absorber plates interspersed with scintillating tiles, while the end-caps are each split into four layers which use the same LAr design as the ECAL. To ensure a high material density in the transition region the barrel and end-caps sightly overlap, providing combined sensitivity up to $|\eta| < 3.2$.

LAr forward calorimeter

Lastly a dedicated calorimeter system is located in the forward region extending the calorimeter reach to $|\eta| < 4.9$. The LAr forward calorimeter [60] is placed around 1.2 m from the ECAL necessitating a design with a much higher density to be sufficiently protected against punch-through. The FCAL is split into three layers all of which use liquid argon as the sensitive material. The first layer is optimised to be most sensitive to EM interactions and uses copper as the absorber material, while the latter two layers are designed for hadronic interactions and use a tungsten absorber.

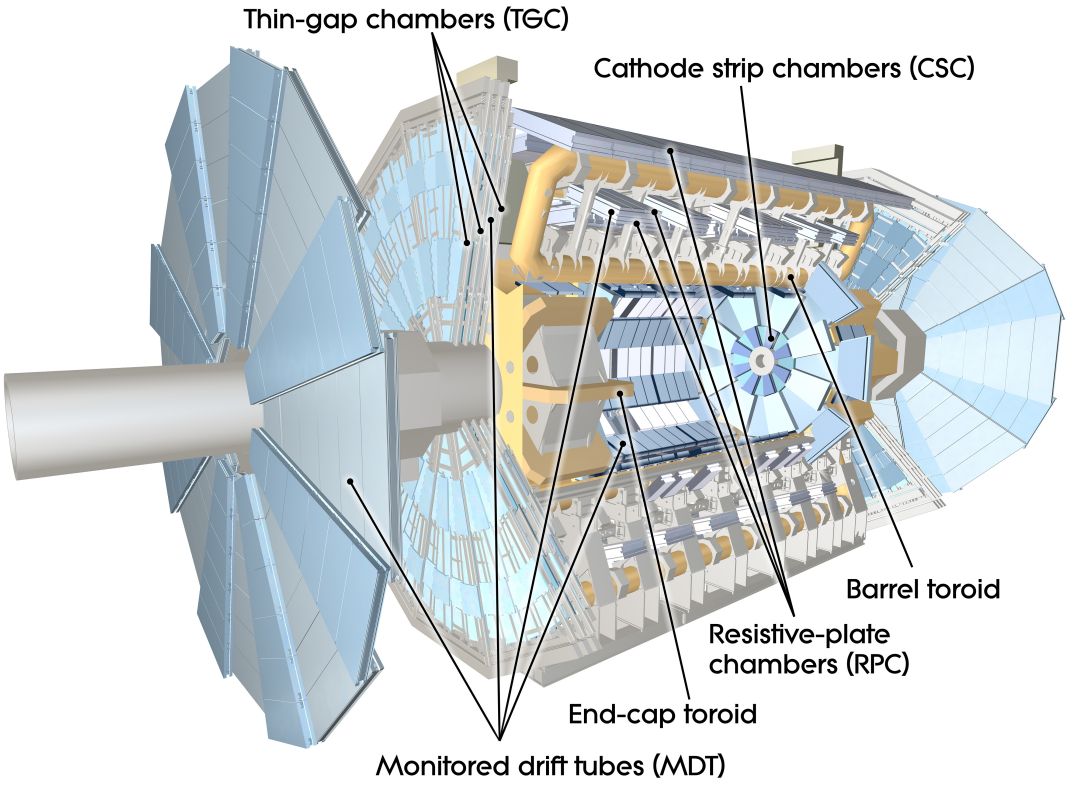

Figure 3.8: Schematic of the ATLAS muon spectrometer highlighting the different detector technologies and the location of the toroid magnets [63].

3.2.3. ATLAS Muon Spectrometer

The outer radius of the ATLAS detector is dedicated to measuring the momentum of charged particles that are not fully absorbed by the calorimeters. Such particles will overwhelmingly be muons and as such the final layer of the ATLAS detector consists of a large muon spectrometer (MS) [62]. The MS is comprised of four principle detector technologies: Monitored Drift Tubes (MDT) and Cathode Strip Chambers (CSC) which primarily handle precision tracking, and Resistive Plate Chambers (RPC) and Thin Gap Chambers (TGC) which are suited to the rapid muon identification required for event triggering (see Chapter 4). Both of these functions rely on measuring the deflection of muons passing through the magnetic field generated by a large air-core toroidal magnet system. A cut-away view of the MS is shown in Figure 3.8 which highlights the positions of the different detector chambers and the toroid magnets.

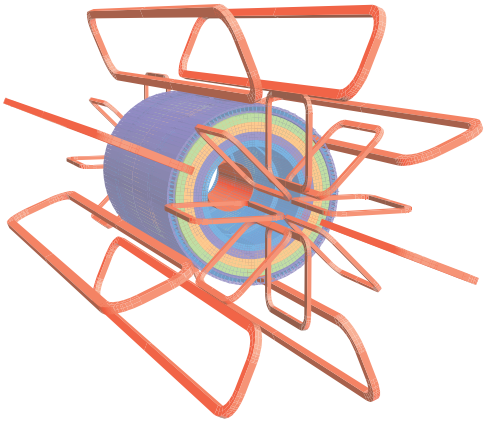

Figure 3.9: Layout of the ATLAS magnets (red) composed of the 2 T central solenoid, surrounded by the eight barrel and endcap toroid coils [37].

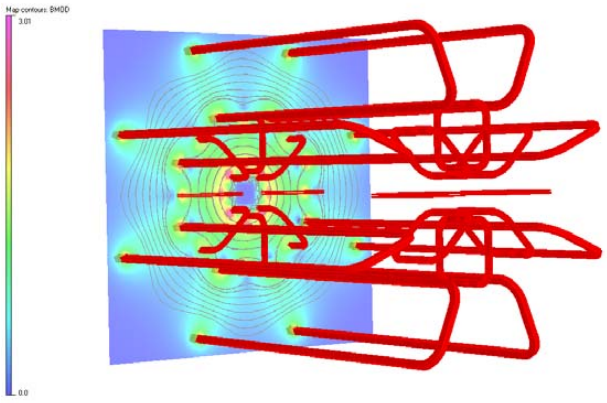

Figure 3.10: Simulated mapping of the magnetic field generated by the ATLAS superconducting toroid. Unlike the solenoid, the toroidal field is not perfectly uniform [64].

Toroid magnet system

The superconducting toroid is composed of three sets of air-core magnets, a barrel and two smaller endcap disks, each with 8 coils and cooled to 4.5 K using liquid Helium. This layout, shown alongside the central solenoid in Figure 3.9, provides a magnetic field roughly orthogonal to the direction of incident muons while minimising the volume of dead material. The field strength varies in the barrel, as shown in Figure 3.10, ranging between 0.15 – 2.5 T with an average strength of 0.5 T, and between 0.2 – 3.5 T in the endcaps. The field is notably weaker in the transition region ($1.4 < |\eta| < 1.6$) despite attempts to strengthen it by rotating the coils within the endcap magnets by 22.5° with respect to those in the barrel.

Precision muon tracking detectors

The majority of muon tracking in both the barrel and endcaps is handled by MDTs which work in a very similar manner to the TRTs found within the inner detector. In the case of the MDTs the drift medium takes the form of aluminium tubes of diameter 3 cm filled with a gas mixture of 93% Argon and 7% CO_2. Each of the three MDT layers in the barrel and endcap consist of between 3 and 8 layers of drift tubes giving a precision of roughly 35 µm in the bending plane (r-z). The barrel MDTs cover a

pseudorapidity range of $|\eta| < 2.7$, however due to the more demanding muon rate at low angles the innermost layer of endcap MDTs is shortened to only cover up to $|\eta| < 2.0$ and is then supplemented with an additional cathode strip chamber spanning $2.0 < |\eta| < 2.7$. The CSC is a multi-wire proportional chamber which incorporates additional cathodes strips alongside an array of anode wires within a gas volume. This reduces the overall drift time allowing it to deal with higher rates, and results in improved spatial resolution as two position measurements are produced for each ionisation event.

Fast muon tracking detectors

While the spatial and momentum resolution of the MDT and CSC systems allow for good tracking performance they are limited by a slow response time and a lack of orthogonal position measurements (r-ϕ plane). Additional dedicated hardware is thus needed to provide rapid muon identification and momentum measurement to allow for the fast trigger decisions outlined in Section 4.1 while also supplementing the tracking vectors. Three layers of resistive plate chambers (RPCs) provide the standalone trigger hardware in the barrel region ($|\eta| < 1.05$). These are gaseous detectors which use two parallel electrode plates with a large electric field between them causing ionising particles between the plates to form avalanches providing a larger signal and allowing for almost instantaneous response. The hardware for the level-1 endcap trigger is formed from three layers of thin gap chambers (TGC) covering the pseudorapidity region $1.05 < |\eta| < 2.4$. These are another form of multi-wire proportional chamber designed to provide improved time resolution and rate compared to the CSCs.

Figure 3.11 shows a quarter slice of the MS along the beam-line with the positions of the various tracking and triggering chambers marked. The straight lines indicate example muon trajectories with no magnetic field active and show how the MS layout is designed to maximise the probability of an incident muon within the active region interacting with at-least three chambers. All together the combined muon spectrometer chambers provide 99% coverage in the endcap region ($1.05 < |\eta| < 2.7$) and ∼80% in the barrel region ($|\eta| < 1.05$) with losses mainly due to gaps in the detector feet region and maintenance shafts around $\eta = 0$.

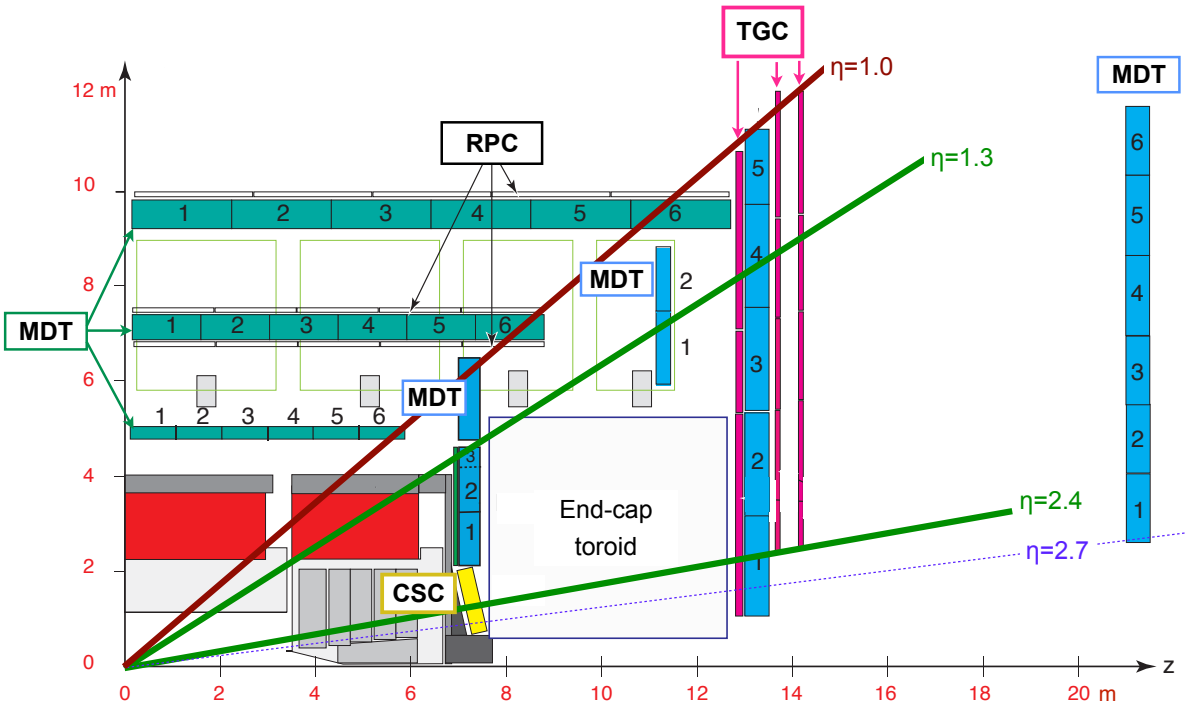

Figure 3.11: Schematic showing a quarter slice along the beam direction (z) of the ATLAS muon spectrometer systems as it was at the end of Run-1 [65]. The apparent fourth MDT layer positioned above the endcap toroid is treated as an extension of the lowest z layer. For Run-2 the endcap MDT chambers were extended and an additional set of RPCs were added around the feet region [66].

Chapter 4.

ATLAS trigger and data acquisition

"On Saturday he ate through one piece of chocolate cake, one icecream cone, one pickle, one slice of Swiss cheese, one slice of salami, one lollipop, one piece of cherry pie, one sausage, one cupcake, and one slice of watermelon. That night he had a stomach ache!"

— Eric Carle, The Very Hungry Caterpillar, Day 6

The event rate within ATLAS during normal proton-proton collisions is extremely high, it is thus not feasible in terms of computing power, nor data storage capacity, to try and record the results of every interaction.[1] Instead, collisions that produce interesting physics are prioritised by analysing detector deposits in real-time via various fast algorithms and lookup tables known collectively as 'triggers'. These are each tuned to pick out signals of different high energy final-state particles, e.g. leptons or hadronised quarks. In many cases single object triggers are combined to search for more complex combinations of objects indicative of a specific physics event.

The ATLAS Trigger and Data Acquisition (TDAQ) system [67] consists of two stages aimed at reducing the data rate to a manageable level before writing out to disk. This starts with a level-1, hardware-based trigger designed to reduce the event rate from $\sim$40 MHz to $\sim$100 kHz using information from the calorimeters and muon spectrometer. This is followed by a series of slower but higher precision software-based algorithms with access to information from the full detector, collectively known as the high Level Trigger (HLT). Algorithms which require access to ID tracks or provide more precise object reconstruction are inherently more CPU intensive, the HLT

[1] Doing so would also not result in tremendously efficient physics analyses.

algorithms are thus organised into dependency chains with the possibility to reject events at each stage and more computationally heavy algorithms run later in the chain. In this way resources are not wasted running intensive algorithms unless necessary. The HLT is designed to further reduce the event rate from ∼100 kHz to ∼1 kHz.

In order to optimally saturate the TDAQ output the various level-1 and HLT triggers are organised into a modular menu, from which individual triggers can be added or removed easily. This allows the physics program to be changed on the fly to target certain types of events and also helps maintain the output rate around 1 kHz to ensure the maximum possible data yield is achieved. Prescale factors are also applied to certain triggers which randomly reject a certain percentage of events that would normally pass, thus helping control the rate as the luminosity changes [66].

The following sections cover the design and performance of the ATLAS muon trigger system in more detail along with a summary of the work I have done producing a standalone monitoring trigger for use during the last year of Run-2. The effectiveness of the muon trigger system is particularly important for the analysis discussed in Part II of this thesis which picks events based on both muon and electron triggers, with ∼50% of events being triggered by the presence of a high p_{T} muon.

4.1. Muon trigger system

4.1.1. Level-1 muon trigger

At level-1, dedicated electronics use spatial and timing information from hits in either of the fast tracking detectors (RPCs or TGCs) to produce very rough p_{T} estimates for passing muons. To ensure fast operation (∼2 µs) these estimates are made relative to straight line, infinite momentum, tracks extrapolated from the innermost hit through the nominal interaction point. Wherever these tracks pass through outer RPC or TGC layers, coincidence windows are drawn with size based on p_{T}. Muon candidates are then split into three high p_{T} and three low p_{T} thresholds based on hits within the coincidence windows in each layer. In this way rough p_{T} estimates can be made using as few as two hits in the muon detector with the IP taken as a third data point. The requirements for each threshold for barrel and endcap regions is shown in Table 4.1. The (η, ϕ) values for each level-1 muon are passed on to the HLT in the next stage to allow for more efficient reconstruction within regions of interest (RoIs).

Table 4.1: Minimum p_T and hit coincidence requirements for the low p_T (1–3) and high p_T (4–6) thresholds of the level-1 muon trigger during Run 2.

Threshold	L1 trigger	p_T [GeV]	RPC layers (barrel)	TGC layers (endcap)
1	MU4	4	2	3*
2	MU6	6	2	3
3	MU10	10	2	3
4	MU11	10	3	3
5	MU20	20	3	3
6	MU21	20	3†	3

*Only two hits required in certain regions.
†Except in the detector feet region where the MU21 trigger is not active.

4.1.2. Muon high level trigger

The combined high level trigger provides more detailed software reconstruction of muon candidates using algorithms falling broadly into two categories; fast reconstruction algorithms - designed primarily for rate reduction, and precision algorithms - to provide more accurate muon reconstruction.

The fast reconstruction algorithms are derived from the legacy level-2 trigger and use the RoI information passed from the level-1 decision as a starting point. Muon candidate tracks are refined using data from nearby hits in the MDT chambers, using look up tables for reduced computational complexity. These improved MS stand-alone tracks are then extrapolated backwards into the inner detector volumes and combined with the closest-fit ID track in η, ϕ space. From this, a new combined muon object is formed with p_T given by a weighted average of the two tracks.

The precision reconstruction follows a similar process, starting from already refined tracks and producing MS stand-alone muons, this time using offline style track reconstruction (Section 5.2.2). These are then extrapolated inwards and combined with additional ID track information including potential track segments and calorimeter tagged ID tracks allowing for more combination possibilities. If no combined track can be formed in this way the process is reversed extrapolating unmatched ID tracks outwards and combining these with hits from the muon spectrometer.

Lastly, full scan searches are carried out over the full detector volume with the aim to reconstruct muons with trajectories outside of the original RoIs that were missed by the level-1 muon system. The same methods as the precision reconstruction are used but with access to the full detector geometry. The full scan reconstruction is significantly more resource intensive as a result.

4.2. Online muon trigger efficiency monitoring

During periods of active data-taking it is useful to make efficiency measurements in order to monitor the status of the trigger in real time. Parallel to the main analysis work I also created a new muon trigger which allowed for such online efficiency measurements to be produced and monitored during Run-2.

4.2.1. Tag and probe algorithm

Different tag and probe variants exist and are a fairly ubiquitous tool for per-object efficiency monitoring across LHC experiments. The underlying process requires exploiting some known resonance, in this case the di-muon resonance $Z \rightarrow \mu\mu$, to measure an unbiased trigger efficiency directly from data. Provided the two muons are sufficiently independent the event can be *tagged* by one muon and the other used as a *probe* to determine the trigger efficiency. Studies comparing tag and probe efficiencies with those calculated from simulated events [68] have shown that correlations between the tag and probe objects are negligible ensuring this is a valid approach.

This method can be used to measure the level-1 trigger efficiency relative to muons reconstructed by the precision HLT full scan. Events which pass an existing full scan di-muon trigger are selected and the muon tracks are matched to RoI information from the level-1 trigger. Tight matching criteria are then applied to determine tag muons based on proximity to valid RoIs, whilst looser selections are employed to find probe muon candidates. By ΔR matching probes to the remaining RoIs an estimate of the efficiency of the level-1 trigger can be obtained.

4.2.2. Trigger selection

A new trigger was implemented to perform online efficiency monitoring starting from the existing HLT trigger: 'HLT_mu22_mu8noL1' using the MU20 level-1 threshold. This should only allow events with at least one muon with $p_{\mathrm{T}} > 20\,\mathrm{GeV}$ as measured by the level-1 system and $p_{\mathrm{T}} > 22\,\mathrm{GeV}$ as measured by the HLT, as well as at least one separate muon with $p_{\mathrm{T}} > 8\,\mathrm{GeV}$ as measured by the HLT, with no level-1 trigger requirement on the second muon. A higher minimum p_{T} requirement of $p_{\mathrm{T}} > 10\,\mathrm{GeV}$ is applied to all HLT muons on top of the base trigger to improve the reliability of the efficiency measurement. A further requirement is then placed on all HLT reconstructed muons in the event to ensure they are formed from combined rather than stand-alone tracks. Lastly, events with more than two muons of opposite sign are dealt with by picking the muon pair with the closest invariant mass to that of the Z-boson and discarding the rest.

4.2.3. Tag and probe definitions

After these selections are applied, the level-1 information is accessed and ΔR values are calculated for each muon-RoI pair. Tag criteria are applied to each muon in the pair separately defining a valid tag (μ_T) as requiring both:

- $p_{\mathrm{T}} > 10\,\mathrm{GeV}$ and
- $\Delta R(\mu_T, \mathrm{RoI}_{\geq 5}) < 0.1$,

where $\mathrm{RoI}_{\geq 5}$ is a level-1 RoI of threshold 5 or 6 (MU20 or MU21).

As described above every instance of a valid tag muon within a pair is equivalent so for each pair there is the potential for up to two contributions to the efficiency. For each tag a candidate probe (μ_P) is then any other muon satisfying all three of:

- $p_{\mathrm{T}} > 10\,\mathrm{GeV}$ and
- $\Delta R(\mu_P, \mu_T) > 0.2$ and
- $|m_Z - m(\mu_P, \mu_T)| < 10\,\mathrm{GeV}$.

Probe candidates are then specified as being level-1 matched if they are $\Delta R < 0.1$ away from a different RoI than the tag. Figure 4.1 shows a schematic of the tag and probe process with the above selection criteria applied.

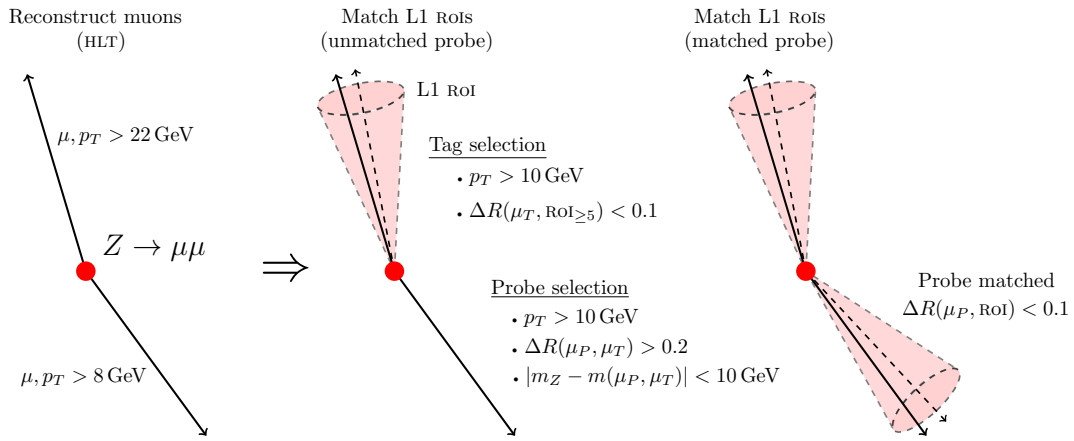

Figure 4.1: Schematic of the $Z \to \mu\mu$ tag and probe selection criteria used for online muon efficiency monitoring.

4.2.4. Efficiency measurement

To calculate an unbiased efficiency all final state muons must be initially considered as valid tags. Thus a set number of $Z \to \mu\mu$ events can be split into three groups based on the tag and probe outcome:

1. Events where both muons pass the tag criteria (N_{TT})
2. Events where one muon is a valid tag and the other passes the probe selection **and** is matched with a RoI from the level-1 (N_{TP})
3. Events with one tag and and one valid probe without a matching RoI (N_{TF})

Any possibilities without a valid tag are ignored as these criteria are determined by the hardware trigger so events without a tag muon are not recorded. Every occurrence of a tag is counted as a new event and the total number of probe candidates given by:

$$N_{\text{Probe}} = 2N_{TT} + N_{TP} + N_{TF} \tag{4.1}$$

The level-1 trigger efficiency (ϵ_{L1}) can then be calculated as the ratio of events with matched probes to the total probe candidates:

$$\epsilon_{L1} = \frac{2N_{TT} + N_{TP}}{2N_{TT} + N_{TP} + N_{TF}} \tag{4.2}$$

4.3. Efficiency results

Measurements are made as a function of the transverse momentum (p_{T}), pseudo-rapidity (η), and the azimuthal angle (ϕ) of the muon. Additionally, as the initial level-1 threshold decision for each muon is retained, efficiencies are also calculated separately for each of the six thresholds. It should be noted that the level-1 thresholds are inclusive, thus e.g. a probe candidate tagged with threshold decision 5 (MU20) is counted towards the efficiency of thresholds 1-5 but not 6. Any probe muon candidates without a matching RoI are counted in all thresholds to avoid biasing towards higher efficiencies at p_{T} lower than the threshold acceptance.

Several tests were performed to validate the online algorithm before it was added to the ATLAS software packages. Figures 4.2–5 show a selection of efficiency results from these tests, derived from the re-processing of a single run of 13 TeV pp events recorded by ATLAS in 2017. The results correspond to an integrated luminosity of $5.276 \times 10^4\,\mathrm{nb}^{-1}$ and only statistical uncertainties are included on the plots.

Figure 4.2 shows the barrel and endcap efficiencies with respect to the probe muon p_{T} for all six level-1 thresholds defined in table 4.1. A noticeably lower overall efficiency is observed in the barrel region compared to the endcap. This disparity is primarily due to gaps present in the muon spectrometer coverage to accommodate maintenance tunnels around $\eta = 0$, with some additional gaps found around the detector feet region. Both plots also demonstrate the expected efficiency turn on at low p_{T} with a shallower slope observed for higher thresholds, matching the higher p_{T} requirements used.

Similarly Figure 4.3 shows the barrel and endcap efficiencies with respect to ϕ of the probe muon, demonstrating the same lower overall efficiency in the barrel compared to the endcap. A significantly flatter distribution overall is observed in the endcap region suggesting a relative ϕ invariance. This is expected and highlights the geometric differences between the two regions with respect to the beam pipe. The endcap is composed of discs positioned transverse to the beam direction making it perfectly symmetrical in ϕ whilst the toroidal barrel geometry completely surrounds the beam line naturally resulting in an angular dependence of the flat RPC modules. Figure 4.3a also shows a notable efficiency drop between $-2 < \phi < -1$ for threshold 6 only, due to the MU21 trigger specifically being disabled in the detector feet region.

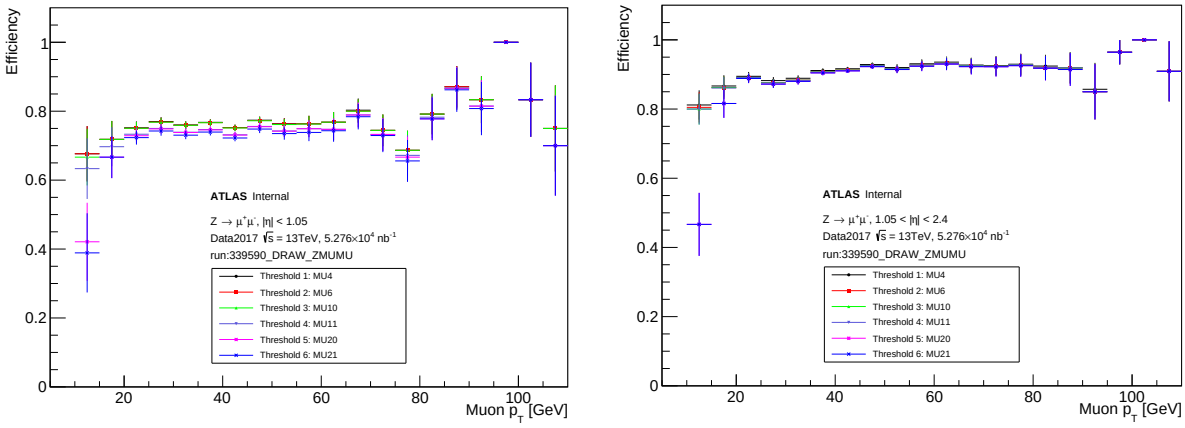

(a) **(b)**

Figure 4.2: Level-1 trigger efficiency in bins of probe muon p_{T} within (a) barrel, (b) endcap pseudorapidity regions. Efficiencies for all six level-1 thresholds are shown.

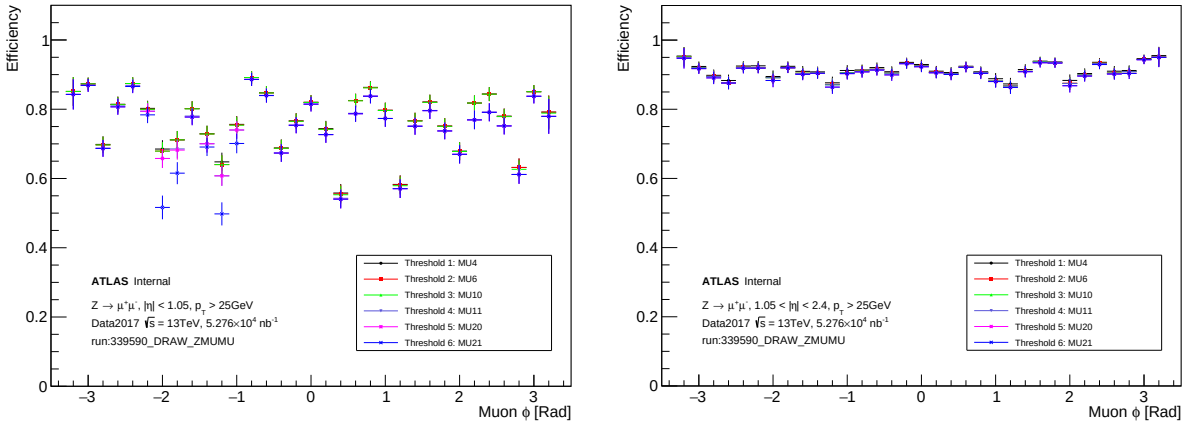

(a) **(b)**

Figure 4.3: Level-1 trigger efficiency in bins of the azimuthal angle ϕ within (a) barrel, (b) endcap pseudorapidity regions. Efficiencies for all six level-1 thresholds are shown.

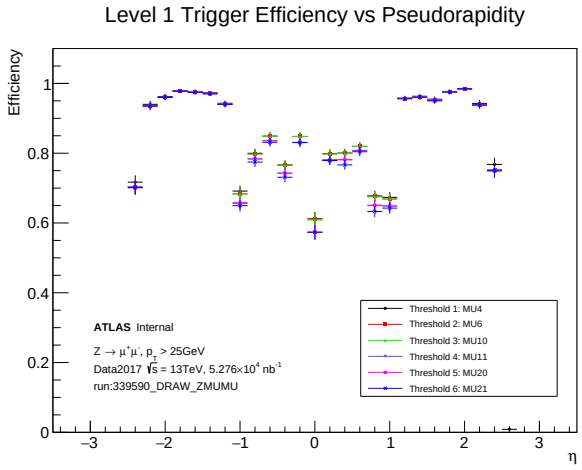

Figure 4.4: Level-1 trigger efficiency in bins of pseudorapidity (η). Efficiencies for all six level-1 thresholds are shown.

Figure 4.4 shows the combined barrel and endcap efficiencies with respect to the probe muon pseudorapidity. A more detailed view of the efficiency separation between the barrel and endcap regions is observed here as well as clear structures within both regions. The sharp drop off at high $|\eta|$ defines the cutoff for the detector acceptance and a reduced efficiency can be seen in the expanded acceptance region $2.4 < |\eta| < 2.7$ due to a lack of TGC chambers beyond $|\eta| = 2.4$. Significant drops in efficiency are also observed around the transition region between the barrel and endcap at $|\eta| \approx 1$. Here the RPC layers in the barrel are more parallel to incident muons and this, combined with overlapping of the endcap MDT layers, results in an increased number of fake offline muon tracks. As before, lower efficiencies are also present around $\eta = 0$.

Figure 4.5 shows a 2D representation of the level-1 efficiency in the barrel and endcap regions, providing a more detailed geometric overview of the trigger performance, again this is done separately for each threshold but only MU21 is shown here. The 2D plots are still able to retain reasonable statistics despite a significant increase in overall bins. The same trends observed in the individual ϕ and η plots are also visible here making these plots useful as a cross check for problems flagged up in the 1D figures.

In general, the results of these tests are excellent, showing that the ϕ and η resolutions are fine enough to reliably monitor the status of single RPC modules. Additionally, the ability to monitor all thresholds individually for drops in efficiency is a distinct advantage of this method. As an additional cross-check results were compared against offline efficiency measurements [69] and were found to be in good agreement.

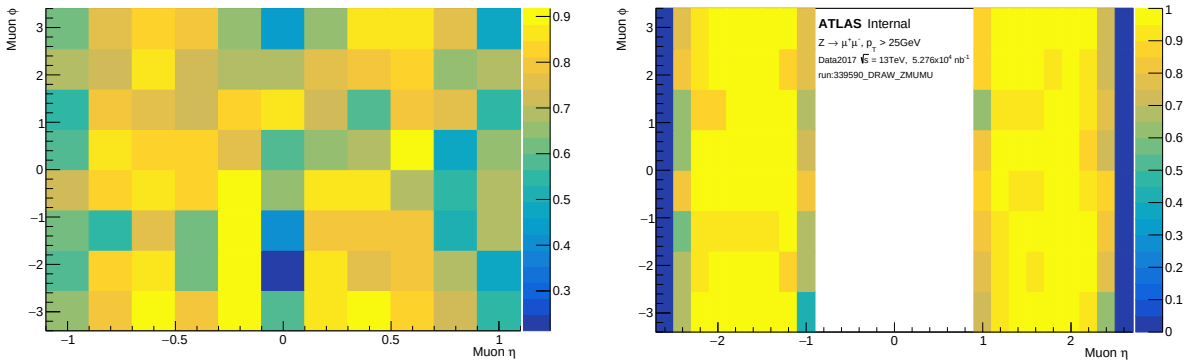

(a) (b)

Figure 4.5: Level-1 trigger efficiency for the MU21 threshold in combined bins of probe muon ϕ and η within (a) barrel, (b) endcap pseudorapidity regions.

4.4. ATLAS control room monitoring

Once validated, the output of the online tag and probe algorithm was integrated into the ATLAS monitoring framework [70] as part of the Data Quality Monitoring Display (DQMD) as well as the Online Histogram Presenter (OHP) [71]. The DQMD is the primary interface used for monitoring the various trigger subsystems within the ATLAS control room. This uses a system of individually calibrated tests to compare the output of each algorithm in the ROOT [72] data analysis framework to a unique reference taken from the output of recently verified events. In this way any dramatic changes in the output distribution can be automatically flagged allowing on-site experts to view the output manually and check the underlying cause. A per-bin comparison test was chosen which checks the number of bins (n_b) that are $N\sigma$ away from their reference value, where σ is the combined statistical error of the test and reference samples. During Run-2 data taking this test was applied to the one dimensional plots shown above with $n_b = 2$, and $N = 4$.

The OHP is a secondary monitoring display where additional histograms can be presented without the need for automatic checks. This is used as an extension to the DQMD for debugging purposes and as a fast cross-check for problems identified elsewhere. For this purpose the OHP was also updated to include the two dimensional η vs ϕ plots shown above.

The updates to the DQMD and OHP were in use for the final four months of Run-2 data taking, during which time the system flagged up several drops in the muon trigger

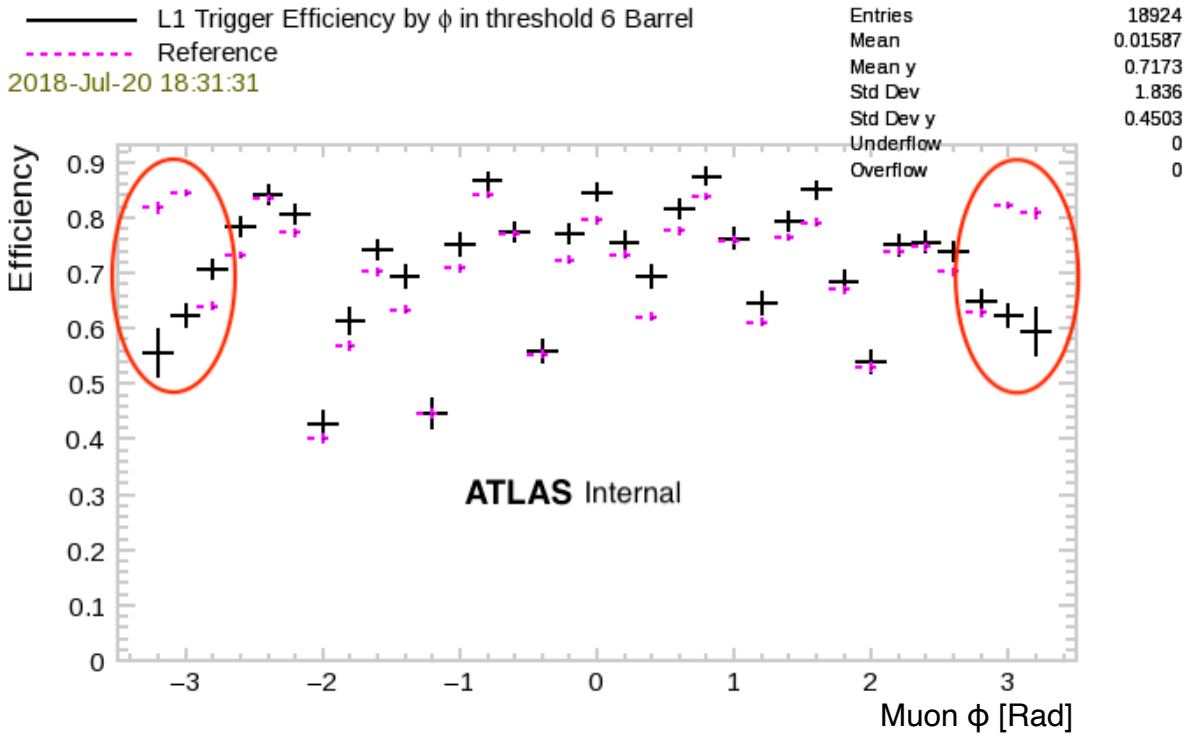

Figure 4.6: Screenshot of the trigger efficiency monitoring output used within the ATLAS control room. Measured values of the MU21 level-1 efficiency vs ϕ_μ from the online tag and probe algorithm (black) are compared to reference values from previously validated events (pink) showing drops in efficiency at high $|\phi|$.

efficiency allowing the underlying cause to be discovered and fixed as designed. An example of one such monitoring plot is shown in Figure 4.6, which was used during data taking in 2018 to signal an unexpected drop in efficiency at high $|\phi|$ values, due to several RPC modules running at low voltage, significantly reducing the overall trigger rate. The figure shows output from the efficiency monitoring algorithm in black along with reference values in pink, with areas of significantly lower efficiency circled. In general, the level-1 efficiencies vary slightly from the reference values due to expected variations in overall trigger efficiency between runs, these variations are not considered problematic. However, in the high $|\phi|$ regions, the level-1 efficiencies are significantly below the reference values indicating a more significant problem which was subsequently fixed, reducing the volume of data collected with compromised muon trigger performance.

Chapter 5.

Object reconstruction

"In the game of chess you can never let your adversary see your pieces."
— Zapp Brannigan, Futurama S1, E14 - Love's Labors Lost in Space

Before being analysed the raw information recorded by the detector systems needs to be combined and reconstructed into sensible physics objects e.g. electrons or jets of hadronic particles. Performance of the reconstruction is measured in data control samples and used to derive per-object calibrations. This chapter describes the reconstruction and relevant calibration processes for all physics objects used in the analysis outlined in Part II.

5.1. Low-level objects

Despite many different technologies being used across the various sub-detectors the resultant measurements can be split simply into either spatial hits or energy deposits. These give rise to two low-level objects: tracks produced from spatial hits and topological clusters (topo-clusters) formed from energy deposits. Additionally 'particle flow objects' are built by combining tracks and topo-clusters and are used as the input to jet clustering algorithms. The high-level objects used in physics analyses are created using combinations of these, as depicted in Figure 5.1, which shows the ATLAS event display for a candidate boosted $t\bar{t}$ event. Uncertainties related to the reconstruction of these low-level objects are not considered in the analysis in Part II as they are superseded by uncertainties on the physics objects themselves.

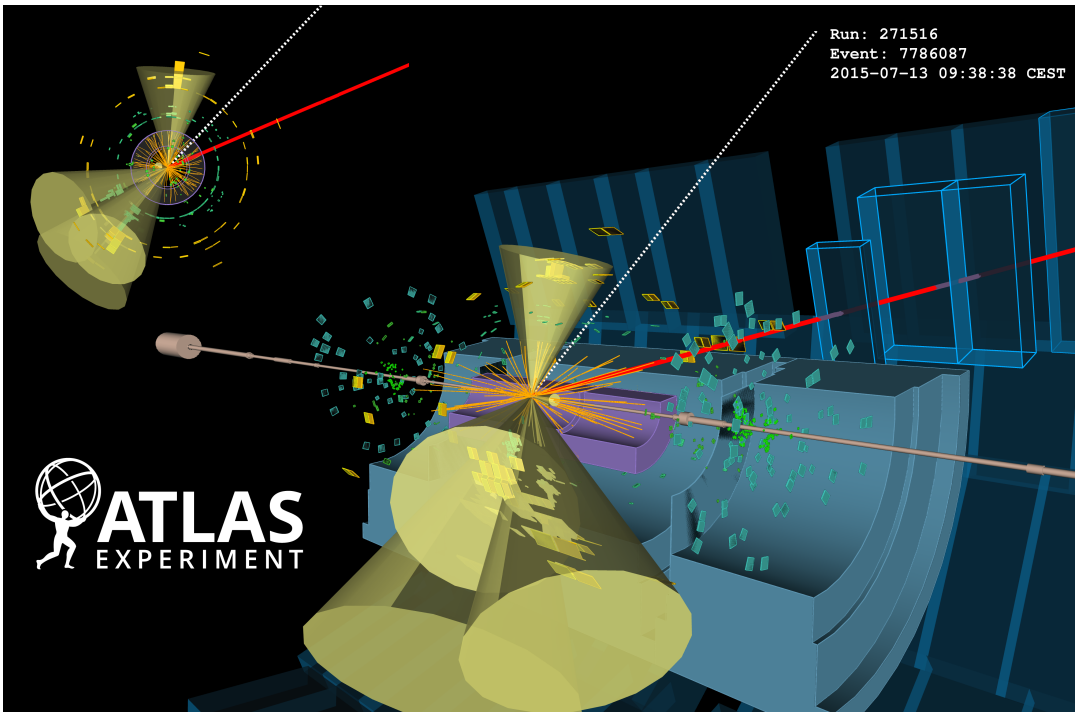

Figure 5.1: Event display of a candidate boosted top-quark pair production event recorded by ATLAS at a collision energy of 13 TeV in 2015 [73]. The red line shows the path of a muon reconstructed from deposits in the inner detector and muon spectrometer. The dashed white line indicates the direction of missing transverse momentum in the event. The green and yellow bars represent energy deposits in the electromagnetic and hadronic calorimeters from which four small-radius jets (yellow) are constructed. The three lower jets are overlapping and can be re-clustered into a single large radius jet with a mass close to the top-quark mass. The upper jet contains a secondary vertex and is tagged as likely containing a b-quark decay. Curved tracks from charged particles in the inner detector are shown in orange.

5.1.1. Tracks

The trajectories of charged particles as they pass through the ATLAS detector are mapped out by connecting detector hits together to form track objects in both the inner detector and the muon spectrometer. Strong magnetic fields result in helical tracks allowing both the charge and momentum of particles to be inferred. In high energy collisions, and with several pp interactions expected per bunch crossing, the ATLAS tracking detectors become densely populated with hits. This makes fitting tracks a particularly difficult process requiring several steps, outlined in more detail in [74].

Inner detector tracks

In the ID this process begins by grouping nearby hits together to form three-dimensional space-points. This is done separately in the pixel and SCT sub-systems. To start the iterative fitting procedure a collection of track seeds are created by connecting sets of three space-points within the same sub-system giving a first rough momentum estimate. Seed trajectories are then extrapolated in both directions and a combinatorial Kalman filter [75] is used to find additional space-points which are compatible with the initial path. At this stage multiple track candidates can be created from a single seed, thus containing shared space-points. A cyclical ambiguity-solving step is then run to determine which track candidates to accept and which to reject. The first step is to give each track a score based on several criteria including the number of space-points, the quality of the fit, and the number of layers in the pixel and SCT that do not have a space-point compatible with the track (holes). A neural-network [76] is then used to help distinguish cases where common space-points truly contain hits from multiple incident particles (merged) or where one of the tracks is mis-assigned (shared). Merged space-points are kept in both tracks and shared space-points are assigned to the track candidates with the highest score. After these steps, the final set of accepted tracks are those which pass a series of basic selection criteria:

- $p_{\mathrm{T}} > 400\,\mathrm{MeV}$
- $|\eta| < 2.5$
- Minimum of 7 clusters between pixel (4 available) and SCT (8 available)
- Maximum of one shared space-point
- ≤ 2 holes overall with ≤ 1 hole in the pixel detector
- $|d_0^{\mathrm{BL}}| < 2.0\,\mathrm{mm}$
- $|z_0^{\mathrm{BL}} \sin(\theta)| < 3.0\,\mathrm{mm}$

where the transverse impact parameter (d_0^{BL}) is defined as the distance of closest approach of the track to the beam-line in the transverse plane. The longitudinal impact parameter (z_0^{BL}) is the distance along z from the primary interaction vertex (see Section 5.1.2) to where d_0^{BL} is measured, and θ is the polar angle of the track. Lastly a final high resolution fit is performed on the accepted tracks using additional neural networks [76] to determine more accurate space-point coordinates.

Muon spectrometer tracks

For the reconstruction of muons, tracks fitted in the ID are matched to separate track objects in the muon spectrometer. These MS tracks are built using a similar procedure to those in the ID; however analytical fitting methods cannot be used due to the increased complexity of the toroidal magnetic field. Instead a Hough transform [77] is used to fit straight line track segments by mapping hits to crossing points in a line parameter space. This is done separately for each layer of MDT chambers, with hits in the trigger chambers (RPCs and TGCs) used to provide additional coordinates in the orthogonal (r, ϕ) plane. The MS tracks are completed by extending fitted "seed" segments in the central layers to the inner and outer layers as described in [78]. To ensure high quality tracks, information from at least two segments must be combined to form a track, except for track candidates in the barrel-endcap transition region $(1.0 < |\eta| < 1.4)$ in which a single, high-quality segment may be used. As individual track segments can belong to multiple track candidates an overlap removal procedure is followed; assigning segments to tracks with the best χ^2 fit. If two tracks share segments in the two innermost layers but are each associated with unique track segments in the outermost layer then both tracks are kept.

5.1.2. Vertices

Reconstructed tracks in the ID can be extrapolated backwards to search for locations where several tracks meet. These indicate an *interaction vertex* - a point in space in which a particle-particle interaction or a single particle decay produced a series of new tracks. The primary vertex in each event is defined as the vertex containing the maximum total track p_{T} calculated by summing the squared transverse momenta for all tracks associated to the vertex: $\sum (p^2_{\mathrm{T,track}})$. The primary vertex is assumed to correspond to the hard-scatter pp interaction. The remaining vertices are labelled secondary vertices and are assumed to originate from either pileup or decays of long-lived particles from the hard-scatter, such as B-hadrons.

5.1.3. Topological clusters

The energy loss of incident particles in the calorimeters is mapped by sequentially grouping the energy deposits in individual cells into larger three-dimensional clusters.

These topo-clusters are not necessarily a proxy for the total energy contribution from a single particle but can equally capture only a fraction of a particle's interaction within the calorimeters or include fractional or whole contributions from multiple particles. The method for topo-cluster formations is outlined in [79] and relies on the cell significance:

$$\zeta_{\text{cell}}^{\text{EM}} = \frac{E_{\text{cell}}^{\text{EM}}}{\sigma_{\text{noise,cell}}^{\text{EM}}}, \tag{5.1}$$

where $E_{\text{cell}}^{\text{EM}}$ is the total cell signal and $\sigma_{\text{noise,cell}}^{\text{EM}}$ is the expected average noise of the cells estimated separately for each data taking year using simulated events. The EM superscript denotes that the cell output for these values are set to the EM scale[1] ensuring correct energy reconstruction for electrons and photons.

Topo-clusters are built starting from a seed cell which requires a significance greater than 4. The cells neighbouring this seed, in the same or adjacent layers, that have significance greater than 2 are then collected and merged to form a proto-cluster. This process is repeated looking at the neighbours of the last added cells until no direct neighbours have the required significance. At this point all remaining neighbouring cells with a non-negative signal are added. This final step results in a form of dynamic noise suppression allowing for a higher noise threshold but still ensuring cells in one layer adjacent to active clusters are included even if they are below the regular noise threshold.

Before the final topo-cluster is defined an additional step is run to split proto-clusters with multiple local energy maxima, defined as a cell with $E_{\text{cell}}^{\text{EM}} > 500\,\text{GeV}$, with at least four neighbours, and with each neighbour having a lower cell energy. The clustering algorithm is run again starting from pairs of two local maximum and splitting energy contribution from any cells shared between the two. The splitting fractions are determined by the energy of the maxima and the cell's proximity to the centre of mass of each proto-cluster.

To improve the η resolution of the jets constructed from constituent topo-clusters a per-event "origin correction" is applied to each topo-cluster such that its origin better matches the position of the primary vertex. This process is dependent on the depth

[1] The calorimeter response to hadrons is not the same as for electrons and photons thus an alternative scale (LCW) is available including specific corrections for hadrons. Only the EM scale is used when reconstructing objects used in the analysis in Part II.

within the calorimeter and η of the original topo-cluster and is designed not to change the measured energy.

5.1.4. Particle flow objects

In order to improve the resolution of the final reconstructed jet objects a particle flow algorithm [80] is used which combines information from the tracking and calorimetric sub-detectors to build *particle flow objects*. This allows the improved momentum and angular resolution of the tracker at low momentum to be used while also improving robustness to pileup by virtue of integrating vertex information.

To ensure energy information is not double counted between tracks and topo-clusters a multi-step process is followed to systematically remove energy contributions in the topo-clusters which correspond to matched tracks. The steps of the process are shown in Figure 5.2, and detailed below:

1. Select high quality tracks (≥ 9 total silicon hits and no pixel holes)
2. Match each track to a best-fit cluster ($\frac{E^{\text{clust}}}{p^{\text{trk}}} > 0.1$) and Min($\Delta R'$)
3. Calculate the expected energy deposit given the track momentum $\langle E_{\text{dep}} \rangle$
4. Decide if additional topo-clusters are needed to fully account for expected energy
5. Subtract expected energy from matched topo-cluster(s) cell-by-cell
6. Remove leftover topo-cluster energy if it is consistent with shower fluctuations

where E^{clust} and p^{trk} are the energy and momentum of the topo-cluster and track respectively and the matching parameter $\Delta R'$ is given by:

$$\Delta R' = \sqrt{(\frac{\Delta\phi}{\sigma_\phi})^2 + (\frac{\Delta\eta}{\sigma_\eta})^2}, \tag{5.2}$$

where σ_ϕ and σ_η represent the phi and eta widths of the topo-cluster. The expected energy deposited by a track with momentum p^{trk} is given by:

$$\langle E_{\text{dep}} \rangle = p^{\text{trk}} \langle E^{\text{clus}}_{\text{ref}} / p^{\text{trk}}_{\text{ref}} \rangle, \tag{5.3}$$

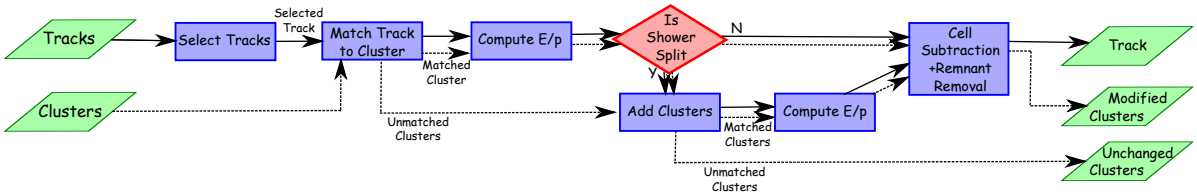

Figure 5.2: Flow chart the particle flow algorithm, starting from a selection of tracks and topo-clusters and resulting in a combined particle-flow object. The output consists of high quality tracks representing charged particles, remnants of track-matched topo-clusters which have had a portion of their energy subtracted, and unmodified topo-clusters representing energy deposits of neutral particles. Figure from [80].

where the expectation value $E_{\text{ref}}^{\text{clus}} / p_{\text{ref}}^{\text{trk}}$ is determined from simulation. Figure 5.3 demonstrates an idealised example of the energy subtraction process from step 5. Any topo-clusters not matched to a track are left unmodified and retained in the output as neutral particle-flow objects, representing energy deposits from neutral particles.

5.2. Leptons

Unless otherwise specified the use of the term lepton in this thesis refers to the group of electrons and muons, along with their respective anti-particles, which can be identified and reconstructed with high efficiency. For the analysis in Part II, tau leptons are not used explicitly. Taus which decay into electrons or muons are capable of triggering a valid event, however no distinction is made between these and regular electrons or muons.

5.2.1. Electrons

Reconstruction

Electrons are reconstructed by matching tracks from the inner detector to topo-clusters built only using energy deposited in the EM calorimeters, as described in [81]. Before additional event-based selections are applied the electrons must have at least transverse energy $E_{\text{T}} > 27$ GeV and be reconstructed fully within the active regions of the EM calorimeter ($|\eta| < 1.37$ or $1.52 < |\eta| < 2.47$ to avoid the barrel-endcap transition region). Extra requirements are imposed on the track candidates to ensure they are

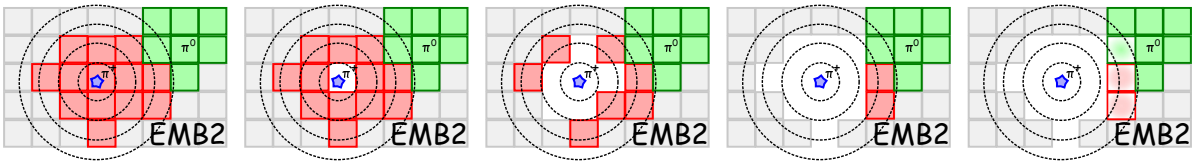

(a) (b) (c) (d) (e)

Figure 5.3: An idealised example of particle flow cell-by-cell subtraction for incident π^+ and π^0 particles. Cells in a single EM calorimeter layer are shown coloured in grey if they are not within a topo-cluster and red(green) if they belong to a $\pi^+(\pi^0)$ topo-cluster. The π^+ track (blue star) is extrapolated to the EM layer and rings are placed around this. Cells are subtracted from the topo-cluster ring by ring starting with the centre of the shower, and moving outwards, (a) $\rightarrow$ (e). The final ring contains more energy than the expected energy $\langle E_{\text{dep}} \rangle$, thus the cells are only partially subtracted. Figures taken from [80].

closely associated to the primary vertex, reducing the effect of tracks from pileup. The requirements are:

- $(|d_0^{\text{BL}}|/\sigma_{d_0} < 5)$
- $(|\Delta z_0 \sin\theta| < 0.5\,\text{mm})$

where Δz_0 is the longitudinal impact parameter corrected for the position of the reconstructed primary vertex, d_0^{BL} is the transverse impact parameter relative to the beam line and σ_{d_0} is its associated uncertainty.

To ensure that electron candidates are suitably distinct from other physics objects with similar signatures (low energy jets) each candidate is given a probability score using a multivariate likelihood method [81, 82]. Variables with good electron discriminating power are used as inputs including information from the calorimeters, tracks, and track-cluster matching. Different working points are defined with the 'Tight' working point used in the analysis in this thesis corresponding to an average selection efficiency of 80% and a background rejection factor of 3.5 [81].

Lastly electron candidates are required to be further isolated from activity in the detectors by applying maximum allowances on the total sum of nearby energy in the calorimeter and the sum of the transverse momentum of nearby tracks in the ID. 'Tight' requirements are used for both of these resulting in $E_{\text{T}}^{\text{cone20}}/p_{\text{T}} < 0.06$ for the calorimeter isolation and $p_{\text{T}}^{\text{varcone20}}/p_{\text{T}} < 0.06$ for the track isolation. Here $E_{\text{T}}^{\text{cone20}}$ is the sum of transverse energy in a cone of $\Delta R = 0.2$ around the electron candidate,

similarly $p_{\mathrm{T}}^{\mathrm{varcone20}}$ is the p_{T} sum of tracks ($p_{\mathrm{T}} > 1\,\mathrm{GeV}$) in a variable cone around the electron, with maximum $\Delta R = 0.2$, which shrinks for electrons with larger p_{T}.

In Section 7.3.1 a sample with looser electron and muon reconstruction criteria is used to estimate the background from multijet events. For this sample no isolation requirements are used and the 'medium' likelihood working point is selected, corresponding to an average selection efficiency of 88% and a background rejection factor of 2.0 [81].

The analysis in Part II makes use of simulated collision events reconstructed without simulating the relevant detector response (particle-level), described in more detail in Chapter 6. Only stable particles (those with a lifetime > 30 ps) in the generator event record are used to construct particle-level objects. The definition of electrons and muons at particle-level includes an additional *dressing* step in which the four-momenta of any prompt[2] photons within $\Delta R < 0.1$ around the lepton are added to the lepton four-momentum and the corresponding photon removed from the event record. In this way, partial QED radiation within the detector volume is correctly attributed to the parent lepton, improving the agreement between data and simulation.

Scale factors and systematic uncertainties

The reconstruction, identification, and isolation performance for electrons can differ between data and simulation. Efficiency scale factors are thus derived in order to correct events in simulation so that they match more closely to data. The scale factors are derived from the ratio of the electron reconstruction efficiency in simulation to the efficiency in data derived from $Z \to ee$ and $J/\psi \to ee$ events using a Tag and Probe method [83]. Similar measurements are made for the momentum scale and momentum resolution using $Z \to ee$ events, as described in [81]. Corrections to the momentum scale are applied to data and resolution corrections are applied to simulation.

The electron reconstruction process is sensitive to variations in the reconstruction, identification, isolation, and trigger efficiencies. Systematic uncertainties are estimated to cover these possible variations by deriving the efficiencies for each case using alternative selections for both the tag and probe electron candidates as well as varying the details of the background subtraction [81, 84]. For each set of variations

[2] Throughout this thesis a 'prompt' photon, lepton, or neutrino refers to those particles that do not originate from a secondary hardon.

the central value is taken as the measured efficiency in the scale-factor calculation and the root-mean-square (RMS) value as the systematic uncertainty. The electron energy scale and resolution measurements are sensitive to several factors including pileup, data/simulation differences, calibration of layers in the EM calorimeter, and the response of areas of dead material. Systematic uncertainties related to these variations are derived and then propagated to the momentum and scale corrections as described in [85].

5.2.2. Muons

Reconstruction

Muon candidates are built by combining tracks reconstructed separately in the ID and MS. The majority of combined muons are reconstructed using an outside-in approach by extrapolating MS tracks into the ID and matching to tracks there. During this process the tracks are re-fit to allow hits in the MS to be dropped if doing so improves the overall fit [86]. Similar to the requirements for electrons the combined muon tracks must have $p_{\mathrm{T}} > 27$ GeV, and $|\eta| < 2.5$ such that they are fully within the ID acceptance. To mitigate pileup effects the muons must also satisfy good track-to-vertex association via impact parameter requirements of $|d_0|/\sigma_{d_0} < 3$ and $|\Delta z_0 \sin\theta| < 0.5$ mm.

In order to suppress background contamination from pion and kaon decays, muon candidates must also pass identification requirements related to the quality of the MS tracks and their compatibility with tracks in the ID. For events in the $t\bar{t}$ analysis in Part II the 'medium' identification working point is used which requires MS tracks to have at least three hits across at least two layers of the MDT. An exception is made for tracks in the $|\eta| < 0.1$ region in which tracks with ≥ 1 MDT layer and ≤ 1 MDT hole are permitted. To improve the quality of matching to tracks in the ID a requirement of $(q/p)_{sig} < 7$ is also imposed where $(q/p)_{sig}$ is defined as the absolute difference between the charge/momentum ratio for muons measured in the ID and MS, divided by the sum in quadrature of the charge and momentum uncertainties.

Muons must also pass very similar ID and calorimeter isolation requirements to electrons. Here the 'Tight' requirement is used corresponding to $p_{\mathrm{T}}^{\mathrm{varcone30}}/p_{\mathrm{T}} < 0.04$ and $E_{\mathrm{T}}^{\mathrm{topocone20}}/p_{\mathrm{T}} < 0.15$ for the ID and calorimeter respectively [86]. For the muons $E_{\mathrm{T}}^{\mathrm{topocone20}}$ corresponds to the sum of the transverse energy from full topo-clusters

within a radius of $\Delta R = 0.2$ surrounding the muon candidate after energy contributions from the muon and expected pileup have been subtracted. The isolation requirements are dropped outright for the "loose" lepton selection used in Section 7.3.1, the 'medium' identification working point is still used for this sample. Particle-level muons undergo the same dressing procedure as electrons, outlined above.

Scale factors and systematic uncertainties

Analogous to the process for electrons a series of scale factors are derived to correct the differences in reconstruction, identification, isolation, and track-to-vertex association performance between data and simulation as described in [86]. The muon momentum scale and resolution are also calibrated in much the same way as for electrons, with separate corrections derived for the momentum measurement in the MS and ID before being combined. For the efficiency, momentum, and resolution scale calculations $Z \to \mu\mu$ and $J/\psi \to \mu\mu$ events are used.

The systematic uncertainties applied to muon reconstruction are very similar to the electrons with variations of the isolation, identification, trigger, and track-to-vertex association corrections applied directly to the associated scale-factors. The statistical and systematic components of these variations are kept as separate uncertainties to avoid large correlations. For muons the momentum scale and resolution corrections for the ID and MS measurements are sensitive to different parameters with the main impacts coming from: the $Z \to \mu\mu$ mass width, low p_{T} muon backgrounds, template fit accuracy for the ID scale correction, and chamber alignment in the MS. Two additional uncertainties related to the accuracy of the sagitta measurement in the muon spectrometer are extrapolated to the muon objects from the MS track reconstruction.

5.3. Jets

Both quarks and gluons are colour charged and interact via QCD, as a result they cannot be observed in the detector as isolated particles like the leptons discussed above. Instead they undergo a process of hadronisation forming sprays of colour-neutral hadrons which are reconstructed experimentally as a single jet object. While it is simple enough to visualise a jet of high p_{T} hadrons in the final state it becomes somewhat more complicated to provide a robust jet definition. This is especially true

within complicated events with many jets originating from the hard scatter alongside jets from pileup and underlying events. Providing this definition is the role of jet clustering algorithms.

There are many clustering algorithms available, see [87] for just some examples, but in the analysis outlined in Part II the anti-k_t algorithm [88] is used. This uses a sequential recombination approach that relies on a distance measure between objects i and j, which could be the initial inputs or pseudo-jets in the process of being clustered:

$$d_{ij} = \min(k_{t,i}^{2p}, k_{t,j}^{2p}) \frac{\Delta R_{ij}^2}{R^2}, \tag{5.4}$$

where $\Delta R_{ij} = (y_i - y_j)^2 + (\phi_i - \phi_j)^2$ and $k_{t,i}$, y_i and ϕ_i are the transverse momentum, rapidity, and azimuthal angle of object i respectively. R is an adjustable radius parameter and p is a factor to control the order of the clustering procedure, set to -1 for the anti-k_t algorithm. For the same objects a separate value for the distance between each object and the beam-line is also produced:

$$d_{iB} = k_{t,i}^{2p}. \tag{5.5}$$

For each set of objects the minimum of these two values is then found. If it is d_{ij} then objects i and j are clustered together into a pseudo-jet and the process repeated. If d_{iB} is minimum however there must be no other unclustered particles within a distance R from object i so this becomes a final jet and is removed from the list of objects before repeating the process with the remaining objects.

Additionally, the topology of reconstructed jets originating from the decay of b-quarks can be distinguished from those originating from light quarks or gluons. This process, known as b-tagging, is described more fully in Section 5.4.

Jets at particle-level are reconstructed using only stable final-state particles and excluding muons, neutrinos, and any particles associated to pileup. Differences in jet definitions between simulation and data are corrected as part of the jet calibration process outlined in the next section.

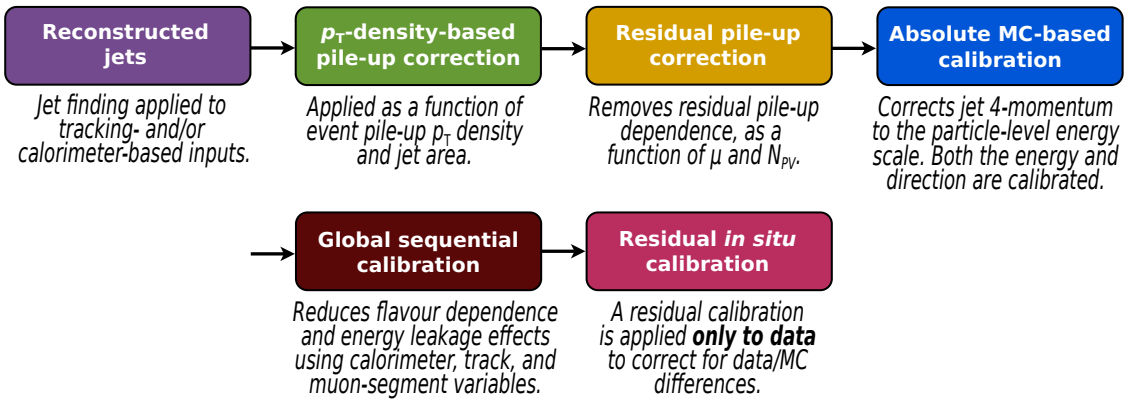

Figure 5.4: Summary of the steps in the energy scale calibration of small-radius jets. Each step in the chain is applied to the four-momentum of the jet [89].

5.3.1. Jet calibration

Before they can be used for physics analysis the reconstructed particle flow jets must be calibrated to remove pileup and detector related effects, correct offsets in the energy scale, and ensure good agreement between jets measured in data and simulation [89].

Jet energy scale

There are several steps in the calibration process for the energy scale of small-radius jets that are run sequentially, as summarised in Figure 5.4. Energy deposits within the reconstructed jets are affected by the presence of multiple pp collisions in the same bunch crossing (in-time pileup) and residual signals from nearby bunch crossings (out-of-time pileup). The first steps of the jet energy scale calibration corrects for these pileup effects by initially using an estimate of the p_T density of central jets ($|\eta| < 2.0$) in simulation. From this, the median p_T-density (ρ) is extracted and the ratio of $(p_T^{reco} - \rho)/p_T^{reco}$ is applied as a correction to the jet p_T. Residual pileup effects not fully corrected by the p_T-density method are then parameterised as functions of the number of interactions per bunch crossing (μ) and the number of primary vertices in the event (N_{PV}) by comparing jet p_T values in simulation before and after simulating the detector response. The effect of these calibrations on particle-flow jets is much less pronounced than jets built only from topo-clusters due to the inherent robustness to pileup gained from using tracking information.

The reconstructed jet energy and η are also sensitive to non-homogeneous detector effects, in particular those originating from transition regions between detector technologies. This covers effects such as the variation in readout energy scale for jets partially reconstructed in both the EM and hadronic calorimeters (calorimeter non-compensation), energy lost in inactive or insensitive regions of the detector (dead material) and energy fractions not fully reconstructed within the calorimeters (leakage). The next step in the calibration chain tackles these using two corrections based on simulated events (MC-based calibration). One is for the jet energy scale (JES) and another is applied to the jet η to correct for a residual bias. In both cases the four-momentum of simulated jets after modelling the detector response (detector-level), and after applying the pileup corrections, are calibrated to match the true energy scale of jets in at particle-level. Detector- and particle-level jets are geometrically matched ($\Delta R < 0.3$) and for the JES correction the average jet response, $\mathcal{R}$, is measured, where $\mathcal{R}$ is defined as the mean of a Gaussian fit to the $E^{\text{reco}}/E^{\text{true}}$ distribution with tails removed. The inverse of $\mathcal{R}$ as a function of both E^{reco} and η^{det} is then used as a correction factor for the energy of the reconstructed jets. For the additional η calibration, the inverse jet response is replaced by $(\eta^{\text{reco}} - \eta^{\text{true}})$, again binned in E^{reco} and η^{det}.

After the MC-based calibration and pileup corrections the individual jet response is still found to be dependent on various factors relating to the shape and flavour content of the jets as well as the difference between quark and gluon initiated jets. A global sequential calibration (GSC) is thus applied which sequentially and independently corrects the following six variables:

- f_{charged} - jet p_{T} fraction coming from charged particles
- f_{Tile0} - jet energy fraction measured in the first layer of the Tile calorimeter
- f_{LAr3} - jet energy fraction measured in the third layer of the LAr calorimeter
- n_{trk} - number of charged tracks in the jet
- w_{trk} - average p_{T}-weighted transverse distance in the $\eta - \phi$ plane between the jet axis and all tracks with $p_{\text{T}} > 1\,\text{GeV}$ (track width)
- n_{segments} - number of muon track segments associated to the jet (punch-through)

In each case the correction is derived similarly to the MC-based calibration but using the p_{T} response in place of the energy response such that only the dependence

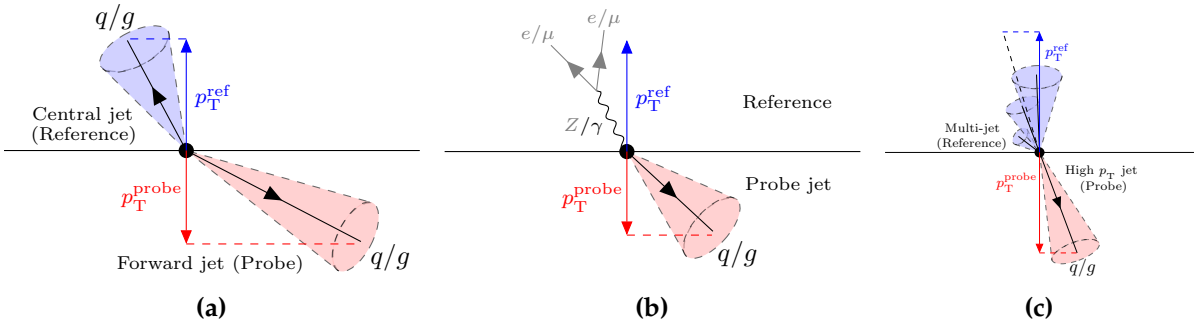

Figure 5.5: Example diagrams showing the processes used in the in-situ calibration of small-radius jets: (a) η-intercalibration, (b) Z/γ + jet, (c) multi-jet balance.

on each of the six observables is corrected for and the average JES is unchanged. The corrections are parameterised in terms of p_{T} and η apart from the n_{segments} correction, which replaces p_{T} with the jet energy.

The final step in the energy calibration is to apply corrections derived from events in data (in-situ) to account for the observed differences between jets in data and simulation. Three separate methods are used to target jets in different regions but in each case the underlying idea is the same; to use a well measured reference object to calibrate the p_{T} response of a recoiling jet. The three processes are shown in Figure 5.5, starting with an η-intercalibration where jets in the forward regions $(0.8 < |\eta| < 4.5)$ are corrected relative to well measured central jets $(|\eta| < 0.8)$ to bring their energy scales in line. An additional absolute calibration is then carried out using events in which a single jet is balanced by either a photon or a Z-boson decaying leptonically ($Z \to ee$ or $Z \to \mu\mu$). The results from all three physics processes are combined allowing the calibration to cover a wide p_{T} range of 17 GeV – 1.2 TeV. Lastly high p_{T} jets up to 2.4 TeV are calibrated against several low p_{T} jets that have already been corrected using Z/γ + jet events (multi-jet balance). Results from the Z/γ + jet and multijet-balance corrections are then statistically combined to derive a single calibration valid over the full jet momentum range. Lastly, jets with p_{T} above 2.4 TeV are covered by introducing a dedicated uncertainty based on studies of the jet response to individual high energy hadrons [90].

Jet energy resolution

In order to get accurate jet and missing energy measurements the jet energy resolution (JER) also needs to be measured to account for the limited accuracy of the detector. The jet energy resolution on the p_{T} of small-radius jets ($\sigma(p_{\mathrm{T}})$) can be parameterised by:

$$\frac{\sigma(p_{\mathrm{T}})}{p_{\mathrm{T}}} = \frac{N}{p_{\mathrm{T}}} \oplus \frac{S}{\sqrt{p_{\mathrm{T}}}} \oplus C \tag{5.6}$$

Where N is a noise term; encompassing both electronic noise and pileup effects, and S is a stochastic term; capturing the effects of statistical fluctuations. Lastly C is a constant correction term which includes various shape and detector hardware effects with similar origins to those corrected in the GSC step of the JES calibration. The JER in data is measured using di-jet events and the same in-situ methods as for JES, additionally a separate random cones method is used to get a more accurate estimation of the noise term [89]. The final JER calibration is derived by fitting the results from the di-jet measurements using a functional form of equation (5.6) with the noise term fixed to the value measured by the random cones method. To ensure good consistency between simulation and data a smearing is applied to simulated events such that the average JER for a particular range of jet p_{T} matches between simulation and data. This is only done in regions where the JER in simulation is lower than in data, in the reverse case no correction is applied to data. The remaining data/simulation difference in these regions is accounted for by an additional systematic uncertainty.

5.3.2. Jet uncertainties

Each stage of the JES calibration process is affected by various systematic uncertainties with the full uncertainty consisting of 125 individual terms. The bulk of these (98) originate from the absolute in-situ Z/γ + jets and multi-jet balance corrections and correspond to: propagated calibration uncertainties on the measured objects (photons, electrons, and muons), limited statistics, selection and topology uncertainties, and modelling uncertainties. These variations only depend on the jet p_{T} and so can be reduced into a smaller set of orthogonal terms via an eigenvector decomposition with only minimal loss of correlation information. The category reduction [89] scheme is used, reducing these 98 terms into 15 reduced components. These are then combined with the remaining two-dimensional uncertainty terms coming from: the

η-intercalibration (18), pile-up correction (4), GSC punch-through (1), and additional universal effects related to: jet flavour (3) and the detector response to individual high p_{T} particles (1). Several uncorrelated uncertainties related to the η-intercalibration can be combined for simplicity, reducing the total contribution from 18 to 6 terms. This results in a total of 30 independent variations which parameterise the uncertainties on the jet energy scale. The fractional uncertainty breakdown in terms of jet p_{T} is shown in Figure 5.6a, with groups further combined by adding uncertainties in quadrature. In this plot the reduced in-situ uncertainties are labelled 'absolute in-situ' while those originating from the η-intercalibration are labelled 'relative in-situ'. The total uncertainty is only around 1% for high p_{T} jets in the region 250 GeV $< p_{\mathrm{T}} <$ 2 TeV, and increases up to a maximum of 5% at very low p_{T} (20 GeV), driven by increased uncertainty from pileup and flavour effects. The uncertainty also increases sharply to around 3.5% for jets above 2 TeV due to the loss of statistics in the multi-jet balance method at high p_{T}, and inclusion of the single-particle uncertainty for jets with p_{T} above 2.4 TeV.

The jet energy resolution systematic uncertainties are dominated by the uncertainty on the jet energy scale at low p_{T} and a non-closure in the di-jet method at high p_{T}. Like the JES the number of individual terms are reduced via eigenvector composition resulting in 7+1 independent variations. The additional uncertainty accounts for the data/simulation disagreement as discussed above. The JER uncertainties are applied by only varying jets in simulation in one direction even when the uncertainty component passes through 0, resulting in the $\pm\sigma$ variations being symmetrised. This results in forced positive correlation in cases where a JER uncertainty component increases the JER in some regions but decreases it in others. Due to the small overall size of the JER relative to other uncertainties this simplification was not considered problematic for the analysis covered here. The fractional uncertainty breakdown in terms of jet p_{T} for the JER components is shown in Figure 5.6b.

5.3.3. Jet reconstruction

The analysis in Part II uses particle flow jets [80] with a radius value of $R = 0.4$ (small-R jets) that have been calibrated using the methods discussed above. Before any additional event requirements are imposed all jets must be reconstructed within the inner detector acceptance ($|\eta| < 2.5$) and have $p_{\mathrm{T}} > 25$ GeV. To remove jets originating from pile-up an additional requirement on the jet vertex tagger (JVT) score is applied

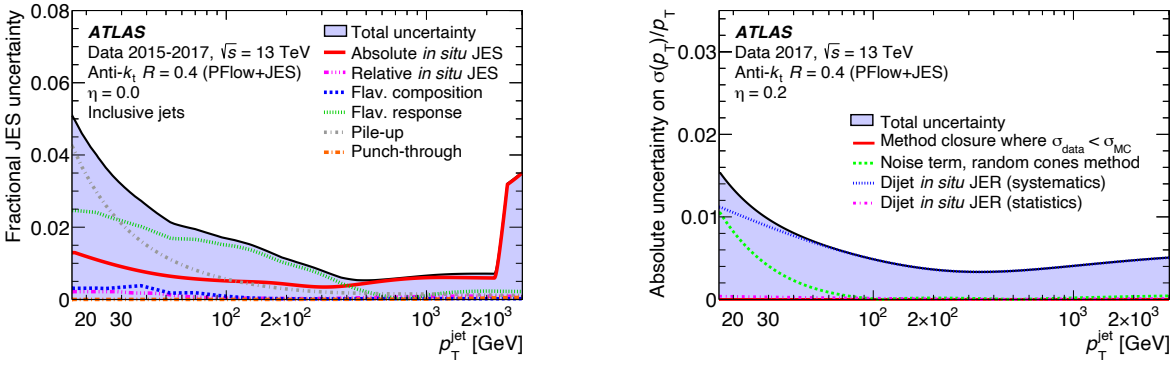

Figure 5.6: Summary of major uncertainty sources in terms of jet p_{T} originating from the calibration of the (a) jet energy scale, (b) jet energy resolution of small-radius particle-flow jets [89]. The total uncertainty, shown by the blue shaded region, is the sum in quadrature of all individual uncertainty contributions.

to jets with $p_{\mathrm{T}} < 60\,\mathrm{GeV}$ as described in [91]. Additional isolation requirements are imposed to avoid double counting energy contributions from leptons. Jets in close proximity to an electron ($\Delta R(e,j) < 0.2$) are removed and if a jet with less than three tracks is close to a muon ($\Delta R(\mu,j) < 0.2$) or if a jet has a track that is part of the muon definition then that jet is removed. After these requirements leptons and jets are additionally specified to be well separated in the detector by requiring $\Delta R(\ell,j) > 0.4$ otherwise the lepton is removed and the event is skipped.

5.4. *b*-tagged jets

It is possible to distinguish jets originating from a b-quark (b-jets), from light-quark and gluon initiated jets. This is due to the long lifetime of b-hadrons resulting in an increased likelihood for b-jets to contain a secondary vertex and associated tracks with high impact parameters. There are several tools available to discriminate between jet types but for the analysis in Part II b-jets are demarcated as such using the DL1r multivariate b-tagging algorithm, which uses a deep neural network (DNN) model. DL1r is an extension of the DL1 algorithm [92] with additions based on an additional recurrent neural network exploiting the correlation between the tracks' impact parameters. The algorithm is tuned to balance both b-tagging efficiency and rejection of jets originating from other quarks. A working point is chosen which ensures a tagging

efficiency of 77% per b-jet in $t\bar{t}$ events, resulting in c-, and light-quark rejection rates of 5 and 171 respectively [93].

5.4.1. b-tagging uncertainties

The performance of the DL1r b-tagging algorithm is evaluated using di-leptonic $t\bar{t}$ events in data and simulation [92]. The process of calibrating the b-tagging efficiency and the mistag rates is sensitive to many individual uncertainties derived by varying the simulated $t\bar{t}$ and background samples. Like the small-radius jet uncertainties the overall number of terms can be reduced via an eigenvector decomposition to a smaller set of orthogonal terms. These include independent variations related to: the b-tagging efficiency calibration (9), the c-jet mistag calibration (4), the light-jet mistag rate (4), and two additional components to cover extrapolation of b-tagging results to high-p_{T} jets. The uncertainties are propagated by varying the tagging efficiency in simulation.

5.5. Re-clustered large-radius jets

Measuring boosted $t\bar{t}$ events relies on accurate reconstruction of high p_{T} top quarks ($p_{\mathrm{T}} \geq 2m_t$) which decay hadronically. At these energies the three decay products of the top-quark cannot always be resolved as three separate jets and instead are reconstructed as a single large-radius jet object to ensure the full hadronic decay is captured. The analysis in Part II uses re-clustered (RC) jets constructed using the anti-k_t clustering algorithm applied to the already calibrated small-radius (R=0.4) jets from Section 5.3 and with radius parameter R=1.0 [94]. After re-clustering, the RC jets have a trimming procedure applied [94, 95] in which any R=0.4 sub-jets with less than 5% of the total p_{T} of the RC jet are removed. This is designed to remove jets originating from pileup interactions. Due to the possibility for individual jets to overlap, no requirement is put on the number of small-radius jets used to build a single RC jet but typically RC jets that match well with the signature of a boosted top-quark decay contain either two or three sub-jets. The use of calibrated jets in the re-clustering process means that the resulting RC jets are already fully calibrated to the correct energy scale and resolution. No additional dedicated systematic uncertainties are needed.

5.6. Missing transverse momentum

Due to the unknown momentum fraction carried by colliding partons at the LHC it is not possible to know the full expected momentum sum of any interaction. However, in an ideal collision particles are collided perfectly head on in the longitudinal z-direction and thus the transverse momenta for all objects in an event should sum to 0. The vector of missing transverse momentum in an event can be measured and the missing transverse energy is given as the magnitude of this vector ($E_{\mathrm{T}}^{\mathrm{miss}}$). Missing transverse momentum is either the result of mis-measurement of known final-state particles or a signature of undetected SM or BSM particles. As neutrinos are the only long-lived SM particle which cannot be measured directly within ATLAS, the value of $E_{\mathrm{T}}^{\mathrm{miss}}$ is often used as a proxy for the neutrino transverse momentum in analyses concerned with measuring Standard Model processes.

The missing transverse momentum is constructed from the negative vector sum of the x and y momentum components ($\vec{p_{\mathrm{T}}} = (p_x, p_y)$) of all other reconstructed and calibrated objects in the event. This includes leptons, photons, jets, and an additional term which captures the remaining soft radiation in the form of ID tracks with $p_{\mathrm{T}} > 400\,\mathrm{MeV}$ that are matched to the primary vertex but are not included in any other object. To ensure energy is not double counted between reconstructed objects the $E_{\mathrm{T}}^{\mathrm{miss}}$ calculation adopts its own dedicated overlap removal process [96]. For the boosted $t\bar{t}$ analysis the 'Tight' working point is used, this adds an extra requirement of $p_{\mathrm{T}} > 30\,\mathrm{GeV}$ for small-radius jets in the forward region ($|\eta| > 2.5$). Any forward jets below this threshold are not included in the calculation as they are assumed to be poorly measured.

The performance of the $E_{\mathrm{T}}^{\mathrm{miss}}$ reconstruction depends on the accuracy of the individual p_{T} measurements of the hard and soft terms. The scale and resolution uncertainties applied to the leptons and jets are thus propagated to the value of $E_{\mathrm{T}}^{\mathrm{miss}}$, taking correlation between uncertainty sources into account. Independent scale and resolution uncertainties on the soft term are also included which modify the magnitude and direction of the missing momentum. These uncertainties are derived from data/simulation comparisons using $Z \to \mu\mu$ events without any jets as described in [96].

Chapter 6.

Monte-Carlo simulation

"I choose to believe what I was programmed to believe"
— Robo-Hungarian farmer, Futurama S2, E18 - The Honking

In order to compare the results measured by the detector to theoretical calculations we need a method to generate the expected detector response starting from a given physics process. This is achieved by simulating individual collision events, following the full chain from the initial parton-parton interaction to the response of stable-particles within a simulation of the ATLAS detector. Monte-Carlo (MC) methods, based on random sampling, are used throughout this process. These methods are particularly suited to simulating particle physics events as the probabilistic nature of QFT naturally provides the distributions from which to draw values.

6.1. Generating LHC events

The calculations needed to generate accurate collision data are complex but can be broken down into several steps, shown schematically in Figure 6.1, and outlined in the proceeding sections.

Firstly the matrix element (ME) calculation for the hard-scatter process of interest (e.g. $pp \to t\bar{t}$) is calculated. The picture is made significantly more complicated as any incoming/outgoing gluons or quarks will radiate showers of lower energy (soft) and collinear additional partons, far too many to realistically calculate using Feynman amplitudes as is done for the hard scatter. Instead these emissions are simulated

using a parton shower (PS) as described in Section 6.3. Any resulting partons will then undergo hadronisation, this process can not be calculated directly and is instead simulated using a non-perturbative model as discussed in Section 6.4.

Things are further complicated as the remnants of the protons after collisions can also enter the detector volume and interact further, or decay forming part of the underlying event (UE). This also needs to be modelled as described in Section 6.5. Protons are also not collided in isolation at the LHC, every bunch crossing results in around 30-40 other interactions, known as pileup (PU) which also needs to be accounted for as in Section 6.6. Lastly the final-state particles must be passed through a simulation of the ATLAS detector geometry in order to simulate an accurate detector response which can be compared to data, this is described in Section 6.7.

This step-by-step process allows for various "levels" to be defined at which recorded data and simulation can be compared:

- **Parton-level:** Where the process is cut-off before hadronisation, leaving only quarks and gluons in the final state. In some cases unstable particles, such as top quarks and W-bosons, are left without calculating their decay.
- **Particle-level:** Where the hadronisation process is simulated leaving leptons, photons, and stable hadrons in the final-state. Additional effects from modelling of the underlying event are also often included.
- **Detector-level:** The full results of the event generation after passing stable-particles through a detector simulation.

The analysis outlined in Part II is performed at particle-level with events in data corrected for the limited acceptance and precision of the detector (see Chapter 8).

6.2. Matrix element generation

As described in Chapter 2 calculating the cross-section for QCD interactions requires knowledge of the strong coupling (α_S) which decreases with increasing energy. This is problematic when considering pp collisions as these involve a mix of high-energy interactions; between colliding partons from separate protons, and low-energy interactions; between the partons inside each individual proton. In this low-energy regime

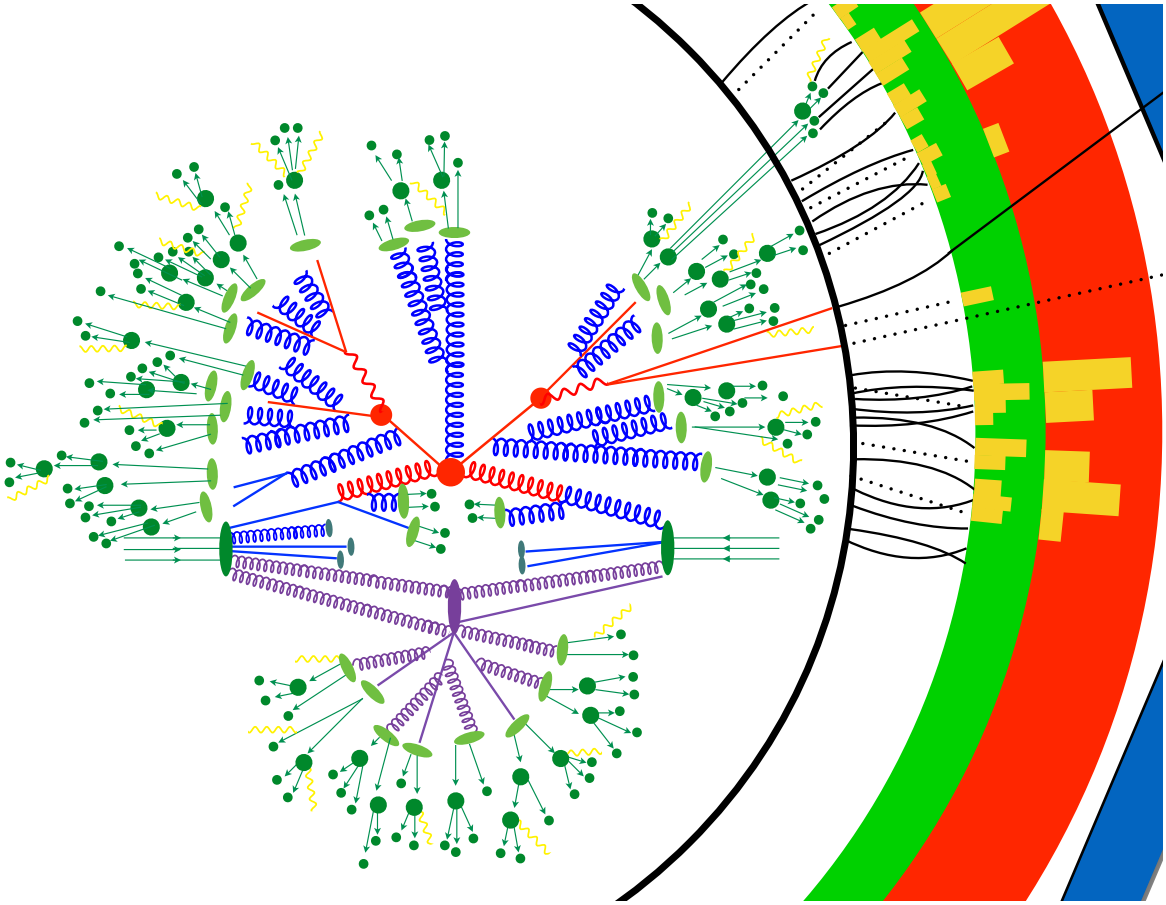

Figure 6.1: Schematic depicting the various steps in generating a simulated $gg \to t\bar{t} \to q\bar{q}b\mu\nu_{\mu}\bar{b}$ event using Monte-Carlo methods. The process starts with the incoming protons represented by the large dark green blobs and arrows pointing towards the centre of the figure. Two partons then interact in the main hard scatter process, depicted in red, from which a top-quark and anti-top-quark are generated. The parton-shower is depicted in blue with the initial stages of the hadronisation process shown by light green blobs. The subsequent decay of the initial hadrons into stable final-state particles is shown in dark green with any generated photons indicated in yellow. The lower part of the image depicts additional decays from multiple parton interactions (MPI) in purple, and proton decay remnants which make up part of the underlying event (UE). Finally the right hand side of the image depicts the process of simulating interactions with different layers of the ATLAS detector. Original image courtesy of [97]

($\alpha_S > 1$) higher-order contributions to the collision cross-section do not converge and thus the calculation can not be solved perturbatively.

The factorisation theorem [98] states that by defining a factorisation energy scale (μ_f) as the crossing point between perturbative and non-perturbative behaviour then the cross-section calculation can be factorised into high-energy and low-energy parts which can be solved independently. The hard-scatter cross-section for $t\bar{t}$ production in a pp collider can then be written in a simplified form as:

$$\sigma_{pp\to t\bar{t}} = \sum_{i,j\in\{q,\bar{q},g\}} \int_0^1 \mathrm{d}x_1 \int_0^1 \mathrm{d}x_2 \, f_i(x_1,\mu_f)\, f_j(x_2,\mu_f)\, \hat{\sigma}_{ij\to t\bar{t}}\,, \tag{6.1}$$

where $x_{1(2)}$ is the fraction of the first(second) proton's total momentum that is carried by the interacting parton. The function $f_i(x_{1(2)},\mu_f)$ is the parton distribution function (PDF) which denotes the probability of a parton of type i with momentum fraction $x_{1(2)}$ originating from the first(second) proton. These PDFs encode the non-perturbative part of the calculation and depend on the choice of factorisation scale. Lastly $\hat{\sigma}_{ij\to t\bar{t}}$ is the partonic cross-section for the $t\bar{t}$ production process.

6.2.1. Parton distribution functions

In the SM protons consist of three valence quarks (uud) and at any given time a "sea" of other miscellaneous quarks and gluons which are not fully bound at high energies. Each of these partons carry some fraction of the proton's total energy and the PDFs parameterise this distribution of energy. The energy fractions cannot be calculated analytically and are instead derived by fitting to data from various experiments, such as those dedicated to measurements of proton structure like experiments at HERA [99, 100], as well as general purpose collider experiments like those at the LHC. The PDFs themselves are not constant and depend on the interaction energy. This dependence is perturbatively calculable and described by the DGLAP equations [101–103].

6.2.2. Fixed order calculation

The high energy part of the matrix element is calculable to a fixed order in α_S via perturbative expansion as described in Chapter 2. This calculation must also account

for several divergent effects from both high energy loops (ultraviolet (UV) divergences), and low energy collinear radiation (infrared (IR) divergences). The UV divergences can appear at any given order and require renormalisation of the SM Lagrangian [104] to remove. This gives rise to an additional scale, the renormalisation scale (μ_r) which along with the factorisation scale introduced above can be freely chosen within sensible limits. In practice they are usually chosen based on some sensible energy scale of the hard-scatter interaction, for $t\bar{t}$ production the top-quark mass is most commonly used, e.g. $\mu_r = \mu_f \propto m^2_{top}$.

Fixed-order calculations that take into account both real emissions and loops very quickly become complicated beyond leading order, with state-of-the-art $t\bar{t}$ predictions available up to next-to-next-to-leading-order (NNLO) [16, 17, 105]. It is often desirable to simulate hard-scatter events with many more emissions in order to better mimic real events. The majority of additional radiation is simulated in the parton-shower, however most ME generators are also capable of calculating a small number of additional partons, at higher-order precision, within the matrix element itself. This process, known as *multijet-merging* [106, 107], involves combing fixed-order calculations of a single underlying process with increasing numbers of additional parton emissions, e.g. $t\bar{t}$ at NLO + $t\bar{t}$ +1 parton at NLO. This can be supplemented further by including LO diagrams of the same process with many more additional partons, e.g. $t\bar{t}$ +2,3,4 partons at LO. Such calculations are often referred to as e.g. $t\bar{t}$ generated at NLO in QCD for up to 1 additional parton and at LO for up to x additional partons. Special care has to be taken to avoid any overlap of emissions when matching such calculations with a parton shower. [108, 109]

6.3. Parton shower

After the fixed-order interaction the next step is to simulate many additional emissions coming from the resulting partons using a dedicated algorithm known as a parton shower. This helps "fill in" some of the missing higher order effects and results in a more accurate prediction of the collision process. At a given energy each parton has some finite probability to split into two with momentum fractions z and $(1-z)$, and angle θ between them. The parton shower relies on the fact that in both the soft ($z \to 0$) and collinear ($\theta \to 0$) limits the correction to add an additional emission into

the calculation is independent of the origin of the emitting parton. The parton shower can thus be factorised out from the matrix element and calculated separately.

Parton splittings are strictly ordered in either virtuality (closely related to momentum) or angle from the parent parton and calculated iteratively using MC sampling to choose the evolution, momentum fraction, and type of emission at each step. This process is controlled by the *Sudakov factor* which gives the probability of a parton evolving from virtuality(angle) t_0 to a new virtuality(angle) t **without** emitting a parton:

$$\Delta(t_0, t) = \exp\left[-\int_{t_0}^{t} \frac{\mathrm{d}t'}{t'} \int_{z_{\min}}^{z_{\max}} \mathrm{d}z\, P(z) \right], \tag{6.2}$$

where $P(z)$ is a splitting function containing the probabilities for quark/gluon splitting. To avoid IR and collinear divergences a cut-off energy scale is defined at which point the shower evolution is stopped. In most parton-shower implementations this cut-off is set around 1 GeV.

Many MC event generators implement parton shower algorithms. The choice of shower ordering and associated splitting function differs between generators with HERWIG [110] implementing an angular-ordered shower using the methods described above[1]. Alternatively both the PYTHIA [111] and SHERPA [112] showers are momentum-ordered relying on slightly different dipole splitting algorithms [104].

In order to avoid double-counting emissions, some care must be taken when joining the results of the hard-scatter with the parton shower in a process known as *matching*. There are currently two widely used methods for tackling this problem at NLO, known as POWHEG [113] and MC@NLO [114]. The former restricts emissions from the PS to be below a threshold momentum, ensuring the highest energy additional emissions originate from the matrix element. The MC@NLO method by contrast finds the highest energy emissions in the PS and subtracts this from the ME to avoid any overlap.

6.4. Hadronisation

After the parton-shower, the energy scale of the remaining partons will be around the threshold for quark confinement. The hadronisation process must then be simulated

[1] HERWIG is also capable of providing a momentum-ordered dipole-shower, however the angular variant is more commonly used in order to derive comparisons between the two approaches.

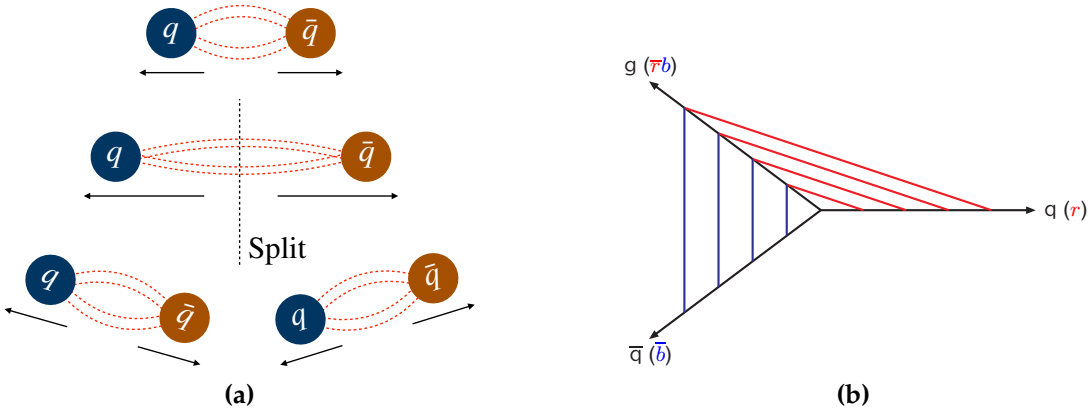

Figure 6.2: Schematic of how partons are treated in the Lund string model. (a) Quark anti-quark pairs are connected by a Lund string, as the partons separate the energy in the string grows until a threshold point where the string breaks in two producing a new quark and anti-quark at the ends. (b) Gluons are introduced into the model as kinks in the string which modify the kinematics [104]. Some extra considerations are also needed for possible colour flow combinations.

giving a collection of colour-neutral hadrons in the final-state. Now we are below the energy scale for perturbation theory this process can only be approximated using models motivated by QCD with parameters tuned to experimental data. There are two different approaches to hadronisation used in modern event generators: the Lund string model [115] - used in PYTHIA, and the cluster model [116] - used by both HERWIG and SHERPA. In the Lund string approach quark anti-quark pairs are modelled with a connecting colour "string" between them, the energy of which grows as the quarks are separated. At some length it becomes energetically favourable for the string to break into two smaller strings and generate new quarks and anti-quarks at the free ends, as in Figure 6.2a. The two new $q\bar{q}$ pairs have a smaller combined energy than the original pair reducing the total energy in the system until the process is no longer kinematically possible. Gluons can be introduced into this model as kinks in the Lund string, as shown in Figure 6.2b, and the formation of baryons made possible by allowing composite di-quark states which are treated the same as a single quark or anti-quark.

The cluster model relies on the concept of *preconfinement* which states that the parton shower follows the flow of colour charge and thus partons with the same colour charge are likely to be close in phase-space after the PS, and can be grouped into colour-singlet clusters. Firstly any gluons from the PS are split into $q\bar{q}$ pairs and colour-singlet clusters are formed. Clusters are then split (decayed) until their

invariant masses match that of a known hadron, with some kinematic shuffling often needed to produce a final-state of stable hadrons.

6.5. Underlying event and multi-parton interactions

The remnants of the colliding protons after the hard-scatter can undergo further interactions, which will be measured by the experiment. All interactions not associated directly to the hard-scatter are collectively labelled as the underlying event (UE). This definition also includes interactions between remnant partons, known as multi-parton interactions (MPI), as well as hadronisation of any non colour-confined remnants. These effects, and the interference between them, are accounted for in the MC simulation using dedicated MPI models. To improve the accuracy of these models various parameters are tuned to experimental data.

6.6. Pileup

The effect of pileup interactions are modelled by overlaying simulations of additional QCD hard-scatter interactions constructed using the same techniques as above. An additional step is taken to re-weight the pileup events such that the distribution of the average number of collisions per bunch crossing ($\langle\mu\rangle$) matches the data. As the pileup profiles differ between years this re-weighting is performed separately for each of the three data taking periods (2015/16, 2017, and 2018).

6.7. Detector simulation

The final step in producing simulated events is to model the interaction between stable particles and the detector hardware so that simulation can be compared directly to data. Provided a detailed enough model of the detector system is used this process can correctly account for the known resolution and acceptance of the detector hardware. The GEANT4 [117] framework is used for most detector simulation within ATLAS. This provides a very accurate approximation of the detector response by individually simulating the passage of each particle through the detector hardware using

Monte-Carlo methods. This often results in the detector simulation dominating the share of CPU time needed for event generation due to the large number of particles involved. As a result a dedicated tool, Atlfast-II (AFII) [118], was developed which uses a parameterised description of interactions within the calorimeters, with values derived from GEANT4 simulations. This simplified approach results in significantly less CPU usage at the expense of poorer modelling of the jet response which can only be somewhat mitigated through dedicated calibrations. As the collision luminosity at the LHC is expected to increase significantly in the future, optimisation for detector simulation will become increasingly important. To this end the next generation of fast-simulation [119] is expected to play an important role in future physics analyses.

Part II.

Boosted $t\bar{t}$ differential cross-section measurement

Chapter 7.

Analysis strategy

"All my life, I've had one dream: To achieve my many goals"
— Homer Simpson, The Simpsons S14, E15 - C.E.D'OH

Measuring the total, or inclusive, fiducial $t\bar{t}$ production cross-section amounts essentially to a counting experiment, tallying the total number of observed $t\bar{t}$ events based on specific selection criteria. However this only provides a single data point from which to extrapolate information about many complex underlying interactions. It is important to also measure how the cross-section changes as a function of variables related to the $t\bar{t}$ system. An example of such a differential measurement might be the cross-section in terms of the transverse momentum of one of the top-quarks. From this one can start to build an understanding of both the energy scale of the individual top-quarks within $t\bar{t}$ events[1], as well as the effect of higher order corrections, parton shower, and hadronisation processes on the kinematics of the final decay products in simulation. Naturally these kinds of measurements are particularly useful for developing and improving the simulated Monte Carlo predictions discussed in Chapter 6 and are often used to help tune their output to provide a better barometer for data measurements.

Figure 7.1 shows the three different $t\bar{t}$ decay channels discussed in Section 2.3, the analysis covered in this thesis measures events that fall within the semi-leptonic, or lepton+jets, channel only. Additionally only events in which the hadronically decaying top-quark has a very high transverse momentum are studied. These *boosted* events are particularly interesting as they provide a unique opportunity to study QCD

[1] at a specific centre of mass energy $\sqrt{s}$

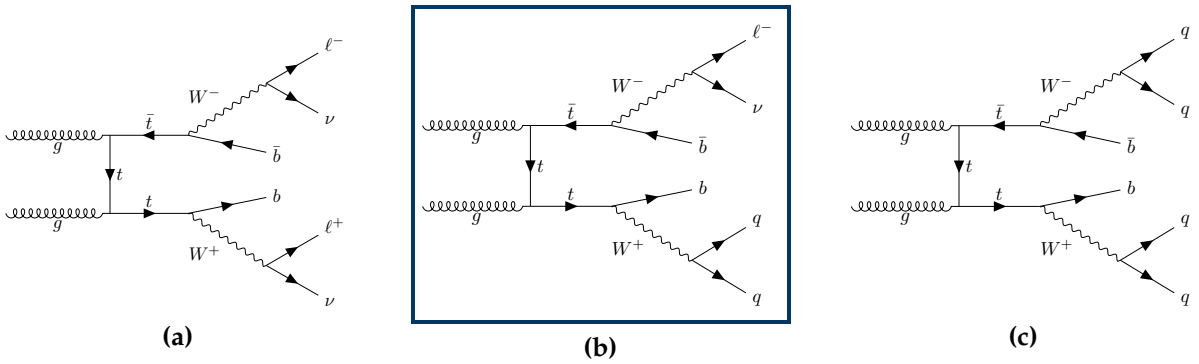

Figure 7.1: Leading order Feynman diagrams of the three $t\bar{t}$ decay channels (a) di-leptonic (b) semi-leptonic or lepton+jets, (c) all hadronic. The analysis in this thesis is set up to select events in the highlighted lepton+jets channel only.

processes at multiple energy scales simultaneously, especially when including events with additional prompt radiation (extra jets) present in the final state. In these cases it is possible to have events with three distinct and vastly different energy scales, with $p_T^t \gg m^t \gg p_{\mathrm{T}}^{j,1}$, where p_T^t and m^t are the transverse momentum and mass of the boosted top-quark, and $p_{\mathrm{T}}^{j,1}$ the transverse momentum of the leading[2] extra jet. There are also several high energy extensions of the SM which are predicted to have effects that increase along with the total energy in the system[28, 120, 121]. Events with high top p_{T} and $t\bar{t}$ invariant mass will be particularly sensitive to this class of effective theory further motivating the study of high energy $t\bar{t}$ events.

The following chapters present a boosted differential $t\bar{t}$ cross-section measurement in the lepton+jets channel published by ATLAS in 2022 [1]. This work builds on the structure and results of previous ATLAS measurements in a similar phase-space at $\sqrt{s} = 8\,\mathrm{TeV}$ [122], and $\sqrt{s} = 13\,\mathrm{TeV}$ [123, 124] but studies a larger 139 fb^{-1} dataset and includes some newly measured observables. New methods are also employed to reduce the effect of systematic uncertainties, with the aim of making the highest precision measurement possible. This work also shares commonalities with measurements made by the CMS collaboration in the lepton+jets channel [125, 126] as well as similar measurements made within the all-hadronic channel by both ATLAS [127, 128] and CMS [129]. The interpretation of the results in terms of new physics using EFT formalism is a new addition for a differential cross-section measurement in the lepton+jets channel at ATLAS. However it is similar to approaches used in more specialised analy-

[2]Throughout this thesis the terms "leading" and "sub-leading" are used to refer to the p_{T} ordering of physics objects with the leading object the one with the highest p_{T}.

ses such as the measurements of charge asymmetry [130] and energy asymmetry [131] in $t\bar{t}$ events.

7.1. Data and simulated samples

The data sample was recorded by the ATLAS detector from 2015 – 2018 and is made up exclusively of pp collisions at $\sqrt{s} = 13\,\text{TeV}$. A small subset of the data is rejected before any analysis takes place to remove known bad events [132], e.g. those recorded while portions of the detector hardware were offline or experiencing problems. The remaining events correspond to an integrated luminosity of 139 fb^{-1}. The luminosity over all four data-taking years is measured and calibrated using the dedicated LUCID-2 detector [133] during specific low-luminosity runs, with more detail given in [134]. This results in an uncertainty of 1.7% on the total integrated luminosity which is included in the total uncertainty for each measurement outlined in Chapter 9. Events are required to pass at least one of the standard single lepton triggers [69, 84].

7.1.1. Simulated MC samples

Simulated MC events are used throughout to provide estimates of the background contamination, derive corrections for detector effects, and compare SM predictions to data. Additionally in Chapter 11 events generated with effective BSM contributions are used to extract limits on new physics operators.

Unless otherwise stated, a value of 172.5 GeV is used for the top-quark mass in all predictions. For each sample the effect of pileup interactions is simulated by overlaying a set of additional inelastic pp collisions with the PYTHIA8 [111] event generator, using the A3 [135] set of tuned parameters. In each case a correction is applied such that the average pileup profile matches data, additionally the average pileup value in MC is scaled by 1/1.03, based on studies of the number of vertices as a function of $\langle\mu\rangle$ as well as the results from the inelastic cross-section measurement.

To improve the prediction of the total cross-section all $t\bar{t}$ samples are also normalised, using a single scale factor, to an inclusive cross-section prediction at next-to-next-to-leading order (NNLO) in QCD, including the resummation of next-to-next-to-leading logarithmic (NNLL) soft-gluon terms using TOP++2.0 [16, 105]. This corre-

sponds to $\sigma(t\bar{t})_{\text{NNLO+NNLL}} = 832 \pm 51\,\text{fb}^{-1}$ at a centre-of-mass energy of $\sqrt{s} = 13\,\text{TeV}$ and a top-quark mass of $m_{\text{top}} = 172.5\,\text{GeV}$. Uncertainties on the PDF, α_S, m_{top}, and from various internal scale variations are added in quadrature to obtain the total quoted value. Variations of this cross-section are calculated separately for the $t\bar{t}$ samples with different values for the top-quark mass.

Nominal $t\bar{t}$ MC sample

The production of $t\bar{t}$ events is modelled using the PowhegBox v2 [113, 136, 137] generator. This provides matrix element predictions at next-to-leading order (NLO) using the `NNPDF3.0nlo` [138] set of parton distribution functions. The h_{damp} parameter, which effectively regulates the high p_{T} radiation in the event from which the $t\bar{t}$ system recoils, is set to $1.5 \times m_{\text{top}}$. The renormalisation and factorisation scales are set using a functional form given by $\sqrt{m_{\text{top}}^2 + p_{\text{T}}^2}$. After generation the events are interfaced with Pythia8.230 [111] which carries out predictions of the parton shower and hadronisation processes and adds estimations of the underlying event. A set of tuned parameters, labelled A14 [139], is used along with the `NNPDF2.3lo` [140] PDF set. Lastly the decays of heavy quarks (b and c) are simulated separately using the EvtGen v1.6.0 program [141], this is the case for all MC samples containing a $t\bar{t}$ pair unless stated otherwise. This sample will be referred to as POWHEG+PYTHIA8, or simply the 'nominal' sample for the remainder of this thesis.

Alternative $t\bar{t}$ MC samples

A set of additional $t\bar{t}$ samples using different generator, and parton-shower and hadronisation setups are used in the analysis. These are used both as extra points of comparison and to estimate uncertainties on the modelling of $t\bar{t}$ events.

An uncertainty on the value of the top mass in MC is estimated using events generated identically to the nominal $t\bar{t}$ sample but using alternative values for the top-quark mass of $m_{\text{top}} = 169, 171, 172, 173, 174$ and $176\,\text{GeV}$. Another sample based on the nominal setup but with the h_{damp} parameter set to $3 \times m_{\text{top}}$ is generated to assess sensitivity to initial-state radiation (ISR). Remaining ISR effects from changing the μ_{r} and μ_{f} scales by factors of 0.5 and 2.0, and simultaneously choosing the Var3c up/down variants of the A14 tune, are tested by re-weighting the events from the nominal sample.

Similarly changes to the final-state radiation (FSR), due to the renormalisation scale within the parton shower, are handled by re-weighting the nominal MC sample to simulate changing μ_r by factors of 0.5 and 2.0 with respect to the nominal value.

Two additional samples that can be directly compared to the POWHEG+PYTHIA8 setup are needed to assess the impact of the hard-scatter matching, and the shower and hadronisation modelling. For the alternative matching scheme the PowhegBox v2 generator is replaced by MADGRAPH5_aMC@NLO v2.6.0 [142] using the same PDF set and renormalisation and factorisation scale settings. The shower starting scale has the functional form $\mu_q = H_T/2$ [143], where H_T is defined as the scalar sum of the p_T of all outgoing partons. Top quarks are decayed at LO using MADSPIN [144, 145] to preserve spin correlations. The events are again interfaced with PYTHIA8.230 using the same PDF set and the A14 set of tuned parameters specific to use with MADGRAPH5_aMC@NLO [139]. Most notably these settings do not include the matrix-element corrections present in the POWHEG+PYTHIA8 sample so as to avoid double-counting radiation between the matrix-element and shower. The impact of the parton shower and hadronisation model is evaluated using a sample produced with POWHEGBOX v2 interfaced to HERWIG7.04 [110, 116]. The settings in POWHEGBOX are the same as the nominal sample and the H7UE set of tuned parameters [110] and the MMHT2014LO PDF set [146] are used for HERWIG7.04. These samples will be referred to as MC@NLO+PYTHIA8 and POWHEG+HERWIG7 respectively.

A final NLO $t\bar{t}$ prediction is produced using the SHERPA2.2.1 generator [108] in order to investigate the impact of generating higher-order additional radiation in the matrix-element calculation compared to the parton-shower. The sample includes NLO accurate matrix element calculations for up to one additional parton, and LO calculations for up to four additional parton emissions using the Comix [147], and OpenLoops [148–150] libraries. Matrix-element calculations are matched to the SHERPA parton shower [112] using the MEPS@NLO prescription [106, 109, 151, 152]. A set of tuned parameters are used, provided by the SHERPA authors and derived to match the `NNPDF3.0nnlo` PDF set [138]. The central renormalisation and factorisation scales are set to the same functional form: $\mu^2 = m^2_{\text{top}} + 0.5(p^2_{T,t} + p^2_{T,\bar{t}})$, and the CKKW scale, used to control the overlap between jets from the ME and PS, is set to 30 GeV [143].

As described above the different $t\bar{t}$ predictions are each normalised to the total $t\bar{t}$ cross-section calculated at NNLO + NNLL. However the expanded matrix element calculation in the SHERPA sample contains some of the same NNLO corrections thus it is not immediately obvious how to correctly normalise the sample. Two different

normalisations are included in the analysis; the first using the prediction as it is provided by the generator, labelled SHERPA (NLO norm.); and the second normalising the total cross-section to the NNLO + NNLL prediction, simply labelled SHERPA.

Estimation of higher-order corrections

Simulated $t\bar{t}$ events at NNLO in α_S are not yet available matched to a parton-shower, thus it is not possible to produce full NNLO + PS predictions. To assess the impact of missing NNLO corrections an estimate is derived by starting from the existing NLO + PS samples and re-weighting the events at parton-level to match a QCD prediction at NNLO. The re-weighting is performed recursively using the top-quarks in the event record after initial- and final-state radiation and applied such that the re-weighted parton-level distributions match well with the predictions for the three variables: $p_T(t)$, $p_T(t\bar{t})$, and m($t\bar{t}$). This is done using the recursive form of the NNLO $t\bar{t}$ re-weighting tool [153]. This implementation uses predictions for $p_T(t)$ and m($t\bar{t}$) at NNLO in α_S with NLO EW corrections from [17] using the `NNPDF3.0QED` PDF set [17]. The $p_T(t\bar{t})$ prediction is calculated at NNLO in QCD [154, 155] using the `NNPDF3.0` PDF set [138]. The top-quark mass is set to 173.3 GeV in all of these predictions and dynamic renormalisation and factorisation scales are used with functional forms: $m_T(t)/2$ for $p_T(t)$, and $H_T/4$ for $p_T(t\bar{t})$ and m($t\bar{t}$).

MC samples with new physics effects

In Chapter 11 results from the cross-section measurement are used to set limits on new physics effects above some energy scale (Λ) using an EFT framework. Simulated samples with added EFT effects are generated by varying values of the Wilson coefficients corresponding to dimension six operators in the Warsaw basis [26]. In this scheme the SM prediction is recovered by setting the Wilson coefficients under study to zero. The O_{tG} and $O_{tq}^{(8)}$ operators, outlined in Section 2.4.2, are chosen for the study. Samples are generated with different values for the two Wilson coefficients: $\left(C_{tG}, C_{tq}^{(8)}\right) = (\pm 1 \text{ or } 0, \pm 1 \text{ or } 0)$. The SMEFTATNLO 1.0.0 UFO model [30] at leading order is used, with the new physics scale set to $\Lambda = 1$ TeV. The renormalisation and factorisation scales are set to $\mu_r = \mu_f = m_t$ and the $\{m_W, m_Z, G_f\}$ EW input scheme is used as outlined in [156]. The parton shower and hadronisation are performed using PYTHIA8 (v8.244) [111]. Two sets of the nine samples are produced; a *linear* set and a

quadratic set. The linear samples only include EFT terms which are proportional to Λ^{-2}, these terms correspond to the interference between the SM and the EFT operators. The quadratic samples include the linear terms as well as terms proportional to Λ^{-4}, which correspond to the square of individual dimension six operators, as well as the interference between operators. One additional quadratic sample is produced with $\left(C_{tG}, C_{tq}^{(8)}\right) = (0.2, 0.2)$ and $\Lambda = 1\,\text{TeV}$, and two linear samples are created by re-scaling existing samples to mimic values of $\left(C_{tG}, C_{tq}^{(8)}\right) = (0.25, 0.0)$ and $(0.0, 0.25)$. These sample are used to test for possible biases in the EFT fit originating from the unfolding procedure, as described in Section 8.5.3.

Background MC samples

Associated production of a top-quark with a W-boson (tW) is modelled with the nominal POWHEGBOX setup using the five-flavour scheme. Interference and overlap with $t\bar{t}$ production is dealt with using the diagram removal (DR) scheme [157]. To assess the uncertainty on this choice an alternative setup using the diagram subtraction (DS) scheme [157, 158] is also produced. In both cases events are interfaced with PYTHIA8.230 with the same settings as the nominal $t\bar{t}$ sample. Single-top s-channel production is simulated using the same setup as for tW events but without any treatment needed for $t\bar{t}$ diagrams. Single-top t-channel production uses the same setup as s-channel but with the POWHEGBOX generator in the four-flavour scheme.

Events with an additional vector boson (W or Z) produced alongside a $t\bar{t}$ pair are generated with the same setup as the MC@NLO+PYTHIA8 alternative $t\bar{t}$ sample but using older version of both MADGRAPH5_aMC@NLO (v2.3.3) [142] and PYTHIA8 (v8.210) [111], as well as EVTGEN (v1.2.0) [141] for the b and c hadron decays. The production of a Higgs boson in conjunction with $t\bar{t}$ is modelled using an identical setup to the POWHEG+PYTHIA8 sample.

The simulation of W+jets and Z+jets events is done using the SHERPA v2.2.1 generator with similar settings as the $t\bar{t}$ SHERPA sample but using the default factorisation and normalisation scales, and with the CKKW merging scale set to 20 GeV. Both samples are normalised to a next-to-next-to-leading order prediction [159].

Samples of diboson final states (VV) where V is either a W or Z boson are simulated with the SHERPA v2.2.1 or v2.2.2 generator depending on the process. Off-shell effects and Higgs-boson contributions are included where appropriate. Samples for the loop-

induced processes $gg \to VV$ are generated using LO-accurate matrix elements for up to one additional parton emission, all other processes are generated at NLO in QCD for up to one additional parton and LO for up to three additional parton emissions. The matrix element calculations are matched and merged with the SHERPA parton shower based on Catani-Seymour dipole factorisation [112, 147] using the MEPS@NLO prescription. Virtual QCD corrections are provided by the OPENLOOPS 1 library. The same PDF set and SHERPA parameters as the $t\bar{t}$ and V+jets samples are used.

Lastly three additional samples that do not contain any real leptons deriving from the decay of a boson are used to estimate the uncertainty on the multijet background. See Sections 7.3.1 and 9.3.1 for details on the estimation of this background and associated uncertainty. One sample simulates $t\bar{t}$ events decaying in the all-hadronic channel rather than lepton+jets and uses the same settings as for the nominal sample. The other samples simulate W+jets and Z+jets events with the W or Z having p_{T} above 280 GeV and decaying hadronically. These are simulated using SHERPA v2.2.5, with similar settings to the diboson samples.

7.2. Measurement strategy

The measurement strategy is outlined here. Firstly a set of background events (non-$t\bar{t}$ processes with the same final state) are estimated from a combination of MC simulation and extrapolations from data events, this is described in Section 7.3. A series of kinematic requirements are then used to select events consistent with the topology of boosted $t\bar{t}$ events in the lepton+jets decay channel, described in Section 7.4. A selection of one- and two-dimensional differential observables are chosen, as outlined in Section 8.1, and the distributions at detector-level are extracted from the data. The distributions are then run through an iterative unfolding procedure outlined in Section 8.3, which first subtracts the expected backgrounds and then corrects for the limited resolution, efficiency, and acceptance of the detector. After this the distributions can be compared directly to simulation at particle-level.

The impact of systematic uncertainties on the measurement is estimated by repeating all of the analysis steps above but replacing the data and background samples with simulated pseudo-data where the expected source of a single systematic uncertainty is varied by $\pm 1\sigma$ from its nominal value. In this way the unfolding procedure is kept fixed and the input data is varied. This procedure is outlined in Chapter 9 along with

the treatment of the statistical uncertainty which is estimated by generating several toy inputs via a Poisson smearing process. All uncertainties are defined such that they can be treated as fully uncorrelated from each other, the total uncertainty is then calculated as the sum of the statistical and systematic covariance matrices.

A new method to reduce the impact of jet energy scale uncertainties is introduced in Section 9.5. An additional jet scale factor (JSF) is derived using the relationship between the top-quark mass (m_{top}) and the measured hadronic top-quark mass distribution at detector-level ($m^{t,h}$). This correction is then applied to the energy of individual jets in each event **before** kinematic selections are applied, bringing the boosted top-quark mass distributions in data and simulation into agreement. The entire analysis is repeated using this JSF method following the strategy outlined above, including measuring a separate JSF value for each systematic variation. This results in a significant reduction in jet energy scale uncertainties.

7.3. Background estimation

Several non-$t\bar{t}$ physics processes can result in the same reconstructed final-state objects as $t\bar{t}$ events in the lepton+jets channel. As a result the selected data sample will contain a non-negligible fraction of background events which need to be understood in advance. The largest portion of these is expected to come from processes involving the production of a single top-quark which come in three flavours: s-channel, t-channel, and tW. Some example leading-order Feynman diagrams for these are shown in Figure 7.2. The tW events are expected to be the dominant background

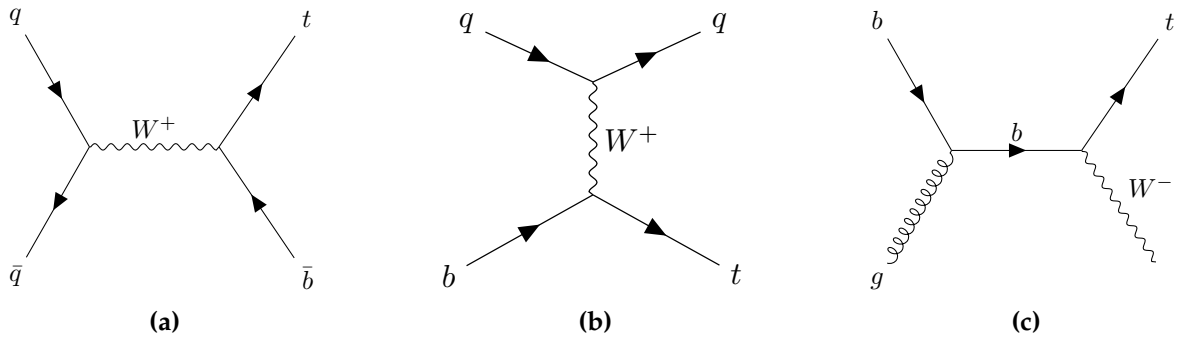

Figure 7.2: Leading order Feynman diagrams of the three single-top production channels (a) s-channel (b) t-channel (c) tW.

process in boosted events as the W-boson can decay leptonically leaving the top-quark free to decay hadronically, matching the boosted jet signal. In both the s-channel and t-channel cases the top-quark must decay leptonically to supply the lepton and neutrino signatures, requiring the high p_{T} top-quark signature to be mis-reconstructed from the remaining jets.

Another significant source of background events is expected to come from processes in which $t\bar{t}$ pairs are produced in conjunction with a heavy vector boson (Z or W) or with a Higgs boson, known collectively as $t\bar{t}V$. A sub-set of tree-level Feynman diagrams for these processes is shown in Figure 7.3. With a $t\bar{t}$ pair directly produced in these events there are many possible decay modes of the Z, W, and Higgs which can result in the desired final-state, however the lower overall cross-section of such events reduces the contribution of these processes.

Processes which do not include any top-quarks can also contribute, including the production of W and Z bosons in conjunction with QCD jets and diboson (ZZ, ZW, WW) events, examples of which are shown in Figure 7.4. Only the tree-level Z-boson decay with the lowest branching fraction ($Z \to \ell\bar{\ell}$) contains real leptons for the event trigger, and in this case the other lepton must be mis-reconstructed for the event to resemble a $t\bar{t}$ decay, thus the Z+jets and ZZ backgrounds are heavily reduced.

Lastly events not containing a lepton from a boson decay can still contribute if a lepton from a hadronic decay of a heavy quark is sufficiently isolated, or if jet constituents are mis-reconstructed as a lepton. These events are collectively known as multijet background. Multijet events are particularly tricky to simulate using existing MC frameworks and so are derived using a data-driven method described below. The other backgrounds are estimated using simulated samples outlined in Section 7.1.

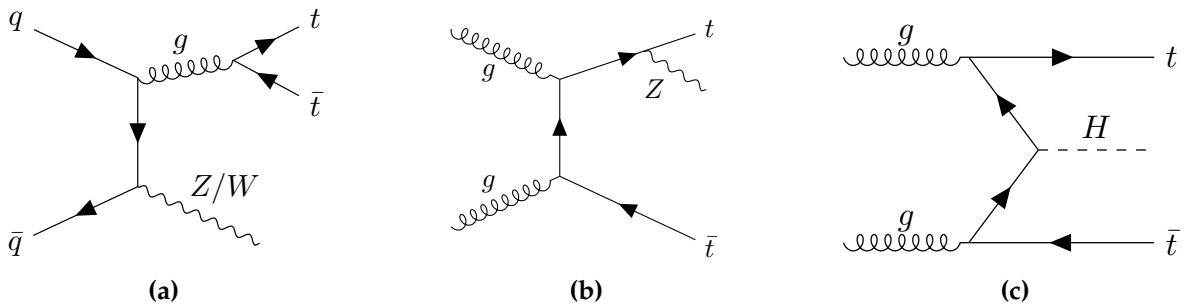

Figure 7.3: Example tree-level Feynman diagrams for different $t\bar{t}$ + boson processes, (a) $t\bar{t}Z$ and $t\bar{t}W$ (ISR) (b) $t\bar{t}Z$ (FSR) (c) $t\bar{t}H$

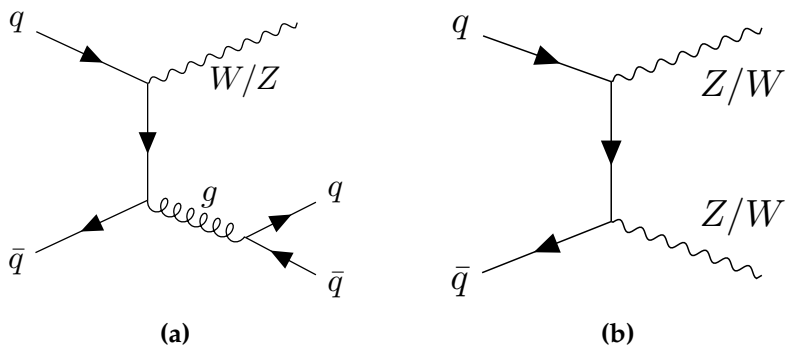

Figure 7.4: Example tree-level Feynman diagrams for background events which do not include a top-quark, (a) $W(Z)$+jets (b) diboson

7.3.1. Multijet background estimate

The level of multijet background contamination is highly dependent on the detector performance and is made up of various processes, many of which are not well simulated by Monte Carlo generators. Predictions of the multijet background are derived using a data-driven method instead. A general purpose technique, known as the matrix-method, is used. This is based on comparing datasets produced with two different lepton selections: *Tight* and *Loose*. The Tight selection is equivalent to the lepton requirements in the nominal sample, described in Section 7.4. The Loose selection has less strict identification and isolation requirements but otherwise uses the same kinematic requirements as the Tight selection and is thus expected to result in a higher fraction of multijet events. The number of multijet events in the Tight signal region is given by:

$$N_{mj}^{T} = \frac{\epsilon_f}{\epsilon_r - \epsilon_f}(\epsilon_r N^L - N^T), \tag{7.1}$$

where ϵ_f is the fraction of non-prompt (fake) leptons in the Loose selection which also pass the Tight selection, ϵ_r is the fraction of real leptons in the Loose selection which also pass the Tight requirements, N^L and N^T are the total number of events in the Loose and Tight selections respectively. The values of ϵ_f and ϵ_r are the fake and real efficiencies of the Tight selection respectively. These are derived using standard techniques in control regions enriched in either real or fake leptons as described in [160], and depend on the lepton kinematics and characteristics of events in the Loose selection. To correctly account for these dependencies the multijet background estimate in the signal region is derived using event weights, w_i, calculated for each event, i, in

the Loose lepton selection:

$$w_i = \frac{\epsilon_f}{\epsilon_r - \epsilon_f}(\epsilon_r - \delta_i), \tag{7.2}$$

where δ_i is a per-event boolean that is 1 if the event passes both selections and 0 for events which exclusively pass the Loose selection. The final number of multijet events in each bin of the signal region is calculated as the sum of the weights in that bin.

7.4. Event selection

Events are selected based on the number and kinematics of various reconstructed objects. Due to slight differences in how objects are defined at detector-level and particle-level separate selections are needed for both but identical requirements are used where possible to reduce the extrapolation between them. The selection is defined to be consistent with the boosted lepton+jets decay topology shown schematically in Figure 7.5, with specific values chosen to achieve a high purity of $t\bar{t}$ events and to ensure the full $t\bar{t}$ system can be reconstructed unambiguously. A summary of the exact selection requirements at both detector- and particle-level is given in Table 7.1.

Events are required to have exactly one lepton, either an electron or muon, which is matched to the trigger decision. Events with $W \to \tau\nu_\tau$ can also be picked up by the lepton triggers provided the tau decays into an electron or muon with sufficient transverse momentum. Leptons must pass combined *Tight* isolation and identification requirements as described in Section 5.2 and must have a transverse momentum larger than 27 GeV and also be within the acceptance of the inner detector ($|\eta| < 2.5$) to facilitate accurate tracking. Additionally electrons with an η value in the transition region between the barrel and endcap calorimeters ($1.37 < |\eta| < 1.52$) are vetoed. This electron requirement is dropped for the selection at particle-level where detector geometry is not a limiting factor. At particle-level leptons are dressed, as discussed in Chapter 5, before p_{T} and η requirements are imposed.

Small radius ($R = 0.4$) calibrated jets are required to fall within the acceptance of the inner detector ($|\eta| < 2.5$) and have a transverse momentum greater than 26 GeV. This is raised from the typical threshold of 25 GeV used in previous measurements as a consequence of the jet scale factor method outlined in Section 9.5. Jets originating from a b-quark (b-jets) are selected at detector-level using the DL1r b-tagging algorithm

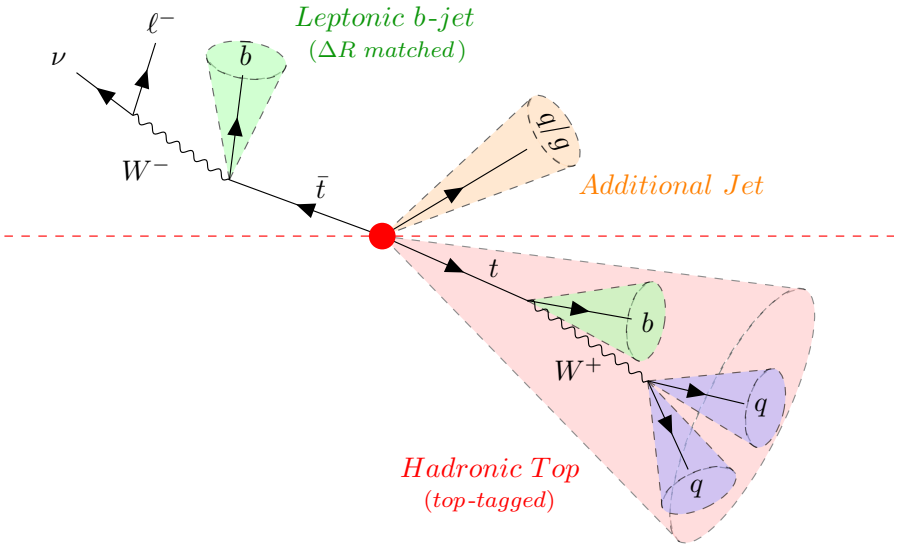

Figure 7.5: Schematic of an idealised boosted $t\bar{t}$ event

as described in Section 5.4. At particle-level b-jets are defined by a process of ghost-matching [161] b-hadrons with $p_{\mathrm{T}} > 5\,\mathrm{GeV}$ to jets.

The boosted top-quark is selected using the $R = 1.0$ trimmed reclustered jets described in Section 5.5. These RC jets are required to have transverse momentum larger than 355 GeV, again raised from the initial value due to the JSF method, and have stricter acceptance requirements of $|\eta| < 2$ due to their larger radius. Reclustered jets must also be suitably isolated from the electron in relevant events ($\Delta R(e, j_{\mathrm{RC}} > 1.0)$) to remove cases of RC jets seeded by high p_{T} electrons. In each event a single RC jet must be chosen as the top candidate (top-tagged). To ensure the jet is consistent with a top decay the jet mass is required to be around the top-quark mass (120 GeV $< m <$ 220 GeV) and the jet must contain at least one b-tagged sub-jet. If more than one RC jet passes these requirements the jet with the highest p_{T} is chosen.

To match the expected lepton+jets decay topology events are required to contain at least two b-jets with one a constituent of the hadronically decaying top-quark and another separate from the hadronic top-quark and matched to the lepton ($\Delta R(\ell, b\text{-jet}) < 2.0$). If more than one b-jet is matched to the lepton then the jet with the highest p_{T} is deemed the leptonic b-jet (b_ℓ-jet). This is used to build observables and approximate the leptonic top-quark kinematics, as described in Section 7.5. After these selections any other small-R jets that are not constituents of the top-tagged jet or the b_ℓ-jet itself, are referred to as additional jets.

Lastly, events are required to have a minimum amount of missing energy given by $E_{\mathrm{T}}^{\mathrm{miss}} > 20$ GeV and $E_{\mathrm{T}}^{\mathrm{miss}} + m_T^W > 60\,\mathrm{GeV}$, where m_T^W is transverse mass of the leptonically decaying W-boson. This is to reduce the contamination from multijet processes which are more common in regions of phase space with lower $E_{\mathrm{T}}^{\mathrm{miss}}$ as they originate from purely QCD processes and thus do not contain real neutrinos.

7.4.1. Reduction of single-top backgrounds

Previous measurements [124] suffered from large single-top modelling uncertainties in regions of high top-quark p_{T}. In particular the systematic uncertainty related to the choice of diagram removal or diagram subtraction (DR/DS) was found to be significant. To try and reduced the impact of this uncertainty an additional requirement on the invariant mass of the lepton and b_ℓ-jet is introduced. This aims to reduce the background contamination from Wt single-top processes, shown in Figure 7.2c, by removing events with a lepton and b_ℓ-jet which do not originate from the same top decay. The chosen threshold value is expected to be close to the top-quark mass, motivated by the fact that for on-shell top decays $m_{\ell,b} < m_{\mathrm{top}}$ by definition [162]. A comparison of the hadronic top p_{T} spectrum with and without an $m_{\ell,b}$ requirement in place is shown in Figure 7.6. Different threshold values were tested and an upper limit of 180 GeV was chosen as it provides the largest reduction in DR/DS difference in the high p_{T} region, whilst removing less than 1% of the $t\bar{t}$ signal. The direct effect of this selection on the background uncertainties is discussed separately in Section 9.3.2.

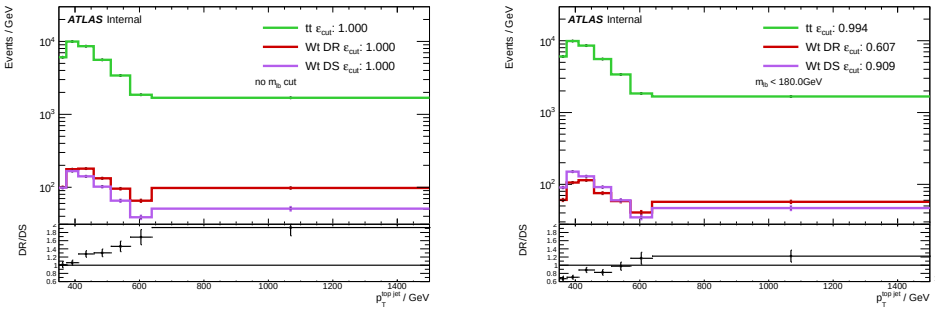

Figure 7.6: Comparison of the detector-level hadronic top-quark p_{T} distribution with (left) and without (right) an upper limit of 180 GeV on $\mathrm{m}_{\ell,b}$. Simulated $t\bar{t}$ events from the nominal sample are compared to generated single-top background events using either the diagram removal (DR) or diagram subtraction (DS) interference removal schemes. Events in each sample are weighted such that the total number of events before selection correspond to the same data luminosity.

Table 7.1: Summary of the selection requirements defining the fiducial volume at detector-level and particle-level.

Object	Detector-level requirements		Particle-level requirements
Leptons	**Exactly 1 lepton**		**Exactly 1 dressed lepton**
	Electrons	Muons	
	$p_{\mathrm{T}} > 27\,\mathrm{GeV}$	$p_{\mathrm{T}} > 27\,\mathrm{GeV}$	$p_{\mathrm{T}} > 27\,\mathrm{GeV}$
	$\lvert\eta\rvert < 1.37$ or $1.52 < \lvert\eta\rvert < 2.47$	$\lvert\eta\rvert < 2.5$	$\lvert\eta\rvert < 2.5$
Small-R jets ($R = 0.4$)	$p_{\mathrm{T}} > 26\,\mathrm{GeV}$ $\lvert\eta\rvert < 2.5$		Same as detector-level
b-tagged jets ($R = 0.4$)	DL1r multivariate tagger at 77% efficiency		Jet ghost-matched to b-hadron
	≥ 1 b-tagged jet is constituent of top-jet		Same as detector-level
	≥ 1 b-tagged jet near lepton: $\Delta R(\ell, b) < 2.0$ **and not constituent of top-jet**		
Hadronic top-jet ($R = 1.0$) ($R = 0.4$ jets as input)	**≥ 1 top-tagged trimmed RC-jet candidate** $p_{\mathrm{T}} > 355\,\mathrm{GeV}$ $\lvert\eta\rvert < 2.0$ $120\,\mathrm{GeV} < m < 220\,\mathrm{GeV}$ ≥ 1 b-tagged sub-jet		Same as detector-level
$E_{\mathrm{T}}^{\mathrm{miss}}$ & $\mathrm{m}_{\mathrm{T}}^{\mathrm{W}}$	$E_{\mathrm{T}}^{\mathrm{miss}} > 20\,\mathrm{GeV}$ $E_{\mathrm{T}}^{\mathrm{miss}} + \mathrm{m}_{\mathrm{T}}^{\mathrm{W}} > 60\,\mathrm{GeV}$		Same as detector-level
Electron isolation	$\Delta R(e, t) > 1.0$		Same as detector-level
$m_{\ell,b}$	$m_{\ell,b} < 180\,\mathrm{GeV}$		Same as detector-level

7.5. Top-quark reconstruction

After events are selected the kinematics of the $t\bar{t}$ system can be approximated using the selected objects. The hadronic top-quark properties are taken from the top-tagged RC jet. The kinematics of the leptonic top-quark are estimated by summing the four-momenta of the lepton, b_ℓ-jet, and the neutrino. The x and y components of the neutrino three-momentum are taken from the $E_{\mathrm{T}}^{\mathrm{miss}}$ vector. The z component is estimated using the assumption that the lepton-neutrino system has invariant mass equal to the W-boson mass [4], assuming a massless neutrino, and then solving for p_z, the details of this calculation can be found in Appendix A.1. The result is a quadratic formula for the missing neutrino z-momentum given by:

$$p_{z,\nu} = \frac{-b \pm \sqrt{b^2 - 4ac}}{2a}, \tag{7.3}$$

with: $a = E_\ell^2 - p_{z,\ell}^2 \quad b = -2kp_{z,\ell} \quad c = E_\ell^2 p_{T,\nu}^2 - k^2$, and

$$k = \frac{m_W^2 - m_\ell^2}{2} + p_{x,\ell}p_{x,\nu} + p_{y,\ell}p_{y,\nu},$$

where E_ℓ is the energy of the lepton, $p_{X,\ell}$ and $p_{X,\nu}$ are the X-component of the lepton and neutrino 3-momenta respectively, $p_{T,\nu}$ is the component of the neutrino momentum transverse to the beam-line, and m_W, m_ℓ are the rest mass of the W-boson and lepton respectively. If the solution to equation (7.3) is complex only the real part is used and the imaginary part ignored. Where two real solutions exist, the solution that gives the smallest invariant mass for the b_ℓ-jet, lepton, and neutrino system is chosen.

7.6. Event yields

The total number of events after applying the event selection to the signal and background samples in Section 7.1 are given in Table 7.2. Roughly 16% more events are expected from simulation than observed in data. This is in line with previous boosted measurements [122–124] and is likely due to mis-modelling of the top-quark p_{T} spectrum in the NLO $t\bar{t}$ prediction. Any mis-modelling in this distribution will affect all observables due to the explicit requirement of $p_{\mathrm{T}}(t) > 355\,\mathrm{GeV}$ used to select events.

Before proceeding further it is also useful to compare some sample kinematic distributions from data to the sum of the nominal signal and background predictions. For these comparisons the predicted events are normalised to match the total number of events observed in data in order to capture only the shape agreement and remove the normalisation offset observed in Table 7.2. Doing this helps show if the remaining modelling of $t\bar{t}$ events within the selected phase-space is sufficiently accurate. This is typically done for observables that are not planned to be included in the final measurement to ensure that the modelling is robust in general and is not biased towards the chosen variables. Some examples of these *control plots* are shown in Figure 7.7 for the p_{T} of the lepton, the missing transverse momentum, and the total number of small-R jets in each event. In each case the dashed band represents the combination of the uncertainty from limited data statistics and detector related systematic uncertainties on the predictions, outlined in detail in Chapter 9. This does not include uncertainties related to the modelling of $t\bar{t}$ or background processes. In general good agreement is observed between data and prediction with any differences within the uncertainties in most bins of the variables shown. Slight tension is observed in regions of high jet multiplicity in Figure 7.7c, however the differences are likely to be covered when considering the missing modelling uncertainties.

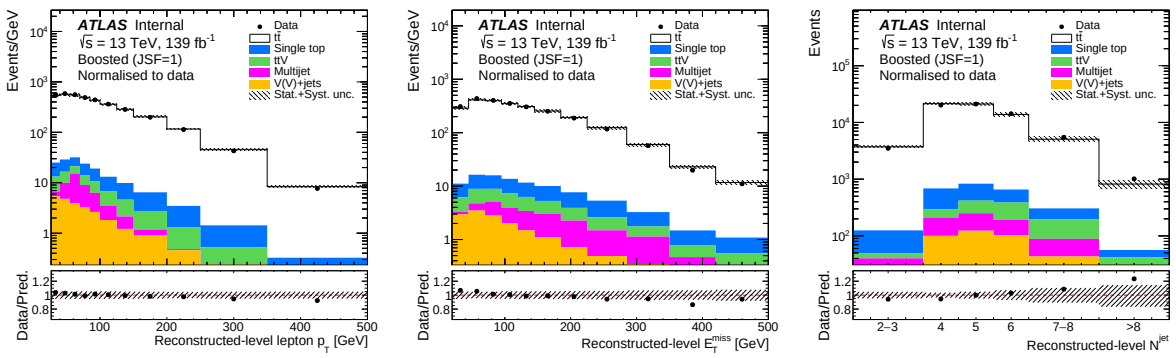

(a) **(b)** **(c)**

Figure 7.7: Detector-level distributions of the number of events as a function of (a) p_{T} of the lepton, (b) $E_{\mathrm{T}}^{\mathrm{miss}}$, and (c) the number of small-R jets in the event. The data are compared to the expectation from simulation and background estimates normalised to match the number of entries in data. The lower panel shows the ratio of the data to the normalised expectation. The dashed band represents the total statistical and systematic uncertainties but does not include modelling uncertainties.

Table 7.2: Event yields for measured data and predicted signal and background events. The uncertainty values are symmetrised and indicate the combined effect of statistical, detector and background modelling uncertainties. The total expected yield and associated uncertainty, as well as statistical uncertainties, are calculated prior to rounding.

Process	Expected events (JSF $= 1$)
$t\bar{t}$	84 170 $\pm$ 4210
Single top-quark	1710 $\pm$ 280
$t\bar{t}\,V(t\bar{t}W{+}t\bar{t}Z{+}t\bar{t}H)$	840 $\pm$ 110
Multijet	550 $\pm$ 360
W+jets	420 $\pm$ 160
Z+jets	80 $\pm$ 40
Diboson	40 $\pm$ 20
Total prediction	87 810 $\pm$ 4240
Data	75631

Chapter 8.

Observables and unfolding

"Coming back to where you started is not the same as never leaving"
— Terry Pratchett, A Hat Full of Sky

8.1. Choice of observables

The goal of this analysis is not only to measure the total $t\bar{t}$ cross-section but also to make several differential cross-section measurements defined as:

$$\frac{d\sigma_i}{dX_i} = \frac{N_i^{\text{event}}}{\mathcal{L} \cdot \Delta X_i}\,, \tag{8.1}$$

where i denotes a specific bin and X represents the variable being measured, thus ΔX_i is the bin width. It is useful at this stage to outline and motivate the choice of variables that will be measured, which can be split into two broad categories; those characterising the kinematics of the $t\bar{t}$ system and those related to additional radiation in the events. The chosen observables related to the $t\bar{t}$ kinematics are:

- $p_{\mathrm{T}}^{t,h}$, $p_{\mathrm{T}}^{t,\ell}$: the transverse momenta of the hadronic and leptonic top quarks,
- $|y^{t,h}|$, $|y^{t,\ell}|$, $|y^{t\bar{t}}|$: the rapidity of the top quarks and the $t\bar{t}$ system,
- $m^{t\bar{t}}$: the invariant mass of the $t\bar{t}$ system,

- $H_{\mathrm{T}}^{t\bar{t}}$: the scalar sum of the transverse momentum of the two top quarks,

- $\frac{\Delta\phi}{\pi}(b_\ell, t_h)$: the azimuthal angle separation between the hadronically decaying top quark and the b-jet associated to the lepton.

These variables are fundamental properties of the $t\bar{t}$ decay and are in many cases sensitive to the dynamics of the boosted system. All of these variables have been measured in previous ATLAS analyses [123, 124], though at lower integrated luminosities. Additionally the $H_{\mathrm{T}}^{t\bar{t}}$, $m^{t\bar{t}}$ and top quark p_{T} distributions are expected to be most sensitive to new physics effects. Similarly the rapidity distributions are expected to be useful for studies probing the parton distribution functions [163], however these were not a focus of this analysis. The second set of variables, used to probe the effects of additional radiation in detail, are:

- $p_{\mathrm{T}}^{t\bar{t}}$: the transverse momentum of the $t\bar{t}$ system,

- N^j: the number of additional jets in each event,

- $p_{\mathrm{T}}^{j,1}$, $p_{\mathrm{T}}^{j,2}$: transverse momenta of the leading and sub-leading additional jets,

- $\frac{\Delta\phi}{\pi}(j_1, t_h)$, $\frac{\Delta\phi}{\pi}(j_2, t_h)$: difference in azimuthal angle between the leading additional jets and the hadronically decaying top quark,

- $\frac{\Delta\phi}{\pi}(j_1, j_2)$, $\frac{\Delta\phi}{\pi}(t_h, t_\ell)$: difference in azimuthal angle between the leading and sub-leading additional jets and between the two top-quarks,

- $m(j_1, t_h)$: invariant mass of the leading additional jet and the hadronically decaying top quark,

- $H_{\mathrm{T}}^{t\bar{t}+\mathrm{jets}}$: scalar sum of the transverse momenta of the top quarks and all additional jets.

Lastly a set of two dimensional observables are defined by combining several of the variables discussed above. These allow for double-differential cross-section measurements that characterise the kinematics of the leading additional jet as functions of $p_{\mathrm{T}}^{t,h}$ and N^j:

- $p_{\mathrm{T}}^{j,1}$ in regions of increasing $p_{\mathrm{T}}^{t,h}$,

- $\boldsymbol{p_{\mathrm{T}}^{j,1}}$ in regions of increasing $\boldsymbol{N^{j}}$,
- $\boldsymbol{\frac{\Delta\phi}{\pi}(j_1, t_h)}$ in regions of increasing $\boldsymbol{p_{\mathrm{T}}^{t,h}}$,
- $\boldsymbol{\frac{\Delta\phi}{\pi}(j_1, t_h)}$ in regions of increasing $\boldsymbol{N^{j}}$.

All variables including the leading or sub-leading additional jet use a subset of the total selected events which contain at least one or two additional jets respectively. These same variables and the scalar p_{T} sum of the full event ($H_{\mathrm{T}}^{t\bar{t}+\mathrm{jets}}$) have not been measured previously in highly boosted $t\bar{t}$ events at ATLAS.

The effect of additional emissions is clear for several of these variables, such as the p_{T} of the $t\bar{t}$ system which one would expect to be heavily correlated with the p_{T} of any additional radiation, particularly those emissions originating from the initial state. However some observables, including the subsets of angular and 2D variables, have more complex interactions that can not be as easily understood. To provide more context a series of studies were performed on the expected precision of the measurements and the sensitivity of each observable to both the SM $t\bar{t}$ modelling and possible new physics effects. These are outlined in the proceeding sections, along with a summary of the measured observables in Table 8.1.

Table 8.1: List of differential observables measured in the analysis. Variables in **bold** have not previously been measured by ATLAS in highly boosted $t\bar{t}$ events.

Variable ($t\bar{t}$)	Variable (j)	Variable (2D)
$p_{\mathrm{T}}^{t,h}$	$p_{\mathrm{T}}^{t\bar{t}}$	$\boldsymbol{p_{\mathrm{T}}^{j,1}}$ **Vs** $\boldsymbol{p_{\mathrm{T}}^{t,h}}$
$p_{\mathrm{T}}^{t,\ell}$	N^{j}	$\boldsymbol{p_{\mathrm{T}}^{j,1}}$ **Vs** $\boldsymbol{N^{j}}$
$\lvert y^{t,h}\rvert$	$\boldsymbol{p_{\mathrm{T}}^{j,1}}$	$\boldsymbol{\frac{\Delta\phi}{\pi}(j_1, t_h)}$ **Vs** $\boldsymbol{p_{\mathrm{T}}^{t,h}}$
$\lvert y^{t,\ell}\rvert$	$\boldsymbol{p_{\mathrm{T}}^{j,2}}$	$\boldsymbol{\frac{\Delta\phi}{\pi}(j_1, t_h)}$ **Vs** $\boldsymbol{N^{j}}$
$\lvert y^{t\bar{t}}\rvert$	$\boldsymbol{\frac{\Delta\phi}{\pi}(j_1, t_h)}$	
$m^{t\bar{t}}$	$\boldsymbol{\frac{\Delta\phi}{\pi}(j_2, t_h)}$	
$H_{\mathrm{T}}^{t\bar{t}}$	$\boldsymbol{\frac{\Delta\phi}{\pi}(j_1, j_2)}$	
$\frac{\Delta\phi}{\pi}(b_\ell, t_h)$	$\boldsymbol{\frac{\Delta\phi}{\pi}(t_h, t_\ell)}$	
	$\boldsymbol{m(j_1, t_h)}$	
	$\boldsymbol{H_{\mathrm{T}}^{t\bar{t}+\mathrm{jets}}}$	

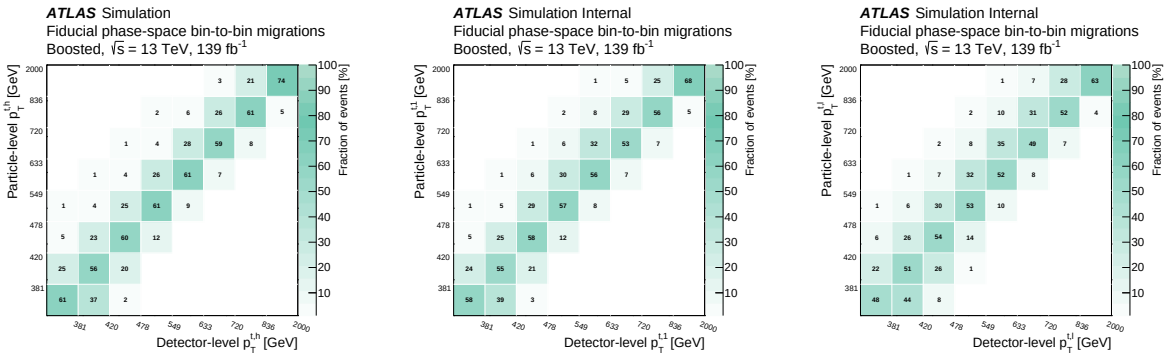

(a) **(b)** **(c)**

Figure 8.1: Fraction of total events (in percent) in each bin at detector-level and particle-level in the nominal POWHEG+PYTHIA8 MC sample for (a) hadronic top p_{T}, (b) leading top p_{T}, (c) leptonic top p_{T}. All variables use identical binning.

8.1.1. Choice of top-quark

For variables that indirectly measure the kinematics of the top-quark, e.g. $\frac{\Delta\phi}{\pi}(j_1, t_h)$, a choice has to be made of which top-quark definition to use; the hadronically decaying top-quark (t_h), the leptonically-decaying top-quark (t_ℓ), or the leading top-quark (t_1). Assuming a perfect detector, the leading top-quark is a sensible choice for variables aiming to probe recoil kinematics between the top-quark and additional radiation. However the detector resolution is not perfect in reality, as demonstrated in Figure 8.1 which compares the migration matrices for the p_{T} distributions of the three top-quark choices, obtained during the unfolding process (see Section 8.3). These show the fraction of total events in each bin at detector-level compared to all bins at particle-level. In all bins the fraction of events on the diagonal is higher for the p_{T} of the hadronic-top indicating fewer migration effects occur between detector-level and particle-level phase spaces during unfolding. This behaviour is expected as the leptonic top-quark is reconstructed using the pseudo-top algorithm which has reduced momentum resolution compared to using large-radius RC jets. In some events the leptonic top-quark will have the highest p_{T} and thus the resolution of $p_{\mathrm{T}}^{j,1}$ is also expected to be less than $p_{\mathrm{T}}^{t,h}$. As a result the tagged hadronic top-quark is used for all relevant observables.

8.1.2. Sensitivity to $t\bar{t}$ modelling

The alternative $t\bar{t}$ predictions discussed in Section 7.1.1 provide an opportunity to examine whether any observables are particularly sensitive to different choices made when modelling $t\bar{t}$ production. Figures 8.2a–d show the differential cross-sections at particle-level for each sample and the ratio of each to the nominal POWHEG+PYTHIA8 distribution for several of the studied observables. The cross-sections in each bin are divided by the total cross-section of the relevant sample so that the differences in shape can be directly compared. Uncertainty bands are also displayed which account for all sources of detector and modelling uncertainty derived via the unfolding process as described in Chapter 9, but omit uncertainty on the data statistics as the data is not included. This study was carried out before samples using the SHERPA generator were available and so the SHERPA predictions are not included in the plots.

Firstly the matching between the NLO matrix element to the parton shower is not unambiguous and is handled using two different methodologies (POWHEG and MC@NLO) matched to the same parton shower (PYTHIA8) in the POWHEG+PYTHIA8 and MC@NLO+PYTHIA8 samples. Comparing these directly effectively probes differences beyond NLO + PS accuracy. The first-order expectation is that any differences would be most visible in variables probing the first additional jet; where the matching is most relevant, and less extreme for variables related to any subsequent additional jets; which are handled primarily by the parton shower. This behaviour is observed most easily when comparing the p_{T} of the leading and sub-leading additional jets in Figures 8.2a and 8.2b, with the MC@NLO+PYTHIA8 sample showing incompatibility with both POWHEG+PYTHIA8 and POWHEG+HERWIG7 for the leading additional jet case ($p_{\mathrm{T}}^{j,1}$) and much better agreement for the sub-leading additional jet ($p_{\mathrm{T}}^{j,2}$).

Comparing the POWHEG+HERWIG7 and POWHEG+PYTHIA8 MC samples helps probe the impact of using different parton shower and hadronisation implementations. Firm conclusions are harder to obtain from these comparisons since both the shower and hadronisation models are changed simultaneously. However one notable area of difference is observed for the $\Delta\phi$ between the leading and sub-leading additional jets in Figure 8.2c, which is potentially due to the difference in shower ordering between PYTHIA8 (p_{T} ordered) and HERWIG7 (angle ordered).

The POWHEG+PYTHIA8 prediction with modified h_{damp} parameter should in theory probe variations in the kinematics of the leading extra radiation but in practice this is not observed to have a strong effect. Figure 8.2d shows the p_{T} distribution of

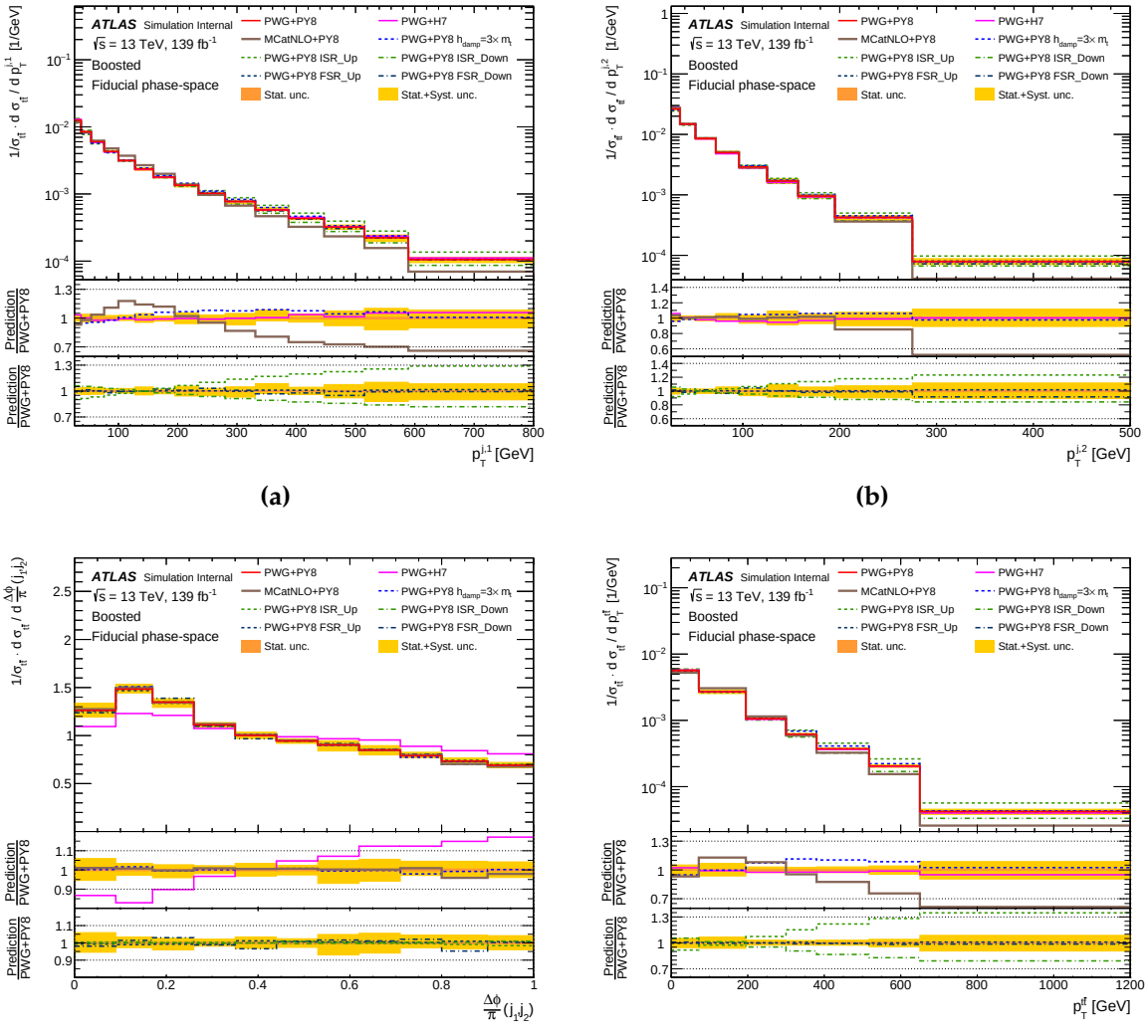

Figure 8.2: Particle-level generator comparisons of the relative $t\bar{t}$ cross-section in bins of (a) $p_{\mathrm{T}}^{j,1}$, (b) $p_{\mathrm{T}}^{j,2}$, (c) $\frac{\Delta\phi}{\pi}(j_1, j_2)$, (d) $p_{\mathrm{T}}^{t\bar{t}}$. The lower ratio pads compare different predictions to the POWHEG+PYTHIA8 distribution at particle-level. The yellow band represents combined detector, modelling, and MC statistical uncertainties derived from the unfolding whilst the orange band shows only the MC statistical component.

the $t\bar{t}$ system in which a slight shape difference between the h_{damp} varied sample and the nominal prediction is visible. Additionally the samples with modified initial- and final-state radiation alter the overall effects of additional radiation coming from each process. A priori the samples with varied strengths of ISR are expected to show larger differences compared to FSR as the probability of initial-state radiation is significantly higher in gg initiated $t\bar{t}$ production. Effects from the ISR variations are much more significant than both FSR and h_{damp} variations, as seen in the lower panels of Figures 8.2a, 8.2b and 8.2d.

8.1.3. EFT sensitivity

The $t\bar{t}$ samples which include additional EFT contributions, outlined in Section 7.1.1, can be used to assess the sensitivity of given observables to the new physics effects probed in Chapter 11. Several variables, including $p_{\text{T}}^{t,\ell}$, $m^{t\bar{t}}$, and $H_{\text{T}}^{t\bar{t}}$, exhibit sensitivity to EFT effects. However the $p_{\text{T}}^{t,h}$ distribution was found to be particularly sensitive to the chosen operators, especially in the highest p_{T} bins, as shown in Figure 8.3. This shows the particle-level cross section as a function of $p_{\text{T}}^{t,h}$ for leading-order SM, $\left(C_{tG}, C_{tq}^{(8)}\right) = (0,0)$, and SM + EFT predictions with $\left(C_{tG}, C_{tq}^{(8)}\right) = (1,0)$ and $(0,1)$. The overall effect of the O_{tG} operator on the total rate is greater than for $O_{tq}^{(8)}$, however the p_{T} dependence of the EFT contribution at high p_{T} is stronger for $O_{tq}^{(8)}$. This difference in shape allows the effects of the two operators to be disentangled using a single differential measurement.

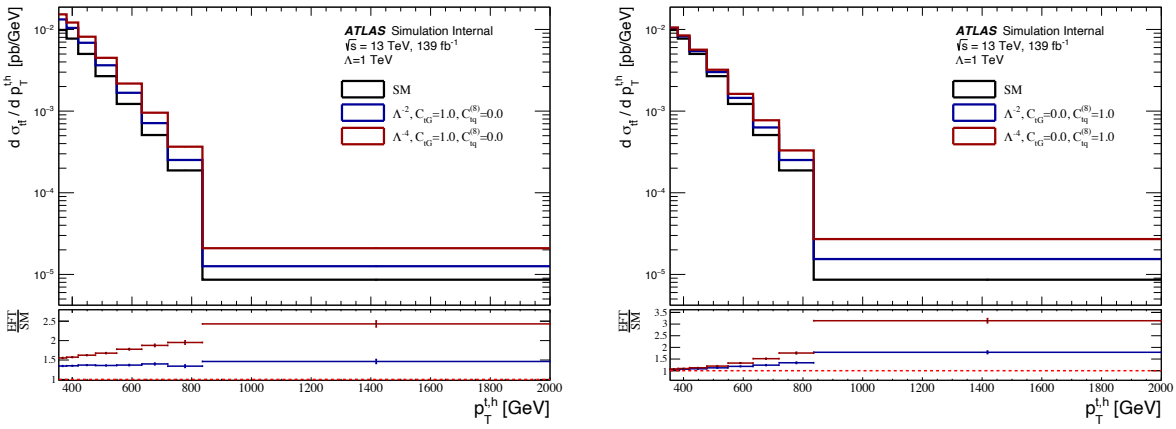

(a) **(b)**

Figure 8.3: Standard Model particle-level cross-section prediction as a function of the p_{T} of the hadronic top-quark, compared to predictions with EFT effects turned on.
(a) Only effects of the chromo-magnetic dipole operator O_{tG} are included ($C_{tG} = +1, C_{tq}^{(8)} = 0$). This significantly enhances the total rate and the quadratic terms exhibit a mild energy dependence.
(b) Only effects of the 4-fermion operator $O_{tq}^{(8)}$ are included ($C_{tG} = 0, C_{tq}^{(8)} = +1$). This shows a stronger energy dependence at high p_{T} for both linear and quadratic terms but has a lower overall effect on the rate.

8.1.4. Correlation between variables

The correlations between individual variables are also evaluated. Distributions sensitive to the same underlying physics effects will exhibit natural correlations parameterised by the correlation factor:

$$\rho_{X,Y} = \frac{\mathrm{cov}(X,Y)}{\sigma_X \sigma_Y}, \tag{8.2}$$

where $\mathrm{cov}(X,Y)$ is the covariance between variables X and Y and $\sigma_{X(Y)}$ is the standard deviation of $X(Y)$. The correlation factor for each pair of variables is evaluated in Figure 8.4 using events in the full Run-2 data sample at detector-level. Several variable pairs exhibit strong correlation; though in each case this behaviour is expected and can be explained. For example $\rho(p_{\mathrm{T}}^{t,h}, H_{\mathrm{T}}^{t\bar{t}}) = 0.78$ is understandably high as $p_{\mathrm{T}}^{t,h}$ is included directly in the definition of $H_{\mathrm{T}}^{t\bar{t}}$.

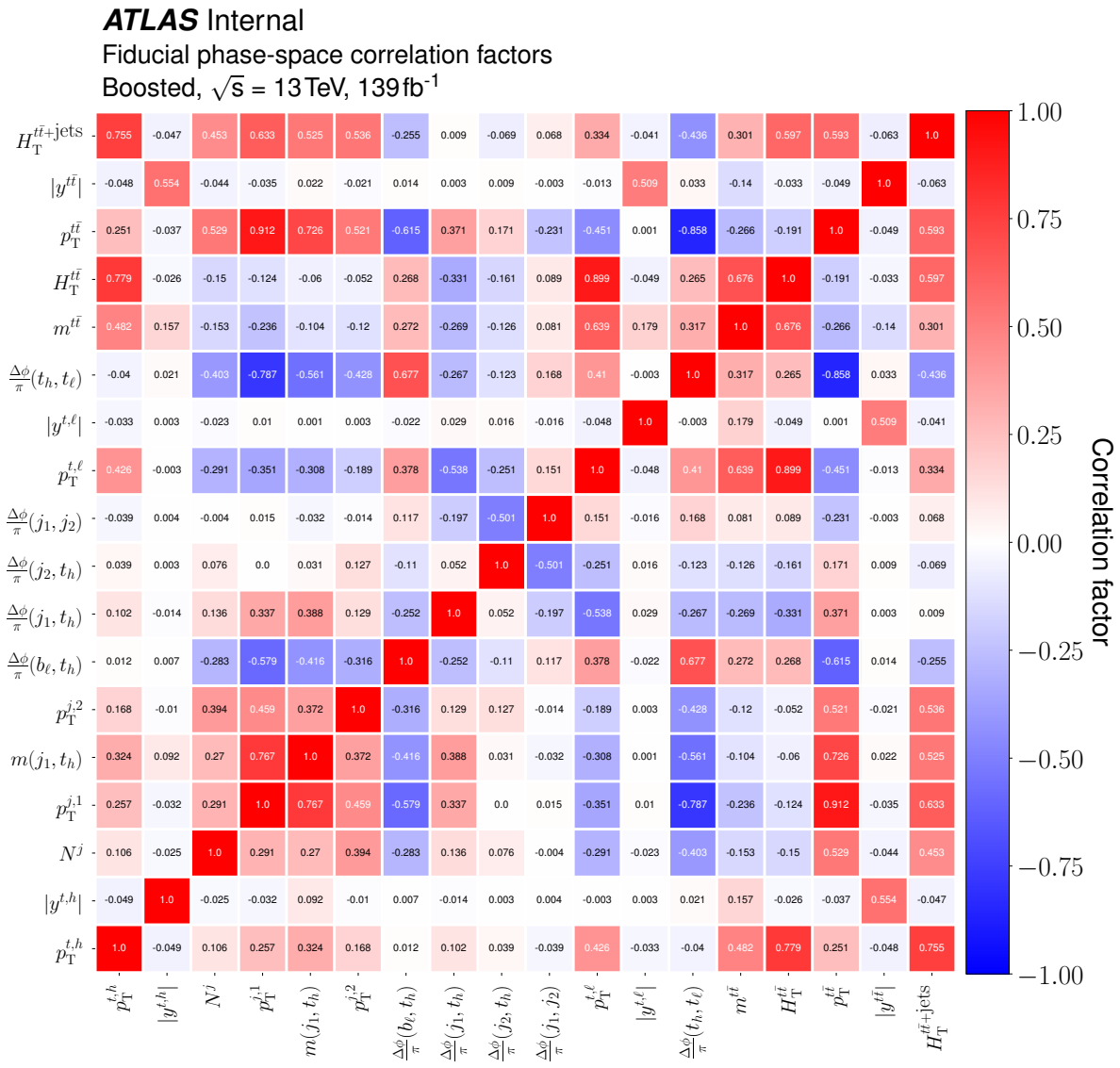

Figure 8.4: Un-binned correlation coefficients between each pair of single-differential kinematic variables, calculated from 139 fb^{-1} of data.

8.2. Data distributions at detector-level

Single differential variables

Figures 8.5 and 8.6 show the detector-level data distributions compared to the nominal signal+background prediction for the measured one-dimensional observables. The sum of the $t\bar{t}$ and expected background yields is normalised to the data to better visualise the level of agreement in the shape of the distributions. The nominal prediction is found to give a reasonable description of the data overall; however, in some distributions trends can be observed. In particular the $p_{\mathrm{T}}^{t,h}$, $p_{\mathrm{T}}^{t,\ell}$ and $H_{\mathrm{T}}^{t\bar{t}}$ distributions (Figures 8.5a, 8.5b, and 8.5c) are softer in data than predicted. Additionally the shapes of the N^j and $\frac{\Delta\phi}{\pi}(t_h, t_\ell)$ distributions (Figures 8.6a and 8.6f) are notably different between data and simulation. To ensure these discrepancies will not cause problems for the final measurement they are used in Section 8.5 to verify the robustness of the unfolding procedure against potential mis-modelling.

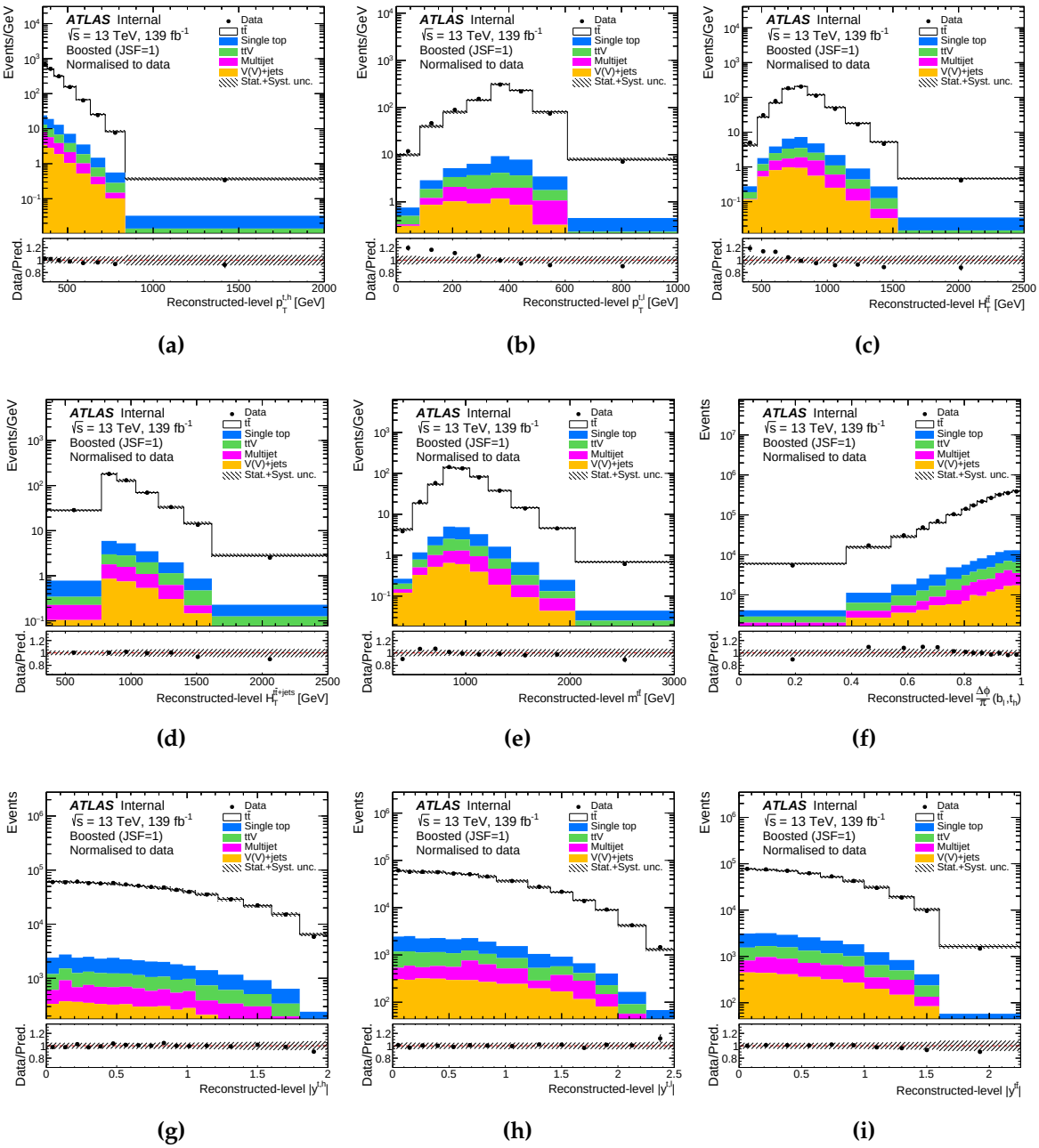

Figure 8.5: Detector-level distributions of the number of events as a function of (a) $p_{\mathrm{T}}^{t,h}$, (b) $p_{\mathrm{T}}^{t,\ell}$, (c) $H_{\mathrm{T}}^{t\bar{t}}$, (d) $H_{\mathrm{T}}^{t\bar{t}+\mathrm{jets}}$, (e) $m^{t\bar{t}}$, (f) $\Delta\phi(b_\ell, t_h)$, (g) $|y^{t,h}|$, (h) $|y^{t,\ell}|$, and (i) $|y^{t\bar{t}}|$. The data are compared to the expectation from simulation and background estimates normalised to match the number of entries in data. The lower panel in each subfigure shows the ratio of the data to the normalised expectation. The dashed band represents the total statistical and systematic uncertainty but does not include modelling uncertainties.

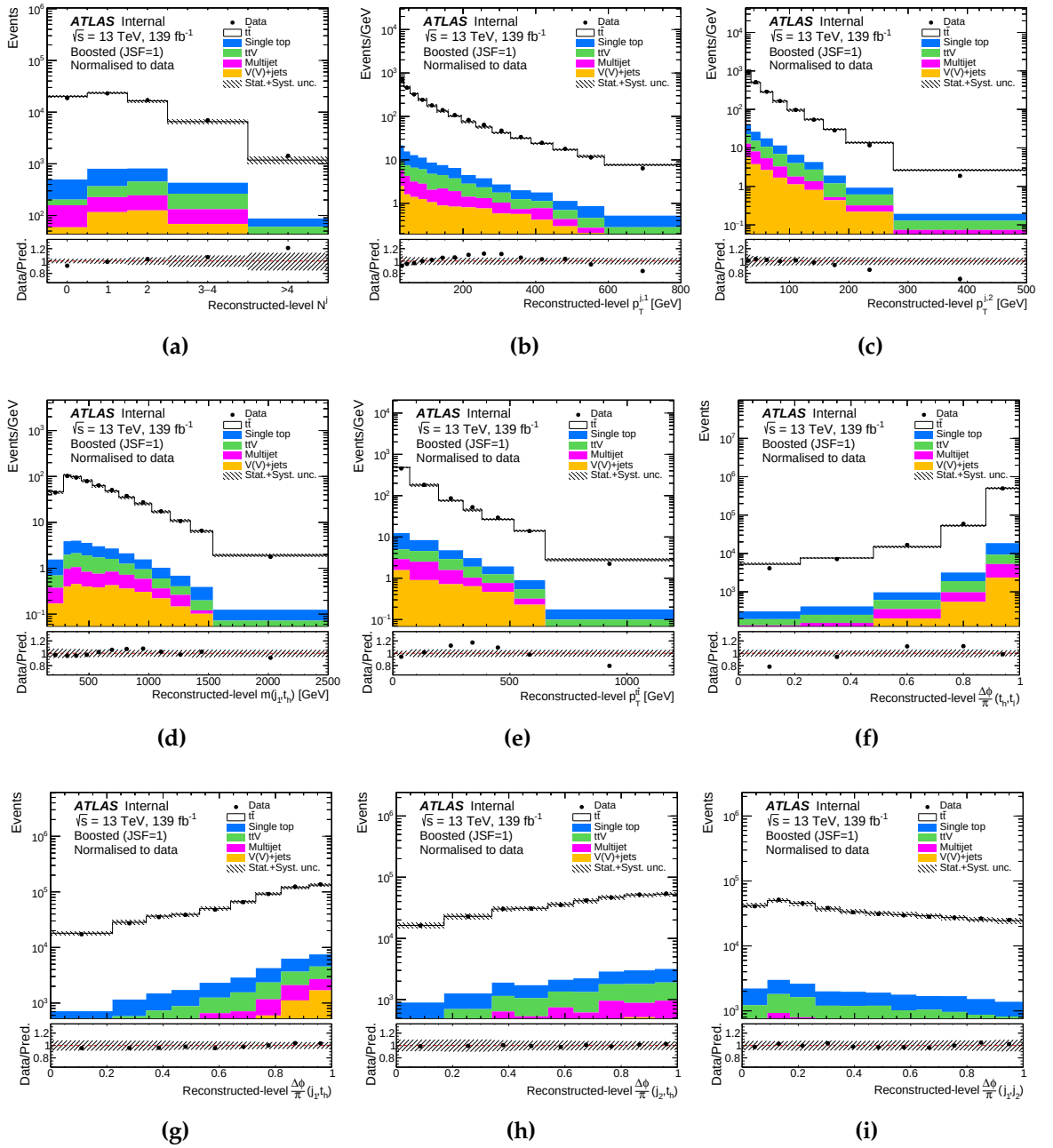

(a) **(b)** **(c)**

(d) **(e)** **(f)**

(g) **(h)** **(i)**

Figure 8.6: Detector-level distributions of the number of events as a function of (a) N^j, (b) $p_{\mathrm{T}}^{j,1}$, (c) $p_{\mathrm{T}}^{j,2}$, (d) $m(j_1, t_h)$, (e) $p_{\mathrm{T}}^{t\bar{t}}$, (f) $\Delta\phi(t_h, t_\ell)$, (g) $\Delta\phi(j_1, t_h)$, (h) $\Delta\phi(j_2, t_h)$, and (i) $\Delta\phi(j_1, j_2)$. The data are compared to the expectation from simulation and background estimates normalised to match the number of entries in data. The lower panel in each subfigure shows the ratio of the data to the normalised expectation. The dashed band represents the total statistical and systematic uncertainty but does not include modelling uncertainties.

8.3. Unfolding

Any kinematic measurements made at detector-level will have some inherent bias towards specifics of the ATLAS detector hardware and reconstruction. As discussed in Section 6.7 the final step in the generation of simulated events involves modelling the response of the ATLAS detector to incoming particles. As a result it is possible to make direct comparisons between data and simulation at detector-level. In practice this situation is not ideal as measurements cannot be compared directly to results from other experiments, such as CMS, likewise any new theory predictions would need to be passed through the same CPU expensive detector simulation which would considerably slow down the rate at which new theories could be tested against measurement.

The solution to this is to first remove any effects related to the detector from the measured distributions and then compare them directly to simulation at particle-level in a process known as *unfolding*. Due to complex interactions between these various detector effects this unfolding problem is not as straightforward as it initially appears and there are several possible approaches. The Iterative D'Agostini-Bayes method [164], commonly known as iterative Bayesian unfolding (IBU), is chosen for this analysis, using the implementation in the RooUnfold package [165]. This approach is designed to be applied directly to binned distributions and has the advantage of being easily expanded to multiple dimensions. Using IBU, the number of events in bin j of the unfolded particle-level distribution is found using the number of events in each bin i of the data and background samples at detector-level (N_i^{data} and N_i^{bkg}):

$$N_j^{\text{unf}} = \frac{1}{f_j^{\text{eff}}} \sum_i \mathcal{M}_{ij}^{-1} f_i^{\text{acc}} (N_i^{\text{data}} - N_i^{\text{bkg}}), \tag{8.3}$$

where the three correction factors: f^{eff}, $\mathcal{M}_{ij}^{-1}$, and f_i^{acc}, are constructed to deal with the three primary areas where detector performance can impact the measured data. The efficiency term (f^{eff}) corrects for events which pass the event selection at particle-level but fail one or more selections at detector-level. It is defined for each particle-level bin as:

$$f_j^{\text{eff}} = \frac{N_j^{\text{MC,reco}} \cap N_j^{\text{MC,particle}}}{N_j^{\text{MC,particle}}}, \tag{8.4}$$

where the numerator represents all events that pass the selections at **both** detector- and particle-level. In essence this parameterises the combined effects of limited object reconstruction efficiencies on the final event yields. Similarly the acceptance correction (f^{acc}) is defined for each bin at detector-level as:

$$f_i^{\text{acc}} = \frac{N_i^{\text{MC,reco}} \cap N_i^{\text{MC,particle}}}{N_i^{\text{MC,reco}}}, \tag{8.5}$$

and accounts for events that pass the detector-level selection but do not pass at particle-level. This corrects for events originating outside of the fiducial region which are incorrectly selected due to an imperfect detector (limited resolution, electronic noise, etc.). Figure 8.7 shows an example of the acceptance and efficiency factors for each bin of the p_{T} distribution of the hadronic top-quark. The acceptance correction is fairly consistent at around 80% due to the matched selections at detector- and particle-level but is considerably lower in the first p_{T} bin due to the low edge value of 355 GeV being a pre-requisite for event selection. The efficiency is more p_{T} dependent and is considerably lower at ∼30% due mainly to the limited b-tagging efficiency (∼77% per b-jet) that only effects events at detector-level.

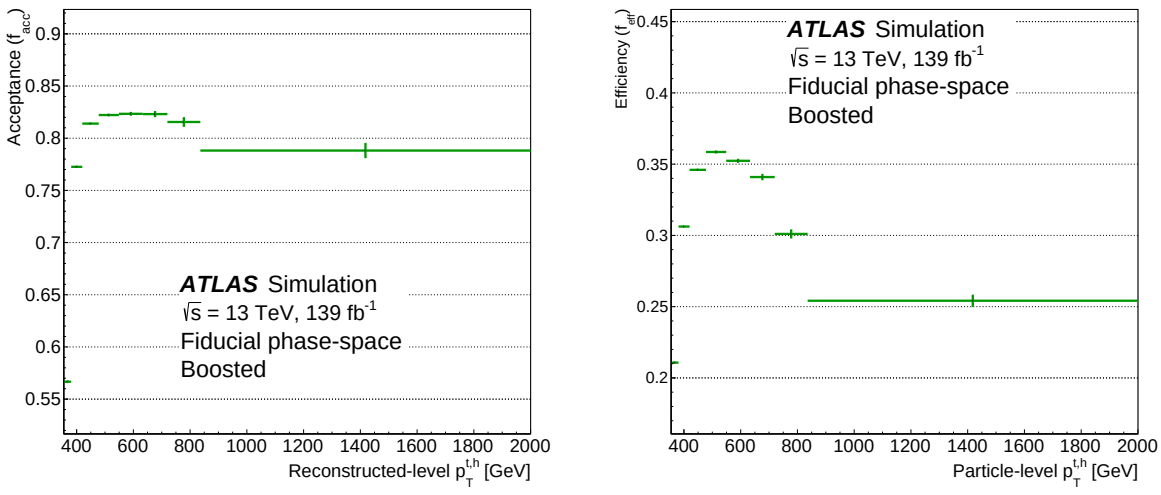

(a) **(b)**

Figure 8.7: (a) Acceptance (f^{acc}) (b) Efficiency (f^{eff}) unfolding corrections for the p_{T} of the hadronic top-quark, derived using events from the POWHEG+PYTHIA8 prediction. Under/overflows are not included.

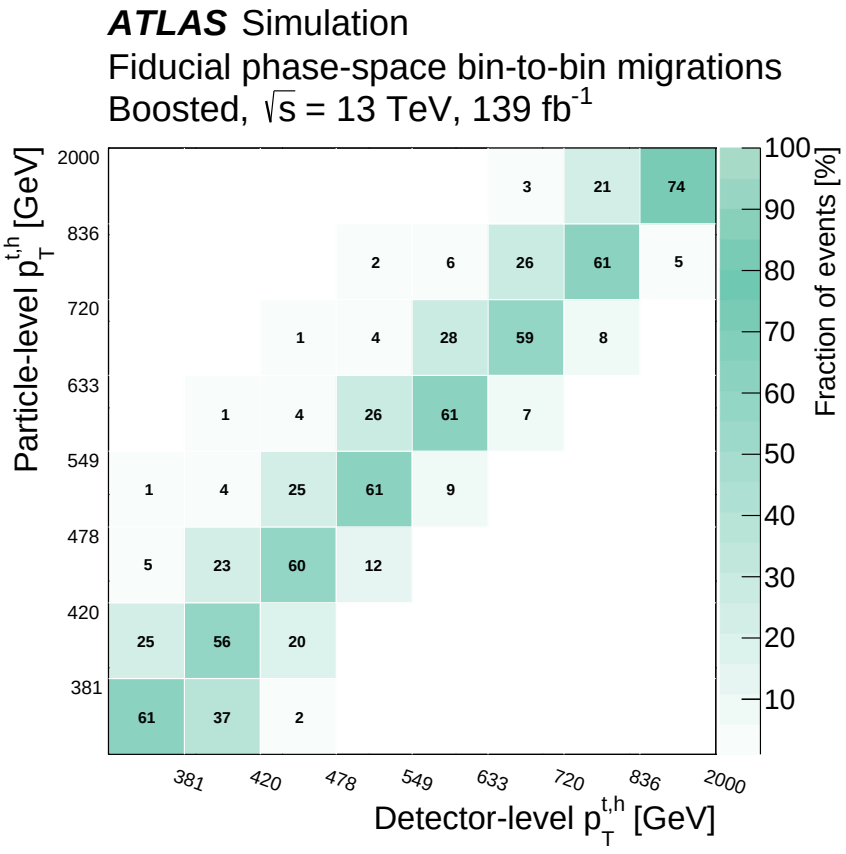

(a)

Figure 8.8: Migration matrix for the p_{T} of the hadronic top-quark. The matrix shows the fraction of particle-level events in each bin on the y-axis that appear in every detector-level bin on the x-axis, derived from events in the POWHEG+PYTHIA8 MC sample.

Lastly $\mathcal{M}_{ij}$, referred to as a *migration matrix*, accounts for the resolution of the detector. Resolution effects are those which result in events generated in bin j at particle-level becoming "smeared" and migrating across bin boundaries entering bin i ($i \neq j$) when reconstructed at detector-level. The entries of the matrix encode the fraction of events in a given particle-level bin that are reconstructed in a particular bin at detector-level. Figure 8.8 shows an example migration matrix for bins of the hadronic top-quark p_{T}.

The negative power on the migration matrix ($\mathcal{M}^{-1}$) indicates the application of the IBU unfolding itself which achieves a similar effect to that of a matrix inversion but is probabilistic in nature. As suggested by its name the IBU method uses Bayes' theorem:

$$P(A|B) = \frac{P(B|A)P(A)}{P(B)}, \tag{8.6}$$

with $P(A|B)$ denoting the conditional probability of outcome A given the input B, $P(B|A)$ the inverse of this and $P(A)$ and $P(B)$ the individual probabilities of A and B. Re-framed in the context of detector smearing this can be re-written as:

$$P(\text{unf}_i|\text{fold}_j) = \frac{P(\text{fold}_j|\text{unf}_i)P(\text{unf}_i)}{\sum_k P(\text{fold}_j|\text{unf}_k)P(\text{unf}_k)}, \tag{8.7}$$

$$P(\text{unf}_i|\text{fold}_j) \equiv \mathcal{M}_{ij}^{-1},$$

where $P(\text{unf}_i|\text{fold}_j)$ is the probability of an event observed in bin j of the detector-level (or folded) distribution originating from bin i of the true (unfolded) distribution. $P(\text{fold}_j|\text{unf}_i)$ is the reverse of this which equates to individual bins of the migration matrix ($\mathcal{M}_{ij}$), and $P(\text{unf}_x)$ is an estimate of the unfolded probability distribution based on our prior knowledge, often referred to as simply the *prior*. In the RooUnfold implementation the normalised particle-level MC simulation is used as the prior as we assume this is a good approximation for the true probability distribution.

Equation (8.7) provides an estimate of the inverted migration matrix in a single step, however the result of this will depend heavily on the MC prediction used in the prior, which is based only on Standard Model processes. This bias is reduced by repeating the process iteratively, with the prior replaced by the output of equation (8.3) using the result from the previous iteration as $\mathcal{M}_{ij}^{-1}$. As a result the number of iterations becomes a parameter within the unfolding that can be freely chosen with more iterations reducing the SM bias that could "unfold away" true BSM effects. However in the presence of limited MC statistics increasing the iterations can also lead to small statistical fluctuations quickly growing in a form of positive feedback loop ultimately producing unphysical results. Choosing a sensible and fairly low number of iterations is then used as a method to regularise the unfolding and protect against these statistical effects.

Finally the output of equation (8.3) can be combined with equation (8.1) in order to take detector-level event distributions directly to measurements of the absolute differential $t\bar{t}$ cross-section at particle-level:

$$\frac{d\sigma_j}{dX_j} = \frac{1}{\mathcal{L} \cdot \Delta X_j} \frac{1}{f_j^{\text{eff}}} \sum_i \mathcal{M}_{ij}^{-1} f_i^{\text{acc}} (N_i^{\text{data}} - N_i^{\text{bkg}}). \tag{8.8}$$

Normalised differential cross-sections are calculated by dividing each measured differential cross-section by the sum over all bins of the absolute cross-section. The normalised distributions help highlight shape differences between data and prediction but contain less information overall.

8.3.1. Two-dimensional unfolding

A strength of the IBU method is that the governing equation (8.8) is valid for distributions with any number of bins of arbitrary size and thus is easily expanded to include double-differential observables. In practice two-dimensional histograms in X and Y are first transformed by concatenating the distributions in X for each bin of Y to form a new single-dimensional distribution in X'. This new observable is defined as:

$$X' = X + i_Y \times \Delta X, \tag{8.9}$$

where i_Y is the index of the bin in Y and ΔX is the full range of the variable X. These flattened double-differential distributions are then unfolded in the same way as described above. Example acceptance and efficiency correction factors are shown for the $\Delta\phi$ difference between the leading additional jet and the hadronic top-quark in regions of increasing numbers of additional jets in Figure 8.9. The discontinuities observed where the second dimension (N^j) changes can potentially cause instability in the unfolding in a similar way to the inflation of statistical fluctuations discussed above. Evidence of this is monitored using tests to validate the efficacy of the unfolding process, outlined in Section 8.5, and no specific issues were observed for double-differential variables. The migration matrix for the same variable is shown in Figure 8.10.

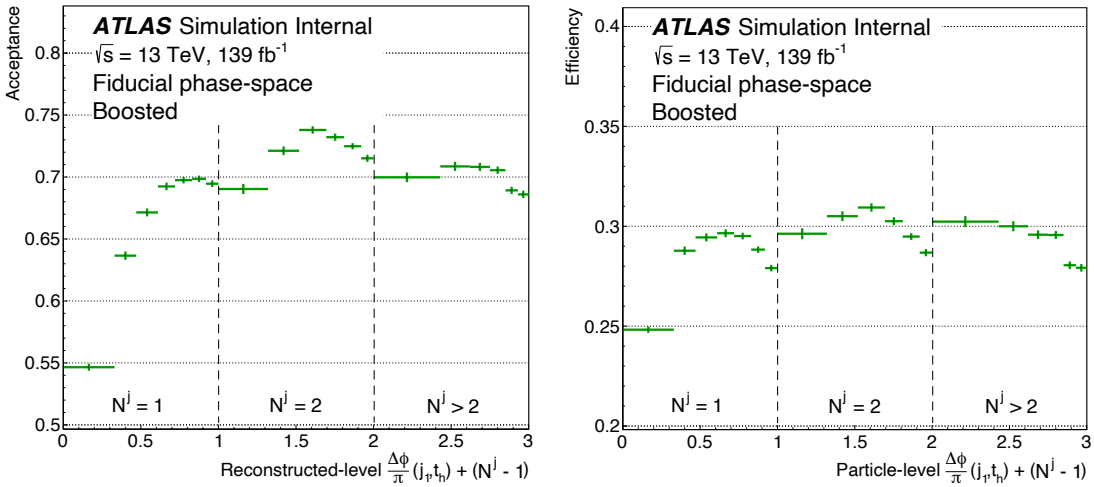

(a) **(b)**

Figure 8.9: (a) Acceptance (f^{acc}) (b) Efficiency (f^{eff}) unfolding corrections for the $\Delta\phi$ between the leading additional jet and the hadronic top-quark in regions of additional jet multiplicity. Discontinuities at $\frac{\Delta\phi}{\pi} + (N^j - 1) = 1$ and $\frac{\Delta\phi}{\pi} + (N^j - 1) = 2$, where $N^j = 3$ for events with 3 or more additional jets, are due to the mapping of a 2D distribution to one dimension.

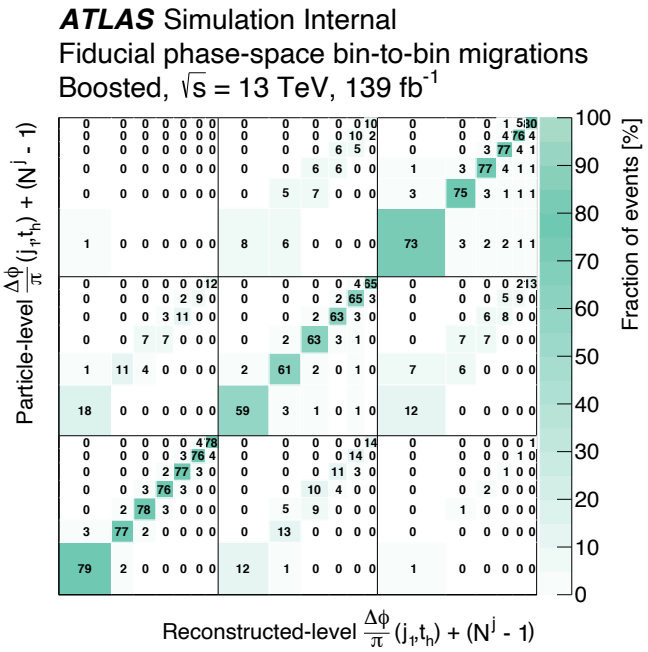

Figure 8.10: Migration matrix for the $\Delta\phi$ between the leading additional jet and the hadronic top-quark in regions of additional jet multiplicity. The matrix shows the fraction of particle-level events in each bin on the y-axis that appear in every detector-level bin on the x-axis for the modified one-dimensional variable: $\frac{\Delta\phi}{\pi} + (N^j - 1)$, where $N^j = 3$ for events with 3 or more additional jets.

8.4. Unfolding optimisation

8.4.1. Choice of binning

The use of binned distributions as inputs to the unfolding means the results are dependent on the initial choice of bin edges. These can then be optimised to improve the performance and stability of the unfolding with the overall aim of reducing unfolding related biases while ensuring that there are a sufficient number of simulated events in each bin to produce stable uncertainty estimates.

As the analysis aims to measure several different variables, often with many individual bins, it becomes necessary to automate part of the binning optimisation process. This initial step defines bin edges for each variable based on the diagonal resolution of the migration matrix and the statistical uncertainty in each bin of the POWHEG+PYTHIA8 MC sample, with different criteria defined for 1D and 2D distributions. After initial testing the set of one-dimensional angular distributions ($\frac{\Delta\phi}{\pi}(x,y)$) were found to exhibit less extreme migrations in general resulting in distributions with a large numbers of bins. Separate tighter requirements on the resolution and per-bin statistical power are applied for these variables in order to reduce the initial number of bins. The criteria for the different classes of observables are:

- 1D: $\geq$ 65% of events on the diagonal of the migration matrix and a maximum MC statistical uncertainty in each bin of 1.2%
- 1D angular: $\geq$ 75% of events on the diagonal of the migration matrix and a maximum MC statistical uncertainty in each bin of 1.0%
- 2D external variable (Y): $\geq$ 75% of events on the diagonal of the migration matrix and a maximum MC statistical uncertainty in each bin of 0.5%
- 2D internal variable (X): Same requirements as 1D variables.

In general the automatic binning for non-angular single-differential variables is dominated by the resolution requirement while angular and double-differential variables are more sensitive to the requirement on the maximum statistical uncertainty. The bin edges are further refined by hand to use more sensible values where appropriate. The number of bins was also reduced in a small number of cases to improve the robustness of the unfolding to statistical closure as described in Section 8.5.2, for

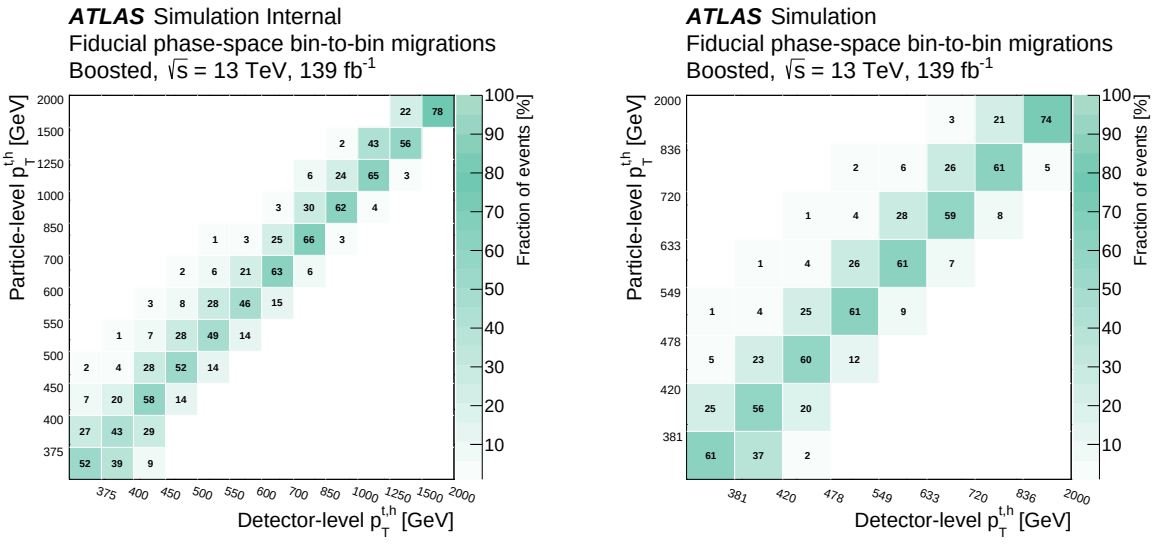

(a) **(b)**

Figure 8.11: Migration matrix for the p_{T} of the hadronic top-quark: (a) with arbitrarily chosen bin edges, (b) after automatic optimisation of bins and further refinement by-hand.

several variables, including $p_{\mathrm{T}}^{t,h}$, this results in less than 65% of events falling on the diagonal of the migration matrix.

Figure 8.11 shows the migration matrix for the p_{T} of the hadronic top-quark before and after optimising the bin edges, with the initial binning chosen arbitrarily. The optimised bins used in Figure 8.11b results in a higher fraction of events along the diagonal on average, especially at low p_{T}, and less severe migrations.

8.4.2. Choice of number of iterations

The number of iterations used in the unfolding can be freely chosen with lower numbers resulting in stronger regularisation. In terms of overall performance the optimum number of iterations for each variable is dependent on both the scale of the correlation between bins and the statistical uncertainty related to the unfolding. In order to parameterise both of these effects the average global correlation factor (ρ_{avg})

is used, as described in [166]. It is defined as:

$$\rho_i = \sqrt{1 - \left(V_{ii} \cdot (V^{-1})_{ii}\right)^{-1}}\,, \tag{8.10}$$

$$\rho_{\text{avg}} = \frac{1}{N_{\text{bin}}} \sum_{i=1}^{N_{\text{bin}}} \rho_i\,, \tag{8.11}$$

where i represent the bin number of a particular observable, and N_{bin} is the total number of bins. Lastly V is the statistical covariance matrix for the variable which quantifies the covariance induced by the unfolding between events in each pair of bins. In order to derive a covariance between pairs of individual bins a series of 1000 pseudo-experiments are created. Each pseudo-experiment is the result of smearing the expected number of events in each bin at detector-level using a Poisson distribution with mean equal to the original bin content and width equal to the statistical uncertainty of the bin. Each pseudo-experiment is then unfolded using the nominal corrections and the covariance matrix is derived from the unfolded results.

In general where there are non-negligible migration effects ρ_{avg} is expected to be non-zero and in the case of iterative unfolding methods this tends to produce a single minimum when plotted against N_{iter} [166]. For each variable the optimum number of iterations is taken as the value which minimises ρ_{avg} and thus introduces minimal bin-to-bin correlations. Figure 8.12 shows the change in ρ_{avg} for increasing iterations for the p_{T} of the hadronic top-quark, with the minimum clearly visible at 4 iterations. Figure 8.13 shows the bin-to-bin statistical correlation matrix for the p_{T} of the hadronic top at 2, 4, and 8 iterations with the minimum correlations observed for 4 iterations. Larger positive correlations are observed for iterations below this optimum number while for larger numbers the correlations become increasingly negative.

Table 8.2 summarises the optimum number of unfolding iterations for all of the variables considered in the analysis. Generally the ideal number of iterations is low and very similar for all variables (either 2, 3 or 4). This is expected as the average correlation is tied to the diagonality of the migration matrix which is kept consistent between variables by design.

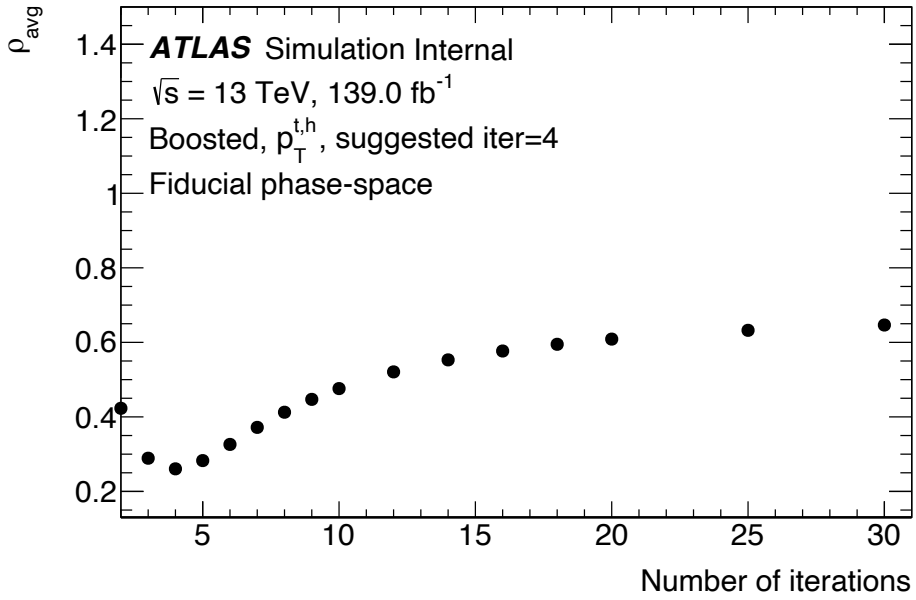

Figure 8.12: Average correlation factor as a function of the number of iterations for the p_{T} of the hadronic top-quark.

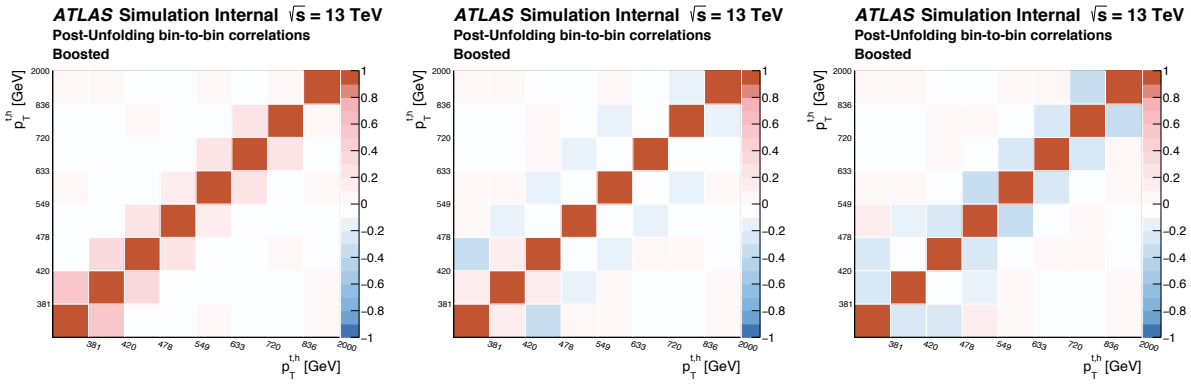

Figure 8.13: Post-unfolding bin-to-bin statistical correlations in the hadronic top-quark p_{T} distribution for (a) 2, (b) 4, and (c) 8 unfolding iterations. For this variable the optimum number of iterations is 4 corresponding to the minimum of ρ_{avg}.

Table 8.2: Optimised number of unfolding iterations for each observable considered in the analysis

Variable ($t\bar{t}$)	N_{iter}	Variable (j)	N_{iter}	Variable (2D)	N_{iter}
$p_{\text{T}}^{t,h}$	4	$p_{\text{T}}^{t\bar{t}}$	3	$p_{\text{T}}^{j,1}$ Vs $p_{\text{T}}^{t,h}$	4
$p_{\text{T}}^{t,\ell}$	3	N^{j}	2	$p_{\text{T}}^{j,1}$ Vs N^{j}	3
$\lvert y^{t,h}\rvert$	2	$p_{\text{T}}^{j,1}$	3	$\frac{\Delta\phi}{\pi}(j_1, t_h)$ Vs $p_{\text{T}}^{t,h}$	3
$\lvert y^{t,\ell}\rvert$	3	$p_{\text{T}}^{j,2}$	3	$\frac{\Delta\phi}{\pi}(j_1, t_h)$ Vs N^{j}	3
$\lvert y^{t\bar{t}}\rvert$	2	$\frac{\Delta\phi}{\pi}(j_1, t_h)$	2		
$m^{t\bar{t}}$	3	$\frac{\Delta\phi}{\pi}(j_2, t_h)$	2		
$H_{\text{T}}^{t\bar{t}}$	4	$\frac{\Delta\phi}{\pi}(j_1, j_2)$	2		
$\frac{\Delta\phi}{\pi}(b_\ell, t_h)$	2	$\frac{\Delta\phi}{\pi}(t_h, t_\ell)$	2		
		$m(j_1, t_h)$	3		
		$H_{\text{T}}^{t\bar{t}+\text{jets}}$	3		

8.5. Validation of unfolding method

Since the IBU method is regularised it is necessary to perform a series of tests to verify the statistical fluctuations and induced biases are sufficiently small. These tests can be split into three categories: those which assess the stability of the unfolding as the regularisation is loosened, those which test stability in the presence of statistical fluctuations (closure and pull), and those which probe the extent of bias in the unfolded results (stress). In each case it is not desirable to asses the unfolding machinery using the measured data itself. Similarly it is best to avoid testing with the same MC sample used to derive the unfolding correction factors. The solution is to use pseudo-data samples, either by smearing the nominal MC events, splitting the sample into dedicated testing and training sets, or using an alternative prediction.

8.5.1. Iteration stability

The effect of loosening the regularisation parameter (N_{iter}) on the unfolding is tested. A statistical χ^2 test is used to determine the overall change in the unfolded distributions

with respect to the previous iteration, calculated according to the equation:

$$\chi^2_{\text{iter}} = V^{\text{T}}_{(i,i-1)}\, C_i^{-1}\, V_{(i,i-1)}, \tag{8.12}$$

where $V_{(i,i-1)}$ is the vector of residuals between the i^{th} and $i^{\text{th}} - 1$ unfolding iteration and C_i is the statistical covariance matrix for the i^{th} iteration. The alternative POWHEG+HERWIG7 sample is used as pseudo-data and is unfolded using the corrections derived from the POWHEG+PYTHIA8 sample. Results for the p_{T} of the hadronic top and the number of additional jets are shown in Figure 8.14. In both cases the χ^2 values reduce as N_{iter} increases, which is expected behaviour, as the particle-level bias reduces with each subsequent iteration. The per-bin statistical uncertainty is also assessed as a function of N_{iter}. The results from the first and fifth bin of the $p_{\text{T}}^{t,h}$ distribution are shown in Figure 8.15, again the distributions behave as expected with the statistical uncertainty increasing along with the number of iterations. The results validate that a low number of iterations is reasonable as the reduction in χ^2 becomes less with each subsequent iteration and is already in fairly good agreement after only three iterations on average. In contrast the increase in statistical uncertainty for each subsequent iteration grows at a faster rate suggesting lower iterations are optimal.

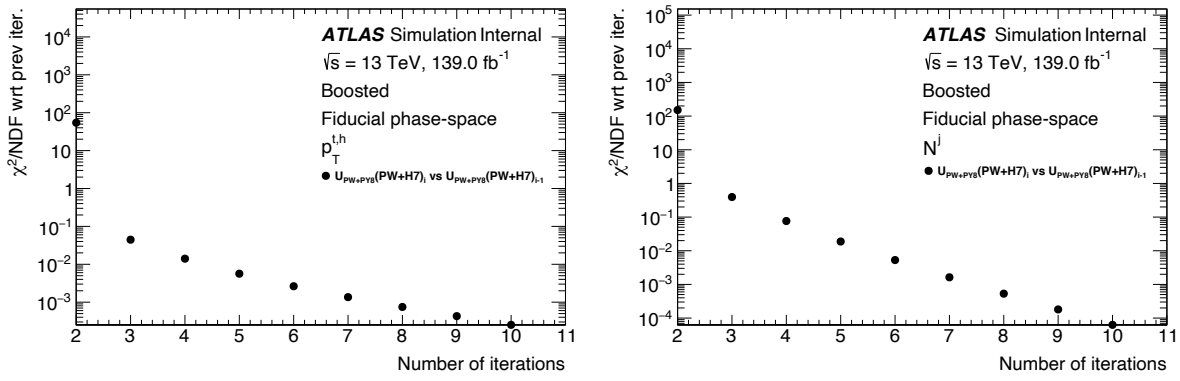

Figure 8.14: Statistical χ^2 test of unfolded pseudo-data with respect to the previous unfolding iteration as a function of the number of iterations for (a) the p_{T} of the hadronic top-quark, (b) the number of additional jets in the event. In the χ^2 calculations only the covariance related to the higher number of iterations is considered.

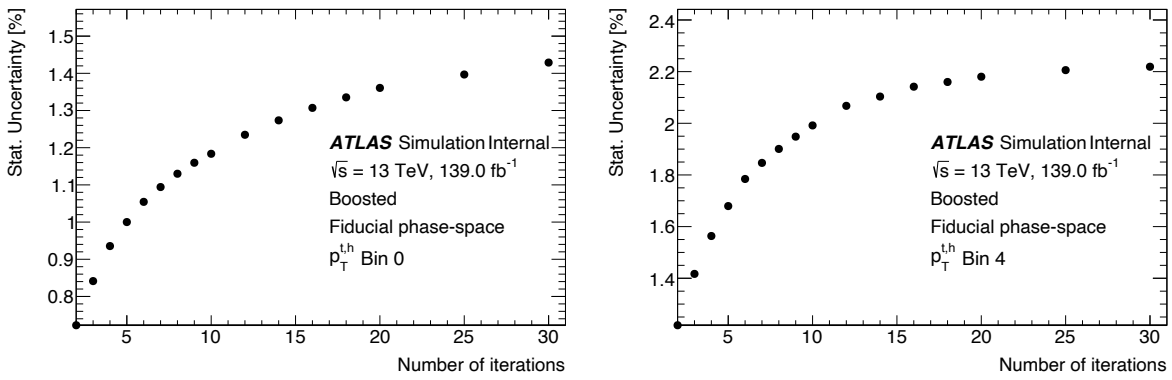

(a) **(b)**

Figure 8.15: Statistical uncertainty as a function of the number of iterations for the p_{T} of the hadronic top-quark in (a) the first bin (b) the fifth bin. The POWHEG+HERWIG7 sample is used as input and is re-weighted to match the data luminosity.

8.5.2. Statistical stability

Closure test:

A closure test is performed to ensure the unfolding is able to correctly reproduce the particle-level distributions of MC events that it has not seen before. Simulated events from the same generator setup as those used to derive the corrections are used for this by splitting the set of POWHEG+PYTHIA8 MC events into two halves based on odd and even event numbers. One set (labelled H_0) is used as pseudo-data and input to the unfolding, while the other half (H_1) is used to derive the acceptance and efficiency corrections and construct the migration matrix. Results from the H_0 pseudo-data unfolded using N_{iter} from Table 8.2 are compared to both H_0 and H_1 at particle-level, with results normalised to the total cross-section in each case. To consider the test passed with good closure the unfolded H_0 distributions should be compatible with the particle-level of H_0, with the compatibility determined using a χ^2 test:

$$\chi^2_{\mathrm{closure}} = V^{\mathrm{T}}_{(U(H_0),P(H_0))}\, C^{-1}_{H_0+H_1}\, V_{(U(H_0),P(H_0))}, \tag{8.13}$$

where $V_{(U(H_0),P(H_0))}$ is the vector of residuals between the unfolded H_0 distribution and the same distribution at particle-level, and $C_{H_0+H_1}$ is the full covariance matrix formed by summing the two individual covariances from each half. Combining both covariances in this test means the statistical uncertainty of both distributions

is considered, analogous to combining the covariance matrices for the MC and Data statistical uncertainties used when unfolding the final measured distributions.

Figure 8.16 shows the outcome of the closure test for the p_{T} of the hadronic top and the number of additional jets. Both of these variables show good closure between the unfolded and particle-level H_0 distributions with $p_{\mathrm{T}}^{t,h}$ displaying significantly better agreement. The closure success is partially dependent on the bin edges used for each variable, thus the binning can be tuned where appropriate to give the best unfolding performance. The χ^2 per degree of freedom (χ^2/NDF) and associated p-values are shown for all variables considered in the analysis in Table 8.3. The majority of variables show good agreement, however both $p_{\mathrm{T}}^{t\bar{t}}$ and the two-dimensional variable $p_{\mathrm{T}}^{j,1}$ Vs $p_{\mathrm{T}}^{t,h}$ have χ^2 values which correspond to a probability of $< 5\%$ suggesting the unfolded distributions do not match the original particle-level. Normally this level of disagreement might constitute introducing an additional uncertainty to cover for the non-closure in these observables. However since the test is performed on a large set of variables (22) a small number having this level of agreement can be expected. As a result the unfolding is considered to have passed the closure test and no additional uncertainty is required. The test was not repeated using different dataset splittings as the same events would ultimately be used, thus the results of each test would be correlated in a non-trivial way making the outcomes difficult to compare.

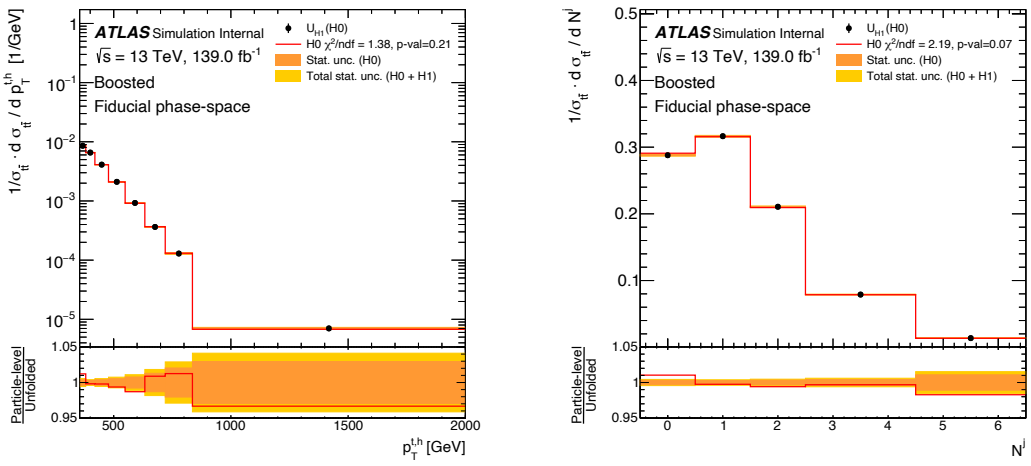

(a) **(b)**

Figure 8.16: Unfolding closure test for (a) $p_{\mathrm{T}}^{t,h}$ and (b) N^{j}. The red line represent the particle-level distribution of the testing half (H_0), while the markers represent the result of unfolding H_0 with corrections derived from H_1. To pass the test closure is required between the markers and the line, shown as compatibility of the line with unity in the ratio panel. The uncertainty bands contain only statistical uncertainty derived from H_0 in orange and $H_0 + H_1$ in gold.

Table 8.3: Statistical χ^2 test results and associated p-values from the unfolding closure test. Values denote the agreement between the particle-level and unfolded distributions derived from the testing set (H_0) for all observables considered in the analysis. The samples differ as the unfolding corrections are derived from a statistically independent sample (H_1). The reported χ^2 values have been rounded to reflect the measurement precision while the p-values are calculated using the full precision.

Variable ($t\bar{t}$)	χ^2/NDF	p-value	Variable (j)	χ^2/NDF	p-value	Variable (2D)	χ^2/NDF	p-value
$p_{\mathrm{T}}^{t,h}$	10/7	0.21	$p_{\mathrm{T}}^{t\bar{t}}$	18/6	0.01	$p_{\mathrm{T}}^{j,1}$ Vs $p_{\mathrm{T}}^{t,h}$	30/16	0.02
$p_{\mathrm{T}}^{t,\ell}$	10/7	0.17	N^{j}	9/4	0.07	$p_{\mathrm{T}}^{j,1}$ Vs N^{j}	18/20	0.56
$\lvert y^{t,h}\rvert$	12/16	0.74	$p_{\mathrm{T}}^{j,1}$	14/14	0.42	$\frac{\Delta\phi}{\pi}(j_1,t_h)$ Vs $p_{\mathrm{T}}^{t,h}$	25/20	0.21
$\lvert y^{t,\ell}\rvert$	16/13	0.24	$p_{\mathrm{T}}^{j,2}$	7/8	0.57	$\frac{\Delta\phi}{\pi}(j_1,t_h)$ Vs N^{j}	24/18	0.14
$\lvert y^{t\bar{t}}\rvert$	11/9	0.29	$\frac{\Delta\phi}{\pi}(j_1,t_h)$	7/8	0.57			
$m^{t\bar{t}}$	8/9	0.58	$\frac{\Delta\phi}{\pi}(j_2,t_h)$	8/8	0.44			
$H_{\mathrm{T}}^{t\bar{t}}$	7/9	0.63	$\frac{\Delta\phi}{\pi}(j_1,j_2)$	16/10	0.10			
$\frac{\Delta\phi}{\pi}(b_\ell,t_h)$	15/12	0.26	$\frac{\Delta\phi}{\pi}(t_h,t_\ell)$	5/4	0.27			
			$m(j_1,t_h)$	12/11	0.36			
			$H_{\mathrm{T}}^{t\bar{t}+\mathrm{jets}}$	8/6	0.24			

Pull test:

The second statistical test does not split events and instead uses the full expected $t\bar{t}$ spectrum at detector-level to build a series of 1000 pseudo-experiments (toys) by smearing each bin at detector-level using a Poisson distribution. All toys are then unfolded using the corrections and N_{iter} derived from the nominal (non-smeared) sample. The unfolded cross-section in each bin i is calculated for each toy j and from these the pull is defined:

$$p_j^i = \frac{\text{XS}_j^i - \text{XS}_T^i}{\sigma^i}, \tag{8.14}$$

where XS_j^i is the unfolded cross-section of toy j in bin i, XS_T^i is the particle-level cross-section of the nominal sample in bin i and σ^i is the error on the unfolded nominal distribution in bin i (XS_N^i) coming from the unfolding. In each bin the pull p_j^i is fitted using a Gaussian with mean: μ_{pull}, and standard deviation: σ_{pull}. If the error estimated from the unfolding (σ^i) is sufficient then σ_{pull} should be consistent with unity and for the case of no bias, μ_{pull} should be consistent with zero. The results of the pull test on the absolute cross-sections are shown for the p_{T} of the hadronic top-quark and the number of additional jets in Figure 8.17. The uncertainty bands on these plots are very faint but represents the error on the individual σ_{pull} and μ_{pull} derived from the Gaussian fit. For the p_{T} of the hadronic top-quark, the σ_{pull} values are all slightly greater than unity suggesting that the expected statistical uncertainty does not fully cover unfolding variations for this variable. However this non-closure is very small and not considered problematic. For all other studied observables no significant fluctuations are observed between the fitted μ_{pull} and σ_{pull} and their expected values indicating that in general the unfolding is robust against statistical fluctuations.

8.5.3. Tests for regularisation bias

Data/MC stress test:

The unfolded results can potentially become biased due to the fact that simulated MC events are used in the unfolding process. To ensure the results are valid the extent of any unfolding-induced biases must be assessed. Effects related to the choice of $t\bar{t}$

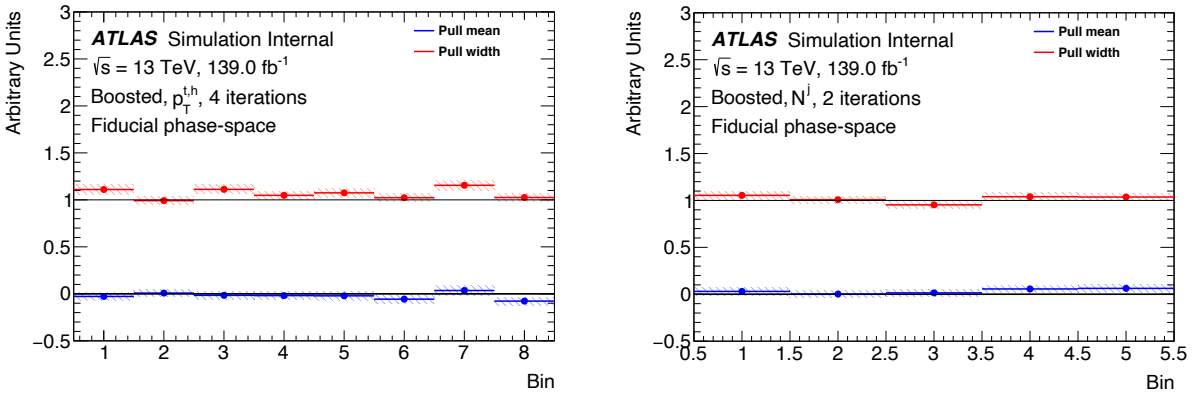

(a) **(b)**

Figure 8.17: Unfolding pull test for (a) $p_{\mathrm{T}}^{t,h}$, (b) N^{j}. The markers denote the mean (μ) in blue and standard deviation (σ) in red of a Gaussian fit to the pull distribution formed from the absolute cross-sections of all 1000 pseudo-experiments.

model are covered by the modelling uncertainties outlined in Section 9.4. A series of *stress* tests are also carried out using controlled changes to the MC simulation in order to check the dependence of the unfolding results on the shape of the distributions used to derive the corrections. Provided the regularisation is sufficiently loose any shape differences between simulation and data should be corrected for by the iteration process. In each test the particle- and detector-level POWHEG+PYTHIA8 samples are re-weighted using a different function $f(x)$, where x represents the variable in question. These re-weighting (or stress) functions are derived from a set of observables which show noticeable shape disagreement between data and simulation at detector-level:

- $\frac{\Delta\phi}{\pi}(t_h, t_\ell)$
- N^{j}
- $p_{\mathrm{T}}^{t,h}$

The stress functions are shown in Figure 8.18. Second-order polynomials are used to fit the Data/MC disagreements for $\frac{\Delta\phi}{\pi}(t_h, t_\ell)$ and N^{j}, while a linear fit is used for $p_{\mathrm{T}}^{t,h}$.

To make consistent comparisons between re-weighted (stressed) events at both particle-level and detector-level only events that pass both selections in the POWHEG+PYTHIA8 MC are used. The detector-level distributions, stressed using the functions above, are used as pseudo-data and unfolded using nominal corrections. Differences between the similarly stressed particle-level and the unfolded pseudo-data

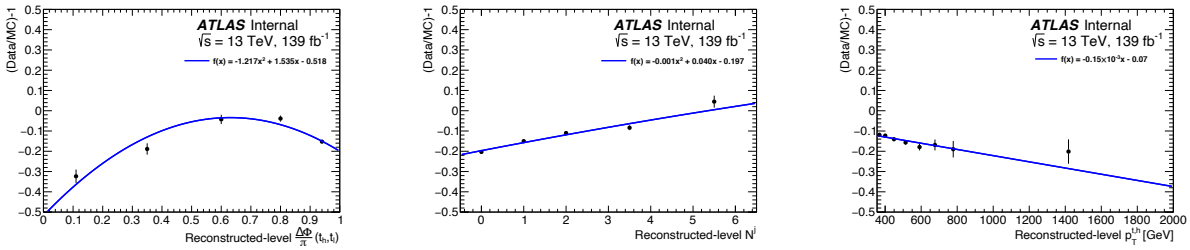

(a) **(b)** **(c)**

Figure 8.18: Re-weighting functions used to stress test the unfolding. Functions are obtained by fitting the data/MC differences ((Data/MC)-1) in the detector-level distributions of variables: (a) $\frac{\Delta\phi}{\pi}(t_h, t_\ell)$ (polynomial), (b) N^j (polynomial), and (c) $p_{\mathrm{T}}^{t,h}$ (linear).

are then evaluated with any significant variations being considered indicative of a bias in the unfolding step. The results of the stress test are shown in Figure 8.19, again for the p_{T} of the hadronic top and the number of additional jets. In these plots the solid lines indicate the ratio between the stressed pseudo-data after unfolding and the particle-level distributions with the same stress applied. Markers are placed at the centre of each bin and error bars are included which reflect the expected data statistical uncertainty. The dotted lines indicate the ratio between the nominal and stressed particle-level predictions and thus display the raw effect of the stress functions. The solid lines evaluate the performance of the unfolding in the presence of stress by their compatibility with unity. The plots shown here, and the results from the remaining observables, show only a very small bias, which is well inside the statistical uncertainties for most bins thus the test is considered passed.

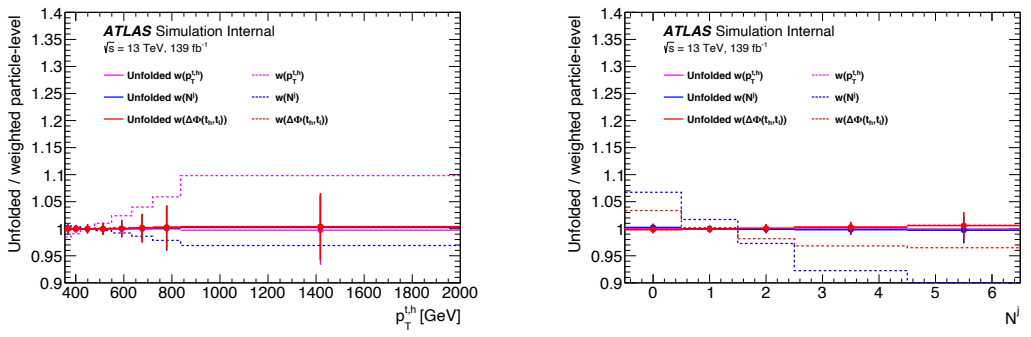

(a) **(b)**

Figure 8.19: Results of the unfolding stress test for (a) $p_{\mathrm{T}}^{t,h}$, (b) N^j. The dotted lines show the functions used for the re-weighting while the solid lines show the ratio between the unfolded and particle-level distributions after adding additional stress to the input. The error bars show the expected statistical uncertainty on the data.

EFT stress test:

To ensure the unfolding is not biased against possible new physics effects in data another stress test is performed, replacing the stressed samples with pseudo-data consisting of the nominal $t\bar{t}$ prediction with additional EFT contributions added. Three tests are again performed, using the samples outlined in Section 7.1.1 which correspond to EFT contributions:

- $\left(C_{tG}, C_{tq}^{(8)}\right) = (0.25, 0.0)$ with terms up to Λ^{-2},
- $\left(C_{tG}, C_{tq}^{(8)}\right) = (0.0, 0.25)$ with terms up to Λ^{-2},
- $\left(C_{tG}, C_{tq}^{(8)}\right) = (0.2, 0.2)$ with terms up to Λ^{-4}.

The Wilson coefficient values are chosen to roughly match the expected size of the limits given the measurement precision. Figure 8.20 shows the results of the EFT stress test for the p_{T} of the hadronic top-quark. In this case the solid lines indicate the ratio between the EFT pseudo-data after unfolding and the particle-level distributions from the EFT samples. The dotted lines indicate the ratio between the EFT and SM predictions at particle-level and correspond to the right-hand y-axis. The error bars show the expected data statistical uncertainty. For each of the EFT variations the ratio is compatible with unity indicating there is no significant bias on the EFT interpretation coming from the measurement technique.

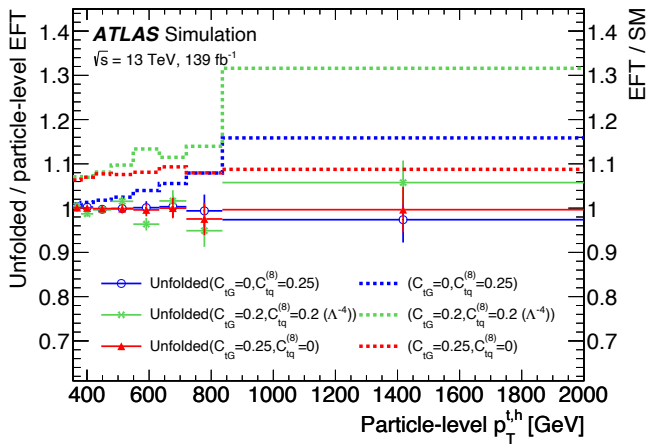

Figure 8.20: Results of the EFT stress test for the p_{T} of the hadronic top-quark. The dotted lines show the magnitude of the injected EFT effects and correspond to the right-hand y-axis. The solid lines show the ratio between the unfolded EFT pseudo-data and the corresponding EFT particle-level prediction. The error bars show the expected statistical uncertainty on the data.

Chapter 9.

Uncertainties

"Our calculations are always correct, for we are gigantic brains!"
— Big Space Brain, Futurama S5, E8 - The Why of Fry

The cross-section measurements presented here are affected by various sources of statistical and systematic uncertainty, with the latter broken down into those derived from the experimental procedure and those from theoretical assumptions used in the signal and background modelling. These are each evaluated via the unfolding process and applied to the final results at particle-level. The total uncertainty is then calculated via standard error propagation, assuming all systematic effects are uncorrelated.

Each experimental systematic uncertainty is evaluated in the same way; by creating a pseudo-data sample (signal+background) with the relevant uncertainty source modified to mimic a $\pm 1\sigma$ change in the underlying property. The full analysis procedure is then repeated, including unfolding using corrections derived from the nominal MC. The difference between the cross-sections extracted from the pseudo-data sample and from the nominal simulation are used as an estimate for the uncertainty. In some cases only a $+1\sigma$ change is available for the relevant uncertainty in which case this is propagated through and then symmetrised to give the $\pm 1\sigma$ estimate. For uncertainties related to the physics objects, described in Chapter 5, the systematic variation will affect the signal and background predictions and so modified versions of both signal and background are produced. For uncertainties related to the background determination itself the nominal MC without any modification is used for the signal and only the relevant background samples are modified to estimate the uncertainty.

A similar method is used for uncertainties related to the underlying theory calculation and the phenomenological $t\bar{t}$ modelling; in both cases alternative $t\bar{t}$ simulations exist at both particle-level and detector-level, described in Section 7.1.1. The alternative signal samples and nominal background predictions are combined to form pseudo-data samples which are analysed as before using the nominal unfolding corrections. The uncertainty estimate is taken from comparisons of the unfolded cross-sections to the corresponding distributions at particle-level from the alternative simulation. In this way the associated uncertainty is not a comparison between the nominal and alternative predictions at particle-level but an estimate of the bias that would be observed in data if the true underlying physics matched the alternative prediction.

This method of estimating the systematic uncertainties means only the inputs to the analysis are ever varied (as pseudo-data), rather than changing the corrections derived for the unfolding. This matches the approach taken in many previous $t\bar{t}$ cross-section analyses [122–124]. The following sub-sections detail the different sources of uncertainty affecting the measurement followed by details of a new method used to reduce the impact of jet energy scale uncertainties. The chapter is concluded with an overview of the achieved measurement precision.

9.1. Statistical uncertainty

The uncertainty due to limited data statistics is propagated through the unfolding in the same way as described for many of the unfolding validation tests in Chapter 8. The expectations in each bin are used to create 10,000 Poisson smeared pseudo-experiments that are individually passed through the unfolding procedure. The root mean squared error of the resulting bin values are taken as the statistical error on each bin of the unfolded distribution.

The uncertainty due to limited MC statistics is evaluated in an analogous way, but smearing the bins of the nominal MC sample using a Gaussian with mean and standard deviation taken from the nominal expectation in that bin and the bin error respectively. Again 10,000 toys are produced, unfolded using the nominal corrections, and the resulting RMS is taken as the MC statistical uncertainty on the unfolded results.

9.2. Detector uncertainties

The detector systematic uncertainties cover all uncertainties related to the reconstruction and calibration of physics objects, the underlying sources of which were discussed previously. There are two possible methods for propagating the resulting uncertainty. In the first method the systematic uncertainty is assessed by applying event weights to the simulated events. While for the second method the systematic uncertainty is assessed by modifying the four-vector(s) of the selected objects in MC and re-applying the event selection.

Lepton uncertainties

Electrons and muons both have uncertainties associated with the energy/momentum scale and resolution. These variations modify the momentum of the leptons (method 2). The calibration of the lepton reconstruction and ID efficiencies come with associated uncertainties that are propagated via changes to the lepton scale-factors (method 1). In a similar way, the scale factors for the trigger efficiencies are varied to account for uncertainties in measured lepton trigger efficiencies (method 1).

Jet uncertainties

The uncertainty related to the jet energy scale for small radius $R = 0.4$ jets is assessed using the Category Reduction scheme described in Section 5.3.2 which results in 30 independent variations. Each variation modifies the energy of the jets and thus their four-momentum (method 2). Similarly the scheme used to parameterise the uncertainty on the jet energy resolution for $R = 0.4$ jets provides 8 independent variations which each modify the energy of jets (method 2). Due to the single-sided smearing used in this scheme these systematics provide only $+1\sigma$ variations. The uncertainty originating from the JVT requirement on jets is assessed by varying the associated scale factor (method 1), providing a single systematic uncertainty.

All changes in energy due to the JES and JER uncertainties are propagated to the large-radius jets due to the re-clustering approach, meaning no additional uncertainty is required on the RC jets. This is a particular benefit of the re-clustering method as it provides a self-consistent uncertainty treatment for all jets in the events [167].

Flavour-tagging uncertainties

The calibration of the b-tagging algorithm, described in Section 5.4, results in 17 individual uncertainties with an additional 2 uncertainties related to extrapolating calibrated scale-factors to higher p_{T} regions. In all cases the uncertainties are propagated to the analysis by varying the scale-factor associated with the b-tagging (method 1).

$E_{\mathrm{T}}^{\mathrm{miss}}$ uncertainties

The uncertainties on the energy scale and resolution of leptons and jets are propagated to the missing transverse momentum in a correlated way. Four additional systematic components cover scale and resolution uncertainties on the soft term and are propagated by modifying the magnitude and direction of the $E_{\mathrm{T}}^{\mathrm{miss}}$ vector (method 2).

9.3. Background uncertainties

For the $t\bar{t}V$ background the total uncertainty on the inclusive cross-section for each process is used. This gives 13.3%, 12% and 9.9% normalisation uncertainty on the $t\bar{t}W$ $t\bar{t}Z$, and $t\bar{t}H$ events respectively [168]. As the three processes are combined in the $t\bar{t}V$ background a conservative normalisation uncertainty of 13.3% is used for events in all channels, matching the strategy used in [169].

The uncertainty on the W+jets background is evaluated using alternative predictions in which MC weights are used to simulate varying the renormalisation (μ_{r}) and factorisation (μ_{f}) scales of both the hard scatter and showering simultaneously. Both μ_{r} and μ_{f} scales are shifted independently up or down by factors of 2.0 and 0.5 respectively, with the additional constraint: $0.5 \geq \frac{\mu_{\mathrm{r}}}{\mu_{\mathrm{f}}} \leq 2$, this gives an envelope of seven possible scale variations including the nominal point (1.0,1.0). It was found for all variables the simultaneous scaling of both parameters up (2.0,2.0) and down (0.5,0.5) resulted in the largest impact. As a result only these two variations were used to evaluate the W+jets uncertainty.

As very few Z+jets and diboson events pass the event selection a complex uncertainty breakdown is not needed. Instead a flat 50% uncertainty is chosen to match the size of the μ_{r} and μ_{f} scale uncertainty on the inclusive W+jets cross-section measure-

ment, as outlined in [169]. The uncertainty is applied to the NNLO cross-sections used to normalise each process.

As the most significant background, a more detailed breakdown is used to evaluate the uncertainties related to single top processes. Several different sources of uncertainty are considered, these are:

- The uncertainty due to the choice of the μ_r and μ_f scales in the hard-scatter and showering. This uncertainty is evaluated using the nominal single top setup as described in Section 7.1.1 but with additional weights applied which simulate varying the μ_r and μ_f scales in the hard scatter by factors of 0.5 and 2.0, and the scales in the parton shower to match the Var3c eigentune of the A14 tune.
- The uncertainty due to the final-state radiation simulation. This is evaluated in a similar way as above using the nominal single top sample with 0.5 and 2.0 variations applied to the renormalisation scale for final-state emissions from the parton shower.
- An uncertainty related to removing the double counting of $t\bar{t}$ interference diagrams (DS/DR). The DS/DR uncertainty is evaluated using alternative MC samples which use different schemes to deal with the overlap between the $t\bar{t}$ and tW production diagrams: diagram removal (DR), or diagram subtraction (DS). While the other components affect all single top production channels, the DS/DR uncertainty only affects the tW channel.
- Normalisation uncertainties for the separate single top processes. The uncertainty on the inclusive single-top cross-section in each channel is used, equal to 5.4% for the tW channel [170, 171], and 4.2% and 3.9% for the t-channel and s-channel respectively [171–173].

9.3.1. Uncertainties on multijet background

The multijet background is estimated using a data-driven approach (matrix-method). To derive an uncertainty on this prediction an alternative multijet estimation is produced and the normalisation difference between the yields from the two methods is taken as an uncertainty.

The alternative method is based on the introduction of a simulated Monte Carlo template as an estimate for multijet events. Fully hadronic $t\bar{t}$ and Z/W+jets events that

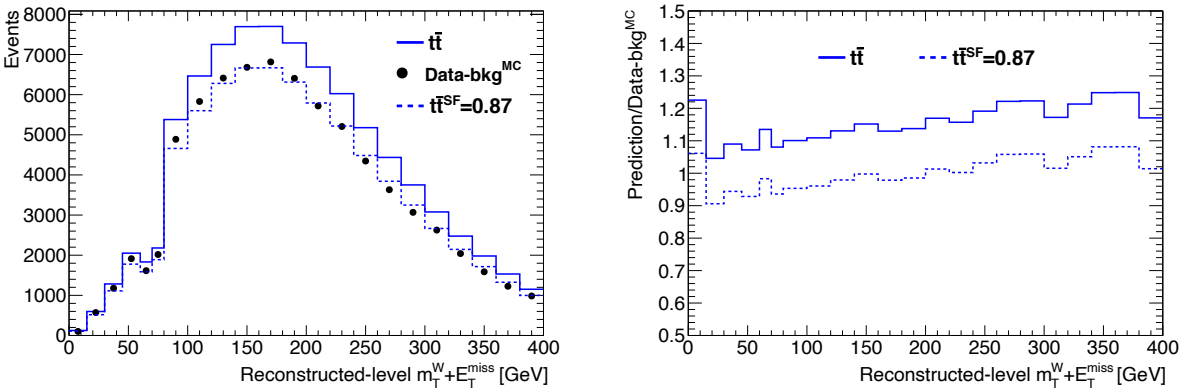

(a) **(b)**

Figure 9.1: Number of events at detector-level in bins of $E_{\mathrm{T}}^{\mathrm{miss}} + m_T^W$ for (a) the data $-$ bkg$^{\mathrm{MC}}$, and the POWHEG+PYTHIA8 $t\bar{t}$ prediction before and after the application of the scale-factor ($t\bar{t}^{\,\mathrm{SF}} = 0.87$). (b) The ratios of the $t\bar{t}$ predictions to the data $-$ bkg$^{\mathrm{MC}}$ are shown.

include a high momentum large-radius jet are used. These processes are well modelled by MC generators and as they are simulated in the all-hadronic channel they do not contain any prompt leptons. The template is normalised to match the expected multijet yield by fitting the template to data in a control region (CR), defined by removing the $E_{\mathrm{T}}^{\mathrm{miss}}$ and $E_{\mathrm{T}}^{\mathrm{miss}} + m_T^W$ requirements from the signal region (SR) selection described in Section 7.4. Multijet events are expected to have lower value of $E_{\mathrm{T}}^{\mathrm{miss}}$ as they do not contain real neutrinos.

Before the CR fit can be performed the known normalisation shift between data and MC simulation, observed in Figure 7.7, must be corrected for. This is done by comparing the nominal POWHEG+PYTHIA8 $t\bar{t}$ simulation in the SR to the data with the other simulated background processes removed (data $-$ bkg$^{\mathrm{MC}}$). A fit is performed using the $E_{\mathrm{T}}^{\mathrm{miss}} + m_T^W$ distribution and a normalisation scale-factor is obtained as the best-fit value for the difference between data and simulation ($t\bar{t}^{\,\mathrm{SF}} = 0.87$). Figure 9.1 shows the result of applying this factor to the $t\bar{t}$ signal compared to data $-$ bkg$^{\mathrm{MC}}$ in the expanded CR with the agreement between data and MC significantly improved after applying the correction. The MC/data ratio in Figure 9.1b also shows that the prediction, with $t\bar{t}^{\,\mathrm{SF}}$ applied, underestimates the data in the low $E_{\mathrm{T}}^{\mathrm{miss}} + m_T^W$ region, particularly in the first four bins, suggesting there is a non-negligible multijet contribution estimate missing in this region of the phase-space.

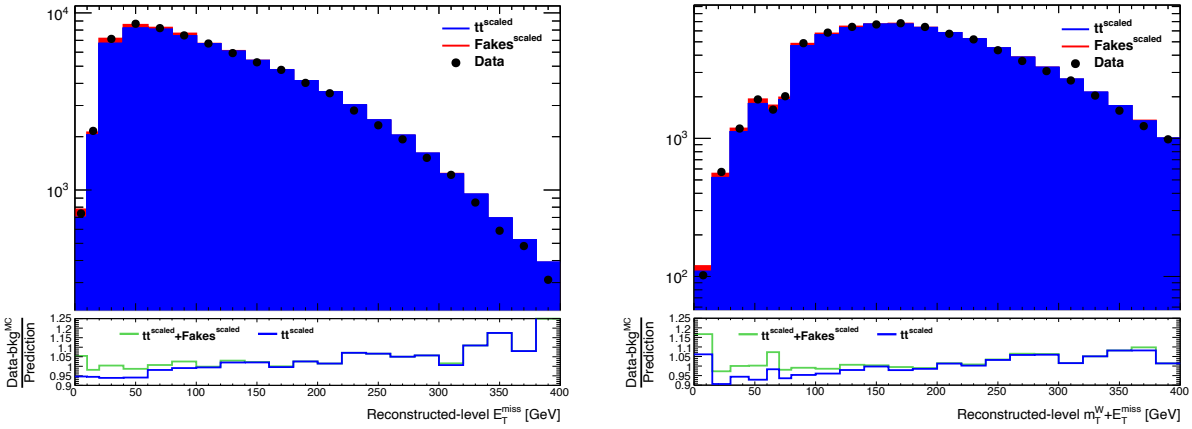

(a) **(b)**

Figure 9.2: Number of events at detector-level in bins of (a) $E_{\mathrm{T}}^{\mathrm{miss}}$, (b) $E_{\mathrm{T}}^{\mathrm{miss}} + m_T^W$ for the data $-$ bkg$^{\mathrm{MC}}$ (markers) and the POWHEG+PYTHIA8 $t\bar{t}$ prediction multiplied by $t\bar{t}^{\,\mathrm{SF}}$ in blue with the addition of template fake estimate in red.

The POWHEG+PYTHIA8 $t\bar{t}$ signal with $t\bar{t}^{\,\mathrm{SF}}$ applied is subtracted from the data $-$ bkg$^{\mathrm{MC}}$ to give an estimate of the missing multijet contribution. This is then fit to the template distribution in the CR to extract the relevant normalisation (multijet$^{\mathrm{SF}}$). This is the factor used to scale events in the multijet template prediction such that they correctly match the normalisation of the data. The fit is performed separately using both the $E_{\mathrm{T}}^{\mathrm{miss}}$ and $E_{\mathrm{T}}^{\mathrm{miss}} + m_T^W$ distributions, giving scale-factor values of 34 and 44 respectively. The multijet$^{\mathrm{SF}}$ values account for QCD multijet events missing from the MC template but also capture differences in the rate of fake lepton reconstruction between data and MC. Figure 9.2 shows the improvement on the agreement between prediction and data when including the appropriately scaled template multijet estimates. This is shown by comparing the data $-$ bkg$^{\mathrm{MC}}$ distributions to those of the $t\bar{t}$ + multijet$^{\mathrm{MC}}$ predictions where the nominal $t\bar{t}$ sample is used. The agreement between data and prediction is improved significantly for both the $E_{\mathrm{T}}^{\mathrm{miss}}$ and $E_{\mathrm{T}}^{\mathrm{miss}} + m_T^W$ distributions when including the multijet$^{\mathrm{MC}}$ estimate.

The multijet predictions from the two different methods are compared to check for shape differences and the two methods were found to agree well within statistical uncertainties. The normalisation difference between the matrix-method (555 events) and the multijet yield from the $E_{\mathrm{T}}^{\mathrm{miss}} + m_T^W$ template fit (910 events) was used to estimate a final uncertainty of 65%.

9.3.2. Effect of $m_{\ell,b}$ on background uncertainties

A targeted selection requirement on the invariant mass of the lepton and b_ℓ-jet system ($m_{\ell,b} < 180\,\text{GeV}$) was introduced in Section 7.4 with the aim of reducing the single top background contamination and its associated uncertainties. This is also expected to have a lesser effect on other background processes in which the b_ℓ-jet does not originate from a top-quark decay. Table 9.1 shows the effect of the $m_{\ell,b}$ requirement on the various background uncertainties and the statistical uncertainty for the inclusive cross-section at detector-level. The bottom row shows the overall signal purity which increases when the requirement is added, similarly a reduction in the total background uncertainty is observed, driven by reductions in single top components.

A much larger impact is expected when looking at differential distributions, especially in bins corresponding to highly boosted events. Figure 9.3 shows the effect of the $m_{\ell,b}$ requirement on the statistical and background uncertainties for the $p_{\text{T}}^{t,h}$ and $H_{\text{T}}^{t\bar{t}}$ distributions at detector-level. The total background modelling uncertainty is considerably reduced in the tails of both distributions. In the most extreme case dropping from 7% to 2.3% in the last bin of the hadronic top p_{T} spectrum, with the largest reduction being the single top DS/DR component that decreases from 5.7% to 1%.

Table 9.1: Detector-level background and data statistical uncertainties on the inclusive measurement with and without the $m_{\ell,b}$ requirement. Single top DS/DR and background normalisation uncertainties are symmetrised. The bottom row indicates signal purity as the fraction of $t\bar{t}$ events over the total $t\bar{t}$+background prediction.

	with $m_{\ell,b}$ cut [%]	without $m_{\ell,b}$ cut [%]
Single top DS/DR	0.32	0.44
Single top ISR	0.31	0.49
Single top FSR	0.1	0.1
Single top normalisation	0.10	0.14
W+jets scale	0.22	0.29
Z+jets normalisation	0.04	0.06
$t\bar{t}V$ normalisation	0.13	0.13
Diboson normalisation	0.02	0.03
Tot. uncertainty	0.54	0.76
Stat. uncertainty	0.36	0.36
Purity	96.4	95.4

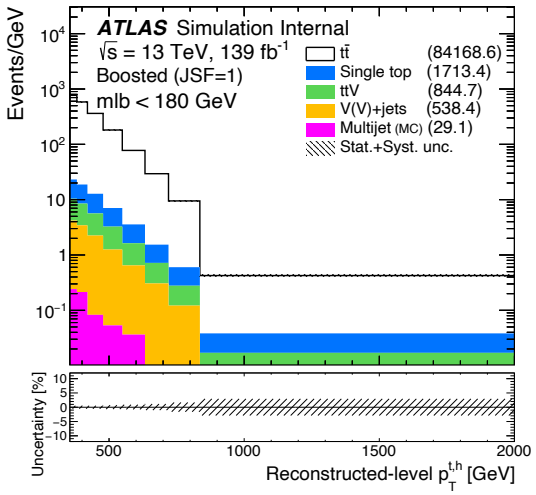

(a)

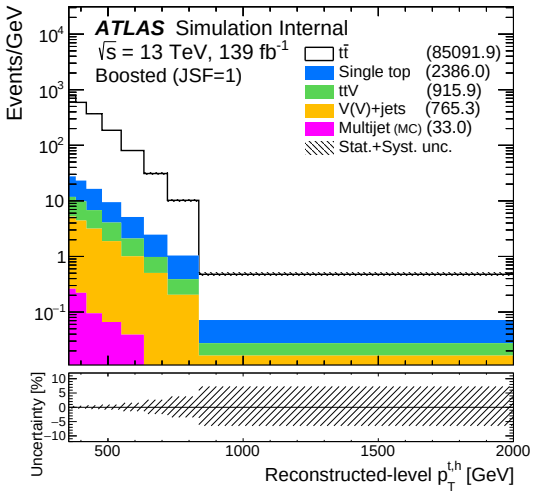

(b)

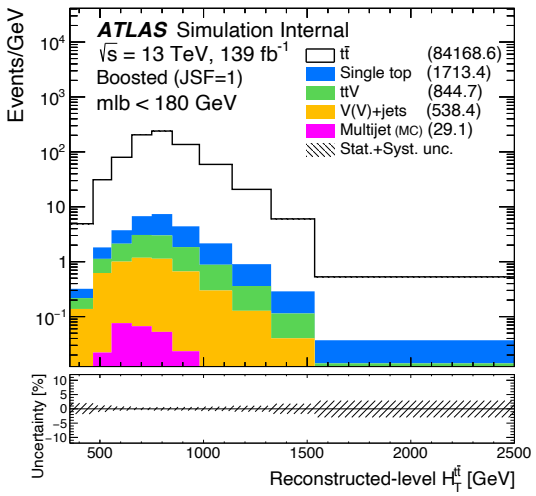

(c)

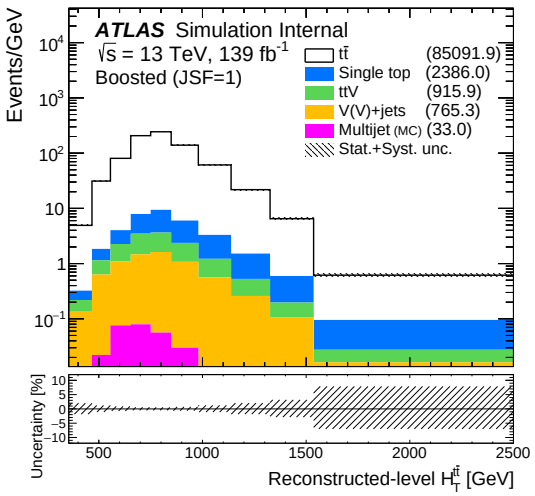

(d)

Figure 9.3: Detector-level distribution with/without the $m_{\ell,b} < 180\,\text{GeV}$ requirement for (a)/(b) $p_{\text{T}}^{t,h}$, (c)/(d) $H_{\text{T}}^{t\bar{t}}$. The dashed band represents the combined statistical and background modelling uncertainties. A different multijet estimation is used in these plots and the multijet uncertainty discussed in Section 9.3.1 is not included. The overflow and underflow are included.

9.4. $t\bar{t}$ modelling uncertainties

The analysis is sensitive to the modelling of simulated $t\bar{t}$ events due to the use of MC predictions to derive the unfolding corrections. The uncertainties on the $t\bar{t}$ modelling are evaluated using alternative $t\bar{t}$ predictions as pseudo-data and calculating the difference between the unfolded pseudo-data and the alternative $t\bar{t}$ prediction at particle-level. Several alternative predictions are used, as well as modifications to the nominal MC settings. The different samples used are described in Section 7.1.1.

9.4.1. Uncertainties due to missing higher-order corrections

Variations in the extent of initial- and final–state radiation are estimated using several approaches. Firstly the uncertainty related to the choice of the μ_r and μ_f scales in the hard-scatter, and the parton shower, is evaluated by re-weighting of the POWHEG+PYTHIA8 sample. These variations affect mainly ISR and are analogous to the methods used for the single-top components. Although the source of this uncertainty is shared between $t\bar{t}$ and single-top the two components are considered uncorrelated, since the underlying physics processes are different.

The h_{damp} parameter in the POWHEG generator regulates the scale of the highest p_T emission before the parton shower and thus primarily effects ISR properties. A dedicated POWHEG+PYTHIA8 sample with modified h_{damp} is used to estimate an uncertainty due to the choice of this parameter.

The uncertainty due to the FSR simulation is obtained using a POWHEG+PYTHIA8 sample where the renormalisation scale is shifted up or down with respect to the nominal value. Again this component is considered uncorrelated with respect to the related uncertainty on the single top modelling.

An additional uncertainty is used to parameterise effects related to the matching between the output of the hard-scatter simulation and the input of the parton shower. A direct comparison to the approach used in the POWHEG generator is provided by an alternative sample generated using MADGRAPH5, which employs the MC@NLO method for the matching. The alternative sample used to derive this uncertainty is interfaced with PYTHIA8, in the same way as the nominal, but includes several showering settings which are optimised for the MC@NLO matching. This creates an inconsistency between the two versions of PYTHIA8 used, most notable is that the

matrix element corrections are turned off in the MC@NLO+PYTHIA8 sample while they are kept on in the POWHEG+PYTHIA8 sample. As a result this uncertainty convolutes showering effects with the choice of the matching algorithm.

9.4.2. Parton shower and hadronisation

An uncertainty is included to cover the choice of parton shower and hadronisation model used in PYTHIA8. The uncertainty is determined using an alternative $t\bar{t}$ prediction, swapping the PYTHIA8 shower and hadronisation model for HERWIG7.

9.4.3. Top-quark mass

The top-quark mass (m_{top}) is a fundamental property of the standard model which has been measured to a high precision of around 0.5 GeV by both ATLAS [174], and CMS [175]. The top-quark mass uncertainty is expected to be larger for this analysis as the method used to reduce the sensitivity to jet uncertainties, outlined in Section 9.5, directly exploits the top-quark mass resulting in increased sensitivity m_{top}.

An uncertainty is estimated using additional simulated samples with varied top-quark mass values. Figure 9.4a shows initial results of the top-quark mass uncertainty for the $p_{\text{T}}^{j,1}$ variable, derived using samples with m_{top} values of 172 and 173 GeV ($\pm$0.5 GeV). Error bars on each point show the statistical uncertainty of the mass varied sample while the orange band shows the expected statistical uncertainty on the measurement as a point of comparison. These samples do not produce a reliable estimate of the true effect due to their limited statistical precision. Samples with m_{top} set to 169 GeV and 176 GeV are used instead, with the final uncertainty values scaled by 1/7 to match the effect of a $\pm$0.5 GeV shift in the top-quark mass. The scaled uncertainties are also shown in Figure 9.4a and are found to be consistent with results from the smaller mass values but with reduced relative statistical uncertainties. Figure 9.4b shows an additional validation check comparing the uncertainty derived from samples with $\pm$1.5 GeV variations of the top-quark mass to results of the 169 and 176 GeV samples scaled by 3/7. These results are naturally larger than the uncertainties derived from the $\pm$0.5 GeV samples but are consistent with each other within the statistical precision of the simulated samples, demonstrating the validity of the scaled uncertainty estimate.

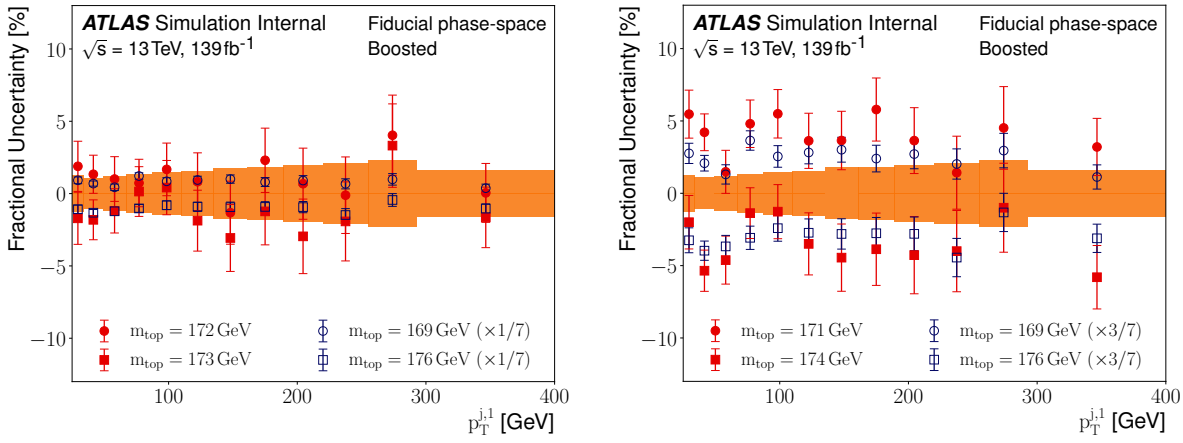

Figure 9.4: Fractional uncertainty due to the precision of the top-quark mass as a function of the p_{T} of the leading additional jet. (a) Comparison between the uncertainty derived using $m_{\mathrm{top}} = 172(173)$ GeV in red, and 169(176) GeV in blue, with results from the latter scaled by 1/7. (b) Comparison between $m_{\mathrm{top}} = 171(174)$ GeV in red, and 169(176) GeV in blue, with results from the latter scaled by 3/7. Error bars show the statistical uncertainty of each MC sample and the orange band shows the statistical uncertainty on the data.

9.4.4. PDF set

An uncertainty on the choice of the PDF set used in the POWHEG+PYTHIA8 sample is estimated using a set of 30 eigenvector variations of the PDF4LHC30 [176] PDF set. The procedure is the same as for the other modelling uncertainties but the prediction using the central PDF4LHC30 variation, rather than the nominal MC sample, is used to derive the unfolding corrections which are applied to the other 30 variations.

9.4.5. Pileup modelling and luminosity

An uncertainty related to the modelling of pileup interactions is evaluated by varying the mean number of interactions in the simulation via the pileup event weights as described in [177]. This is evaluated in the same way as the class of detector uncertainties controlled using weights and is generally found to be small, in part due to the use of particle flow jets which are robust against pileup effects. As described in Section 7.1 an uncertainty of 1.7% on the total integrated luminosity of the Run-2 dataset is provided by an external measurement and included in the total uncertainty.

9.5. Jet uncertainty reduction using JSF

The jet related uncertainties outlined previously, of which the JES components contribute the largest fraction, are expected to make up a large portion of the total measurement uncertainty. Jet uncertainties have historically been a significant source of measurement error in many $t\bar{t}$ cross-section measurements at both ATLAS [124, 128, 169] and CMS [178, 179]. As a particular example Figure 9.5 shows the fractional uncertainty breakdown for the p_{T} of the hadronic top-quark and the scalar p_{T} sum of the two top-quarks from the previous 36 fb^{-1} ATLAS analysis [124]. The combined JES and JER components, in red, are a significant uncertainty in most bins with the uncertainty increasing in the higher p_{T} regions in both cases.

The sensitivity of experimental results to certain classes of systematic uncertainty can be reduced through careful modification of the analysis strategy. A novel approach is introduced here which aims to reduce the overall impact of the jet energy scale uncertainties by using information from the measured mass of the hadronically decaying top-quark ($m^{t,h}$) and the precisely known value of the top-quark mass (m_{top}) [174].

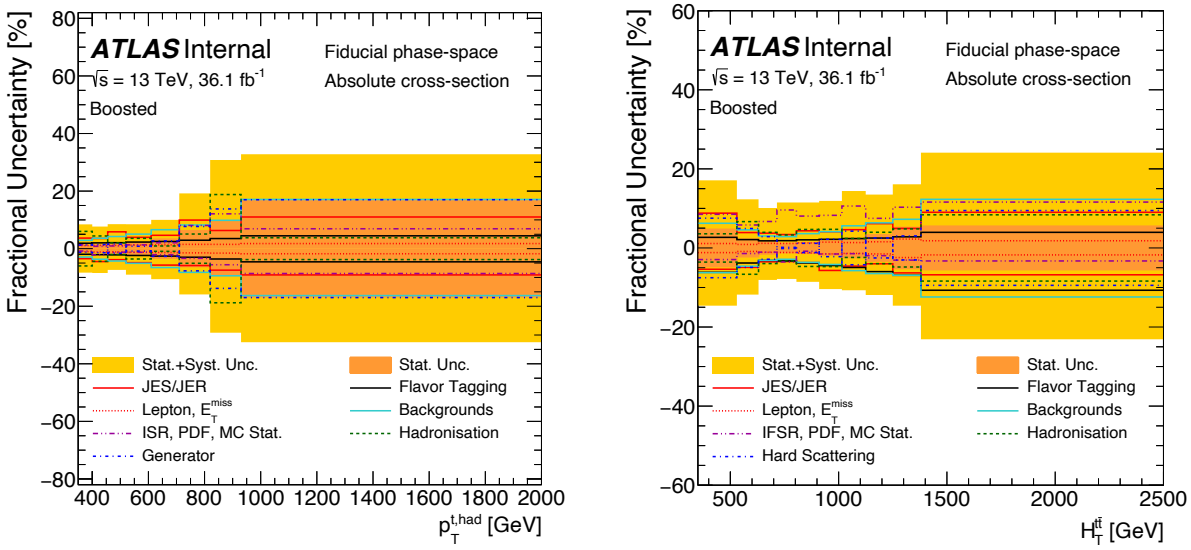

(a) **(b)**

Figure 9.5: Fractional uncertainties on the absolute particle-level cross-section as a function of (a) $p_{\mathrm{T}}^{t,h}$, (b) $H_{\mathrm{T}}^{t\bar{t}}$ from the preceding 36 fb^{-1} ATLAS $t\bar{t}$ measurement [124]. In these results the combined JES and JER components (red) make up the dominant detector uncertainty in most bins. Additionally the large background uncertainties (cyan) in the tails of the distributions are dominated by the DS/DR single-top uncertainty demonstrating the likely scale of this without a maximum $m_{\ell,b}$ requirement.

The method assumes there is an overall difference in jet energy scale between data and simulation that is parameterised with a jet energy scale factor (JSF). The JSF is defined as a constant factor according to:

$$E_j^{\text{corrected}} = E_j^{\text{measured}} \times \frac{1}{\text{JSF}}. \tag{9.1}$$

The correction is applied by scaling the energy of all small-R jets by $1/\text{JSF}$ and is applied on top of the existing jet calibrations outlined in Section 5.3. In this way the analysis procedure is altered to include a measurement of the factor (JSF_{data}) alongside the $t\bar{t}$ cross-section in each bin. When the analysis is repeated with JES variations used as pseudo-data; the extraction of JSF (in this case labelled JSF_{syst}) will absorb any overall differences in the jet energy scale, reducing the impact of the JES uncertainties.

This method shares many commonalities with the JSF fit parameter used to aid in extracting the top-quark mass, first introduced at CDF in 2006 [180], and subsequently used in many top mass analyses including at DØ [181], as well as in more recent measurements by ATLAS [174, 182, 183] and CMS [175, 184, 185]. The notable difference with this implementation is that the re-clustered top-jet mass, rather than the reconstructed W-boson mass, is the variable used to extract the JSF. This is the first use of the method in the context of a differential $t\bar{t}$ cross-section measurement.

9.5.1. JSF extraction

The re-clustered R=1.0 jets used as proxy for the hadronically decaying top-quark in selected events are constructed by summing the 4-momenta of the small radius sub-jets. This provides a direct link between the energy-scale of the small-R jets and $m^{t,h}$. This connection can be exploited by applying a scaling factor (JSF) to the energy components of all small radius jets in the events in order to vary the underlying jet energy scale. The remaining 4-momenta components of each jet are modified to keep the mass and direction of the jet constant:

$$\text{jet}_{\text{scaled}} = \{\alpha p_x, \alpha p_y, \alpha p_z, E \times \text{JSF}\}, \qquad \alpha = \sqrt{\frac{E_j^2 \times \text{JSF}^2 - m_j^2}{|\overrightarrow{\text{jet}}_{\text{nominal}}|^2}}, \tag{9.2}$$

where $\overrightarrow{\text{jet}}_{\text{nominal}}$ is the 3-momentum of the jet prior to applying the JSF.

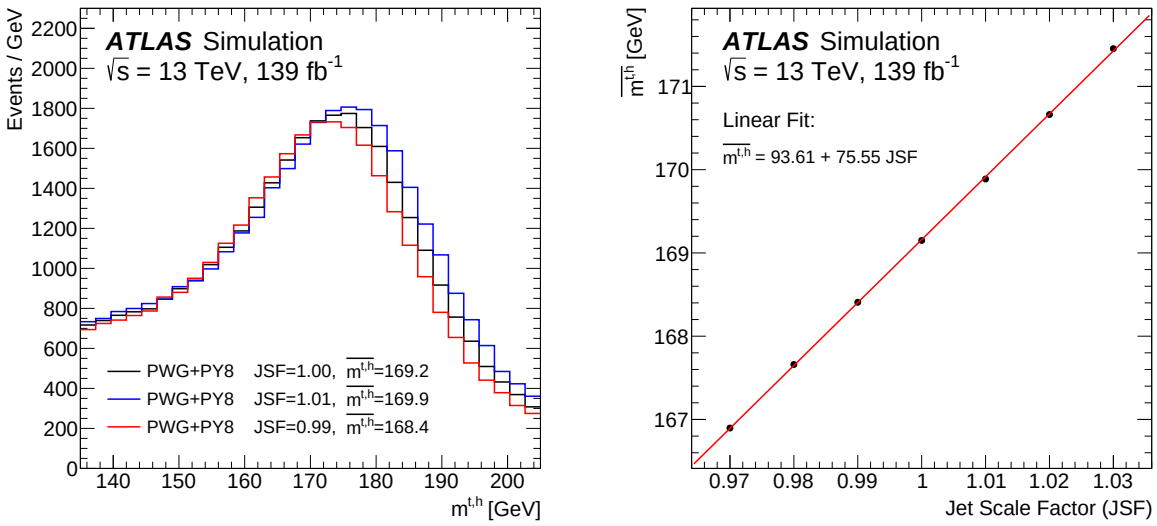

(a) **(b)**

Figure 9.6: (a) The invariant mass distribution of the top-tagged jet ($m^{t,h}$) for expected signal plus backgrounds for three example values of JSF. PWG+PY8 corresponds to the POWHEG+PYTHIA8 sample.
(b) The mean of the same distribution ($\overline{m^{t,h}}$) as a function of JSF and a linear fit to the simulated samples. Uncertainties on the mean (RMS/$\sqrt{(N)}$) are included for each point but are too small to be visible.

Figure 9.6a demonstrates the result of this scaling, showing the $m^{t,h}$ distribution for the nominal $t\bar{t}$+background MC prediction for three example values of JSF. The high and low mass tails are removed from the distributions in order to improve the fit in the next stage. As expected, larger JSF values result in the peak shifting to higher values of $m^{t,h}$, resulting in a higher mean value ($\overline{m^{t,h}}$). In each case the mean of the distribution is below that of the true top-quark mass. This is due to the limited acceptance of the jet re-clustering process which results in a fraction of the top-quark decay energy being lost outside of the R=1.0 cone. The expected number of events is also observed to increase very slightly for larger correction factors, with a $1/\text{JSF}$ correction of 1.01 resulting in a $\sim$4% increase in the total event yield. This is an expected effect due to higher jet energies raising the probability for events to pass the jet selection requirements.

The relationship between $m^{t,h}$ and JSF is parameterised by fitting the mean of $m^{t,h}$ at various values of injected JSF (0.97 – 1.03), again using the nominal $t\bar{t}$+background MC prediction. A simple linear fit is used, shown in Figure 9.6b. A value for JSF_{data} can then be extracted from this linear fit using the measured value of $\overline{m^{t,h}}$.

9.5.2. JSF measurement in data

Prior to extracting a JSF correction the level of agreement between data and MC is examined for the $m^{t,h}$ distribution. Figure 9.7a shows a comparison between the observed data and the sum of the simulated $t\bar{t}$ and background processes for the invariant mass of the top-tagged jet. As the JSF method is only sensitive to the mean of this distribution, the sum of the $t\bar{t}$ and background processes has been normalised to the data yield to better visualise the level of shape agreement. The uncertainty band includes all of the experimental uncertainties discussed earlier, but not the modelling uncertainties. Good agreement is observed between the data and the prediction, indicating the distribution is well modelled in simulation and that the extracted JSF will be close to one. The value of JSF corresponding to the mass distribution in data (JSF_{data}) is measured to be 0.99965. Figure 9.7b compares the $m^{t,h}$distributions with and without the JSF correction. As JSF_{data} is close to 1 there are only small differences between the distributions.

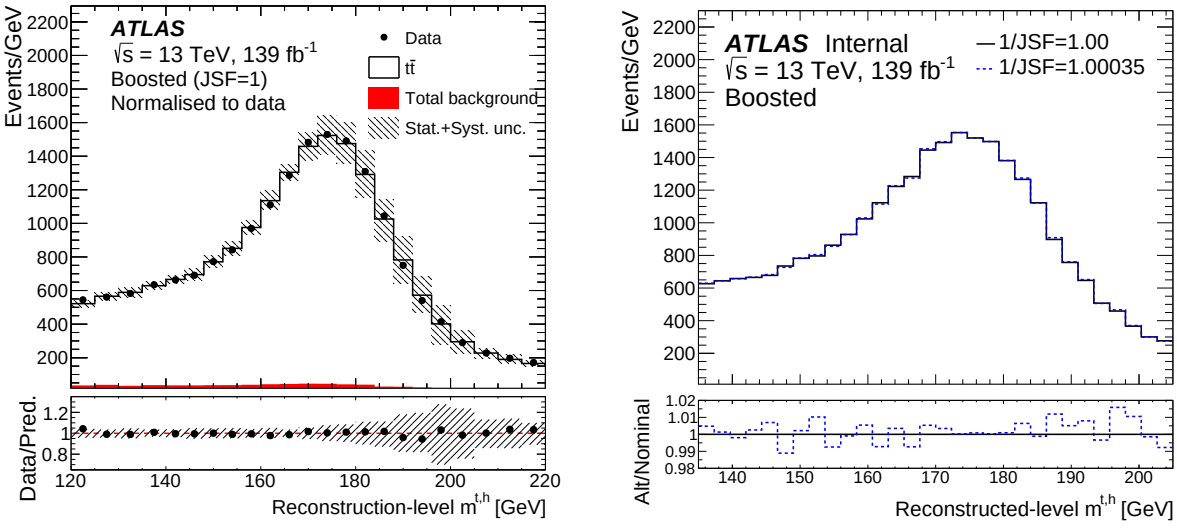

(a) **(b)**

Figure 9.7: (a) The distribution of $m^{t,h}$ in data is compared with the expected $t\bar{t}$+background simulation prior to extracting the JSF. The sum of the $t\bar{t}$ and background processes (red) has been normalised to the data yield in order to visualise the agreement in shape of the distributions. Only measurement and statistical uncertainties are included in the hatched band.
(b) Direct comparison of the $m^{t,h}$ distribution with and without the extracted $1/\text{JSF}$ =1.00035 correction applied, using events from the full Run-2 dataset.

JSF statistical uncertainty:

The limited statistical precision of the data introduces an uncertainty on the derived JSF_{data} value. This is estimated using a very similar procedure to the data and MC statistical uncertainties outlined in Section 9.1. Pseudo-experiments are run and for each a new $m^{t,h}$ distribution is produced by applying a Poisson smearing directly to the measured bin contents. This is repeated 10,000 times and for each smeared distribution the $1/\text{JSF}$ value is calculated. The RMS value of the resulting distribution, shown in Figure 9.8a, is taken as an estimate of the statistical uncertainty. This results in a final correction factor of $1/\text{JSF}_{\text{data}} = 1.00035 \pm 0.00087$. As expected the data agrees well with the simulation, and is found to be compatible within statistical uncertainty.

The fit used in Figure 9.6b is not explicitly required to pass through the point at $\text{JSF} = 1$, as a result the nominal $t\bar{t}$+background simulation also receives a non-unitary $1/\text{JSF}$ correction. This is similarly limited by statistical precision with the uncertainty calculated in the same way but using Gaussian smearing and replacing the data distributions by the sum of the simulated nominal $t\bar{t}$ and background predictions. The results for the nominal MC are shown in Figure 9.8b, giving a final correction of $1/\text{JSF}_{\text{nominal}} = 1.00013 \pm 0.00031$, consistent with unity.

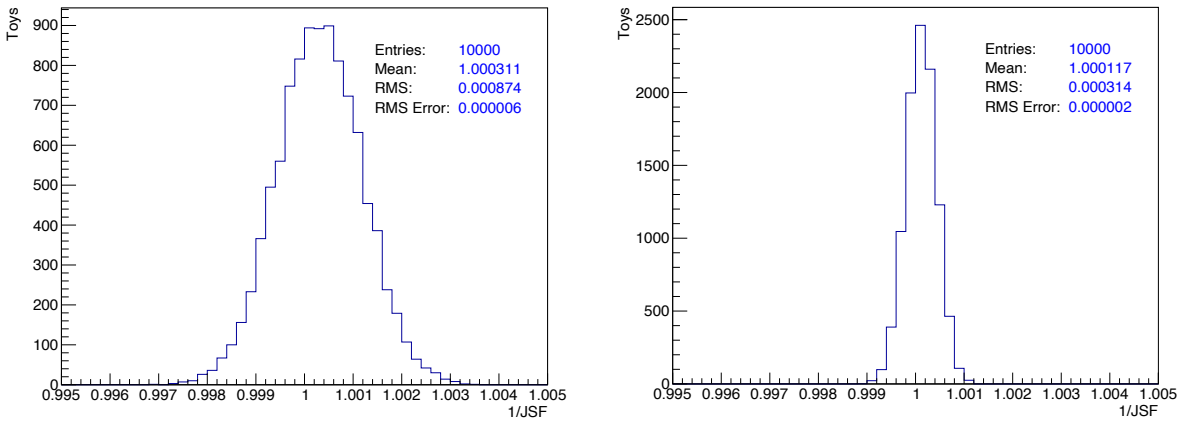

(a) **(b)**

Figure 9.8: Distribution of $1/\text{JSF}$ correction factors from 10,000 toy experiments produced by introducing (a) a random Poisson smear to the contents of each bin in the data $m^{t,h}$ distribution (b) a random Gaussian smear to the contents of each bin of the nominal signal+background $m^{t,h}$ prediction. As the $1/\text{JSF}$ corrections corresponding to the distributions the pseudo-experiments are drawn from are not equal to one, the combined results of the toy experiments are equally not expected to peak at unity in either case.

Four additional variations of the nominal signal and background predictions are produced by varying the jet energies by $1/\left(\mathrm{JSF}_{\text{nominal}} \pm \mathrm{JSF}_{\text{data-stat}}\right)$ and $1/\left(\mathrm{JSF}_{\text{nominal}} \pm \mathrm{JSF}_{\text{MC-stat}}\right)$. These samples are treated as pseudo-data and the uncertainty is estimated by unfolding them using nominal corrections.

Correlation with statistical uncertainty

The statistical uncertainty applied to the extracted JSF naturally originates from the same limited statistics as the data uncertainty. The level of correlation between the two uncertainties was assessed by calculating the unbinned correlation factor (ρ) between each variable and $m^{t,h}$, using selected data events with $135\,\text{GeV} < m^{t,h} < 205\,\text{GeV}$. These values are shown in the second column of Table 9.2, in general the level of correlation was found to be small with many variables under 5% and the largest correlation attributed to the p_{T} of the hadronic top with $\rho = 11.2\%$.

The correlation factors between each bin of the measured observables and $m^{t,h}$ were also calculated in order to monitor for cancellations between highly correlated and anti-correlated regions. Figure 9.9 shows the ρ value for each bin in the $p_{\text{T}}^{t,h}$ and $m(j_1, t_h)$ distributions and the largest positive and smallest negative single bin values for each observable are shown in the third and fourth columns in Table 9.2. Again no significant correlations are observed in the individual bins, with a moderate correlation of 29% observed in the first bin of $m(j_1, t_h)$ being the largest. In the absence of significant correlations the statistical JSF uncertainty is treated as uncorrelated and combined in quadrature with the other uncertainties.

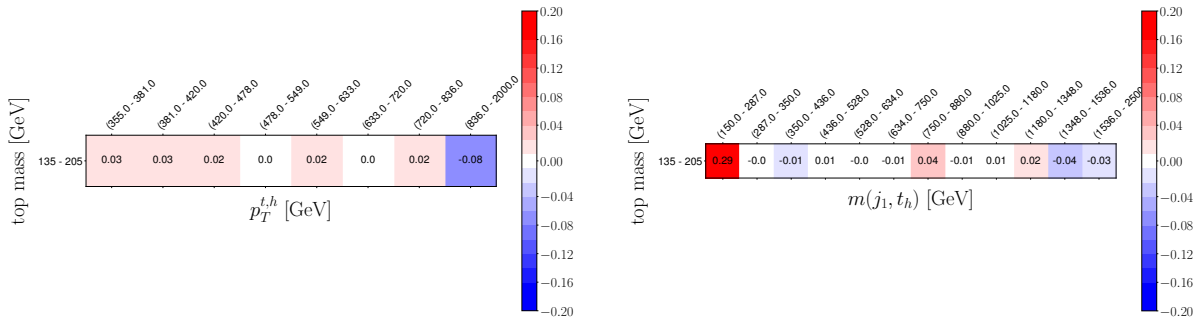

(a) **(b)**

Figure 9.9: Correlation between $m^{t,h}$ and each bin of (a) $p_{\text{T}}^{t,h}$, (b) $m(j_1, t_h)$ for selected events in data with $135\,\text{GeV} < m^{t,h} < 205\,\text{GeV}$. Values are shown on a zoomed scale between -0.2 and 0.2

Table 9.2: Unbinned correlation factor between reconstructed kinematic observables and $135\,\text{GeV} < m^{t,h} < 205\,\text{GeV}$. Calculated using events from the full Run 2 dataset after scaling jet energies by $1/\text{JSF}_{\text{data}}$ and with the boosted $t\bar{t}$+jets event selection applied. The largest $+\rho$ and $-\rho$ values over all bins are included to monitor cancellations between highly correlated and anti-correlated regions.

Observable	Correlation (ρ)	Max $+\rho$ bin	Max $-\rho$ bin
$p_{\text{T}}^{t,h}$	+0.117	+0.028	−0.077
$H_{\text{T}}^{t\bar{t}}$	+0.099	+0.04	−0.011
$m^{t\bar{t}}$	+0.085	+0.053	−0.053
$H_{\text{T}}^{t\bar{t}+\text{jets}}$	+0.064	+0.026	−0.027
$p_{\text{T}}^{t,\ell}$	+0.062	+0.036	−0.017
$m(j_1, t_h)$	+0.049	+0.293	−0.041
$\frac{\Delta\phi}{\pi}(t_h, t_\ell)$	+0.026	+0.035	−0.026
$\frac{\Delta\phi}{\pi}(j_2, t_h)$	+0.020	+0.071	−0.023
$\frac{\Delta\phi}{\pi}(j_1, t_h)$	+0.018	+0.041	−0.017
$\lvert y^{t,\ell}\rvert$	+0.007	+0.09	−0.049
$p_{\text{T}}^{j,1}$	+0.004	+0.056	−0.053
N^j	−0.025	—	−0.02
$\sigma^{t\bar{t}}$ (Inclusive)	−0.024	—	−0.019
$\frac{\Delta\phi}{\pi}(j_1, j_2)$	−0.014	+0.026	−0.064
$p_{\text{T}}^{j,2}$	−0.004	+0.06	−0.038
$p_{\text{T}}^{t\bar{t}}$	−0.002	+0.049	−0.027
$\lvert y^{t,h}\rvert$	−0.001	+0.045	−0.142
$\frac{\Delta\phi}{\pi}(b_\ell, t_h)$	−0.001	+0.016	−0.044
$\lvert y^{t\bar{t}}\rvert$	−0.000	+0.041	−0.02

9.5.3. JSF measurement in simulation

To evaluate the systematic uncertainties in a consistent way each varied pseudo-data sample is treated identically to data in the analysis procedure. This is true also when accounting for the JSF method meaning a unique correction ($1/\text{JSF}_{\text{syst}}$) is extracted for each pseudo-data sample when evaluating the systematic uncertainties. Several systematic variations, in particular those which directly modify the small radius jet energy scale, are expected to produce a more dramatic change in the $m^{t,h}$ distribution from which the JSF is derived, resulting in a more significant correction. As an example the $m^{t,h}$ distribution for the nominal expected $t\bar{t}$+backgrounds as well as the up and down variations of a single JES uncertainty component (flavour response) are shown in Figure 9.10, both with and without the JSF corrections applied. The mean top-jet mass for the two samples with JES variations are different from the nominal value by roughly ± 0.5 GeV before the correction, resulting in correction factors of 1.00607 and 0.99423 for the up and down variations respectively. Applying these factors as described above successfully recovers much of the shape of the nominal distribution and brings the mean value into agreement (± 0.01 GeV). This shows that a large fraction of the original systematic uncertainty can be absorbed by the JSF scaling factor and correcting this leaves only residual JES effects, effectively reducing the impact of the JES uncertainties on the measurement.

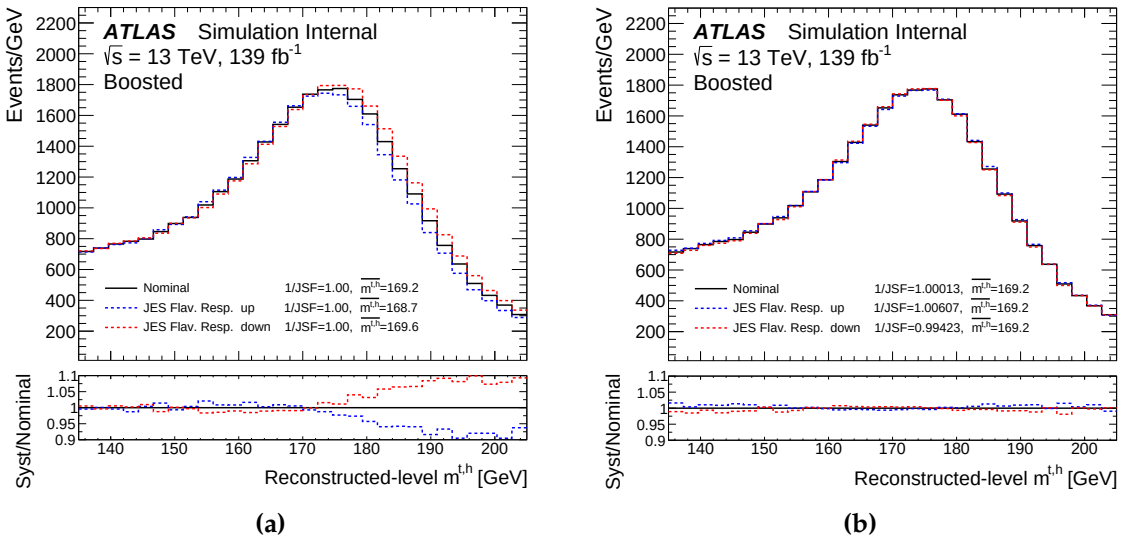

Figure 9.10: The invariant mass distribution of the top-tagged jet ($m^{t,h}$) for the nominal prediction and two sets of pseudo-data with up(down) modifications to the JES flavour response. Events are compared (a) without, (b) with JSF corrections applied.

Table 9.3 shows the 1/JSF correction factors for each systematic uncertainty component in the analysis as well as the values for data and the nominal MC. Only the average corrections are given for groups in which no individual component has a correction factor significantly different from the nominal value. This includes the 30 PDF variations, b-tagging, lepton, and $E_{\mathrm{T}}^{\mathrm{miss}}$ uncertainties. Comparisons of the uncertainties with and without the JSF method are presented in the next section.

Table 9.3: 1/JSF correction factors for data, simulation, and systematic uncertainty components.

Systematic uncertainty	1/JSF				
nominal MC (POWHEG+PYTHIA8)	1.000128 ± 0.000314				
Data	1.000351 ± 0.000874				
MC modelling					
Average PDF (PDF4LHC909 30 eigenvector PDF set)	1.000128	hadronisation (POWHEG+HERWIG7)	1.000694	hard scattering (MC@NLO+PYTHIA8)	1.003181
ISR_down	1.000096	ISR_up	1.000270	h_{damp} radiation (PWG+PY8 $h_{\mathrm{damp}} = 3m_{\mathrm{top}}$)	1.001338
FSR_down	1.002271	FSR_up	0.998290		
top-mass_down (PWG+PY8 $m_{\mathrm{top}} = 169$ GeV)	1.021914	top-mass_up (PWG+PY8 $m_{\mathrm{top}} = 176$ GeV)	0.979307		
Background modelling					
Single top FSR_down	0.999939	Single top FSR_up	1.000168	Single top DS/DR	0.999852
Single top ISR_down	1.000057	Single top ISR_up	1.000220	Single top normalisation	1.000164
W+jets scale_down	1.000221	W+jets scale_up	1.000066	Z+jets normalisation	1.000162
$t\bar{t}V$ normalisation	1.000126	Diboson normalisation	1.000133	Multijet normalisation	1.000214
Jets					
JES_BJES_Response_down	1.001261	JES_BJES_Response_up	0.998976	JES_NP_Detector1_down	1.000534
JES_NP_Detector1_up	0.999689	JES_NP_Detector2_down	1.000186	JES_NP_Detector2_up	1.000061
JES_NP_Mixed1_down	1.001911	JES_NP_Mixed1_up	0.998290	JES_NP_Mixed2_down	0.999006
JES_NP_Mixed2_up	1.001223	JES_NP_Mixed3_down	1.000284	JES_NP_Mixed3_up	0.999973
JES_NP_Modelling1_down	1.004897	JES_NP_Modelling1_up	0.995289	JES_NP_Modelling2_down	1.000636
JES_NP_Modelling2_up	0.999613	JES_NP_Modelling3_down	0.999558	JES_NP_Modelling3_up	1.000700
JES_NP_Modelling4_down	1.000358	JES_NP_Modelling4_up	0.999889	JES_NP_Statistical1_down	1.000405
JES_NP_Statistical1_up	0.999825	JES_NP_Statistical2_down	0.999884	JES_NP_Statistical2_up	1.000386
JES_NP_Statistical3_down	0.999853	JES_NP_Statistical3_up	1.000394	JES_NP_Statistical4_down	1.000379
JES_NP_Statistical4_up	0.999872	JES_NP_Statistical5_down	1.000057	JES_NP_Statistical5_up	1.000203
JES_NP_Statistical6_down	1.000339	JES_NP_Statistical6_up	0.999938	JES_η-icalib_Modelling_down	1.002177
JES_η-icalib_Modelling_up	0.997955	JES_η-icalib_NonClosure_2018data_down	1.001406	JES_η-icalib_NonClosure_2018data_up	0.998783
JES_η-icalib_NonClosure_highE_down	1.000129	JES_η-icalib_NonClosure_highE_up	1.000129	JES_η-icalib_NonClosure_negEta_down	1.000139
JES_η-icalib_NonClosure_negEta_up	1.000126	JES_η-icalib_NonClosure_posEta_down	1.000137	JES_η-icalib_NonClosure_posEta_up	1.000121
JES_η-icalib_TotalStat_down	1.000699	JES_η-icalib_TotalStat_up	0.999557	JES_Flavor_Composition_down	1.000348
JES_Flavor_Composition_up	0.999918	JES_Flavor_Response_down	0.994227	JES_Flavor_Response_up	1.006065
JES_Pileup_OffsetMu_down	1.000932	JES_Pileup_OffsetMu_up	0.999271	JES_Pileup_OffsetNPV_down	1.002448
JES_Pileup_OffsetNPV_up	0.997688	JES_Pileup_PtTerm_down	1.001930	JES_Pileup_PtTerm_up	0.998315
JES_Pileup_RhoTopology_down	1.005510	JES_Pileup_RhoTopology_up	0.994740	JES_PunchThrough_MC16_down	1.000158
JES_PunchThrough_MC16_up	1.000106	JES_SingleParticle_HighPt_down	1.000128	JES_SingleParticle_HighPt_up	1.000128
JER_DataVsMC_MC16_down	0.999923	JER_DataVsMC_MC16_up	0.999923	JER_NP_1_down	0.998248
JER_NP_1_up	0.998248	JER_NP_2_down	0.997688	JER_NP_2_up	0.997688
JER_NP_3_down	0.998959	JER_NP_3_up	0.998959	JER_NP_4_down	0.998902
JER_NP_4_up	0.998902	JER_NP_5_down	0.999138	JER_NP_5_up	0.999138
JER_NP_6_down	0.998861	JER_NP_6_up	0.998861	JER_NP_7restTerm_down	0.998825
JER_NP_7restTerm_up	0.998825	JVT_down	1.000196	JVT_up	1.000034
b-tagging					
b-tag_NP_B_0_down	1.000218	b-tag_NP_B_0_up	1.000038		
Average b-tag_B_down (remaining 8 variations)	1.000139	Average b-tag_B_up (remaining 8 variations)	1.000118		
Average b-tag_C_down (4 variations)	1.000148	Average b-tag_C_up (4 variations)	1.000109		
Average b-tag_Light_down (4 variations)	1.000145	Average b-tag_Light_up (4 variations)	1.000112		
Average b-tag_extrapolation_down (2 variations)	1.000101	Average b-tag_extrapolation_up (2 variations)	1.000148		
Lepton + $E_{\mathrm{T}}^{\mathrm{miss}}$					
Average electron_down (7 variations)	1.000128	Average electron_up (7 variations)	1.000128		
Average muon_down (13 variations)	1.000127	Average muon_up (13 variations)	1.000129		
Average $E_{\mathrm{T}}^{\mathrm{miss}}$ (4 variations)	1.000128				
Luminosity and pileup					
luminosity	1.000126	pileup_down	1.001006	pileup_up	0.999215

9.6. Impact of JSF on measurement

The effect of the JSF method on the total event yield and the statistical and detector uncertainties for data, $t\bar{t}$ signal, and all background samples are shown in Table 9.4. As expected applying a JSF correction greater than one results in a slight increase in the overall data yield. No noticeable change in the $t\bar{t}$ or background yields can be observed within the precision of the estimations. The main difference is seen in the associated uncertainty on the $t\bar{t}$ signal which reduces by ∼40% when using the JSF.

Table 9.5 shows the fractional uncertainty breakdown for the inclusive cross-section measurement with and without the JSF method. The use of the JSF method results in a ∼30% reduction in total uncertainty. The effect of the JSF on the Jets uncertainty is by far the most significant however the JSF is only sensitive to overall differences between the JES in data and simulation thus any differences that depend on the kinematics or flavour of the jets can not be fully corrected for and will still cause uncertainties in the analysis. These residual effects are observed directly in Table 9.5 as the JES uncertainty is not reduced to zero when using the JSF.

Table 9.4: Detector-level event yields for measured data, simulated $t\bar{t}$ signal, and background events with and without JSF corrections applied. The uncertainty values are symmetrised and indicate the combined effect of statistical, detector, and background modelling uncertainties. The total expected yields and associated uncertainties, as well as all statistical uncertainties, are calculated prior to rounding.

Process	Expected events	Expected events (JSF = 1)
$t\bar{t}$	84 210 ± 2650	84 170 ± 4210
Single top	1710 ± 280	1710 ± 280
$t\bar{t}V(t\bar{t}W+t\bar{t}Z+t\bar{t}H)$	850 ± 110	840 ± 110
Multijet	560 ± 370	550 ± 360
W+jets	420 ± 160	420 ± 160
Z+jets	80 ± 40	80 ± 40
Diboson	40 ± 20	40 ± 20
Total (1/JSF = 1.00013)	87 870 ± 2700	87 810 ± 4240
Data (1/JSF = 1.00035)	75743	75631

Table 9.5: Fractional uncertainty breakdown for inclusive $t\bar{t}$ cross-section both with and without the JSF method applied. The IFSR contribution includes effects from both initial- and final-state radiation.

Source	Uncertainty [%]	Uncertainty [%] (no JSF)
Statistical (data)	± 0.4	± 0.4
JSF statistical (data)	± 0.4	—
Statistical (MC)	± 0.2	± 0.1
Hard scatter	± 0.5	± 0.8
Hadronisation	± 2.0	± 1.8
Radiation (IFSR + h_{damp})	$^{+1.0}_{-1.6}$	$^{+1.4}_{-2.3}$
PDF	± 0.1	± 0.1
Top-quark mass	$^{+0.8}_{-1.1}$	± 0.1
Jets	± 0.7	± 4.2
b-tag	± 2.4	± 2.4
Leptons	± 0.8	± 0.8
$E_{\text{T}}^{\text{miss}}$	± 0.1	± 0.1
Pileup	± 0.4	± 0.0
Luminosity	± 1.8	± 1.8
Backgrounds	± 0.6	± 0.6
Total systematic uncertainty	$^{+4.1}_{-4.3}$	$^{+5.8}_{-6.0}$
Total	$^{+4.1}_{-4.3}$	$^{+5.8}_{-6.0}$

The JSF method relies on the modelling of the $m^{t,h}$ distribution and hence the modelling uncertainties limit the precision of the method. This is most obvious for the top-quark mass uncertainty outlined in Section 9.4.3. Without the JSF method the analysis has only a very small impact from the top mass uncertainty. With the JSF method the dependence on the top mass is increased and this leads to an increased systematic uncertainty. The pileup uncertainty is also shown to increase when using the method which can be similarly understood; increased pileup will have a direct impact on the measured $m^{t,h}$distribution due to the higher probability of clustering pileup radiation into the large-radius jet. The analysis will be more sensitive to pileup effects when using the JSF method as a result. The extraction of JSF_{data} alongside the

differential measurements also increases the total statistical uncertainty of the analysis via the two additional uncertainty components outlined above.

The JSF method will only improve the total uncertainty if the gain in reducing the impact of the JES uncertainties is larger than the additional systematic and statistical uncertainty contributions. In practice the increased uncertainty contributions are shown to be comparatively small (<1% in all cases) and are less significant than the reduction in Jets uncertainty.

Figure 9.11 shows the effect of the JSF correction on the JES uncertainty, post-unfolding, for three differential distributions. The total uncertainty is shown by the yellow and grey bands, and the jet energy scale uncertainty is shown by the red and grey lines. As expected a significant reduction in the JES uncertainty due to the JSF correction is observed. In almost all bins the JES uncertainty is significantly reduced. The JES uncertainty is also observed to be larger when using the JSF method in the first bin of the N^j distribution and the last bins of $p_{\mathrm{T}}^{t,h}$. This demonstrates a limitation of using a single correction factor for events covering a wide phase space, i.e: it is likely the shape of $m^{t,h}$ for only the subset of events with zero additional jets will not perfectly match that of Figure 9.7a. The total uncertainty is also seen to be reduced in most bins though the overall reduction is less due to increased uncertainties elsewhere.

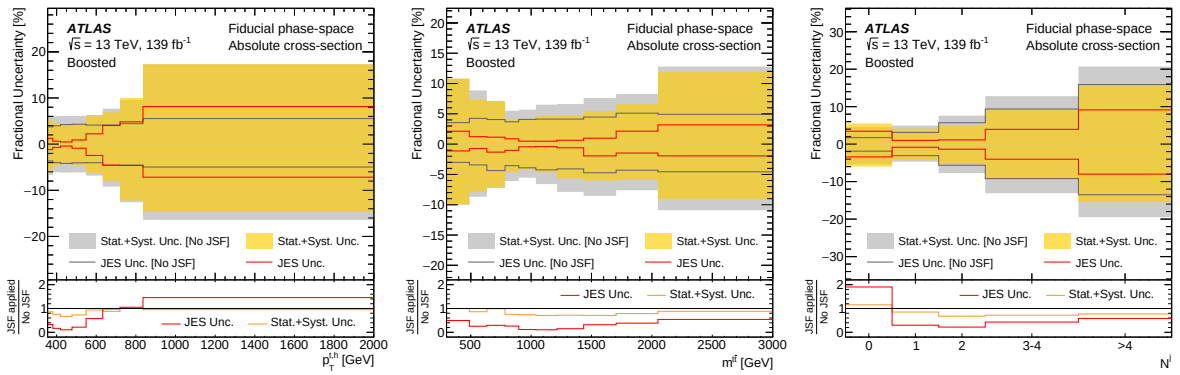

(a) **(b)** **(c)**

Figure 9.11: Effect of the JSF correction on the total uncertainty for the cross-section measurement as a function of (a) $p_{\mathrm{T}}^{t,h}$, (b) $m^{t\bar{t}}$, (c) N^j. The yellow (grey) bands represents the total uncertainty with (without) the JSF correction applied. The red (grey) line in the upper pad shows the JES uncertainty with (without) the JSF method. The bottom panel shows the ratios of the absolute size of the uncertainty with and without the JSF correction applied, in red for the JES uncertainty and in yellow for the total uncertainty.

9.7. Measurement precision

The relative precision on the total fiducial cross-section is ±4.2%, which is smaller than the uncertainty on the theory calculation of $\sigma_{t\bar{t}}^{\text{inc}}$ at NNLO + NNLL of ±6.1%, composed of 4.2% PDF ⊕ 3% scale ⊕ 2.8% m_t uncertainties [105]. The left column of Table 9.5 shows the fractional uncertainty breakdown for the inclusive cross-section measurement. The dominant detector uncertainty comes from the flavour-tagging (±2.4%), the dominant modelling uncertainty is from the choice of hadronisation model (±2.0%).

Figures 9.12–14 show the fractional uncertainty breakdown for some single- and double-differential variables. The precision of the single-differential observables is excellent with absolute uncertainties ranging from ∼4% to ∼17%. In most cases the dominant uncertainty comes from the $t\bar{t}$ modelling while the dominant detector uncertainty originates from the b-tagging. There are some regions of phase-space where jet related uncertainties become comparable, such as the high p_{T} tail of the $p_{\text{T}}^{t,h}$ distribution in Figure 9.12a, and the first and last bins of N^j in Figure 9.13a, where the effectiveness of the JSF method is limited. Figure 9.12b shows the relative uncertainties for the $p_{\text{T}}^{t,h}$ distribution which are generally smaller than the absolute values. The relative impact of the flavour tagging uncertainties is reduced, while the jet uncertainties are more significant. Uncertainty values are generally higher for the double-differential measurements with precision ranging from ∼5% to ∼20%.

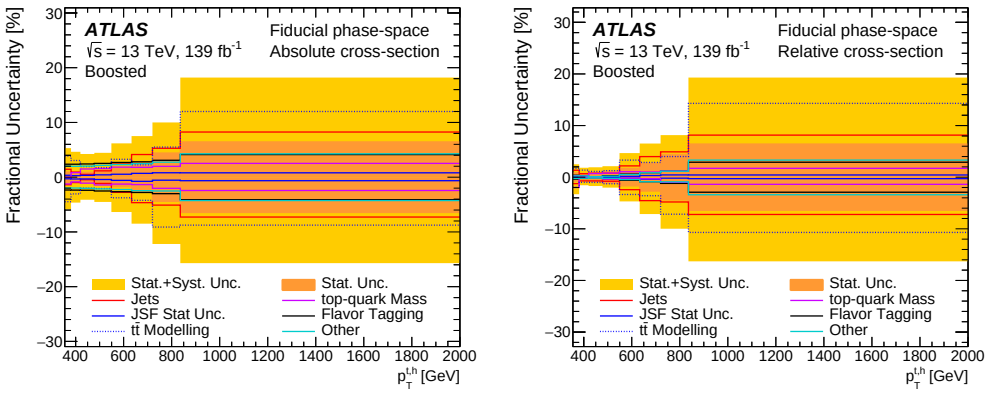

(a) **(b)**

Figure 9.12: Fractional uncertainties for the (a) absolute, (b) normalised particle-level cross section as a function of the p_{T} of the hadronic top quark. The line labelled $t\bar{t}$ modelling includes all uncertainties discussed in Section 9.4, with the exception of the uncertainty on the top-quark mass. The yellow band represents the total uncertainty while the orange band shows the statistical component only.

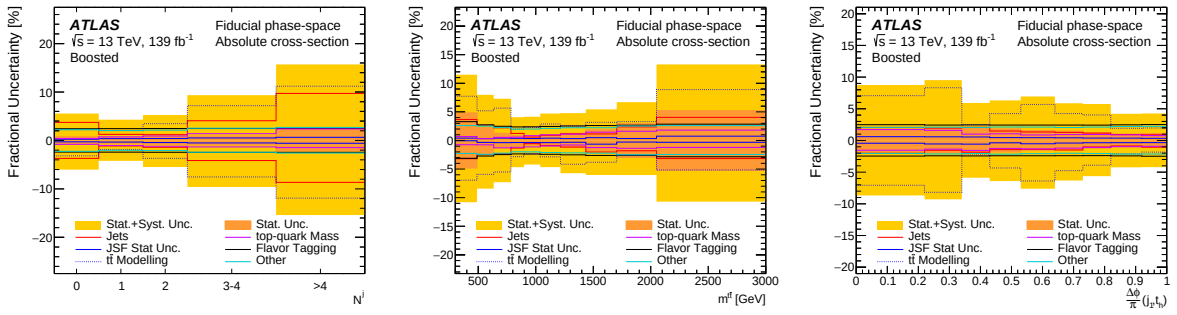

(a) **(b)** **(c)**

Figure 9.13: Fractional uncertainties for the particle-level cross section as a function of (a) N^j, (b) $m^{t\bar{t}}$, and (c) $\Delta\phi(j_1, t_h)$. The line labelled $t\bar{t}$ modelling includes all uncertainties discussed in Section 9.4, with the exception of the uncertainty on the top-quark mass. The yellow band represents the total uncertainty while the orange band shows the statistical component only.

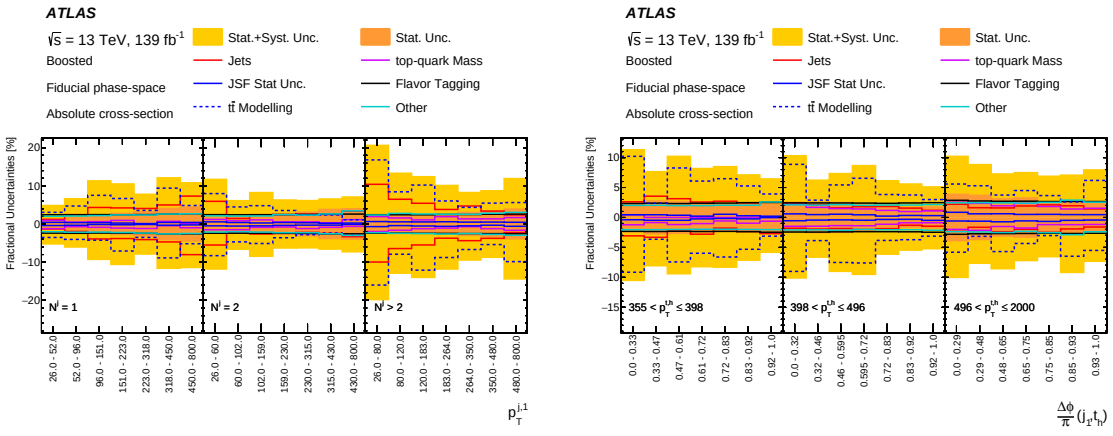

(a) **(b)**

Figure 9.14: Fractional uncertainties for the particle-level cross section as a function of (a) $p_{\mathrm{T}}^{j,1}$ in regions of N^j, (b) $\Delta\phi(j_1, t_h)$ in regions of $p_{\mathrm{T}}^{t,h}$. The line labelled $t\bar{t}$ modelling includes all uncertainties discussed in Section 9.4, with the exception of the uncertainty on the top-quark mass. The yellow band represents the total uncertainty while the orange band shows the statistical component only.

Chapter 10.

Results

"No fair! You changed the outcome by measuring it!"
— Prof. H. J. Farnsworth, Futurama S3, E10 - The Luck of the Fryrish

In this chapter the cross-section results are reported and compared to several state-of-the-art MC predictions. Where appropriate, the results are put in context of recent comparable ATLAS measurements as well as results from other experiments, the most applicable being those from CMS. For brevity only figures with the absolute cross-section values are reported. Normalised distributions are included as auxiliary material in Appendix A.2.

10.1. Total cross-section

The total $t\bar{t}$ production cross-section at $\sqrt{s} = 13\,\text{TeV}$ in the fiducial phase-space is measured to be:

$$\sigma_{t\bar{t}}^{\text{fid}} = 1.267 \pm 0.005\ (\text{stat.}) \pm 0.053\ (\text{syst.})\ \text{pb},$$

where the first uncertainty is due to the limited number of data events and the second due to the systematic effects outlined in Chapter 9. Comparisons between the measured value and different SM predictions obtained using the MC generator setups outlined in Section 7.1 are shown in Figure 10.1. In this, and all other figures in this section, the label **PWG+PY8** refers to the POWHEG+PYTHIA8 sample, **PWG+H7** to the POWHEG+HERWIG7 sample and **MCatNLO+PY8** to the MC@NLO+PYTHIA8 sample.

All of the included NLO MC samples predict a larger $t\bar{t}$ cross-section than is observed in data. Both the POWHEG+PYTHIA8 and MC@NLO+PYTHIA8 setups produce values more than two standard deviations away from the measured cross-section. In comparison, the POWHEG+HERWIG7 and SHERPA setups are much closer to data indicating that the choice in how additional radiation is treated in simulation is significant.

In this same figure three additional SM predictions are included which attempt to introduce missing NNLO corrections to the existing POWHEG+PYTHIA8, MC@NLO+PYTHIA8, and POWHEG+HERWIG7 predictions. In this way the extent to which NNLO corrections improve the agreement between data and simulation can be evaluated. These samples are produced using a recursive re-weighting approach outlined in Section 7.1.1. It is worth re-iterating that the re-weighted predictions at particle-level are **not** equivalent to fully generated NNLO + parton shower calculations and can only be used to broadly estimate the effect of missing NNLO contributions on the measured observables. However it is observed that the data agreement does improve considerably for each of the three generator setups after applying the NNLO re-weighting. This indicates that the missing NNLO corrections are relevant at the current precision of the measurement.

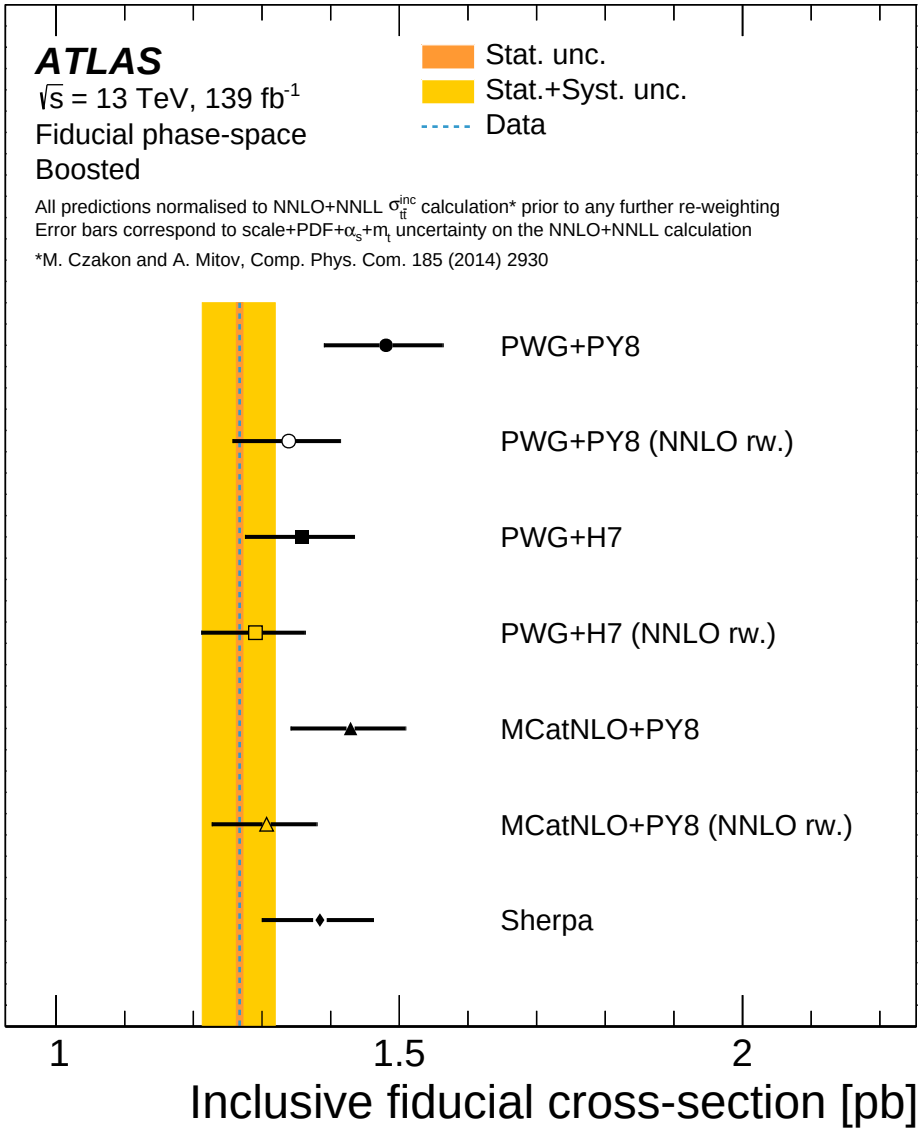

Figure 10.1: The total fiducial cross-section for boosted $t\bar{t}$ production measured at particle-level. Data (dashed line) is compared to several NLO predictions with (open markers) and without (closed markers) the NNLO re-weighting applied. The yellow band represents the total uncertainty on the measured cross-section, while the orange band shows the statistical component. Uncertainties on the markers are the sum in quadrature of theory uncertainties related to the choice of α_S, PDF, m_{top}, and scales in the NNLO + NNLL prediction [105] used to normalise the generated samples.

10.2. Differential cross-sections

To quantify the level of agreement between the measured differential cross-section and the various MC predictions a χ^2 test is used, calculated according to the equation:

$$\chi^2 = V^{\mathrm{T}} C^{-1} V, \tag{10.1}$$

where V is a vector containing the differences between the measured and predicted cross-section in each bin, and C is the covariance matrix for the data. This matrix encodes the expected bin-to-bin correlations induced in the unfolding process due to the presence of statistical and systematic uncertainties. The calculation starts from the statistical covariance matrices for the data and MC samples, both generated using pseudo-experiments as described in Chapter 8. These are summed together with the covariances obtained from unfolding each systematic variation, giving the full covariance matrix. Each systematic uncertainty component represents a correlated effect across the bins and thus the correlation between two bins (ρ_{ij}) is always ± 1. The sign of the correlation is decided based on whether the direction of the uncertainty flips when moving from bin i to j. If both the up and down variations remain the same sign then the bins are taken to be perfectly correlated ($\rho_{ij} = +1$), if both flip sign then the bins are assumed to be perfectly anti-correlated ($\rho_{ij} = -1$), and if only one side experiences a sign flip then the correlation is given by:

$$\rho_{ij} = \mathrm{sign}(\max(|\delta_i^{\mathrm{up}}, \delta_i^{\mathrm{down}}|)) \times \mathrm{sign}(\max(|\delta_j^{\mathrm{up}}, \delta_j^{\mathrm{down}}|)), \tag{10.2}$$

where $\delta_i^{\mathrm{up(down)}}$ is the fractional uncertainty value for the +(-)1σ variation of the given systematic uncertainty in bin i.

To calculate the covariance matrix for each systematic variation applied to data, rather than to the nominal MC, the individual elements of the matrix are given by:

$$C_{ij} = \rho_{ij} \cdot \delta_i \sigma_i \cdot \delta_j \sigma_j, \tag{10.3}$$

where $\delta_{i(j)}$ is the symmetrised ($|\mathrm{up} + \mathrm{down}|/2$) fractional uncertainty value for the given uncertainty in bin $i(j)$, and $\sigma_{i(j)}$ is the measured cross-section in the same bin.

The same method can not be used to obtain the covariance matrix for the normalised spectra as the sign of the uncertainty contributions loses meaning after the values are normalised. Instead the normalised covariance is derived from the absolute covariance matrix using a Cholesky decomposition [186, 187]. This is a matrix operation that can be used to transfer the covariance properties of one matrix to another via a series of un-correlated normal distributions. The absolute covariance is first reduced to lower triangular form using the Cholesky decomposition and then a series of 10,000 Gaussian pseudo-experiments are drawn for each bin in the distribution. Each pseudo-experiment is multiplied by the decomposed absolute covariance, normalised to unity, and then used to calculate the relative covariance.

As the normalised spectra have one less degree of freedom the associated covariance matrix is not invertible. To calculate the χ^2 a single row and column are removed along with the corresponding element in the vector of residuals (V).

Table 10.1 gives the χ^2/NDF and p-values for the NLO + PS and re-weighted NNLO MC predictions versus data for the absolute differential cross-section measurements. As the NLO predicted cross-sections are considerably higher than measured in data the absolute χ^2 agreement between the NLO predictions and data is poor for most observables. The shape agreement is generally better however, as demonstrated by the χ^2/NDF values for the normalised measurements shown in Table 10.2. In general the data agreement is also observed to improve significantly for all three re-weighted samples, indicating that the estimated NNLO predictions provide a closer match to data than predictions generated at NLO.

Tables 10.3 and 10.4 give the absolute and normalised χ^2/NDF and p-values for different POWHEG+PYTHIA8 generator setups with varied shower and ISR settings. Values are also given for the SHERPA setup with both normalisation approaches discussed in Section 7.1.1 included. The column labelled with "NLO norm." uses the default prediction from the SHERPA generator while the column labelled "SHERPA " has distributions normalised to the NNLO + NNLL cross-section calculation.

Table 10.1: χ^2 and p-values to quantify the agreement between the absolute unfolded spectra, several NLO + PS predictions and the respective NNLO re-weighted spectrum.

Observable	PWG+PY8		PWG+PY8(NNLO WEIGHT)		MC@NLO+PY8		MC@NLO+PY8(NNLO WEIGHT)		PWG+H7		PWG+H7(NNLO WEIGHT)	
	χ^2/NDF	p-value	χ^2/NDF	p-value	χ^2/NDF	p-value	χ^2/NDF	p-value	χ^2/NDF	p-value	χ^2/NDF	p-value
$p_{\mathrm{T}}^{t,h}$	26/8	<0.01	5/8	0.79	18/8	0.03	4/8	0.85	7/8	0.56	3/8	0.94
$p_{\mathrm{T}}^{t,\ell}$	78/8	<0.01	28/8	<0.01	144/8	<0.01	10/8	0.27	43/8	<0.01	18/8	0.02
$p_{\mathrm{T}}^{t\bar{t}}$	162/7	<0.01	46/7	<0.01	171/7	<0.01	22/7	<0.01	122/7	<0.01	39/7	<0.01
$H_{\mathrm{T}}^{t\bar{t}+\mathrm{jets}}$	36/7	<0.01	7/7	0.42	17/7	0.02	23/7	<0.01	21/7	<0.01	12/7	0.10
$H_{\mathrm{T}}^{t\bar{t}}$	86/10	<0.01	37/10	<0.01	110/10	<0.01	16/10	0.10	47/10	<0.01	28/10	<0.01
$\lvert y^{t,h}\rvert$	47/17	<0.01	27/17	0.06	37/17	<0.01	23/17	0.15	30/17	0.03	26/17	0.07
$\lvert y^{t,\ell}\rvert$	40/14	<0.01	17/14	0.26	29/14	0.01	12/14	0.58	28/14	0.01	19/14	0.16
$\lvert y^{t\bar{t}}\rvert$	30/10	<0.01	8/10	0.58	23/10	0.01	6/10	0.81	14/10	0.19	7/10	0.74
$m^{t\bar{t}}$	52/10	<0.01	24/10	<0.01	81/10	<0.01	7/10	0.74	29/10	<0.01	22/10	0.02
$p_{\mathrm{T}}^{j,1}$	115/15	<0.01	38/15	<0.01	413/15	<0.01	194/15	<0.01	143/15	<0.01	69/15	<0.01
$p_{\mathrm{T}}^{j,2}$	46/9	<0.01	19/9	0.02	25/9	<0.01	74/9	<0.01	42/9	<0.01	29/9	<0.01
N^j	32/5	<0.01	12/5	0.03	76/5	<0.01	78/5	<0.01	57/5	<0.01	62/5	<0.01
$\Delta\phi(j_1,t_h)$	17/9	0.05	8/9	0.53	150/9	<0.01	80/9	<0.01	42/9	<0.01	30/9	<0.01
$\Delta\phi(j_2,t_h)$	8/9	0.56	5/9	0.84	8/9	0.57	25/9	<0.01	85/9	<0.01	76/9	<0.01
$\Delta\phi(b_\ell,t_h)$	95/13	<0.01	34/13	<0.01	145/13	<0.01	16/13	0.23	52/13	<0.01	25/13	0.02
$\Delta\phi(t_h,t_\ell)$	111/5	<0.01	36/5	<0.01	134/5	<0.01	82/5	<0.01	90/5	<0.01	36/5	<0.01
$\Delta\phi(j_1,j_2)$	24/11	0.01	16/11	0.13	31/11	<0.01	69/11	<0.01	237/11	<0.01	215/11	<0.01
$m(j_1,t_h)$	50/12	<0.01	20/12	0.06	221/12	<0.01	48/12	<0.01	41/12	<0.01	19/12	0.08
$p_{\mathrm{T}}^{j,1}$ vs N^j	355/21	<0.01	205/21	<0.01	633/21	<0.01	316/21	<0.01	263/21	<0.01	159/21	<0.01
$p_{\mathrm{T}}^{j,1}$ vs $p_{\mathrm{T}}^{t,h}$	115/17	<0.01	53/17	<0.01	383/17	<0.01	152/17	<0.01	121/17	<0.01	74/17	<0.01
$\Delta\phi(j_1,t_h)$ vs $p_{\mathrm{T}}^{t,h}$	69/21	<0.01	43/21	<0.01	427/21	<0.01	223/21	<0.01	78/21	<0.01	60/21	<0.01
$\Delta\phi(j_1,t_h)$ vs N^j	109/19	<0.01	64/19	<0.01	545/19	<0.01	250/19	<0.01	85/19	<0.01	60/19	<0.01

Table 10.2: χ^2 and p-values to quantify the agreement between the normalised unfolded spectra, several NLO + PS predictions and the respective NNLO re-weighted spectrum.

Observable	PWG+PY8		PWG+PY8(NNLO WEIGHT)		MC@NLO+PY8		MC@NLO+PY8(NNLO WEIGHT)		PWG+H7		PWG+H7(NNLO WEIGHT)	
	χ^2/NDF	p-value	χ^2/NDF	p-value	χ^2/NDF	p-value	χ^2/NDF	p-value	χ^2/NDF	p-value	χ^2/NDF	p-value
$p_{\mathrm{T}}^{t,h}$	3/7	0.84	2/7	0.95	3/7	0.85	3/7	0.89	3/7	0.90	3/7	0.92
$p_{\mathrm{T}}^{t,\ell}$	24/7	<0.01	15/7	0.03	76/7	<0.01	7/7	0.39	24/7	<0.01	13/7	0.07
$p_{\mathrm{T}}^{t\bar{t}}$	95/6	<0.01	34/6	<0.01	109/6	<0.01	20/6	<0.01	96/6	<0.01	35/6	<0.01
$H_{\mathrm{T}}^{t\bar{t}+\mathrm{jets}}$	9/6	0.17	4/6	0.71	5/6	0.57	21/6	<0.01	14/6	0.03	11/6	0.08
$H_{\mathrm{T}}^{t\bar{t}}$	39/9	<0.01	28/9	<0.01	63/9	<0.01	13/9	0.14	33/9	<0.01	26/9	<0.01
$\lvert y^{t,h}\rvert$	21/16	0.18	23/16	0.12	21/16	0.20	21/16	0.17	23/16	0.10	25/16	0.06
$\lvert y^{t,\ell}\rvert$	14/13	0.40	13/13	0.44	12/13	0.50	11/13	0.63	20/13	0.09	18/13	0.16
$\lvert y^{t\bar{t}}\rvert$	7/9	0.61	6/9	0.77	8/9	0.51	5/9	0.85	8/9	0.51	6/9	0.72
$m^{t\bar{t}}$	18/9	0.03	19/9	0.02	51/9	<0.01	6/9	0.74	20/9	0.02	21/9	0.01
$p_{\mathrm{T}}^{j,1}$	84/14	<0.01	35/14	<0.01	318/14	<0.01	168/14	<0.01	125/14	<0.01	65/14	<0.01
$p_{\mathrm{T}}^{j,2}$	29/8	<0.01	18/8	0.02	20/8	<0.01	51/8	<0.01	37/8	<0.01	28/8	<0.01
N^j	7/4	0.12	8/4	0.08	48/4	<0.01	72/4	<0.01	47/4	<0.01	58/4	<0.01
$\Delta\phi(j_1,t_h)$	9/8	0.32	7/8	0.51	113/8	<0.01	68/8	<0.01	37/8	<0.01	29/8	<0.01
$\Delta\phi(j_2,t_h)$	5/8	0.78	5/8	0.80	6/8	0.67	15/8	0.06	67/8	<0.01	61/8	<0.01
$\Delta\phi(b_\ell,t_h)$	35/12	<0.01	21/12	0.06	92/12	<0.01	13/12	0.35	32/12	<0.01	19/12	0.08
$\Delta\phi(t_h,t_\ell)$	62/4	<0.01	28/4	<0.01	74/4	<0.01	76/4	<0.01	71/4	<0.01	33/4	<0.01
$\Delta\phi(j_1,j_2)$	16/10	0.11	16/10	0.10	26/10	<0.01	51/10	<0.01	197/10	<0.01	186/10	<0.01
$m(j_1,t_h)$	30/11	<0.01	19/11	0.06	166/11	<0.01	34/11	<0.01	34/11	<0.01	18/11	0.07
$p_{\mathrm{T}}^{j,1}$ vs N^j	261/20	<0.01	194/20	<0.01	470/20	<0.01	273/20	<0.01	231/20	<0.01	154/20	<0.01
$p_{\mathrm{T}}^{j,1}$ vs $p_{\mathrm{T}}^{t,h}$	80/16	<0.01	50/16	<0.01	291/16	<0.01	127/16	<0.01	105/16	<0.01	71/16	<0.01
$\Delta\phi(j_1,t_h)$ vs $p_{\mathrm{T}}^{t,h}$	48/20	<0.01	39/20	<0.01	333/20	<0.01	196/20	<0.01	68/20	<0.01	56/20	<0.01
$\Delta\phi(j_1,t_h)$ vs N^j	68/18	<0.01	58/18	<0.01	404/18	<0.01	210/18	<0.01	73/18	<0.01	58/18	<0.01

Table 10.3: χ^2 and p-values to quantify the agreement between the absolute unfolded spectra and several NLO + PS predictions.

Observable	PWG+PY8		PWG+PY8(ISR Down)		PWG+PY8(ISR Up)		PWG+PY8(h_{damp}=3.0 m_t)		SHERPA		SHERPA (NLO norm.)	
	χ^2/NDF	p-value	χ^2/NDF	p-value	χ^2/NDF	p-value	χ^2/NDF	p-value	χ^2/NDF	p-value	χ^2/NDF	p-value
$p_{\text{T}}^{t,h}$	26/8	<0.01	26/8	<0.01	25/8	<0.01	36/8	<0.01	12/8	0.15	11/8	0.19
$p_{\text{T}}^{t,\ell}$	78/8	<0.01	144/8	<0.01	20/8	0.01	50/8	<0.01	12/8	0.13	11/8	0.22
$p_{\text{T}}^{t\bar{t}}$	162/7	<0.01	243/7	<0.01	340/7	<0.01	108/7	<0.01	70/7	<0.01	57/7	<0.01
$H_{\text{T}}^{t\bar{t}+\text{jets}}$	36/7	<0.01	38/7	<0.01	96/7	<0.01	52/7	<0.01	39/7	<0.01	34/7	<0.01
$H_{\text{T}}^{t\bar{t}}$	86/10	<0.01	119/10	<0.01	46/10	<0.01	72/10	<0.01	28/10	<0.01	22/10	0.01
$\lvert y^{t,h}\rvert$	47/17	<0.01	46/17	<0.01	46/17	<0.01	55/17	<0.01	25/17	0.10	20/17	0.29
$\lvert y^{t,\ell}\rvert$	40/14	<0.01	45/14	<0.01	34/14	<0.01	45/14	<0.01	24/14	0.05	18/14	0.19
$\lvert y^{t\bar{t}}\rvert$	30/10	<0.01	32/10	<0.01	23/10	<0.01	35/10	<0.01	22/10	0.02	20/10	0.03
$m^{t\bar{t}}$	52/10	<0.01	78/10	<0.01	75/10	<0.01	53/10	<0.01	31/10	<0.01	25/10	<0.01
$p_{\text{T}}^{j,1}$	115/15	<0.01	136/15	<0.01	272/15	<0.01	74/15	<0.01	140/15	<0.01	98/15	<0.01
$p_{\text{T}}^{j,2}$	46/9	<0.01	12/9	0.23	196/9	<0.01	81/9	<0.01	41/9	<0.01	19/9	0.02
N^j	32/5	<0.01	51/5	<0.01	27/5	<0.01	41/5	<0.01	23/5	<0.01	16/5	<0.01
$\Delta\phi(j_1, t_h)$	17/9	0.05	34/9	<0.01	22/9	<0.01	23/9	<0.01	10/9	0.38	11/9	0.25
$\Delta\phi(j_2, t_h)$	8/9	0.56	7/9	0.67	22/9	0.01	19/9	0.03	6/9	0.74	3/9	0.96
$\Delta\phi(b_\ell, t_h)$	95/13	<0.01	116/13	<0.01	294/13	<0.01	119/13	<0.01	51/13	<0.01	28/13	0.01
$\Delta\phi(t_h, t_\ell)$	111/5	<0.01	164/5	<0.01	207/5	<0.01	79/5	<0.01	36/5	<0.01	39/5	<0.01
$\Delta\phi(j_1, j_2)$	24/11	0.01	17/11	0.12	41/11	<0.01	38/11	<0.01	26/11	<0.01	20/11	0.05
$m(j_1, t_h)$	50/12	<0.01	111/12	<0.01	93/12	<0.01	43/12	<0.01	65/12	<0.01	40/12	<0.01
$p_{\text{T}}^{j,1}$ vs N^j	355/21	<0.01	495/21	<0.01	488/21	<0.01	254/21	<0.01	193/21	<0.01	137/21	<0.01
$p_{\text{T}}^{j,1}$ vs $p_{\text{T}}^{t,h}$	115/17	<0.01	192/17	<0.01	256/17	<0.01	87/17	<0.01	133/17	<0.01	87/17	<0.01
$\Delta\phi(j_1, t_h)$ vs $p_{\text{T}}^{t,h}$	69/21	<0.01	104/21	<0.01	56/21	<0.01	73/21	<0.01	42/21	<0.01	32/21	0.06
$\Delta\phi(j_1, t_h)$ vs N^j	109/19	<0.01	201/19	<0.01	66/19	<0.01	91/19	<0.01	35/19	0.01	26/19	0.14

Table 10.4: χ^2 and p-values to quantify the agreement between the normalised unfolded spectra and several NLO + PS predictions.

Observable	PWG+PY8		PWG+PY8(ISR Down)		PWG+PY8(ISR Up)		PWG+PY8(h_{damp}=3.0 m_t)		SHERPA		SHERPA (NLO norm.)	
	χ^2/NDF	p-value	χ^2/NDF	p-value	χ^2/NDF	p-value	χ^2/NDF	p-value	χ^2/NDF	p-value	χ^2/NDF	p-value
$p_{\text{T}}^{t,h}$	3/7	0.84	3/7	0.90	6/7	0.57	5/7	0.63	5/7	0.69	5/7	0.69
$p_{\text{T}}^{t,\ell}$	24/7	<0.01	57/7	<0.01	2/7	0.95	8/7	0.33	4/7	0.73	4/7	0.73
$p_{\text{T}}^{t\bar{t}}$	95/6	<0.01	133/6	<0.01	258/6	<0.01	59/6	<0.01	57/6	<0.01	57/6	<0.01
$H_{\text{T}}^{t\bar{t}+\text{jets}}$	9/6	0.17	4/6	0.69	64/6	<0.01	20/6	<0.01	28/6	<0.01	28/6	<0.01
$H_{\text{T}}^{t\bar{t}}$	39/9	<0.01	57/9	<0.01	22/9	0.01	26/9	<0.01	18/9	0.03	18/9	0.03
$\lvert y^{t,h}\rvert$	21/16	0.18	20/16	0.24	23/16	0.10	20/16	0.20	15/16	0.51	15/16	0.51
$\lvert y^{t,\ell}\rvert$	14/13	0.40	16/13	0.23	13/13	0.44	11/13	0.65	14/13	0.37	14/13	0.37
$\lvert y^{t\bar{t}}\rvert$	7/9	0.61	9/9	0.45	5/9	0.80	5/9	0.81	14/9	0.13	14/9	0.13
$m^{t\bar{t}}$	18/9	0.03	32/9	<0.01	43/9	<0.01	16/9	0.07	21/9	0.01	21/9	0.01
$p_{\text{T}}^{j,1}$	84/14	<0.01	108/14	<0.01	187/14	<0.01	37/14	<0.01	113/14	<0.01	113/14	<0.01
$p_{\text{T}}^{j,2}$	29/8	<0.01	11/8	0.21	96/8	<0.01	32/8	<0.01	23/8	<0.01	23/8	<0.01
N^j	7/4	0.12	16/4	<0.01	12/4	0.01	12/4	0.02	13/4	0.01	13/4	0.01
$\Delta\phi(j_1, t_h)$	9/8	0.32	27/8	<0.01	4/8	0.86	4/8	0.82	4/8	0.85	4/8	0.85
$\Delta\phi(j_2, t_h)$	5/8	0.78	6/8	0.64	6/8	0.69	6/8	0.63	1/8	1.00	1/8	1.00
$\Delta\phi(b_\ell, t_h)$	35/12	<0.01	48/12	<0.01	192/12	<0.01	46/12	<0.01	29/12	<0.01	29/12	<0.01
$\Delta\phi(t_h, t_\ell)$	62/4	<0.01	76/4	<0.01	156/4	<0.01	41/4	<0.01	29/4	<0.01	29/4	<0.01
$\Delta\phi(j_1, j_2)$	16/10	0.11	15/10	0.13	18/10	0.06	16/10	0.11	19/10	0.04	19/10	0.04
$m(j_1, t_h)$	30/11	<0.01	88/11	<0.01	46/11	<0.01	11/11	0.44	45/11	<0.01	45/11	<0.01
$p_{\text{T}}^{j,1}$ vs N^j	261/20	<0.01	379/20	<0.01	363/20	<0.01	161/20	<0.01	161/20	<0.01	161/20	<0.01
$p_{\text{T}}^{j,1}$ vs $p_{\text{T}}^{t,h}$	80/16	<0.01	151/16	<0.01	170/16	<0.01	42/16	<0.01	103/16	<0.01	103/16	<0.01
$\Delta\phi(j_1, t_h)$ vs $p_{\text{T}}^{t,h}$	48/20	<0.01	82/20	<0.01	27/20	0.13	37/20	0.01	30/20	0.07	30/20	0.07
$\Delta\phi(j_1, t_h)$ vs N^j	68/18	<0.01	146/18	<0.01	36/18	<0.01	40/18	<0.01	23/18	0.18	23/18	0.18

10.2.1. Observables related to $t\bar{t}$ kinematics

Figures 10.2–5 show measured differential cross-section results for the variables related to kinematics of the two top-quarks. For these variables the unfolded measurements are compared to the NLO and re-weighted NNLO generator setups. In each figure the panel on the bottom shows the ratio between the predictions and the data.

The p_{T} distributions of the hadronically and leptonically decaying top-quarks in Figures 10.2a and 10.2b respectively, as well as the $H_{\mathrm{T}}^{t\bar{t}}$ distribution in Figure 10.3a are all observed to be softer (lower p_{T}) in data than in simulation. This trend is in line with previous results in similar phase-spaces from ATLAS [122–124], and CMS [125, 126, 129] and results in simulation consistently predicting more events than data. This difference is believed to originate from missing higher order corrections in the NLO predictions and indeed the data agreement is seen to improve considerably when re-weighting the MC predictions to NNLO, in-line with the inclusive cross-section result. After re-weighting to NNLO the predictions for the $p_{\mathrm{T}}^{t,\ell}$ distribution still display significant differences in shape compared to data. It is possible this effect may originate from mis-modelling of the the p_{T} of the $t\bar{t}$ system as the two variables are partially anti-correlated ($\rho(p_{\mathrm{T}}^{t,\ell}, p_{\mathrm{T}}^{t\bar{t}}) = -0.55$). This anti-correlation is expected due to requiring a minimum cut of 355 GeV on the p_{T} of the hadronic top-quark in the event selection but not imposing a similar lower bound on the leptonic top-quark.

Figure 10.3b shows the cross-section versus $m^{t\bar{t}}$ distribution, again comparing to NLO and NNLO predictions, and shows generally poor agreement for all three NLO predictions around the peak values. The re-weighting results in better agreement with the improvement most significant for the MC@NLO+PYTHIA8 prediction. The $\Delta\phi(b_\ell, t_h)$ distribution in Figure 10.4a also shows an improvement from the NNLO re-weighting especially at the extreme values. The rapidity distributions for the $t\bar{t}$ system and the two individual top-quarks are shown in Figures 10.4b and 10.5 respectively. Generally good shape agreement is observed between data and each prediction.

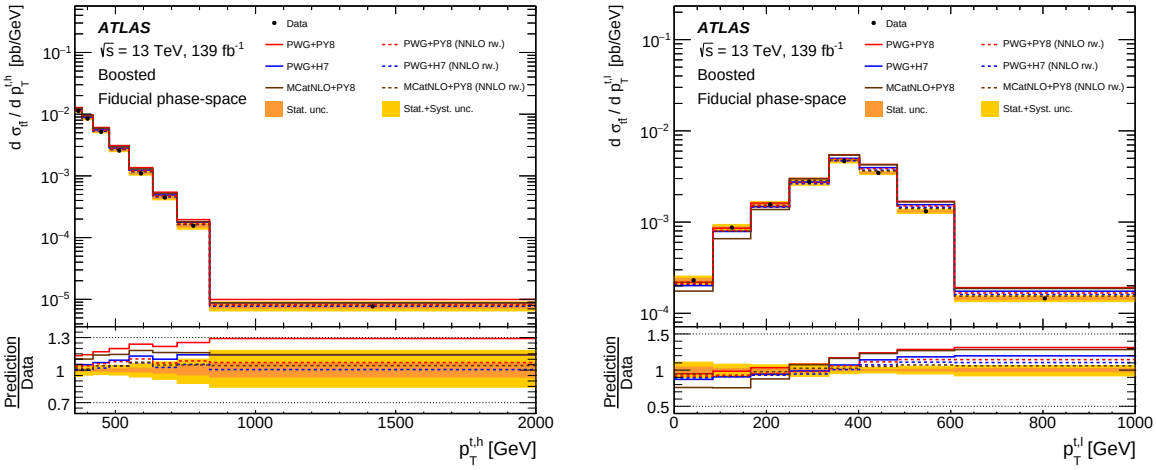

(a) **(b)**

Figure 10.2: Fiducial $t\bar{t}$ cross-section measured as a function of (a) $p_{\mathrm{T}}^{t,h}$ and (b) $p_{\mathrm{T}}^{t,\ell}$. Measured results are compared to SM predictions from various NLO generators with (dashed lines) and without (solid lines) the NNLO re-weighting applied. The yellow band shows the size of the total uncertainty in each bin, while the orange band shows the statistical uncertainty only. The lower panel displays the ratios between the different predictions and data.

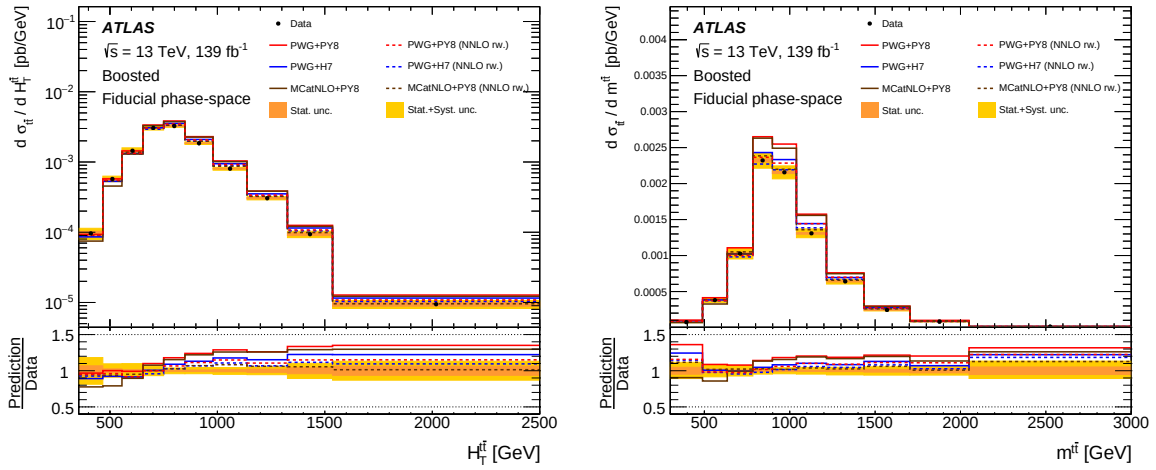

(a) **(b)**

Figure 10.3: Fiducial $t\bar{t}$ cross-section measured as a function of (a) $H_{\mathrm{T}}^{t\bar{t}}$ and (b) $m^{t\bar{t}}$. Measured results are compared to SM predictions from various NLO generators with (dashed lines) and without (solid lines) the NNLO re-weighting applied. The yellow band shows the size of the total uncertainty in each bin, while the orange band shows the statistical uncertainty only. The lower panel displays the ratios between the different predictions and data.

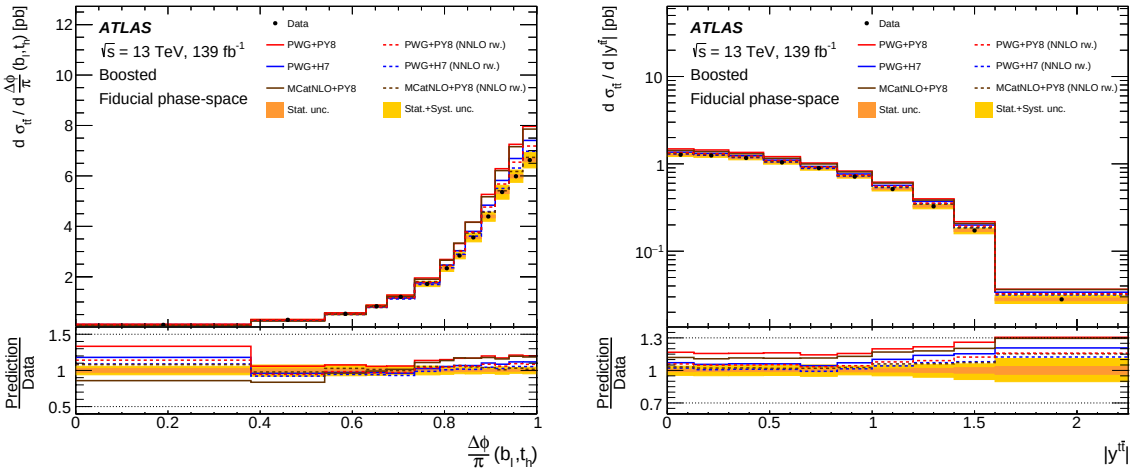

Figure 10.4: Fiducial $t\bar{t}$ cross-section measured as a function of (a) $\Delta\phi(b_\ell, t_h)$ and (b) $|y^{t\bar{t}}|$. Measured results are compared to SM predictions from various NLO generators with (dashed lines) and without (solid lines) the NNLO re-weighting applied. The yellow band shows the size of the total uncertainty in each bin, while the orange band shows the statistical uncertainty only. The lower panel displays the ratios between the different predictions and data.

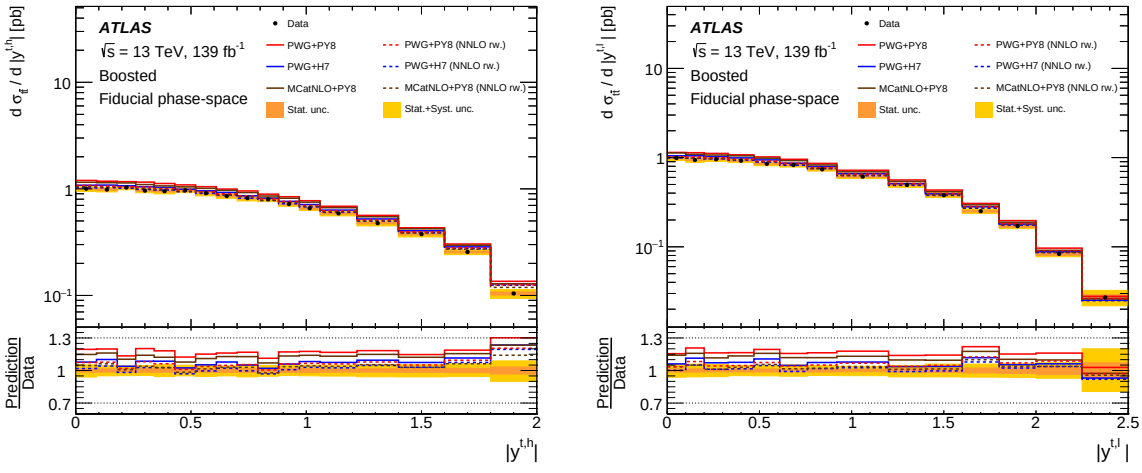

Figure 10.5: Fiducial $t\bar{t}$ cross-section measured as a function of (a) $|y^{t,h}|$ and (b) $|y^{t,\ell}|$. Measured results are compared to SM predictions from various NLO generators with (dashed lines) and without (solid lines) the NNLO re-weighting applied. The yellow band shows the size of the total uncertainty in each bin, while the orange band shows the statistical uncertainty only. The lower panel displays the ratios between the different predictions and data.

10.2.2. Observables related to additional radiation

Figures 10.6–9 show the particle-level $t\bar{t}$ cross-section as functions of variables related to additional radiation in the events. The unfolded measurements are compared to SM predictions from different NLO + PS generator setups with variations in shower settings and ISR. Comparisons are also included for the SHERPA generator which allows the effect of generating additional radiation in the matrix-element calculation to be studied. In each figure the upper ratio panel compares the different generator setups to the data, while the bottom panel compares variations in the shower settings.

Overall none of the generator setups tested were able to provide a good description of the observed distributions for all measured variables. Figure 10.6a shows the cross-section as a function of the number of additional jets in each event for which the SHERPA sample is found to exhibit the best shape agreement over the full range. This demonstrates that the inclusion of additional emissions within the matrix-element calculation results in improved modelling of the amount of additional radiation in boosted events. However the modelling of the kinematic properties of additional radiation, as shown in Figures 10.6b, 10.7a and 10.7b, do not exhibit consistently better results for the SHERPA sample. Worse agreement is observed for both the $m(j_1, t_h)$ and leading additional jet p_{T} distributions, while performance is in-line with other generators for modelling of the sub-leading additional jet p_{T} and the angular variables in Figure 10.8.

The complexity of accurately modelling additional radiation in highly boosted events is best illustrated by the leading and sub-leading additional jet p_{T} distributions in Figure 10.7. Poor agreement with data is observed for all generator setups when modelling the p_{T} of the leading additional jet with the shape of the MC@NLO+PYTHIA8 prediction significantly different from both data and POWHEG+PYTHIA8. This is an indication that at the current level of precision the choice of technique to match the matrix-element calculation and parton shower simulation is very relevant.

In general the sub-leading additional jet p_{T} distribution appears to be better modelled, especially at low values, with the POWHEG+PYTHIA8 variation with reduced ISR giving reasonable shape agreement with data. However Table 10.3 shows this same sample has worse agreement for the leading additional jet p_{T} when compared to the POWHEG+PYTHIA8 sample with nominal ISR settings suggesting that the source of the observed mis-modelling is not easily explained by a single factor.

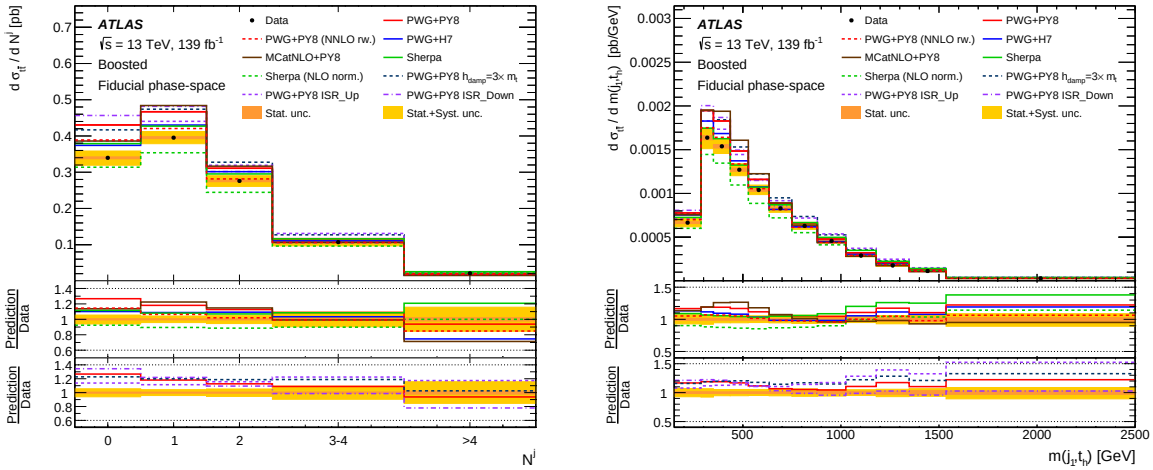

(a) **(b)**

Figure 10.6: Fiducial $t\bar{t}$ cross-section measured as a function of (a) N^j and (b) $m(j_1, t_h)$. Measured results are compared to SM predictions from various NLO + PS generator setups with different shower and radiation settings. The yellow band shows the size of the total uncertainty in each bin, while the orange band shows the statistical uncertainty only. The two lower panels display the ratios between the different predictions and data.

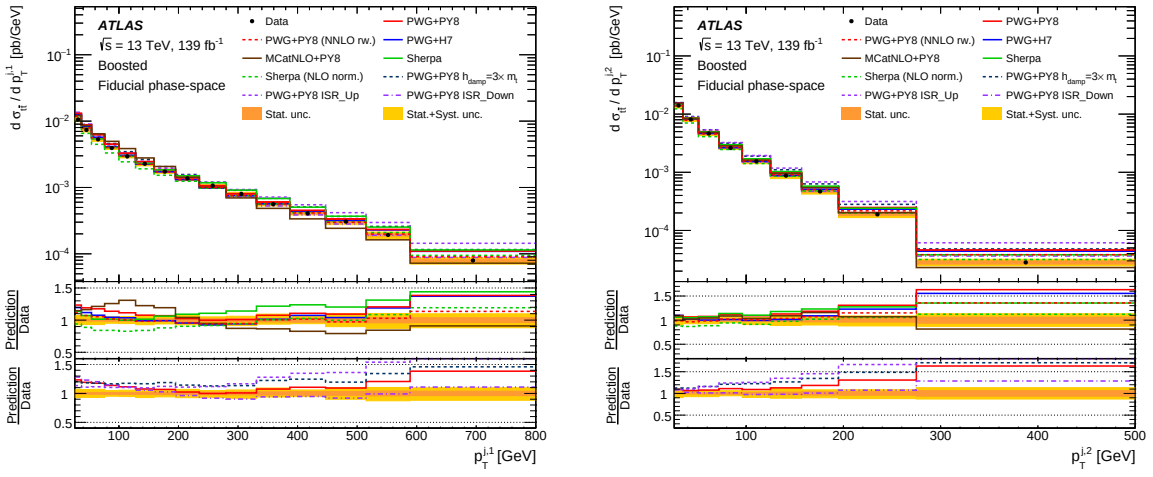

(a) **(b)**

Figure 10.7: Fiducial $t\bar{t}$ cross-section measured as a function of (a) $p_{\mathrm{T}}^{j,1}$ and (b) $p_{\mathrm{T}}^{j,2}$. Measured results are compared to SM predictions from various NLO + PS generator setups with different shower and radiation settings. The yellow band shows the size of the total uncertainty in each bin, while the orange band shows the statistical uncertainty only. The two lower panels display the ratios between the different predictions and data.

Figure 10.8 show a selection of angular variables between the leading and subleading additional jets and the hadronic top-quark. In general these distributions are better modelled than the individual kinematics however there are still large disagreements between data and prediction. In particular the shape of the MC@NLO+PYTHIA8 prediction for the $\Delta\phi(j_1, t_h)$ distribution, and the POWHEG+HERWIG7 predictions for the $\Delta\phi(j_2, t_h)$ and $\Delta\phi(j_1, j_2)$ distributions are noticeably different from both the data and the nominal POWHEG sample. The latter two are likely related to the difference in shower ordering between HERWIG7 (angular ordering) and PYTHIA8 (p_{T} ordering).

Lastly, Figure 10.9 shows kinematics of the $t\bar{t}$ system that are directly affected by the presence of additional radiation. None of the generator setups are able reproduce the data distribution accurately, with the SHERPA sample providing the best agreement with data in each case.

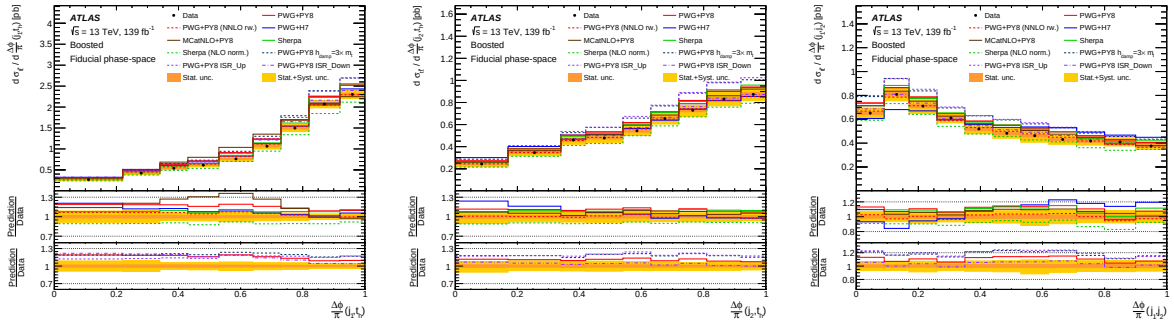

(a) **(b)** **(c)**

Figure 10.8: Fiducial $t\bar{t}$ cross-section measured as a function of (a) $\Delta\phi(j_1, t_h)$, (b) $\Delta\phi(j_2, t_h)$, and (c) $\Delta\phi(j_1, j_2)$. Measured results are compared to SM predictions from various NLO + PS generator setups with different shower and radiation settings. The yellow band shows the size of the total uncertainty in each bin, while the orange band shows the statistical uncertainty only. The two lower panels display the ratios between the different predictions and data.

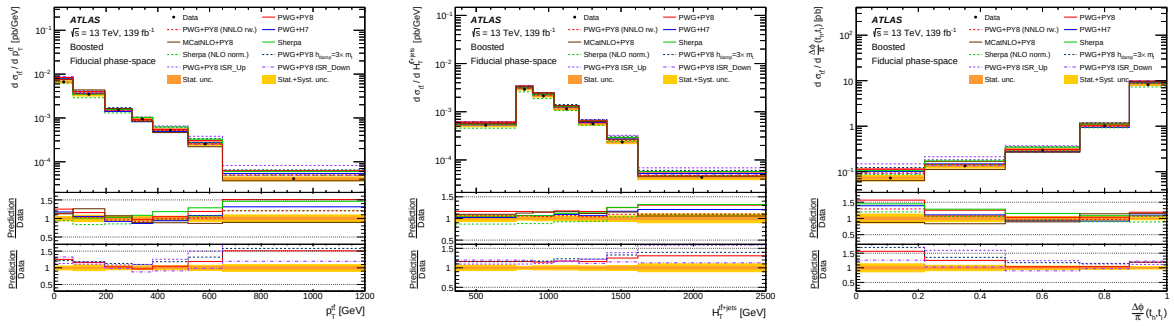

(a) **(b)** **(c)**

Figure 10.9: Fiducial $t\bar{t}$ cross-section measured as a function of (a) $p_{\mathrm{T}}^{t\bar{t}}$, (b) $H_{\mathrm{T}}^{t\bar{t}+\mathrm{jets}}$, and (c) $\Delta\phi(t_h, t_\ell)$. Measured results are compared to SM predictions from various NLO + PS generator setups with different shower and radiation settings. The yellow band shows the size of the total uncertainty in each bin, while the orange band shows the statistical uncertainty only. The two lower panels display the ratios between the different predictions and data.

10.2.3. Double-differential cross-sections

The double-differential cross-section measurements are shown in Figures 10.10–13. Figures 10.10 and 10.11 show the $\Delta\phi(j_1, t_h)$ and $p_{\mathrm{T}}^{j,1}$ distributions versus the p_{T} of the hadronic top-quark. In events with a high p_{T} hadronic top-quark ($p_{\mathrm{T}}^{t,h} > 500\,\mathrm{GeV}$) the modelling of the $\Delta\phi(j_1, t_h)$ distribution is observed to be worse overall. Similarly the modelling of the leading additional jet at low p_{T} is observed to be less accurate for events with $p_{\mathrm{T}}^{t,h} > 500\,\mathrm{GeV}$. These observations hold for all tested predictions apart from the NLO normalised SHERPA sample, which appears to have improved agreement in both cases.

Figures 10.12 and 10.13 show the $\Delta\phi(j_1, t_h)$ and $p_{\mathrm{T}}^{j,1}$ distributions versus the number of additional jets. For events with one or two additional jets the $\Delta\phi(j_1, t_h)$ distribution is better described at high values of $\Delta\phi$ (more back-to-back). However in events with more than two additional emissions the opposite is true; the angular modelling is improved significantly at low values of $\Delta\phi$ (more collinear), but gets worse at higher values. This effect is especially prominent for the NLO generators.

The modelling of low-p_{T} additional jets is observed to be less accurate in events with only one additional emission. Conversely the modelling of high-p_{T} additional radiation disagrees more strongly with data in events with more than one additional jet. Additionally Figure 10.13 suggests that the previously observed mis-modelling of the p_{T} of the leading additional jet by the MC@NLO+PYTHIA8 generator is mostly driven by events with a single additional jet. It should be noted that probing exclusive jet bins in this way is a particular challenge for generators at NLO precision due to the complexities in accurately matching real emissions from the ME to those generated in the parton-shower. It is thus expected that generators with higher-order matrix-element precision matched to a parton-shower would likely see improved agreement for variables like these.

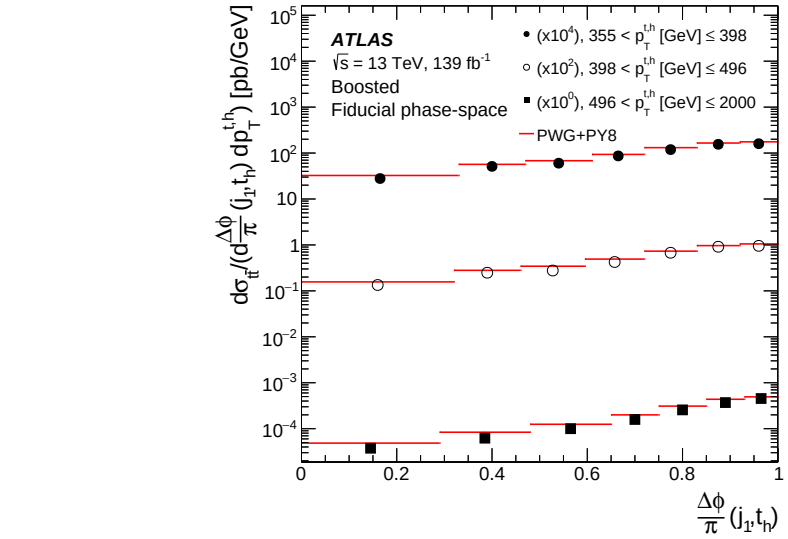

(a)

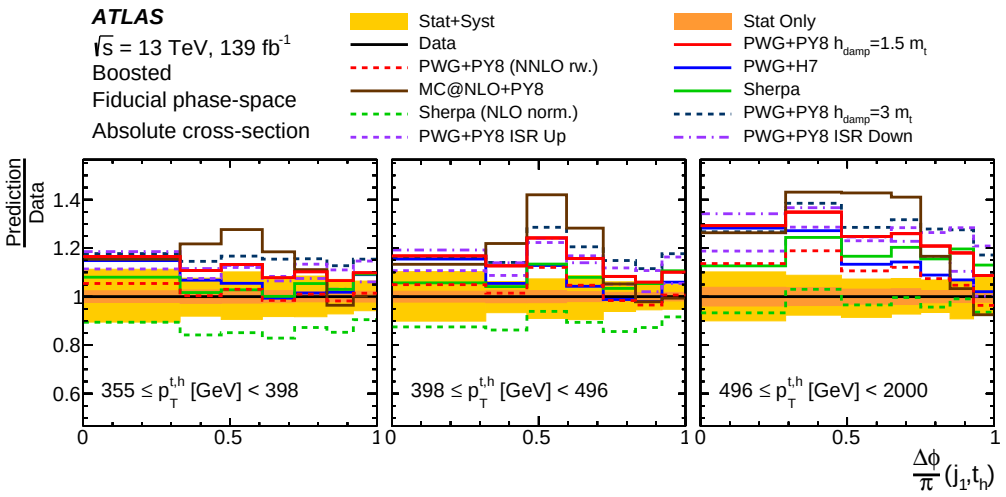

(b)

Figure 10.10: Double-differential fiducial cross-section measurement as a function of $\Delta\phi(j_1, t_h)$ in bins of $p_{\mathrm{T}}^{t,h}$.
(a) Measured differential cross-section compared directly with predictions from the POWHEG+PYTHIA8 MC event generator. The measurement and predictions are normalised by the factors shown in parentheses to aid visibility.
(b) The ratio of the measured absolute cross-section to different NLO + PS and re-weighted NNLO SM predictions. The yellow band shows the size of the total uncertainty, while the orange band shows the statistical uncertainty only.

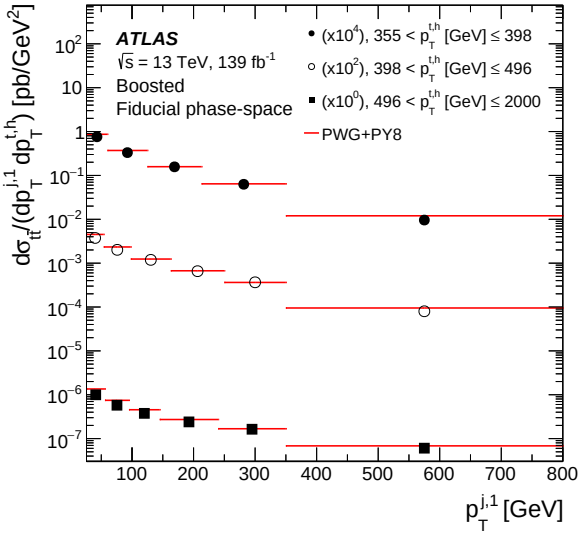

(a)

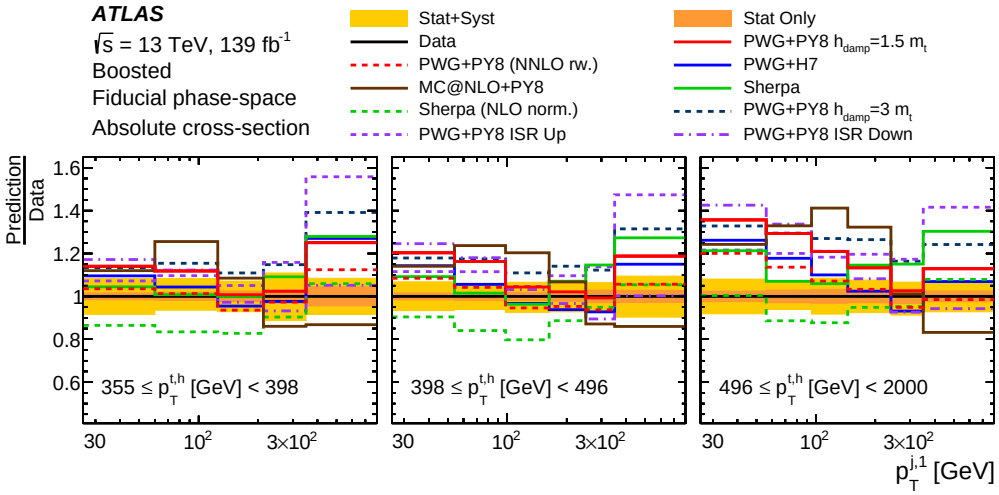

(b)

Figure 10.11: Double-differential cross-section measurement as a function of $p_{\mathrm{T}}^{j,1}$ in bins of $p_{\mathrm{T}}^{t,h}$.
(a) Measured differential cross-section compared directly with predictions from the POWHEG+PYTHIA8 MC event generator. The measurement and predictions are normalised by the factors shown in parentheses to aid visibility.
(b) The ratio of the measured absolute cross-section to different NLO + PS and re-weighted NNLO SM predictions. The yellow band shows the size of the total uncertainty, while the orange band shows the statistical uncertainty only.

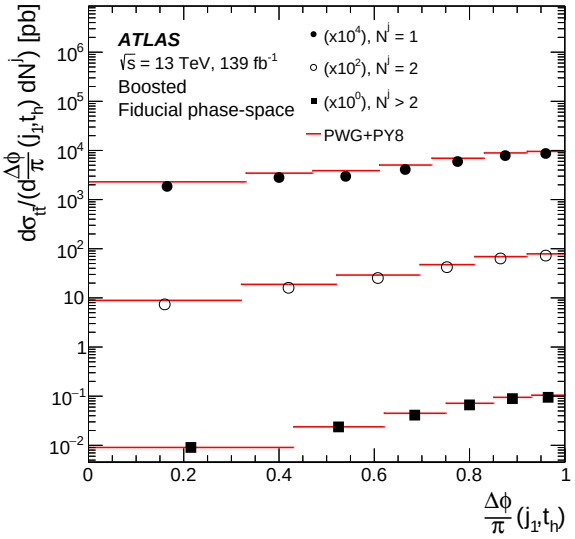

(a)

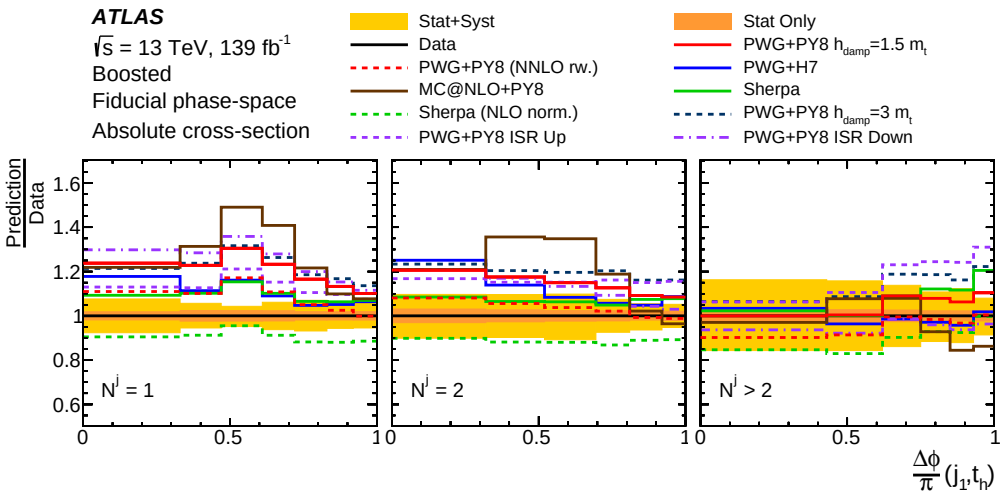

(b)

Figure 10.12: Double-differential cross-section measurement as a function of $\Delta\phi(j_1, t_h)$ in bins of N^j.
(a) Measured differential cross-section compared directly with predictions from the POWHEG+PYTHIA8 MC event generator. The measurement and predictions are normalised by the factors shown in parentheses to aid visibility.
(b) The ratio of the measured absolute cross-section to different NLO + PS and re-weighted NNLO SM predictions. The yellow band shows the size of the total uncertainty, while the orange band shows the statistical uncertainty only.

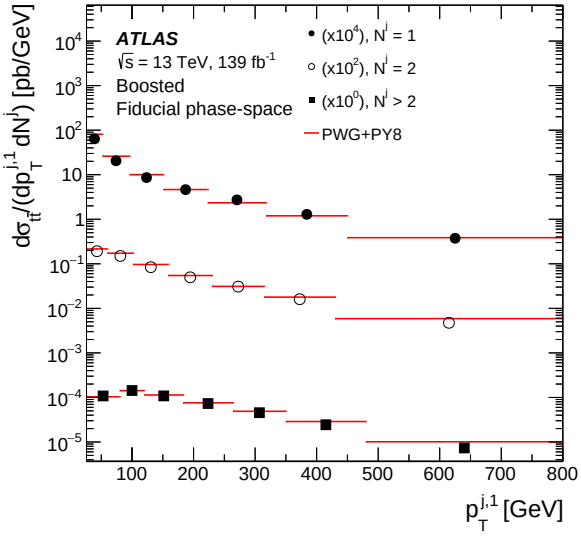

(a)

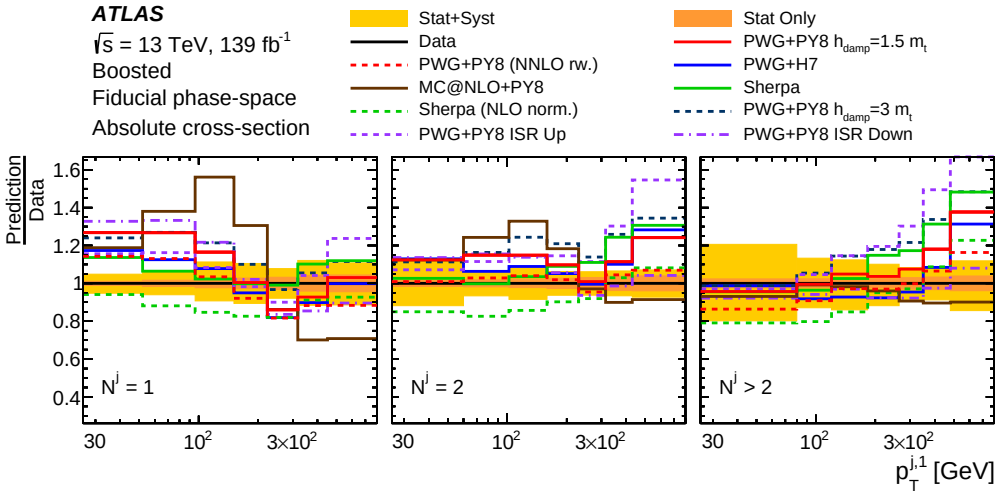

(b)

Figure 10.13: Double-differential cross-section measurement as a function of $p_{\mathrm{T}}^{j,1}$ in bins of N^j. (a) Measured differential cross-section compared directly with predictions from the POWHEG+PYTHIA8 MC event generator. The measurement and predictions are normalised by the factors shown in parentheses to aid visibility. (b) The ratio of the measured absolute cross-section to different NLO + PS and re-weighted NNLO SM predictions. The yellow band shows the size of the total uncertainty, while the orange band shows the statistical uncertainty only.

10.3. Comparison to other measurements

The previous ATLAS measurement of the $t\bar{t}$ cross-section at high energies [124] used a different definition of the fiducial volume, thus the measured cross-sections cannot be compared directly to the values reported here. However the ratio of the measured inclusive fiducial cross-section over the POWHEG+PYTHIA8 SM prediction can be compared. The ratio is $\sigma_{t\bar{t}}^{\text{fid}}/\sigma_{t\bar{t}}^{\text{SM}} = 0.856 \pm 0.036$, which is in agreement with the previous result of $\sigma_{t\bar{t}}^{\text{fid}}/\sigma_{t\bar{t}}^{\text{SM}} = 0.905 \pm 0.071$. The observed improvement in precision from 7.9% to 4.2% is significant. The differential measurement precision is also greatly improved over the previous boosted measurement as shown in Figure 10.14 which compares the fractional uncertainty breakdown for the p_{T} of the hadronic top-quark between the two measurements. The bulk of the improvement originates from reductions in the JES uncertainty, outlined in Section 9.5, and the reduction of large background uncertainties at high top-quark p_{T} outlined in Section 9.3.2. Increased statistics, improved signal purity due to requiring two b-tagged jets instead of one, and improvements to object definition and modelling predictions also contribute.

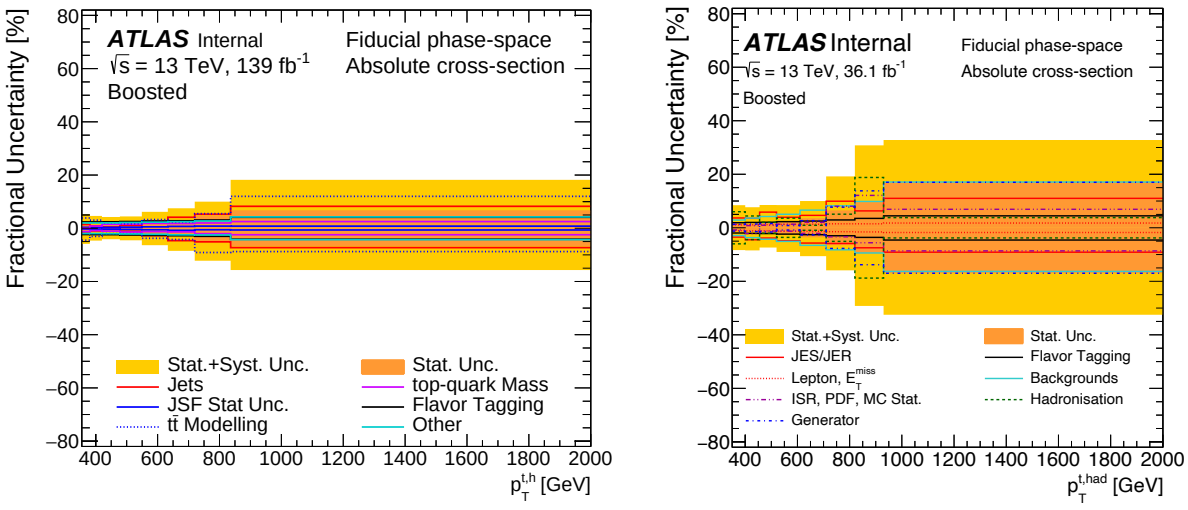

(a) **(b)**

Figure 10.14: Fractional uncertainties on the particle-level cross-section as a function of the p_{T} of the hadronic top-quark for (a) this measurement, (b) the preceding ATLAS $t\bar{t}$ measurement [124]. In the previous result the top-quark mass uncertainty is not included, the "Jets" uncertainty is labelled "JES/JER", and the "$t\bar{t}$ Modelling" uncertainty is split into "Generator", "Hadronisation", "ISR" and "PDF" effects. The "Other" category of the current analysis includes "Backgrounds", "Lepton", "$E_{\text{T}}^{\text{miss}}$" and "MC Stat." error as well as luminosity and pileup uncertainties which are only included in the total uncertainty band of the previous result.

The combination of decay channels and alternative phase-space definitions used in related CMS analyses at $\sqrt{s} = 13\,\text{TeV}$ make it difficult for direct comparisons. The closest equivalent is a measurement of the $t\bar{t}$ production cross-section at particle-level performed using $137\,\text{fb}^{-1}$ of data and without imposing a lower limit on the top-quark p_T [126]. Figure 10.15 shows a comparison of the measured cross-sections as a function of the p_T of the hadronic top-quark between the analysis presented here and the CMS result. Even in the region above 355 GeV the results are not fully comparable due to differences in the event selection, however the disagreement between data and prediction is at a similar level and the softer overall p_T spectrum of simulation compared to data can be observed in both cases.

The total uncertainty in the lower p_T region between 350 GeV and 450 GeV for the ATLAS (CMS) measurement varies between roughly $4.6\% \rightarrow 5.6\%$ $(4.2\% \rightarrow 4.9\%)$. Similarly the jet related uncertainties vary between $1.0\% \rightarrow 1.4\%$ $(2.1\% \rightarrow 2.5\%)$. The total uncertainty in this region is comparable between the two measurements and the relative contribution from jet uncertainties reflects the improvements from the JSF method on the ATLAS result. In a higher p_T region between 700 GeV and 800 GeV the

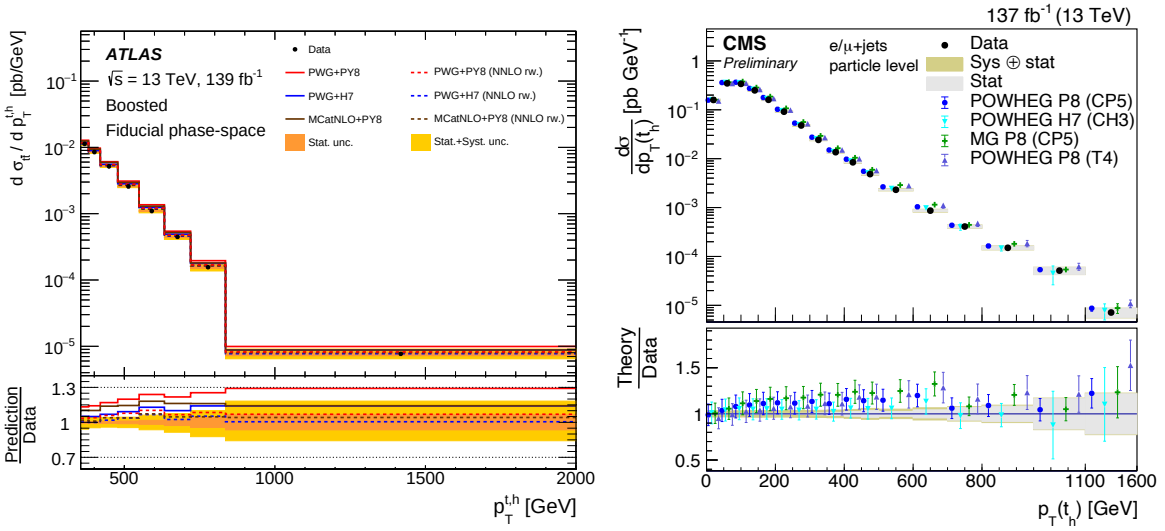

(a) **(b)**

Figure 10.15: Comparison between measurements of the absolute $t\bar{t}$ cross-section at particle-level as a function of the p_T of the hadronically decaying top-quark in lepton+jets events, performed by (a) ATLAS and (b) CMS [126]. Both measurements compare data to several MC predictions and include separate bands indicating the level of statistical (orange on left, grey on right) and total (gold on left, yellow on right) uncertainty. The kinematic phase-spaces of the two analyses are not the same and thus only general trends can be identified.

total uncertainty for the ATLAS (CMS) measurement is roughly 11% (7.8%), and the jet related uncertainties roughly 5.2% (2.0%). As a single scale factor is used, the JSF method is not as effective at high top-quark p_{T}. The CMS measurement is more precise in this region largely due to smaller JES uncertainties at high p_{T} obtained by CMS compared to ATLAS. It should be noted that the treatment of uncertainties related to the modelling of $t\bar{t}$ events is also different between the two results. The measurement covered in this thesis uses an arguably more conservative estimate by comparing between different generators, while the CMS result relies on a single generator setup with a larger number of internal variations. This generally results in measurements made by CMS having smaller modelling uncertainties.

Similar comparisons of the overall precision can be drawn with results from high energy $t\bar{t}$ production in the all-hadronic channel, recently measured by ATLAS [188]. Figure 10.16 compares the normalised fractional uncertainty breakdown on the measured $p_{\mathrm{T}}^{t,h}$ cross-section in this analysis to the relative uncertainties on the normalised leading top-quark p_{T} spectrum from the all-hadronic channel. It should be reiterated that concrete results can not be drawn between these two figures due to differences in the fiducial region and top-quark definitions used. In the region between 500 GeV and 650 GeV the total uncertainty on the normalised hadronic (leading) top-quark p_{T} spectrum from the lepton+jets (all-hadronic) analysis varies between roughly 2.1% $\rightarrow$ 4.7% (4.5% $\rightarrow$ 7.2%). In both cases a significant contribution of between 0.7% $\rightarrow$ 2.2% (3.2% $\rightarrow$ 5.0%) comes from the jet uncertainty. The all-hadronic measurement achieves worse overall precision but gains higher statistics, illustrated by the ability to split the high p_{T} region ($0.8\,\mathrm{TeV} < p_{\mathrm{T}} < 2\,\mathrm{TeV}$) into two bins with statistical uncertainty between 5.0% $\rightarrow$ 11.0% compared to a single bin in the lepton+jets analysis with a statistical uncertainty of 6.4%. In this region the total uncertainty is similar ranging from roughly 12.0% $\rightarrow$ 21.0% using all-hadronic events compared to 17.8% in the lepton+jets measurement.

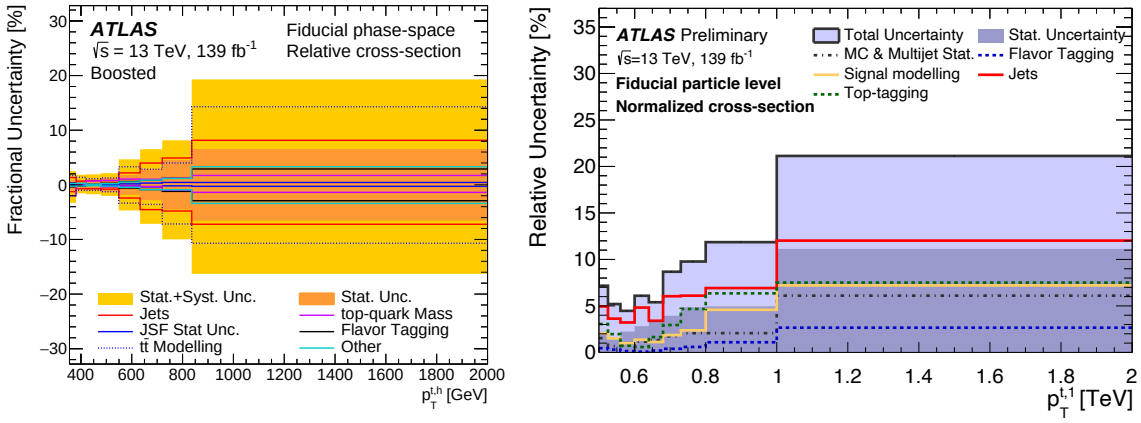

(a) **(b)**

Figure 10.16: Comparison between relative uncertainties on the normalised $t\bar{t}$ cross-section measurement at particle-level as a function of (a) the p_{T} of the hadronically decaying top-quark in lepton+jets events, (b) the p_{T} of the leading top-quark in all-hadronic events, measured by ATLAS [188]. The kinematic phase-spaces of the two measurements are similar but not identical and thus only general trends can be identified. The all-hadronic measurement shows the average of the positive and negative fractional uncertainties (symmetrised) while the lepton+jets measurement shows the full asymmetric uncertainty bands.

Chapter 11.

Limits on EFT operators

"I think I can safely say that nobody understands quantum mechanics"
— Richard P. Feynman

The sensitivity of the analysis to potential new physics is explored by fitting the measured differential cross-section $d\sigma/dp_{\mathrm{T}}^{t,h}$ to obtain limits on BSM contributions from the dimension six EFT operators O_{tG} and $O_{tq}^{(8)}$, introduced in Chapter 2. These operators, parameterised by Wilson coefficients C_{tG} and $C_{tq}^{(8)}$, are chosen as they are particularly sensitive to $t\bar{t}$ production but affect different aspects. The chromo-magnetic operator (O_{tG}) alters the top-gluon coupling and is expected to have a larger overall effect on the rate of $t\bar{t}$ production. The operator $O_{tq}^{(8)}$ adds a non-SM four-quark coupling and is expected to contribute more strongly in events with high energy top-quarks. Effects from the two operators can thus be disentangled by fitting a single differential cross-section measurement that has a strong dependence on the energy of the top-quarks in the event. The hadronic top-quark p_{T} distribution was chosen as a result of the sensitivity studies described in Section 8.1.3.

11.1. Interpretation strategy

The interpretation relies on simulated $t\bar{t}$ samples produced with additional EFT effects, introduced by setting the two Wilson coefficients of interest to non-zero values. The EFT samples used are outlined in Section 7.1.1. For the interpretation it is assumed that all other Wilson coefficients of dimension six and above are 0. It is also assumed that the EFT contributions have negligible effect on the background estimate and thus the nominal background samples, described in Section 7.1.1, are used. This is a reasonable assumption considering the high signal purity demonstrated in the cross-section analysis. The strategy used for the EFT interpretation is outlined in the following sub-sections before the results are reported in Section 11.2.

Parameterisation of cross-section

To extract limits, the cross-section in each bin j is parameterised as a function of the two Wilson coefficients:

$$\sigma^j(C_{tG}, C_{tq}^{(8)}) = p_0^j + p_1^j C_{tG} + p_2^j C_{tq}^{(8)} + p_3^j (C_{tG})^2 + p_4^j (C_{tq}^{(8)})^2 + p_5^j (C_{tG} \cdot C_{tq}^{(8)}), \quad (11.1)$$

where the parameters p_i^j are extracted by performing fits to the EFT samples with varied values of C_{tG} and $C_{tq}^{(8)}$. Two separate fits are produced; one using samples with the full EFT contributions (proportional to Λ^{-2} and Λ^{-4}) and another containing only linear contributions (proportional to Λ^{-2}). In this way it is possible to assess the individual impact of adding quadratic terms, i.e. those proportional to Λ^{-4}, corresponding to squared dimension-six operators in the expanded Lagrangian. The p_0^j parameter is extracted from the Standard Model prediction used in the fit. To ensure an accurate value for p_0^j, the SM component of the EFT samples were replaced with a higher order SM prediction, corresponding to the POWHEG+PYTHIA8 sample re-weighted to the NNLO prediction.

Extraction of best-fit values

The EFT*fitter* program [189] is used to extract simultaneous best-fit values for the Wilson coefficients given the measured differential cross-section of the $p_{\mathrm{T}}^{t,h}$

distribution ($\boldsymbol{m}$). Values are found by minimising the following likelihood:

$$-2\ln P(C_{tG}, C_{tq}^{(8)}|\boldsymbol{m}) = (\boldsymbol{m} - \boldsymbol{\sigma}(C_{tG}, C_{tq}^{(8)}))^T M^{-1}(\boldsymbol{m} - \boldsymbol{\sigma}(C_{tG}, C_{tq}^{(8)})), \tag{11.2}$$

where $\boldsymbol{\sigma}(C_{tG}, C_{tq}^{(8)})$ denotes the set of parameterised cross-section values taken from equation (11.1), and M is the covariance matrix. As before, the covariance matrix is the sum of the covariance matrices from all uncorrelated sources of uncertainty. For the EFT interpretation this includes all of the same experimental uncertainties from the cross-section measurement (M_e), as well as theoretical uncertainties on the NNLO cross-section calculations used in the SM prediction (M_t). The final covariance matrix is then given by: $M = M_e + M_t$, assuming the experimental and theoretical uncertainties are uncorrelated. The covariance matrix for the experimental uncertainties is the same as the one used for the $p_{\mathrm{T}}^{t,h}$ cross-section measurement, defined in Section 10.2. The theory uncertainties are outlined in the next section.

Theory uncertainties

The theoretical uncertainties are taken from variations of the NNLO and NNLO + NLO EW $t\bar{t}$ cross-section calculations used to re-weight the Standard Model prediction. A set of seven scale variations are produced by changing the μ_{r} and μ_{f} scales in the range $(0.5\mu, 2\mu)$ with the additional condition: $0.5 \geq \frac{\mu_{\mathrm{r}}}{\mu_{\mathrm{f}}} \leq 2$. This is repeated for all three variables used for the re-weighting $\left(p_{\mathrm{T}}(t),\ p_{\mathrm{T}}(t\bar{t})\right.$ and $\left.m(t\bar{t})\right)$. The envelopes of the seven variations are then used to define alternative up and down shape variations. Figure 11.1a shows the scale of the variations on the $p_{\mathrm{T}}^{t,h}$ distribution for each variable compared to the nominal prediction at particle-level. The largest effect comes from the $p_{\mathrm{T}}(t)$ variations as expected. The other variations are non-zero due to correlations between the variables in the re-weighting process. To be conservative the variations from the three variables are combined, assuming the uncertainties are uncorrelated. An uncertainty on the choice of PDF set is also included. The scale and PDF uncertainties only cover shape differences in the measured distribution, thus an additional 6% normalisation uncertainty is added to cover the uncertainty from missing higher-order corrections. This is the same as the uncertainty included on the MC predictions in Figure 10.1 and covers variations in the scales, PDF, α_{S}, and m_t in the NNLO + NNLL inclusive cross-section calculation [105]. Figure 11.1b shows the total theory uncertainty on the $p_{\mathrm{T}}^{t,h}$ distribution.

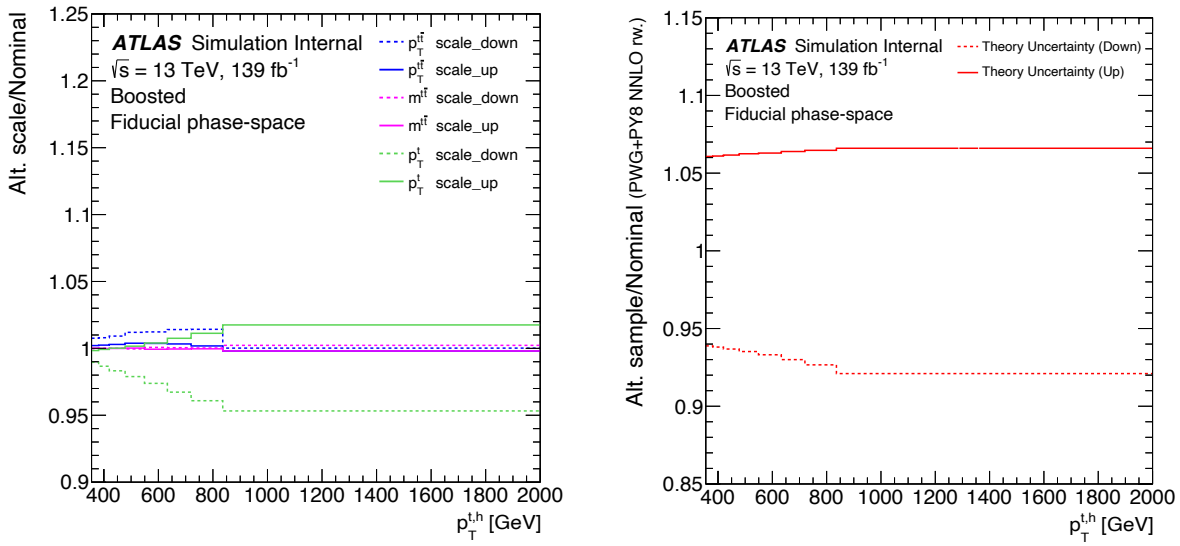

(a) **(b)**

Figure 11.1: (a) The impact of individual scale uncertainties derived from each of the three variables used in the NNLO re-weighting, shown as the ratio of alternative predictions to the nominal $p_{\mathrm{T}}^{t,h}$ distribution at particle-level. (b) The scale of the total theory uncertainty on the $p_{\mathrm{T}}^{t,h}$ distribution as the ratio of the combined uncertainty variations to the nominal NNLO prediction. The total uncertainty is the combination in quadrature of the scale variations from the three variables, the choice of PDF set and an additional 6% normalisation uncertainty.

Probability distribution extraction

The two-dimensional posterior probability distribution is extracted using a numerical implementation of Bayes' theorem in the Bayesian Analysis Toolkit [190]. A flat prior probability for the two Wilson coefficients, within the range $(-5 \leq C_i \leq 5)$, is used. Marginalised credible intervals for each coefficient are produced from the probability distribution by integrating out the other coefficient. Individual fits are also performed for each Wilson coefficient using the same methods above but fixing the value of the other coefficient to zero. The two-dimensional probability distributions, and marginalised and individual 95% credible intervals are presented in the following section.

11.2. EFT results

The best-fit values extracted from the measured $p_{\mathrm{T}}^{t,h}$ distribution are:

$$C_{tG} = -0.24 \pm 0.23\ (\Lambda/\mathrm{TeV})^2,\ C_{tq}^{(8)} = 0.03 \pm 0.17\ (\Lambda/\mathrm{TeV})^2 \qquad (\Lambda^{-2}),$$
$$C_{tG} = -0.11^{+0.16}_{-0.25}\ (\Lambda/\mathrm{TeV})^2,\quad C_{tq}^{(8)} = -0.43^{+0.40}_{-0.06}\ (\Lambda/\mathrm{TeV})^2 \qquad (\Lambda^{-4}).$$

In both cases the best-fit value for the data is found to be slightly more than 1 standard deviation away from the SM, indicating no evidence for new physics is observed in the data. The best-fit values for C_{tG} are shown to prefer negative values in both the linear and quadratic models. This behaviour is consistent with the measured total cross-section being lower than the SM prediction. In the Λ^{-2} samples the effect of C_{tG} is almost linear, as shown in Figure 8.3a, thus the effect of extracting a fit using a lower overall cross-section leads to a negative fit value being preferred. The same is true for the Λ^{-4} fit but to a lesser extent due to the increased shape of the linear+quadratic EFT contribution. Figure 11.2 shows the measured $t\bar{t}$ cross-section as a function of $p_{\mathrm{T}}^{t,h}$ for the SM prediction and the EFT predictions with the Wilson coefficients set to their best-fit values. The errors on the data points are the total uncertainties from the measurement reported in Chapter 10, while the uncertainty band denotes the theory uncertainty on the SM prediction. The SM and SM+EFT predictions are compatible with data.

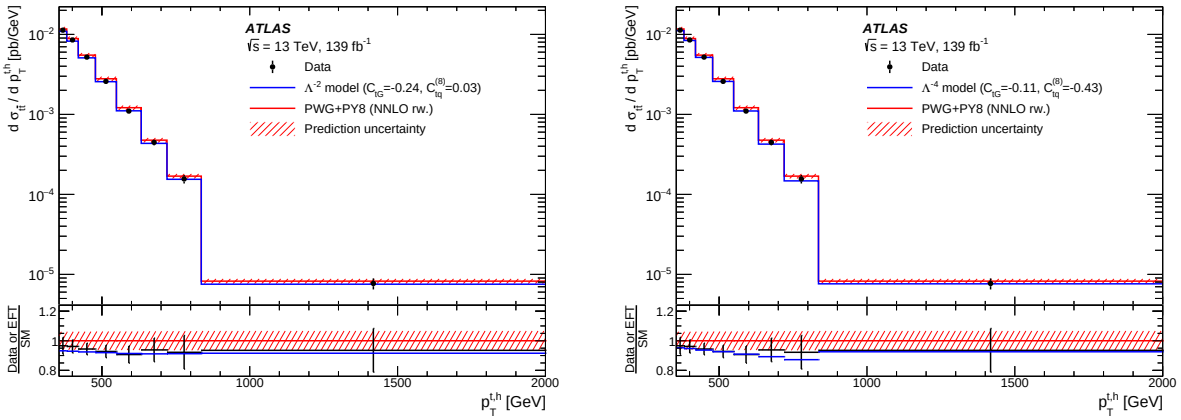

(a) **(b)**

Figure 11.2: The top-quark pair cross-section as a function of $p_{\mathrm{T}}^{t,h}$ used in the EFT interpretation. The data is compared to the SM prediction in red and the EFT model prediction in blue at the respective global modes for (a) the linear (Λ^{-2}) model and (b) the quadratic (Λ^{-4}) model. The lower panel displays the ratio between the data or EFT model and the SM prediction. The error bars indicate the total uncertainty from the cross-section measurement and the shaded red band shows the additional theory uncertainty on the SM prediction used in the EFT fit.

Figures 11.3 and 11.4 show the two-dimensional posterior probability distributions for the linear and quadratic fits for both the expected and observed limits respectively, where the expected limits are extracted using the NNLO SM samples as pseudo-data in the fit. The expected fit recovers the SM values, shown by the global mode and SM points overlapping in Figures 11.3a and 11.3b. Both the expected and observed credible intervals for the linear+quadratic fit are asymmetric, with more of the allowed parameter space covering negative values. This is the expected behaviour as the linear and quadratic EFT terms can cancel in regions of the parameters space where the Wilson coefficients are negative. This has the result of skewing the probability distribution towards negative values and gives rise to the small negative uncertainty on the Λ^{-4} $C_{tq}^{(8)}$ limit. In each case the allowed parameter space is fully defined between -1 and 1 for both Wilson coefficients indicating that the measurement is able to break the degeneracy of the EFT effects and distinguish between the two operators.

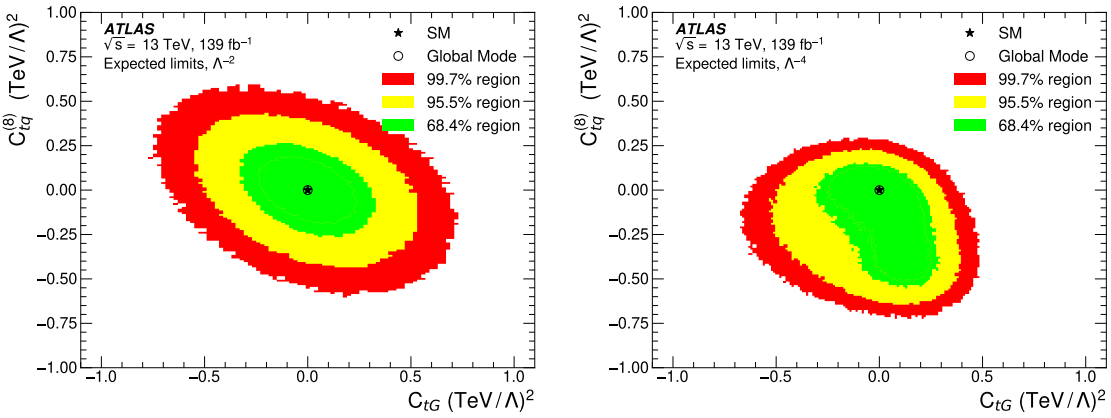

(a) **(b)**

Figure 11.3: Expected two-dimensional posterior distributions for the two Wilson coefficients C_{tG} and $C_{tq}^{(8)}$ obtained from fitting the $p_{\mathrm{T}}^{t,h}$ distribution using the SM prediction as pseudo-data and the (a) linear (b) quadratic EFT model. The 68.4 %, 95.5 %, and 99.7 % credible intervals are shown in green, yellow and red respectively.

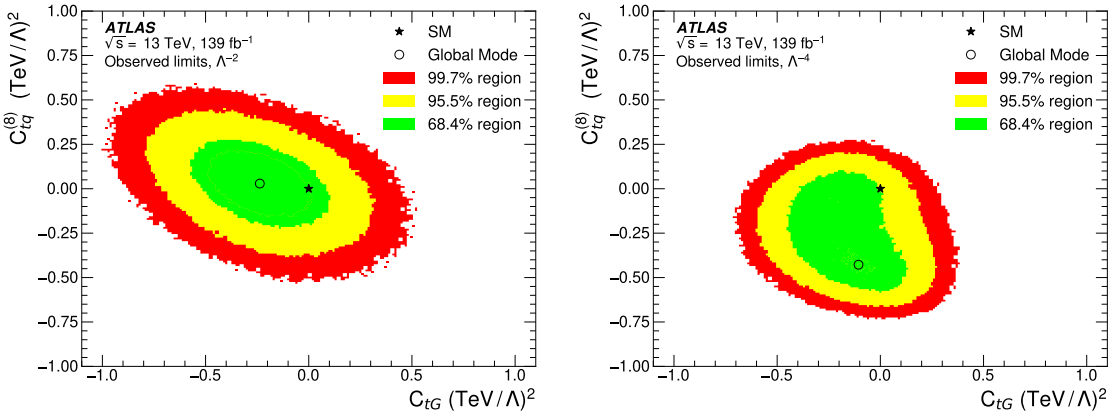

(a) **(b)**

Figure 11.4: Observed two-dimensional posterior distributions for the two Wilson coefficients C_{tG} and $C_{tq}^{(8)}$ obtained from fitting the $p_{\mathrm{T}}^{t,h}$ distribution using the (a) linear (b) quadratic EFT model. The 68.4 %, 95.5 %, and 99.7 % credible intervals are shown in green, yellow and red respectively.

Table 11.1 shows the expected and observed 95% credible intervals for the simultaneous (marginalised) and individual fits. Results from a recent global fit [191] are given in the right-most column. The global fit is obtained by combining results from multiple measurements and provides limits on both C_{tG} and $C_{tq}^{(8)}$, using the same basis and with all other Wilson coefficients set to zero. The global fit values can thus be compared directly to the observed individual limits from this analysis. The observed limits on C_{tG} are significantly weaker than the global fit values, however the observed limits on $C_{tq}^{(8)}$ are more stringent than those obtained from the global fit. The results indicate that the data presented here can provide important constraining power in future global fits. The fact that stronger limits have been extracted from a single measurement also demonstrates the power of using differential measurements to constrain EFT parameters.

Table 11.1: Expected and observed 95% credible intervals on C_{tG} and $C_{tq}^{(8)}$. The marginalised intervals correspond to those extracted from the nominal fit where both Wilson coefficients are allowed to vary. The individual intervals correspond to fits in which only the single Wilson coefficient under study is allowed to differ from zero. The results are compared to the individual limits obtained in a recent global fit [191].

Model	C_i $(\Lambda/\text{TeV})^2$	Marginalised 95% intervals		Individual 95% intervals		
		Expected	Observed	Expected	Observed	Global fit [191]
Λ^{-4}	C_{tG}	[-0.44, 0.35]	[-0.53, 0.21]	[-0.44, 0.28]	[-0.52, 0.15]	[0.006, 0.107]
	$C_{tq}^{(8)}$	[-0.57, 0.17]	[-0.60, 0.13]	[-0.57, 0.18]	[-0.64, 0.12]	[-0.48, 0.39]
Λ^{-2}	C_{tG}	[-0.44, 0.44]	[-0.68, 0.21]	[-0.41, 0.42]	[-0.63, 0.20]	[0.007, 0.111]
	$C_{tq}^{(8)}$	[-0.35, 0.35]	[-0.30, 0.36]	[-0.35, 0.36]	[-0.34, 0.27]	[-0.40, 0.61]

In Figure 8.3 the high p_{T} tail of the $p_{\mathrm{T}}^{t,h}$ distribution was shown to be more sensitive to effects from $C_{tq}^{(8)}$ than C_{tG}. To better understand the effect of using the full differential distribution on the extracted limits the fit was repeated several times using progressively more of the measured bins each time. Figure 11.5 shows the evolution of the observed 95% posterior probability distribution as bins are added one-by-one to the fit. Again both the linear and quadratic fits are shown. Using only a single bin, shown by the red band, the fit is not able to differentiate between the two operators, with neither able to be reasonably constrained without knowledge of the other. This is improved as bins are added to the fit, with the allowed parameter region becoming constrained to smaller areas. The addition of the high p_{T} bins provide the strongest constraining power on $C_{tq}^{(8)}$, indicating that the extracted limits benefit from the use of high p_{T} events in the measurement.

As a further test Figure 11.6 compares the expected limits using a single bin covering the full p_{T} range (inclusive fit) to results from the differential fit with all 8 bins. The inclusive fit results in tighter limits for both $C_{tq}^{(8)}$ and C_{tG} when compared to using a single low p_{T} bin (the red bands in Figure 11.5). However, as expected, the limits on $C_{tq}^{(8)}$ are significantly tighter in the differential fit as the orthogonal behaviour of the different bins can be exploited. Additionally the effects of the two operators can be disentangled in the differential fit, while they are left degenerate when using only a single measurement.

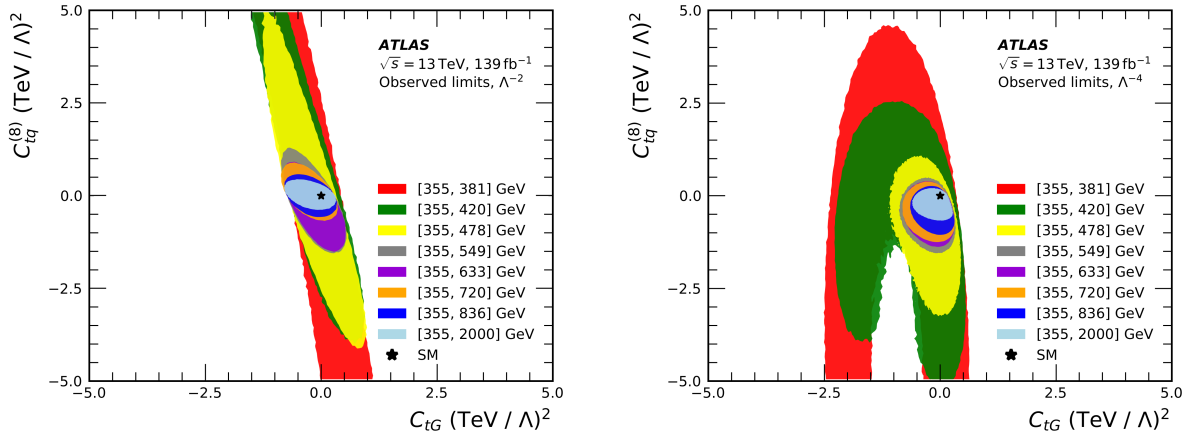

(a) **(b)**

Figure 11.5: Evolution of the observed 95% credible region for the two Wilson coefficients as bins of $p_{\mathrm{T}}^{t,h}$ are progressively added to the interpretation for (a) the linear (Λ^{-2}) model, (b) the quadratic (Λ^{-4}) model. The coloured ellipses show the 95% credible areas obtained from fitting the $p_{\mathrm{T}}^{t,h}$ range indicated in the legend.

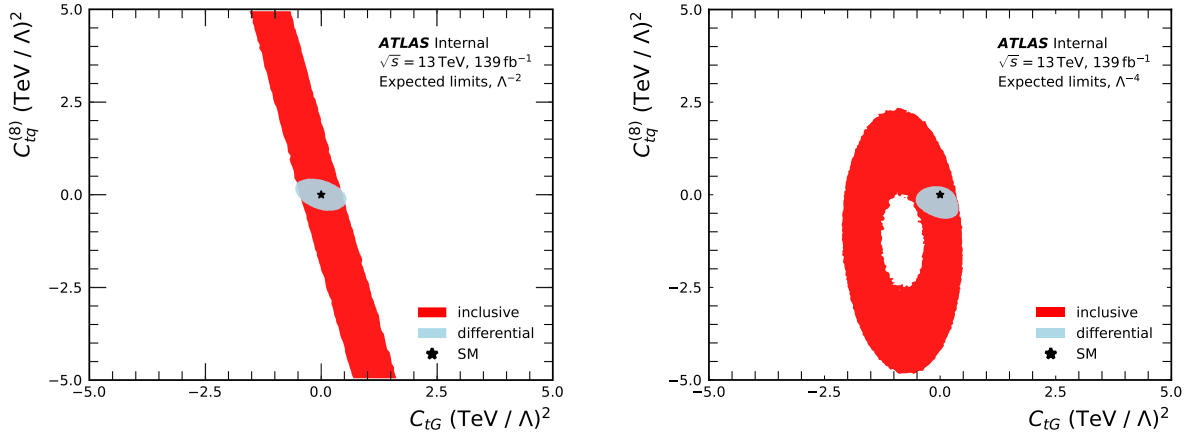

(a) **(b)**

Figure 11.6: Expected 95% credible region for the two Wilson coefficients when fitting the $p_{\mathrm{T}}^{t,h}$ distribution as a single inclusive measurement compared to a differential measurement with 8 bins. In both cases the fits are performed using the SM prediction as pseudo-data and the (a) linear (b) quadratic EFT model.

Chapter 12.

Conclusion

"That's it! You people have stood in my way long enough. I'm going to clown college!"

— Homer Simpson, The Simpsons S6, E15 - Homie the Clown

In this thesis I have presented my contributions to the ATLAS physics programme including work on the muon trigger monitoring system and a detailed overview of the recent differential analysis of top-quark pair cross-sections in boosted events, available publicly at [1].

The ATLAS muon trigger is a vital component in many Standard Model measurements as well as searches for new physics. During the last few months of Run-2 a new trigger was added which allowed the level-1 trigger efficiency to be monitored in real time. A tag and probe technique using $Z \to \mu\mu$ events was used to calculate the efficiency relative to well reconstructed muons from the high level trigger. Output from this trigger was added to the ATLAS run displays and used as an early warning system for drops in trigger efficiency.

For the cross-section measurements, $t\bar{t}$ events containing a hadronically decaying top-quark with high transverse momentum ($p_{\mathrm{T}} > 355\,\mathrm{GeV}$) were selected from the full 139 fb^{-1} Run-2 dataset recorded by the ATLAS detector at the LHC between 2015 – 2018. The cross-sections were extracted from reconstructed physics objects at particle-level via an unfolding process and compared to several simulated NLO + PS Standard Model predictions, as well as to NLO predictions re-weighted at parton-level to match a NNLO(QCD) + NLO(EW) calculation. No single generator prediction was

able to accurately describe all of the measured observables however applying the NNLO re-weighting was shown to improve the agreement with data for all tested generators. This is a strong indication that at the current level of precision the NNLO corrections are relevant to $t\bar{t}$ events in this phase space and further improvements would be possible with the introduction of full NNLO + PS predictions, which will hopefully become available in the near future [192]. Distributions related to additional radiation in the events was a secondary focus of the analysis. The number of additional jets in the events was found to be well modelled by the SHERPA generator which includes matrix-element calculations for up to the first additional jet at NLO accuracy in QCD and up to four additional partons at LO. This suggests that the modelling of additional radiation is improved in models that include higher-order predictions for additional emissions. However none of the generators were able to accurately describe more detailed observables related to additional radiation, indicating there are still further corrections needed beyond this.

A new technique was developed using the measured mass of the hadronically decaying top-quark to reduce the impact of jet energy scale uncertainties. This resulted in a significant drop in jet-related uncertainty of ∼80% on the inclusive measurement and up to ∼90% in individual bins of the differential measurements. This method used in conjunction with higher statistics, improved MC modelling, and techniques to reduce background contamination led to a significant improvement in measurement precision compared to previous results. The inclusive cross-section in the fiducial phase-space was measured to be $\sigma_{t\bar{t}}^{\text{fid}} = 1.267 \pm 0.005\ (\text{stat.}) \pm 0.053\ (\text{syst.})$ pb which constitutes a 47% reduction in total uncertainty on the previous 36 fb^{-1} analysis performed by ATLAS [124].

As well as the improvements in precision, this analysis also measures several observables for the first time within highly boosted $t\bar{t}$ events. These include the majority of the angular variables and all measured double-differential observables, many of which exhibit significant variation between data and simulation. Similarly the addition of an EFT interpretation of the results using a differential cross-section measurement ($p_{\text{T}}^{t,h}$) is new for an analysis of this type and illustrates the sensitivity of the measurement to BSM physics effects. The $p_{\text{T}}^{t,h}$ distribution is used to extract limits on two Wilson coefficients sensitive to $t\bar{t}$ production. No evidence of new physics is observed and the 95% credible intervals on the Wilson coefficients from the simultaneous quadratic fit are: $C_{tG} \in [-0.53, 0.21]\ (\Lambda/\text{TeV})^2$ and $C_{tq}^{(8)} \in [-0.60, 0.13]\ (\Lambda/\text{TeV})^2$. The analysis is able to disentangle effects from the O_{tG} and $O_{tq}^{(8)}$ operators and yields strin-

gent limits on $C_{tq}^{(8)}$, demonstrating the value of this measurement in future combined fits.

The analysis presented here provides some of the most precise boosted $t\bar{t}$ cross-section measurements produced by ATLAS to date. Along with recent results in the di-lepton [193] and all-hadronic [188] channels they help provide a comprehensive picture of the $t\bar{t}$ production cross-section at the LHC. At the time of writing initial testing for the third LHC data-taking run is underway. However with significant upgrades made to all four major experiments; the ramp up to high luminosity data-taking is expected to be slow. A new, higher energy, dataset comparable in size to that of Run-2 is not expected until around 2025 [194]. As a result, the optimisation of existing analysis methods and active development of new techniques, such as the JSF method introduced here, will continue to play a vital role in improving the precision of future measurements.

Part III.

Auxilliary material

Appendix A.

"Surely you can't be serious!?
I am serious, and don't call me Shirley."
— Leslie Nielsen, Airplane!

A.1. Calculation of $p_{z,\nu}$ for leptonic top reconstruction

The longitudinal momentum component of the neutrino in each event is estimated in order to reconstruct the full four momentum of the leptonically decaying top-quark. The calculation is based on the assumption that the lepton-neutrino system has invariant mass equal to the W-boson mass:

$$\begin{aligned} m_{\ell,\nu} &= m_W \\ \implies (E_\ell + E_\nu)^2 - (p_{x,\ell} + p_{x,\nu})^2 - &(p_{y,\ell} + p_{y,\nu})^2 - (p_{z,\ell} + p_{z,\nu})^2 = m_W, \end{aligned} \tag{A.1}$$

where $m_{\ell,\nu}$ is the invariant mass of the lepton-neutrino system in the W-boson rest frame, m_W is the rest mass of the W-boson, E_ℓ and E_ν are the energies of the lepton and neutrino, $p_{X,\ell}$ and $p_{X,\nu}$ are the X-component of the lepton and neutrino 3-momenta respectively.

Assuming $m_\nu = 0$ the energies are given by:

$$E_\nu = \sqrt{p_{x,\nu}^2 + p_{y,\nu}^2 + p_{z,\nu}^2} \text{ and} \tag{A.2}$$

$$E_\ell^2 = m_\ell^2 + (p_{x,\ell}^2 + p_{y,\ell}^2 + p_{z,\ell}^2). \tag{A.3}$$

Expanding equation (A.1) and substituting in equation (A.2) gives:

$$\begin{aligned} & E_\ell^2 - (p_{x,\ell}^2 + p_{y,\ell}^2 + p_{z,\ell}^2) \\ & +2E_\ell\sqrt{p_{x,\nu}^2 + p_{y,\nu}^2 + p_{z,\nu}^2} \\ & -2(p_{x,\ell}p_{x,\nu} + p_{y,\ell}p_{y,\nu} + p_{z,\ell}p_{z,\nu}) = m_W. \end{aligned} \tag{A.4}$$

Substituting equation (A.3) and rearranging gives:

$$\left(\frac{m_W^2 - m_\ell^2}{2} + p_{x,\ell}p_{x,\nu} + p_{y,\ell}p_{y,\nu}\right) + p_{z,\ell}p_{z,\nu} = \sqrt{E_\ell^2 p_{x,\nu}^2 + E_\ell^2 p_{y,\nu}^2 + E_\ell^2 p_{z,\nu}^2}. \tag{A.5}$$

Labelling the first term k and squaring both sides yields a polynomial in powers of $p_{z,\nu}$:

$$(E_\ell^2 - p_{z,\ell}^2)p_{z,\nu}^2 - (2kp_{z,\ell})p_{z,\nu} + (E_\ell^2)p_{\mathrm{T},\nu}^2 - k^2 = 0, \tag{A.6}$$

where $p_{T,\nu} = \sqrt{p_{x,\nu}^2 + p_{y,\nu}^2}$ is the component of the neutrino momentum transverse to the beam-line. The polynomial coefficients are then:

$$\begin{aligned} a &= E_\ell^2 - p_{z,\ell}^2, \\ b &= -2kp_{z,\ell}, \\ c &= E_\ell^2 p_{T,\nu}^2 - k^2, \end{aligned}$$

with $k = \frac{m_W^2 - m_\ell^2}{2} + p_{x,\ell}p_{x,\nu} + p_{y,\ell}p_{y,\nu}$ as required.

A.2. Normalised differential cross-section results

The differential cross-section results are presented here after normalising them to the total cross-section measured in the fiducial region. These results allow for easier comparison of the shape of the measurements in data and different MC predictions.

Figure A.1 shows the normalised differential cross-section results for variables related to kinematics of the $t\bar{t}$ system: $p_{\mathrm{T}}^{t,h}$, $p_{\mathrm{T}}^{t,\ell}$, $H_{\mathrm{T}}^{t\bar{t}}$, $m^{t\bar{t}}$, $\Delta\phi(b_\ell, t_h)$, $|y^{t,h}|$, $|y^{t,\ell}|$, and $|y^{t\bar{t}}|$. These results are compared to various NLO and re-weighted NNLO generator setups. Figures A.2 and A.3 show the normalised differential cross-section results for variables related to additional radiation in the events: N^j, $m(j_1, t_h)$, $p_{\mathrm{T}}^{j,1}$, $p_{\mathrm{T}}^{j,2}$, $\Delta\phi(j_1, t_h)$, $\Delta\phi(j_2, t_h)$, $\Delta\phi(j_1, j_2)$, $p_{\mathrm{T}}^{t\bar{t}}$, $H_{\mathrm{T}}^{t\bar{t}+\mathrm{jets}}$, and $\Delta\phi(t_h, t_\ell)$. These results are compared to SM predictions from different NLO + PS generator setups with variations in shower settings and ISR. The normalised double-differential cross-section results are shown in Figures A.4–7 for: $\Delta\phi(j_1, t_h)$ Vs $p_{\mathrm{T}}^{t,h}$, $p_{\mathrm{T}}^{j,1}$ Vs $p_{\mathrm{T}}^{t,h}$, $\Delta\phi(j_1, t_h)$ Vs N^j, and $p_{\mathrm{T}}^{j,1}$ Vs N^j. These are compared to the same NLO + PS setups.

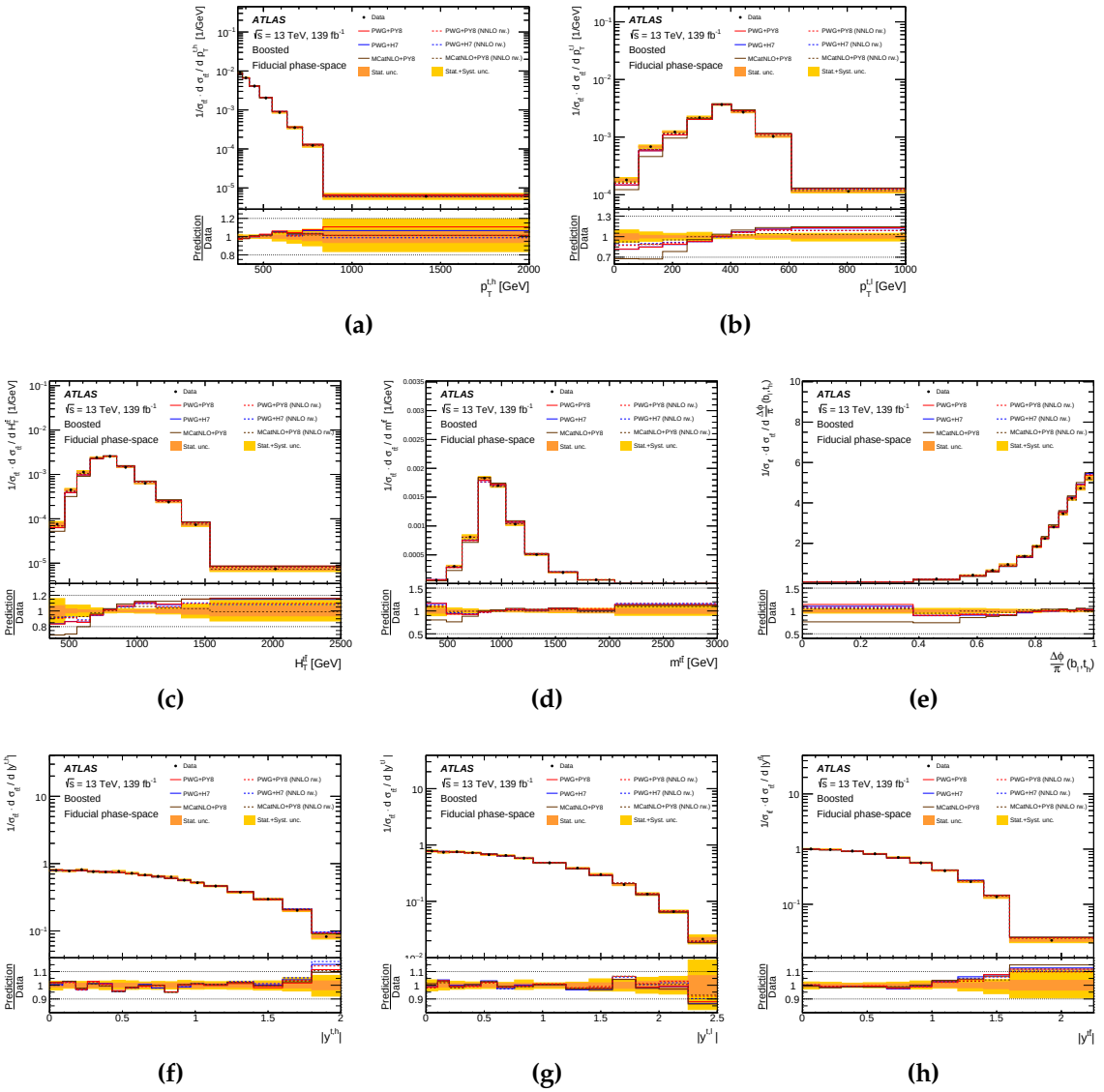

Figure A.1: Normalised differential cross-section measurements for the observables related to the kinematics of the two top-quarks. The cross-section is shown as a function of (a) $p_{\mathrm{T}}^{t,h}$, (b) $p_{\mathrm{T}}^{t,\ell}$, (c) $H_{\mathrm{T}}^{t\bar{t}}$, (d) $m^{t\bar{t}}$, (e) $\Delta\phi(b_\ell, t_h)$, (f) $|y^{t,h}|$, (g) $|y^{t,\ell}|$, and (h) $|y^{t\bar{t}}|$. Measured results are compared to SM predictions from various NLO generators with (dashed lines) and without (solid lines) the NNLO re-weighting applied. The yellow band shows the size of the total uncertainty in each bin, while the orange band shows the statistical uncertainty only. The lower panel displays the ratios between the different predictions and data.

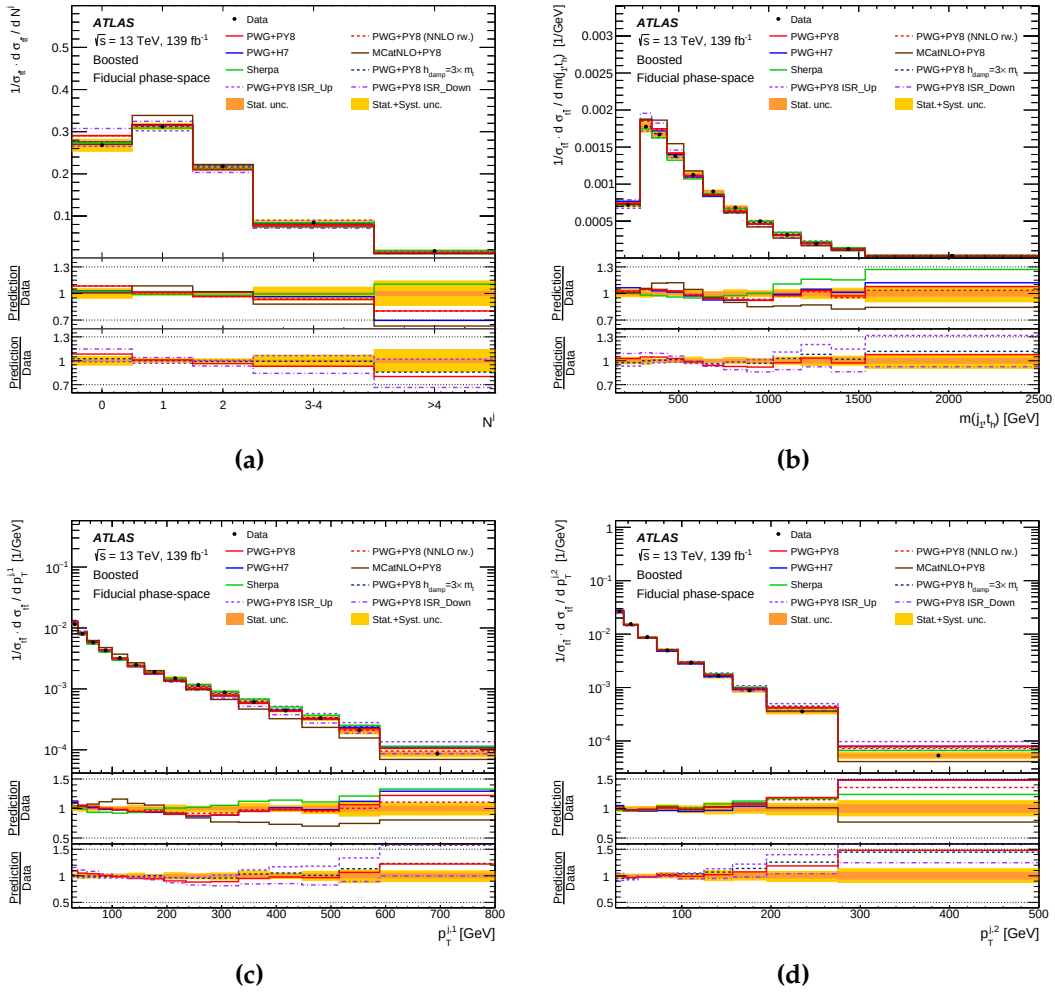

Figure A.2: Normalised differential cross-section measurements for observables related to additional radiation. The cross-section is shown as a function of (a) N^j, (b) $m(j_1, t_h)$, (c) $p_{\mathrm{T}}^{j,1}$, and (d) $p_{\mathrm{T}}^{j,2}$. Measured results are compared to SM predictions from various NLO + PS generator setups with different shower and radiation settings. The yellow band shows the size of the total uncertainty in each bin, while the orange band shows the statistical uncertainty only. The two lower panels display the ratios between the different predictions and data.

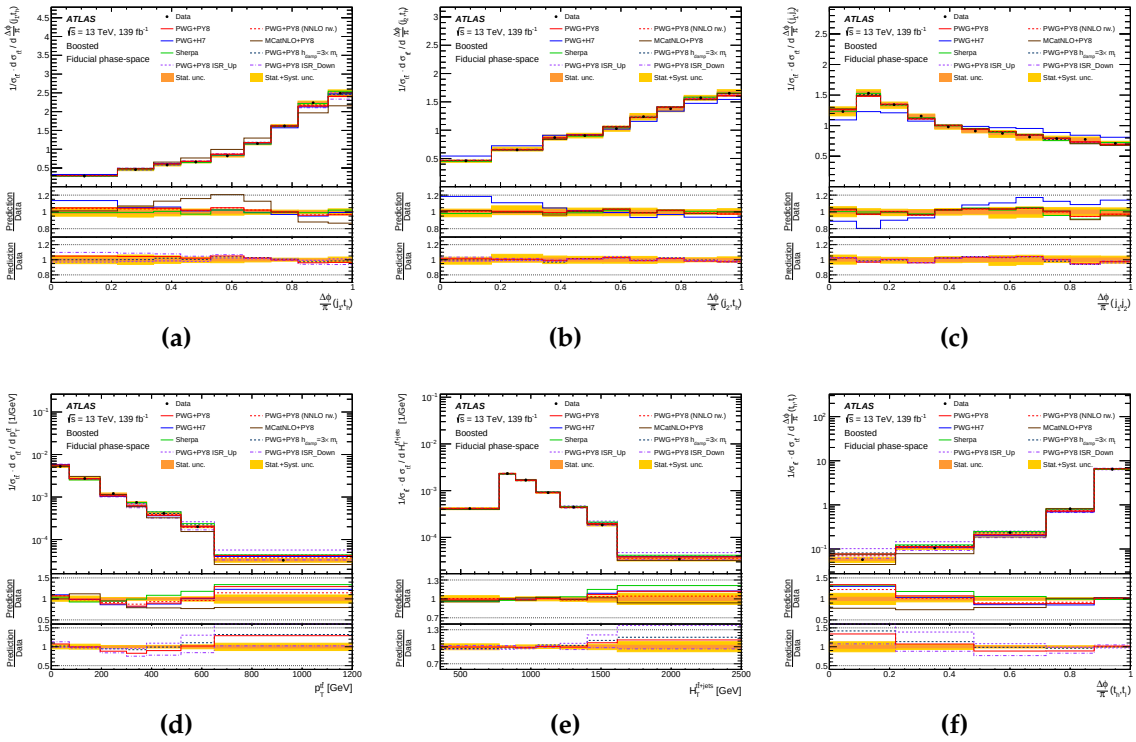

Figure A.3: Normalised differential cross-section measurements for observables related to additional radiation. The cross-section is shown as a function of (a) $\Delta\phi(j_1, t_h)$, (b) $\Delta\phi(j_2, t_h)$, (c)$\Delta\phi(j_1, j_2)$, (d) $p_{\mathrm{T}}^{t\bar{t}}$, (e) $H_{\mathrm{T}}^{t\bar{t}+\mathrm{jets}}$, and (f) $\Delta\phi(t_h, t_\ell)$. Measured results are compared to SM predictions from various NLO + PS generator setups with different shower and radiation settings. The yellow band shows the size of the total uncertainty in each bin, while the orange band shows the statistical uncertainty only. The two lower panels display the ratios between the different predictions and data.

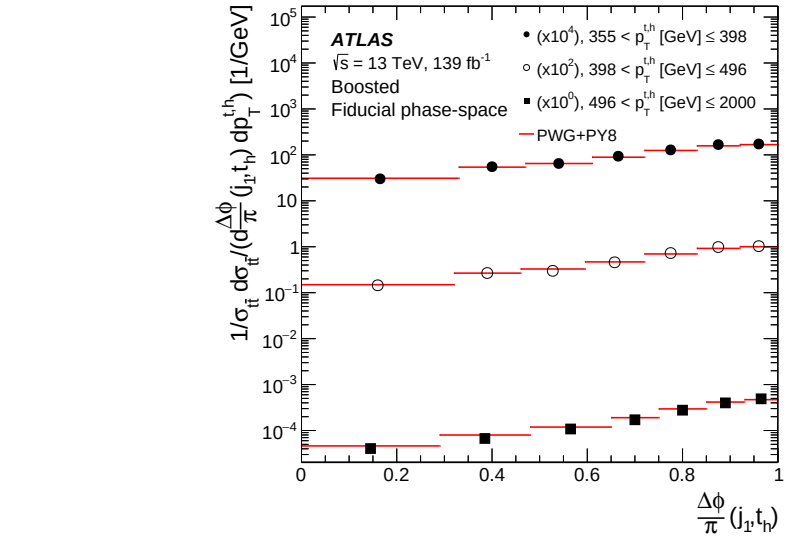

(a)

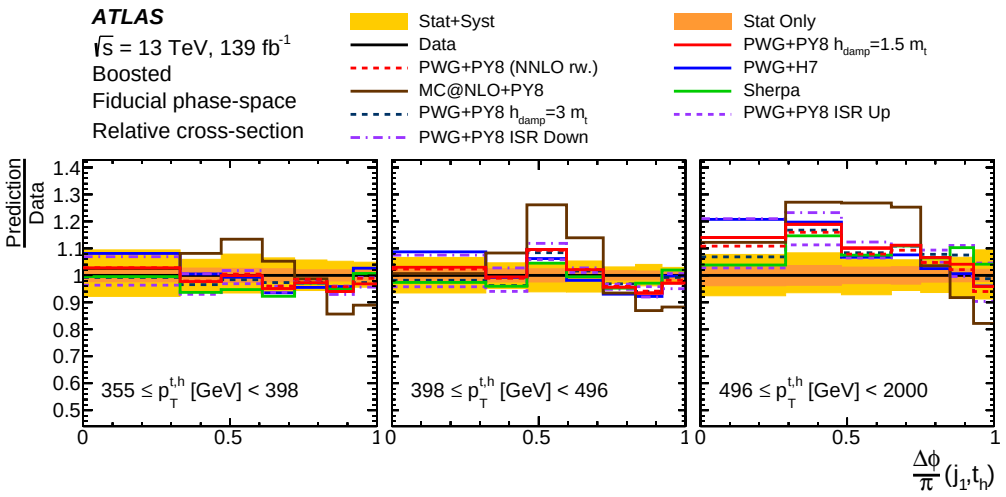

(b)

Figure A.4: Normalised double-differential cross-section measurement as a function of $\Delta\phi(j_1, t_h)$ in bins of $p_{\mathrm{T}}^{t,h}$. (a) Measured differential cross-section compared directly with predictions from the POWHEG+PYTHIA8 MC event generator. The measurement and predictions are multiplied by the factors shown in parentheses to aid visibility. (b) The ratio of the measured normalised cross-section to different NLO + PS and re-weighted NNLO SM predictions. The yellow band shows the size of the total uncertainty, while the orange band shows the statistical uncertainty only.

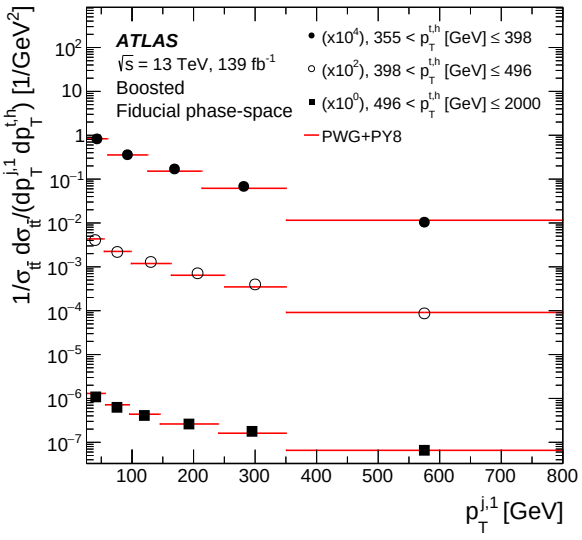

(a)

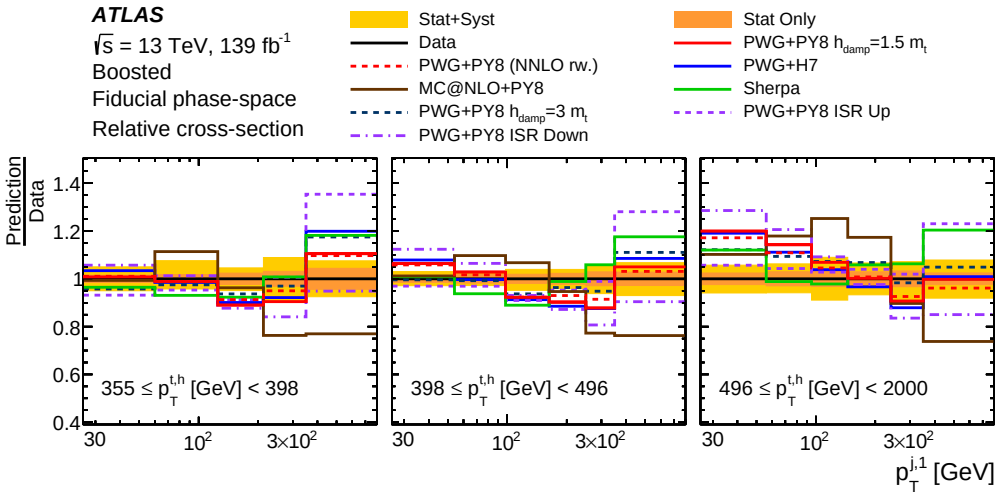

(b)

Figure A.5: Normalised double-differential cross-section measurement as a function of $p_{\mathrm{T}}^{j,1}$ in bins of $p_{\mathrm{T}}^{t,h}$. (a) Measured differential cross-section compared directly with predictions from the POWHEG+PYTHIA8 MC event generator. The measurement and predictions are multiplied by the factors shown in parentheses to aid visibility. (b) The ratio of the measured normalised cross-section to different NLO + PS and re-weighted NNLO SM predictions. The yellow band shows the size of the total uncertainty, while the orange band shows the statistical uncertainty only.

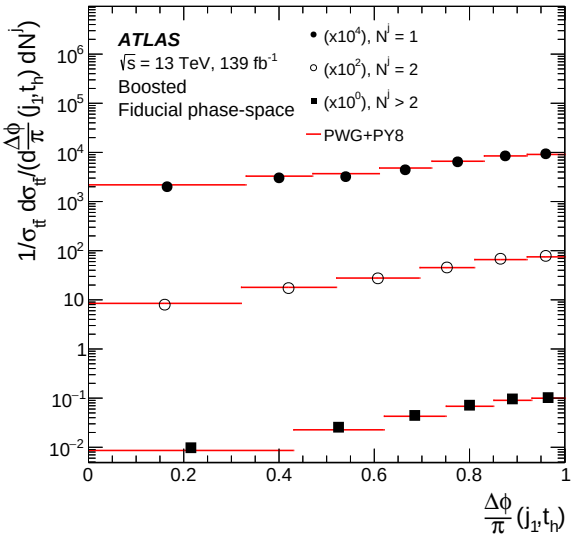

(a)

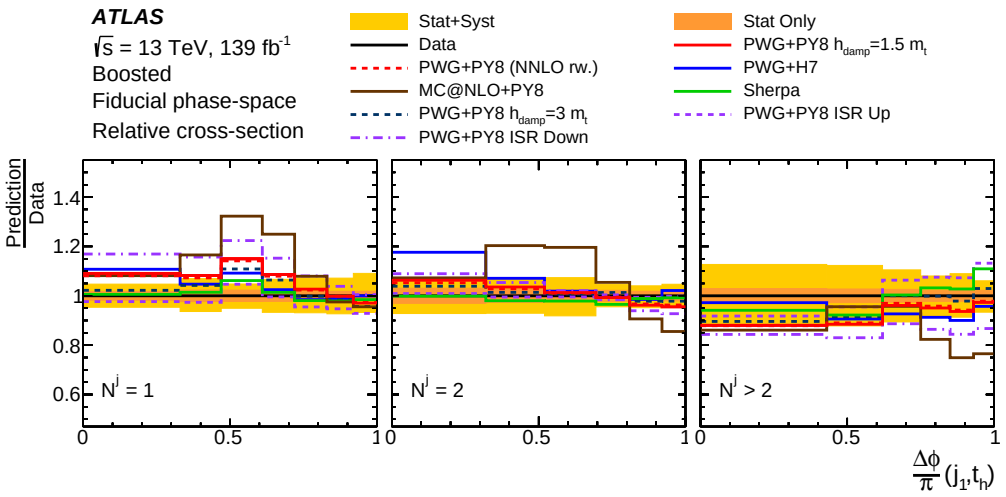

(b)

Figure A.6: Normalised double-differential cross-section measurement as a function of $\Delta\phi(j_1, t_h)$ in bins of N^j. (a) Measured differential cross-section compared directly with predictions from the POWHEG+PYTHIA8 MC event generator. The measurement and predictions are multiplied by the factors shown in parentheses to aid visibility. (b) The ratio of the measured normalised cross-section to different NLO + PS and re-weighted NNLO SM predictions. The yellow band shows the size of the total uncertainty, while the orange band shows the statistical uncertainty only.

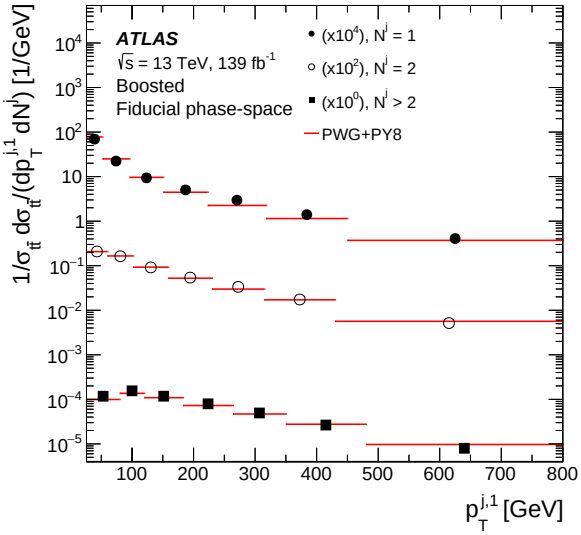

(a)

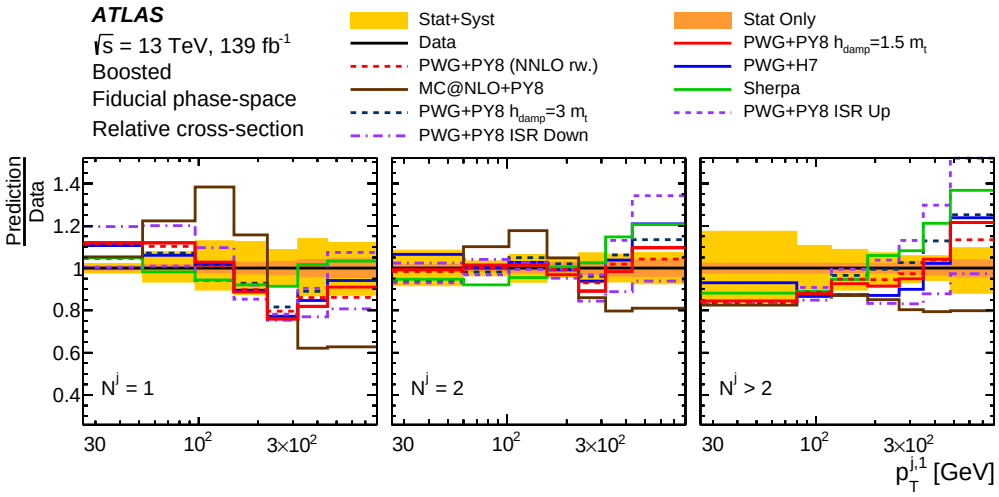

(b)

Figure A.7: Normalised double-differential cross-section measurement as a function of $p_{\mathrm{T}}^{j,1}$ in bins of N^j. (a) Measured differential cross-section compared directly with predictions from the POWHEG+PYTHIA8 MC event generator. The measurement and predictions are multiplied by the factors shown in parentheses to aid visibility. (b) The ratio of the measured normalised cross-section to different NLO + PS and re-weighted NNLO SM predictions. The yellow band shows the size of the total uncertainty, while the orange band shows the statistical uncertainty only.

Bibliography

[1] ATLAS Collaboration, *Measurements of differential cross-sections in top-quark pair events with a high transverse momentum top quark and limits on beyond the Standard Model contributions to top-quark pair production with the ATLAS detector at* $\sqrt{s} = 13\,TeV$, JHEP (2022), Submitted on: 25/02/2022, arXiv: 2202.12134 [hep-ex] (cit. on pp. vi, 72, 179).

[2] Peter W. Higgs, *Broken Symmetries and the Masses of Gauge Bosons*, Phys. Rev. Lett. **13** (16 1964) 508 (cit. on p. 4).

[3] F. Englert and R. Brout, *Broken symmetry and the masses of gauge vector mesons*, Phys. Rev. Lett. **13** (1964) 321 (cit. on p. 4).

[4] (Particle Data Group) P.A. Zyla et al., *Review of Particle Physics*, PTEP **2020** (2020) 083C01 (cit. on pp. 4–7, 10, 86).

[5] Wikimedia Commons, "Standard Model of Elementary Particles", 2021, URL: https://commons.wikimedia.org/wiki/File:Standard_Model_of_Elementary_Particles.svg (cit. on p. 5).

[6] CDF Collaboration, *Observation of top quark production in* $\bar{p}p$ *collisions*, Phys. Rev. Lett. **74** (1995) 2626, arXiv: hep-ex/9503002 [hep-ex] (cit. on p. 6).

[7] DØ Collaboration, *Search for high mass top quark production in* $p\bar{p}$ *collisions at* $\sqrt{s} = 1.8\,\text{TeV}$, Phys. Rev. Lett. **74** (1995) 2422, arXiv: hep-ex/9411001 [hep-ex] (cit. on p. 6).

[8] Makoto Kobayashi and Toshihide Maskawa, *CP Violation in the Renormalizable Theory of Weak Interaction*, Prog. Theor. Phys. **49** (1973) 652 (cit. on p. 6).

[9] Nicola Cabibbo, *Unitary Symmetry and Leptonic Decays*, Phys. Rev. Lett. **10** (1963) 531, [,648(1963)] (cit. on p. 6).

[10] S. L. Glashow, J. Iliopoulos, and L. Maiani, *Weak Interactions with Lepton-Hadron Symmetry*, Phys. Rev. D **2** (7 1970) 1285 (cit. on p. 6).

[11] Ulrich Husemann, *Top-Quark Physics: Status and Prospects*, Prog. Part. Nucl. Phys. **95** (2017) 48, arXiv: 1704.01356 [hep-ex] (cit. on p. 6).

[12] Knut Zoch, *Cross-section measurements of top-quark pair production in association with a hard photon at 13 TeV with the ATLAS detector*, 2020, arXiv: 2007.14701v3 [hep-ex] (cit. on p. 8).

[13] P. Bärnreuther, M. Czakon, and A. Mitov, *Percent-Level-Precision Physics at the Tevatron: Next-to-Next-to-Leading Order QCD Corrections to $q\bar{q} \to t\bar{t} + X$*, Phys. Rev. Lett. **109** (2012) 132001, arXiv: 1204.5201 [hep-ph] (cit. on p. 9).

[14] Michal Czakon and Alexander Mitov, *NNLO corrections to top-pair production at hadron colliders: the all-fermionic scattering channels*, JHEP **12** (2012) 054, arXiv: 1207.0236 [hep-ph] (cit. on p. 9).

[15] Michal Czakon and Alexander Mitov, *NNLO corrections to top pair production at hadron colliders: the quark-gluon reaction*, JHEP **01** (2013) 080, arXiv: 1210.6832 [hep-ph] (cit. on p. 9).

[16] Michal Czakon et al., *Total Top-Quark Pair-Production Cross Section at Hadron Colliders Through $\mathcal{O}(\alpha_S^4)$*, Phys. Rev. Lett. **110** (2013) 252004, arXiv: 1303.6254 [hep-ph] (cit. on pp. 9, 65, 73).

[17] M. Czakon et al., *Top-pair production at the LHC through NNLO QCD and NLO EW*, JHEP **10** (2017) 186, arXiv: 1705.04105 [hep-ph] (cit. on pp. 9, 65, 76).

[18] M. Beneke, P. Falgari, S. Klein, and C. Schwinn, *Hadronic top-quark pair production with NNLL threshold resummation*, Nucl. Phys. B **855** (2012) 695, arXiv: 1109.1536 [hep-ph] (cit. on p. 9).

[19] Matteo Cacciari, Michal Czakon, Michelangelo Mangano, Alexander Mitov, and Paolo Nason, *Top-pair production at hadron colliders with next-to-next-to-leading logarithmic soft-gluon resummation*, Phys. Lett. B **710** (2012) 612, arXiv: 1111.5869 [hep-ph] (cit. on p. 9).

[20] Stephen P. Martin, *A Supersymmetry Primer*, Adv. Ser. Direct. High Energy Phys. **18** (1998) 1, arXiv: hep-ph/9709356 (cit. on p. 11).

[21] Oliver Witzel, *Review on Composite Higgs Models*, PoS **LATTICE2018** (2019) 6, arXiv: 1901.08216 [hep-lat] (cit. on p. 11).

[22] Steven Weinberg, *Phenomenological Lagrangians*, Physica A: Statistical Mechanics and its Applications **96** (1979) 327, ISSN: 0378-4371 (cit. on p. 11).

[23] C.J.C. Burges and Howard J. Schnitzer, *Virtual effects of excited quarks as probes of a possible new hardonic mass scale*, Nuclear Physics B **228** (1983) 464, ISSN: 0550-3213 (cit. on p. 11).

[24] W. Buchmüller and D. Wyler, *Effective lagrangian analysis of new interactions and flavour conservation*, Nuclear Physics B **268** (1986) 621, ISSN: 0550-3213 (cit. on p. 11).

[25] C. N. Leung, S. T. Love, and S. Rao, *Low-energy manifestations of a new interactions scale: Operator analysis*, Zeitschrift für Physik C Particles and Fields **31** (1986) 433 (cit. on p. 11).

[26] Rodrigo Alonso et al., *Renormalization group evolution of the Standard Model dimension six operators III: gauge coupling dependence and phenomenology*, Journal of High Energy Physics **2014** (2014), ISSN: 1029-8479 (cit. on pp. 12, 76).

[27] Frank Krauss, Silvan Kuttimalai, and Tilman Plehn, *LHC multijet events as a probe for anomalous dimension-six gluon interactions*, Phys. Rev. D **95** (2017) 035024, arXiv: 1611.00767 [hep-ph] (cit. on p. 12).

[28] Christoph Englert, Liam Moore, Karl Nordström, and Michael Russell, *Giving top quark effective operators a boost*, Physics Letters B **763** (2016) 9, ISSN: 0370-2693 (cit. on pp. 12, 72).

[29] J. A. Aguilar Saavedra et al., *Interpreting top-quark LHC measurements in the Standard-Model effective field theory*, 2018, arXiv: 1802.07237 [hep-ph] (cit. on p. 12).

[30] Céline Degrande et al., *Automated one-loop computations in the standard model effective field theory*, Phys. Rev. D **103** (2021) 096024, arXiv: 2008.11743 [hep-ph] (cit. on pp. 12, 76).

[31] Ilaria Brivio et al., *O new physics, where art thou? A global search in the top sector*, Journal of High Energy Physics **2020** (2020), ISSN: 1029-8479 (cit. on p. 13).

[32] Lyndon Evans and Philip Bryant, *LHC Machine*, JINST **3** (2008) S08001 (cit. on p. 14).

[33] ATLAS Collaboration, *Observation of a new particle in the search for the Standard Model Higgs boson with the ATLAS detector at the LHC*, Phys. Lett. B **716** (2012) 1, arXiv: 1207.7214 [hep-ex] (cit. on p. 14).

[34] CMS Collaboration, *Observation of a new boson at a mass of 125 GeV with the CMS experiment at the LHC*, Phys. Lett. B **716** (2012) 30, arXiv: 1207.7235 [hep-ex] (cit. on p. 14).

[35] LHCb Collaboration, *The LHCb Detector at the LHC*, JINST **3** (2008) S08005 (cit. on p. 14).

[36] ALICE collaboration, *The ALICE experiment at the CERN LHC*, JINST **3** (2008) S08002 (cit. on p. 14).

[37] ATLAS Collaboration, *The ATLAS Experiment at the CERN Large Hadron Collider*, JINST **3** (2008) S08003 (cit. on pp. 14, 27).

[38] CMS Collaboration, *The CMS Experiment at the CERN LHC*, JINST **3** (2008) S08004 (cit. on p. 14).

[39] Esma Mobs, *The CERN accelerator complex - August 2018.*, (2018), URL: https://cds.cern.ch/record/2636343 (cit. on p. 15).

[40] LEP Collaboration, *The Design, construction and commissioning of the CERN Large Electron Positron collider*, Contemp. Phys. **31** (1990) 387 (cit. on p. 15).

[41] Jean-Luc Caron, "Cross section of LHC dipole.", 1998, URL: https://cds.cern.ch/record/841539 (cit. on p. 17).

[42] Oliver Sim Brüning et al., *LHC Design Report*, Geneva: CERN, 2004, URL: https://cds.cern.ch/record/782076 (cit. on p. 17).

[43] P. Grafström and W. Kozanecki, *Luminosity determination at proton colliders*, Prog. Part. Nucl. Phys. **81** (2015) 97 (cit. on p. 16).

[44] Werner Herr and B Muratori, *Concept of luminosity*, (2006), URL: https://cds.cern.ch/record/941318 (cit. on p. 17).

[45] ATLAS Collaboration, "Run-2 luminosity summary plots", Accessed on 01/12/2021, URL: https://twiki.cern.ch/twiki/bin/view/AtlasPublic/LuminosityPublicResultsRun2 (cit. on p. 18).

[46] ATLAS Collaboration, *ATLAS Detector and Physics Performance: Technical Design Report, Volume 1*, 1999, URL: https://cds.cern.ch/record/391176 (cit. on p. 18).

[47] Joao Pequenao, "Computer generated image of the whole ATLAS detector", 2008, URL: https://cds.cern.ch/record/1095924 (cit. on p. 19).

[48] Joao Pequenao and Paul Schaffner,
"How ATLAS detects particles: diagram of particle paths in the detector", 2013,
URL: https://cds.cern.ch/record/1505342 (cit. on p. 20).

[49] ATLAS Collaboration, *ATLAS Inner Detector: Technical Design Report, Volume 1*,
1997, URL: https://cds.cern.ch/record/331063 (cit. on p. 21).

[50] ATLAS Collaboration, *ATLAS Inner Detector: Technical Design Report, Volume 2*,
1997, URL: https://cds.cern.ch/record/331064 (cit. on p. 21).

[51] A Yamamoto et al., *The ATLAS central solenoid*,
Nucl. Instrum. Methods Phys. Res., A **584** (2007) 53 (cit. on p. 21).

[52] Joao Pequenao, "Computer generated image of the ATLAS inner detector",
2008, URL: https://cds.cern.ch/record/1095926 (cit. on pp. 21, 25).

[53] ATLAS Collaboration,
"Keeping the ATLAS Inner Detector in perfect alignment", 2020,
URL: https://cds.cern.ch/record/2723878 (cit. on p. 22).

[54] ATLAS Collaboration, *ATLAS Pixel Detector: Technical Design Report*, 1998,
URL: https://cds.cern.ch/record/381263 (cit. on p. 22).

[55] Alessandro La Rosa, *The ATLAS Insertable B-Layer: from construction to operation*,
JINST **11** (2016), arXiv: 1610.01994 [physics.ins-det] (cit. on p. 22).

[56] ATLAS Collaboration,
Operation and performance of the ATLAS semiconductor tracker,
JINST **9** (2014) P08009, arXiv: 1404.7473 [hep-ex] (cit. on p. 23).

[57] ATLAS TRT Collaboration, *The ATLAS Transition Radiation Tracker (TRT)
proportional drift tube: Design and performance*, JINST **3** (2008) P02013
(cit. on p. 23).

[58] S. Denisov, *Transition radiation: scientific implications and applications
in high-energy physics*, Physics-Uspekhi **50** (2007) 377 (cit. on p. 24).

[59] ATLAS Collaboration, *ATLAS Calorimeter Performance: Technical Design Report*,
1996, URL: https://cds.cern.ch/record/331059 (cit. on p. 24).

[60] ATLAS Collaboration, *ATLAS Liquid Argon Calorimeter: Technical Design Report*,
1996, URL: https://cds.cern.ch/record/331061 (cit. on pp. 24, 25).

[61] ATLAS Collaboration, *ATLAS Tile Calorimeter: Technical Design Report*, 1996,
URL: https://cds.cern.ch/record/331062 (cit. on p. 25).

[62] ATLAS Collaboration, *ATLAS Muon Spectrometer: Technical Design Report*, CERN, 1997, URL: https://cds.cern.ch/record/331068 (cit. on p. 26).

[63] Joao Pequenao, "Computer generated image of the ATLAS Muons subsystem", 2008, URL: https://cds.cern.ch/record/1095929 (cit. on p. 26).

[64] R.J.M.Y. Ruber, "ATLAS Magnet System: leaflet", 2005, URL: http://cern.ch/atlas-magnet (cit. on p. 27).

[65] ATLAS Collaboration, *Performance of the ATLAS muon trigger in pp collisions at* $\sqrt{s} = 8\,\mathrm{TeV}$, Eur. Phys. J. C **75** (2015) 120, arXiv: 1408.3179 [hep-ex] (cit. on p. 29).

[66] ATLAS Collaboration, *Performance of the ATLAS trigger system in 2015*, Eur. Phys. J. C **77** (2017) 317, arXiv: 1611.09661 [hep-ex] (cit. on pp. 29, 31).

[67] ATLAS TDAQ Collaboration, *The ATLAS Data Acquisition and High Level Trigger system*, JINST **11** (2016) P06008 (cit. on p. 30).

[68] ATLAS Collaboration, *Expected performance of the ATLAS experiment: detector, trigger and physics*, Geneva: CERN, 2009, URL: https://cds.cern.ch/record/1125884 (cit. on p. 33).

[69] ATLAS Collaboration, *Performance of the ATLAS muon triggers in Run 2*, JINST **15** (2020) P09015, arXiv: 2004.13447 [hep-ex] (cit. on pp. 38, 73).

[70] ATLAS TDAQ Collaboration, *Data Quality Monitoring Framework for ATLAS Experiment: Performance Achieved with Colliding Beams at LHC*, J. Phys. Conference Series **331** (2011) 022027 (cit. on p. 39).

[71] ATLAS TDAQ Collaboration., *The online histogram presenter for the ATLAS experiment: A modular system for histogram visualization*, J. Phys. Conference Series **219** (2010) 032037 (cit. on p. 39).

[72] Rene Brun and Fons Rademakers, *ROOT – An object oriented data analysis framework*, Nucl. Instrum. Meth. A **389** (1997) 81, ISSN: 0168-9002 (cit. on p. 39).

[73] ATLAS Collaboration, "Boosted top quark pair candidate event recorded in 2015.", Accessed on 10/08/2021, URL: https://twiki.cern.ch/twiki/pub/AtlasPublic/TopPublicResults/event_display_ttbar_13TeV_boosted_Sep2015.png (cit. on p. 42).

[74] ATLAS Collaboration, *Performance of the ATLAS track reconstruction algorithms in dense environments in LHC Run 2*, Eur. Phys. J. C **77** (2017) 673, arXiv: 1704.07983 [hep-ex] (cit. on p. 42).

[75] R. Frühwirth, *Application of Kalman filtering to track and vertex fitting*, Nuclear Instruments and Methods in Physics Research **262** (1987) 444 (cit. on p. 43).

[76] ATLAS Collaboration, *A neural network clustering algorithm for the ATLAS silicon pixel detector*, JINST **9** (2014) P09009, arXiv: 1406.7690 [hep-ex] (cit. on p. 43).

[77] J. Illingworth and J. Kittler, *A survey of the hough transform*, Computer Vision, Graphics, and Image Processing **44** (1988) 87, ISSN: 0734-189X (cit. on p. 44).

[78] ATLAS Collaboration, *Muon reconstruction performance of the ATLAS detector in proton–proton collision data at* $\sqrt{s} = 13\,TeV$, Eur. Phys. J. C **76** (2016) 292, arXiv: 1603.05598 [hep-ex] (cit. on p. 44).

[79] ATLAS Collaboration, *Topological cell clustering in the ATLAS calorimeters and its performance in LHC Run 1*, Eur. Phys. J. C **77** (2017) 490, arXiv: 1603.02934 [hep-ex] (cit. on p. 45).

[80] ATLAS Collaboration, *Jet reconstruction and performance using particle flow with the ATLAS Detector*, Eur. Phys. J. C **77** (2017) 466, arXiv: 1703.10485 [hep-ex] (cit. on pp. 46–48, 57).

[81] ATLAS Collaboration, *Electron and photon performance measurements with the ATLAS detector using the 2015–2017 LHC proton–proton collision data*, JINST **14** (2019) P12006, arXiv: 1908.00005 [hep-ex] (cit. on pp. 47–49).

[82] Andreas Hoecker et al., *TMVA - Toolkit for Multivariate Data Analysis*, 2007, arXiv: physics/0703039 [physics.data-an] (cit. on p. 48).

[83] ATLAS Collaboration, *Electron reconstruction and identification in the ATLAS experiment using the 2015 and 2016 LHC proton–proton collision data at* $\sqrt{s} = 13\,TeV$, Eur. Phys. J. C **79** (2019) 639, arXiv: 1902.04655 [hep-ex] (cit. on p. 49).

[84] ATLAS Collaboration, *Performance of electron and photon triggers in ATLAS during LHC Run 2*, Eur. Phys. J. C **80** (2020) 47, arXiv: 1909.00761 [hep-ex] (cit. on pp. 49, 73).

[85] ATLAS Collaboration, *Electron and photon energy calibration with the ATLAS detector using 2015–2016 LHC proton–proton collision data*, JINST **14** (2019) P03017, arXiv: 1812.03848 [hep-ex] (cit. on p. 50).

[86] ATLAS Collaboration, *Muon reconstruction and identification efficiency in ATLAS using the full Run 2 pp collision data set at* $\sqrt{s} = 13\,\text{TeV}$, Eur. Phys. J. C **81** (2020) 578, arXiv: 2012.00578 [hep-ex] (cit. on pp. 50, 51).

[87] Gavin P. Salam, *Towards Jetography*, Eur. Phys. J. **C67** (2010) 637, arXiv: 0906.1833 [hep-ph] (cit. on p. 52).

[88] M. Cacciari, G. P. Salam, and G. Soyez, *The anti-k_t jet clustering algorithm*, JHEP **04** (2008) 063, arXiv: 0802.1189 [hep-ph] (cit. on p. 52).

[89] ATLAS Collaboration, *Jet energy scale and resolution measured in proton–proton collisions at* $\sqrt{s} = 13\,\text{TeV}$ *with the ATLAS detector*, Eur. Phys. J. C **81** (2020) 689, arXiv: 2007.02645 [hep-ex] (cit. on pp. 53, 56, 58).

[90] ATLAS Collaboration, *A measurement of the calorimeter response to single hadrons and determination of the jet energy scale uncertainty using LHC Run-1 pp-collision data with the ATLAS detector*, Eur. Phys. J. C **77** (2017) 26, arXiv: 1607.08842 [hep-ex] (cit. on p. 55).

[91] ATLAS Collaboration, *Performance of pile-up mitigation techniques for jets in pp collisions at* $\sqrt{s} = 8\,\text{TeV}$ *using the ATLAS detector*, Eur. Phys. J. C **76** (2016) 581, arXiv: 1510.03823 [hep-ex] (cit. on p. 58).

[92] ATLAS Collaboration, *ATLAS b-jet identification performance and efficiency measurement with $t\bar{t}$ events in pp collisions at* $\sqrt{s} = 13\,\text{TeV}$, Eur. Phys. J. C **79** (2019) 970, arXiv: 1907.05120 [hep-ex] (cit. on pp. 58, 59).

[93] ATLAS collaboration, "Expected performance of the 2019 ATLAS *b*-taggers", Summary plots: figures 03a and 03b, 2019, URL: http://atlas.web.cern.ch/Atlas/GROUPS/PHYSICS/PLOTS/FTAG-2019-005/ (cit. on p. 59).

[94] Benjamin Nachman, Pascal Nef, Ariel Schwartzman, Maximilian Swiatlowski, and Chaowaroj Wanotayaroj, *Jets from Jets: Re-clustering as a tool for large radius jet reconstruction and grooming at the LHC*, JHEP **02** (2015) 075, arXiv: 1407.2922 [hep-ph] (cit. on p. 59).

[95] David Krohn, Jesse Thaler, and Lian-Tao Wang, *Jet Trimming*, JHEP **02** (2010) 084, arXiv: 0912.1342 [hep-ph] (cit. on p. 59).

[96] ATLAS Collaboration, *Performance of missing transverse momentum reconstruction with the ATLAS detector using proton–proton collisions at* $\sqrt{s} = 13\,\mathrm{TeV}$, Eur. Phys. J. C **78** (2018) 903, arXiv: 1802.08168 [hep-ex] (cit. on p. 60).

[97] Benjamin Nachman, *Investigating the Quantum Properties of Jets and the Search for a Supersymmetric Top Quark Partner with the ATLAS Detector*, 2016, arXiv: 1609.03242 [hep-ex] (cit. on p. 63).

[98] R. K. Ellis, W. J. Stirling, and B. R. Webber, *QCD and Collider Physics*, Cambridge University Press, 1996 (cit. on p. 64).

[99] ZEUS Collaboration, *The ZEUS detector: Technical proposal*, 1986, URL: https://cds.cern.ch/record/1478623 (cit. on p. 64).

[100] H1 Collaboration, *Technical proposal for the H1 detector*, Hamburg: DESY, 1986, URL: https://cds.cern.ch/record/108544 (cit. on p. 64).

[101] V N Gribov and L N Lipatov, *Deep inelastic ep scattering in perturbation theory*, Sov. J. Nucl. Phys. **15** (1972) 438 (cit. on p. 64).

[102] Y. L. Dokshitzer, *Calculation of the Structure Functions for Deep Inelastic Scattering and* e^+e^- *Annihilation by Perturbation Theory in QCD*, Sov. Phys. JETP **46** (1977) 641 (cit. on p. 64).

[103] Guido Altarelli and Giorgio Parisi, *Asymptotic Freedom in Parton Language*, Nuclear Physics B **126** (1977) 298, ISSN: 0550-3213 (cit. on p. 64).

[104] Andy Buckley et al., *General-purpose event generators for LHC physics*, Physics Reports **504** (2011) 145, ISSN: 0370-1573 (cit. on pp. 65–67).

[105] M. Czakon and A. Mitov, *Top++: A program for the calculation of the top-pair cross-section at hadron colliders*, Comput. Phys. Commun. **185** (2014) 2930, arXiv: 1112.5675 [hep-ph] (cit. on pp. 65, 73, 144, 148, 171).

[106] Stefan Höche, Frank Krauss, Marek Schönherr, and Frank Siegert, *QCD matrix elements + parton showers. The NLO case*, JHEP **04** (2013) 027, arXiv: 1207.5030 [hep-ph] (cit. on pp. 65, 75).

[107] Frank Krauss, *Matrix Elements and Parton Showers in Hadronic Interactions*, JHEP **08** (2002) 015, arXiv: hep-ph/0205283 (cit. on p. 65).

[108] Enrico et al Bothmann, *Event Generation with Sherpa 2.2*, SciPost Phys. **7** (2019) 034, arXiv: 1905.09127 [hep-ph] (cit. on pp. 65, 75).

[109] Stefan Höche, Frank Krauss, Steffen Schumann, and Frank Siegert, *QCD matrix elements and truncated showers*, JHEP **05** (2009) 053, arXiv: 0903.1219 [hep-ph] (cit. on pp. 65, 75).

[110] Johannes Bellm et al., *Herwig 7.0/Herwig++ 3.0 release note*, Eur. Phys. J. C **76** (2016) 196, arXiv: 1512.01178 [hep-ph] (cit. on pp. 66, 75).

[111] Torbjörn Sjöstrand et al., *An introduction to PYTHIA 8.2*, Comput. Phys. Commun. **191** (2015) 159, arXiv: 1410.3012 [hep-ph] (cit. on pp. 66, 73, 74, 76, 77).

[112] Steffen Schumann and Frank Krauss, *A parton shower algorithm based on Catani–Seymour dipole factorisation*, JHEP **03** (2008) 038, arXiv: 0709.1027 [hep-ph] (cit. on pp. 66, 75, 78).

[113] Stefano Frixione, Paolo Nason, and Carlo Oleari, *Matching NLO QCD computations with parton shower simulations: the POWHEG method*, JHEP **11** (2007) 070, arXiv: 0709.2092 [hep-ph] (cit. on pp. 66, 74).

[114] S. Frixione and B. R. Webber, *Matching NLO QCD computations and parton shower simulations*, JHEP **06** (2002) 029, arXiv: hep-ph/0204244 [hep-ph] (cit. on p. 66).

[115] Torbjorn Sjöstrand, *Jet fragmentation of multiparton configurations in a string framework*, Nucl. Phys. B **248** (1984) 469 (cit. on p. 67).

[116] M. Bähr et al., *Herwig++ physics and manual*, Eur. Phys. J. C **58** (2008) 639, arXiv: 0803.0883 [hep-ph] (cit. on pp. 67, 75).

[117] GEANT4 Collaboration, S. Agostinelli, et al., GEANT4 – *a simulation toolkit*, Nucl. Instrum. Meth. A **506** (2003) 250 (cit. on p. 68).

[118] ATLAS Collaboration, *The simulation principle and performance of the ATLAS fast calorimeter simulation FastCaloSim*, ATL-PHYS-PUB-2010-013, 2010, URL: https://cds.cern.ch/record/1300517 (cit. on p. 69).

[119] ATLAS Collaboration, *AtlFast3: the next generation of fast simulation in ATLAS*, Target journal: CSBS, 2021, arXiv: 2109.02551 [hep-ex] (cit. on p. 69).

[120] Céline Degrande et al., *Non-resonant new physics in top pair production at hadron colliders*, Journal of High Energy Physics **2011** (2011), ISSN: 1029-8479 (cit. on p. 72).

[121] Martin Perello Rosello and Marcel Vos, *Constraints on four-fermion interactions from the $t\bar{t}$ charge asymmetry at hadron colliders*, Eur. Phys. J. C **76** (2016) 200, arXiv: 1512.07542 [hep-ex] (cit. on p. 72).

[122] ATLAS Collaboration, *Measurement of the differential cross-section of highly boosted top quarks as a function of their transverse momentum in $\sqrt{s} = 8$ TeV proton–proton collisions using the ATLAS detector*, Phys. Rev. D **93** (2016) 032009, arXiv: 1510.03818 [hep-ex] (cit. on pp. 72, 86, 121, 153).

[123] ATLAS Collaboration, *Measurements of top-quark pair differential cross-sections in the lepton+jets channel in pp collisions at ($\sqrt{s} = 13$ TeV) using the ATLAS detector*, JHEP **11** (2017) 191, arXiv: 1708.00727 [hep-ex] (cit. on pp. 72, 86, 90, 121, 153).

[124] ATLAS Collaboration, *Measurements of top-quark pair differential and double-differential cross-sections in the ℓ+jets channel with pp collisions at ($\sqrt{s} = 13$ TeV) using the ATLAS detector*, Eur. Phys. J. C **79** (2019) 1028, arXiv: 1908.07305 [hep-ex] (cit. on pp. 72, 84, 86, 90, 121, 132, 153, 165, 180).

[125] CMS Collaboration, *Measurement of the integrated and differential $t\bar{t}$ production cross sections for high-p_T top quarks in pp collisions at $\sqrt{s} = 8$ TeV*, Phys. Rev. D **94** (2016) 072002, arXiv: 1605.00116 [hep-ex] (cit. on pp. 72, 153).

[126] CMS Collaboration, *Measurement of differential $t\bar{t}$ production cross sections in the full kinematic range using lepton+jets events from proton-proton collisions at $\sqrt{s} = 13$ TeV*, Phys. Rev. D **104** (2021) 092013, arXiv: 2108.02803 [hep-ex] (cit. on pp. 72, 153, 166).

[127] ATLAS Collaboration, *Measurements of $t\bar{t}$ differential cross-sections of highly boosted top quarks decaying to all-hadronic final states in pp collisions at $\sqrt{s} = 13$ TeV using the ATLAS detector*, Phys. Rev. D **98** (2018) 012003, arXiv: 1801.02052 [hep-ex] (cit. on p. 72).

[128] ATLAS Collaboration, *Measurements of top-quark pair single- and double-differential cross-sections in the all-hadronic channel in pp collisions at $\sqrt{s} = 13$ TeV using the ATLAS detector*, JHEP **01** (2021) 033, arXiv: 2006.09274 [hep-ex] (cit. on pp. 72, 132).

[129] CMS Collaboration, *Measurement of differential $t\bar{t}$ production cross sections using top quarks at large transverse momenta in pp collisions at $\sqrt{s} = 13$ TeV*, Phys. Rev. D **103** (2021) 052008, arXiv: 2008.07860 [hep-ex] (cit. on pp. 72, 153).

[130] ATLAS Collaboration, *Inclusive and differential measurement of the charge asymmetry in $t\bar{t}$ events at 13 TeV with the ATLAS detector*, ATLAS-CONF-2019-026, Conference publication, 2019, URL: https://cds.cern.ch/record/2682109 (cit. on p. 73).

[131] ATLAS Collaboration, *Measurement of the energy asymmetry in $t\bar{t}j$ production at 13 TeV with the ATLAS experiment and interpretation in the SMEFT framework*, (2021), arXiv: 2110.05453 [hep-ex] (cit. on p. 73).

[132] ATLAS Collaboration, *ATLAS data quality operations and performance for 2015–2018 data-taking*, JINST **15** (2020) P04003, arXiv: 1911.04632 [physics.ins-det] (cit. on p. 73).

[133] G. Avoni et al., *The new LUCID-2 detector for luminosity measurement and monitoring in ATLAS*, JINST **13** (2018) P07017 (cit. on p. 73).

[134] ATLAS Collaboration, *Luminosity determination in pp collisions at $\sqrt{s} = 13$ TeV using the ATLAS detector at the LHC*, ATLAS-CONF-2019-021, 2019, URL: https://cds.cern.ch/record/2677054 (cit. on p. 73).

[135] ATLAS Collaboration, *The Pythia 8 A3 tune description of ATLAS minimum bias and inelastic measurements incorporating the Donnachie–Landshoff diffractive model*, ATL-PHYS-PUB-2016-017, 2016, URL: https://cds.cern.ch/record/2206965 (cit. on p. 73).

[136] Paolo Nason, *A new method for combining NLO QCD with shower Monte Carlo algorithms*, JHEP **11** (2004) 040, arXiv: hep-ph/0409146 (cit. on p. 74).

[137] Simone Alioli et al., *A general framework for implementing NLO calculations in shower Monte Carlo programs: the POWHEG BOX*, JHEP **06** (2010) 043, arXiv: 1002.2581 [hep-ph] (cit. on p. 74).

[138] Richard D. Ball et al., *Parton distributions for the LHC run II*, JHEP **04** (2015) 040, arXiv: 1410.8849 [hep-ph] (cit. on pp. 74–76).

[139] ATLAS Collaboration, *ATLAS Pythia 8 tunes to 7 TeV data*, ATL-PHYS-PUB-2014-021, 2014, URL: https://cds.cern.ch/record/1966419 (cit. on pp. 74, 75).

[140] Richard D. Ball et al., *Parton distributions with LHC data*, Nucl. Phys. B **867** (2013) 244, arXiv: 1207.1303 [hep-ph] (cit. on p. 74).

[141] D. J. Lange, *The EvtGen particle decay simulation package*, Nucl. Instrum. Meth. A **462** (2001) 152 (cit. on pp. 74, 77).

[142] J. Alwall et al., *The automated computation of tree-level and next-to-leading order differential cross sections, and their matching to parton shower simulations*, JHEP **07** (2014) 079, arXiv: 1405.0301 [hep-ph] (cit. on pp. 75, 77).

[143] ATLAS Collaboration, *Studies on top-quark Monte Carlo modelling with Sherpa and MG5_aMC@NLO*, ATL-PHYS-PUB-2017-007, 2017, URL: https://cds.cern.ch/record/2261938 (cit. on p. 75).

[144] Stefano Frixione, Eric Laenen, Patrick Motylinski, and Bryan R. Webber, *Angular correlations of lepton pairs from vector boson and top quark decays in Monte Carlo simulations*, JHEP **04** (2007) 081, arXiv: hep-ph/0702198 (cit. on p. 75).

[145] Pierre Artoisenet, Rikkert Frederix, Olivier Mattelaer, and Robbert Rietkerk, *Automatic spin-entangled decays of heavy resonances in Monte Carlo simulations*, JHEP **03** (2013) 015, arXiv: 1212.3460 [hep-ph] (cit. on p. 75).

[146] L.A. Harland-Lang, A.D. Martin, P. Motylinski, and R.S. Thorne, *Parton distributions in the LHC era: MMHT 2014 PDFs*, Eur. Phys. J. C **75** (2015) 204, arXiv: 1412.3989 [hep-ph] (cit. on p. 75).

[147] Tanju Gleisberg and Stefan Höche, *Comix, a new matrix element generator*, JHEP **12** (2008) 039, arXiv: 0808.3674 [hep-ph] (cit. on pp. 75, 78).

[148] Federico Buccioni et al., *OpenLoops 2*, Eur. Phys. J. C **79** (2019) 866, arXiv: 1907.13071 [hep-ph] (cit. on p. 75).

[149] Fabio Cascioli, Philipp Maierhöfer, and Stefano Pozzorini, *Scattering Amplitudes with Open Loops*, Phys. Rev. Lett. **108** (2012) 111601, arXiv: 1111.5206 [hep-ph] (cit. on p. 75).

[150] A. Denner et al., COLLIER*: A fortran-based complex one-loop library in extended regularizations*, Comput. Phys. Commun. **212** (2017) 220, arXiv: 1604.06792 [hep-ph] (cit. on p. 75).

[151] Stefan Höche, Frank Krauss, Marek Schönherr, and Frank Siegert, *A critical appraisal of NLO+PS matching methods*, JHEP **09** (2012) 049, arXiv: 1111.1220 [hep-ph] (cit. on p. 75).

[152] S. Catani, F. Krauss, B. R. Webber, and R. Kuhn,
QCD Matrix Elements + Parton Showers, JHEP **11** (2001) 063,
arXiv: hep-ph/0109231 (cit. on p. 75).

[153] L. Serkin, "Treatment of top-quark backgrounds in extreme phase spaces: The "top p_{T} reweighting" and novel data-driven estimations in ATLAS and CMS",
13th International Workshop on Top Quark Physics, 2021,
arXiv: 2105.03977 [hep-ex] (cit. on p. 76).

[154] Stefano Catani et al.,
Top-quark pair production at the LHC: Fully differential QCD predictions at NNLO,
JHEP **07** (2019) 100, arXiv: 1906.06535 [hep-ph] (cit. on p. 76).

[155] Massimiliano Grazzini, Stefan Kallweit, and Marius Wiesemann,
Fully differential NNLO computations with MATRIX, Eur. Phys. J. C **78** (2018) 537,
arXiv: 1711.06631 [hep-ph] (cit. on p. 76).

[156] Ilaria Brivio et al., *Electroweak input parameters*,
CERN-LHCEFTWG-2021-001, CERN-LPCC-2021-002, 2021, arXiv: 2111.12515,
URL: https://cds.cern.ch/record/2792440 (cit. on p. 76).

[157] Stefano Frixione et al., *Single-top hadroproduction in association with a W boson*,
JHEP **07** (2008) 029, arXiv: 0805.3067 [hep-ph] (cit. on p. 77).

[158] ATLAS Collaboration, *Studies on top-quark Monte Carlo modelling for Top2016*,
ATL-PHYS-PUB-2016-020, 2016, URL: https://cds.cern.ch/record/2216168
(cit. on p. 77).

[159] C. Anastasiou et al., *High precision QCD at hadron colliders: Electroweak gauge boson rapidity distributions at next-to-next-to leading order*,
Phys. Rev. D **69** (2004) 094008, arXiv: hep-ph/0312266 (cit. on p. 77).

[160] ATLAS Collaboration,
Estimation of non-prompt and fake lepton backgrounds in final states with top quarks produced in proton–proton collisions at $\sqrt{s} = 8$ *TeV with the ATLAS Detector*, ATLAS-CONF-2014-058, 2014,
URL: https://cds.cern.ch/record/1951336 (cit. on p. 81).

[161] Matteo Cacciari, Gavin P. Salam, and Gregory Soyez, *The Catchment Area of Jets*,
JHEP **04** (2008) 005, arXiv: 0802.1188 [hep-ph] (cit. on p. 83).

[162] ATLAS Collaboration,
Probing the Quantum Interference between Singly and Doubly Resonant Top-Quark Production in pp Collisions at $\sqrt{s} = 13$ TeV with the ATLAS Detector,
Phys. Rev. Lett. **121** (2018) 152002, arXiv: 1806.04667 [hep-ex] (cit. on p. 84).

[163] Michał Czakon et al., *Pinning down the large-x gluon with NNLO top-quark pair differential distributions*, JHEP **04** (2017) 044, arXiv: 1611.08609 [hep-ph] (cit. on p. 90).

[164] Giulio D'Agostini, *A multidimensional unfolding method based on Bayes' theorem*, Nucl. Instrum. Meth. A **362** (1995) 487, ISSN: 0168-9002 (cit. on p. 101).

[165] Tim Adye, "Unfolding algorithms and tests using RooUnfold", *PHYSTAT 2011* (CERN, Geneva, Switzerland, Jan. 17–20, 2011) 313,
arXiv: 1105.1160 [physics.data-an] (cit. on p. 101).

[166] Stefan Schmitt, *Data Unfolding Methods in High Energy Physics*,
EPJ Web Conf. **137** (2017) 11008, arXiv: 1611.01927 [physics.data-an] (cit. on p. 109).

[167] ATLAS Collaboration, *Jet reclustering and close-by effects in ATLAS Run 2*,
ATLAS-CONF-2017-062, 2017, URL: https://cds.cern.ch/record/2275649 (cit. on p. 122).

[168] D. de Florian et al., *Handbook of LHC Higgs Cross Sections: 4. Deciphering the Nature of the Higgs Sector*, (2016), arXiv: 1610.07922 [hep-ph] (cit. on p. 123).

[169] ATLAS Collaboration, *Measurement of the $t\bar{t}$ production cross-section in the lepton+jets channel at $\sqrt{s} = 13$ TeV with the ATLAS experiment*,
Phys. Lett. B **810** (2020) 135797, arXiv: 2006.13076 [hep-ex] (cit. on pp. 123, 124, 132).

[170] Nikolaos Kidonakis, *Next-to-next-to-next-to-leading-order soft-gluon corrections in hard-scattering processes near threshold*, Physical Review D **73** (2006) 22,
arXiv: hep-ph/0509079 [hep-ph] (cit. on p. 124).

[171] LHCTopWG, *NLO single-top channel cross sections*, 2017, URL:
https://twiki.cern.ch/twiki/bin/view/LHCPhysics/SingleTopRefXsec (cit. on p. 124).

[172] M. Aliev et al., *HATHOR – HAdronic Top and Heavy quarks crOss section calculatoR*, Comput. Phys. Commun. **182** (2011) 1034,
arXiv: 1007.1327 [hep-ph] (cit. on p. 124).

[173] P. Kant et al., HATHOR *for single top-quark production: Updated predictions and uncertainty estimates for single top-quark production in hadronic collisions*, Comput. Phys. Commun. **191** (2015) 74, arXiv: 1406.4403 [hep-ph] (cit. on p. 124).

[174] ATLAS Collaboration, *Measurement of the top quark mass in the $t\bar{t} \to$ lepton+jets channel from $\sqrt{s} = 8$ TeV ATLAS data and combination with previous results*, Eur. Phys. J. C **79** (2019) 290, arXiv: 1810.01772 [hep-ex] (cit. on pp. 130, 132, 133).

[175] CMS Collaboration, *Measurement of the top quark mass using proton–proton data at $\sqrt{s} = 7$ and 8 TeV*, Phys. Rev. D **93** (2016) 072004, arXiv: 1509.04044 [hep-ex] (cit. on pp. 130, 133).

[176] Jon Butterworth et al., *PDF4LHC recommendations for LHC Run II*, J. Phys. G **43** (2016) 023001, arXiv: 1510.03865 [hep-ph] (cit. on p. 131).

[177] William Buttinger, *Using Event Weights to account for differences in Instantaneous Luminosity and Trigger Prescale in Monte Carlo and Data*, 2015, URL: https://cds.cern.ch/record/2014726 (cit. on p. 131).

[178] CMS Collaboration, *Measurement of the cross section for $t\bar{t}$ production with additional jets and b jets in pp collisions at $\sqrt{s} = 13$ TeV*, JHEP **07** (2020) 125, arXiv: 2003.06467 [hep-ex] (cit. on p. 132).

[179] CMS Collaboration, *Measurement of differential cross sections for the production of top quark pairs and of additional jets in lepton+jets events from pp collisions at $\sqrt{s} = 13$ TeV*, Phys. Rev. D **97** (2018) 112003, arXiv: 1803.08856 [hep-ex] (cit. on p. 132).

[180] CDF Collaboration, *Top quark mass measurement using the template method in the lepton + jets channel at CDF II*, Phys. Rev. D **73** (2006) 032003, arXiv: hep-ex/0510048 (cit. on p. 133).

[181] DØ Collaboration, *Precision Measurement of the Top Quark Mass in Lepton + Jets Final States*, Phys. Rev. Lett. **113** (3 2014) 032002 (cit. on p. 133).

[182] ATLAS Collaboration, *Measurement of the top quark mass with the template method in the $t\bar{t} \to$ lepton + jets channel using ATLAS data*, Eur. Phys. J. C **72** (2012) 2046, arXiv: 1203.5755 [hep-ex] (cit. on p. 133).

[183] ATLAS Collaboration, *Measurement of the top quark mass in the $t\bar{t} \to$ lepton+jets and $t\bar{t} \to$ dilepton channels using $\sqrt{s} = 7$ TeV ATLAS data*, Eur. Phys. J. C **75** (2015) 330, arXiv: 1503.05427 [hep-ex] (cit. on p. 133).

[184] CMS Collaboration, *Measurement of the top-quark mass in $t\bar{t}$ events with lepton+jets final states in pp collisions at $\sqrt{s} = 7$ TeV*, JHEP **12** (2012) 105, arXiv: 1209.2319 [hep-ex] (cit. on p. 133).

[185] CMS Collaboration, *Measurement of the top quark mass with lepton+jets final states using pp collisions at $\sqrt{s} = 13$ TeV*, Eur. Phys. J. C **78** (2018) 891, arXiv: 1805.01428 [hep-ex] (cit. on p. 133).

[186] James Gentle, "Cholesky Factorization", *Numerical Linear Algebra for Applications in Statistics*, Berlin: Springer-Verlag, 1998 93 (cit. on p. 150).

[187] *Behind The Models: Cholesky Decomposition*, https://towardsdatascience.com, Accessed: 24/11/2021 (cit. on p. 150).

[188] ATLAS Collaboration, *Differential $t\bar{t}$ cross-section measurements using boosted top quarks in the all-hadronic final state with 139 fb^{-1} of ATLAS data*, ATLAS-CONF-2021-050, Conference publication, 2021, URL: http://cds.cern.ch/record/2782534 (cit. on pp. 167, 168, 181).

[189] N. Castro, J. Erdmann, C. Grunwald, K. Kröninger, and N. Rosien, *EFTfitter—A tool for interpreting measurements in the context of effective field theories*, Eur. Phys. J. C **76** (2016) 432, arXiv: 1605.05585 [hep-ex] (cit. on p. 170).

[190] Allen Caldwell, Daniel Kollar, and Kevin Kroninger, *BAT: The Bayesian Analysis Toolkit*, Comput. Phys. Commun. **180** (2009) 2197, arXiv: 0808.2552 [physics.data-an] (cit. on p. 172).

[191] Jacob J. Ethier et al., *Combined SMEFT interpretation of Higgs, diboson, and top quark data from the LHC*, JHEP **11** (2021) 089, arXiv: 2105.00006 [hep-ph] (cit. on p. 176).

[192] Javier Mazzitelli et al., *Next-to-Next-to-Leading Order Event Generation for Top-Quark Pair Production*, Phys. Rev. Lett. **127** (2021) 062001, arXiv: 2012.14267 [hep-ph] (cit. on p. 180).

[193] ATLAS Collaboration, *Measurement of the $t\bar{t}$ production cross-section and lepton differential distributions in $e\mu$ dilepton events from pp collisions at $\sqrt{s} = 13$ TeV with the ATLAS detector*, Eur. Phys. J. C **80** (2020) 528, arXiv: 1910.08819 [hep-ex] (cit. on p. 181).

[194] CERN. Geneva. BE Department, *LHC_Schedule_2021*, https://lhc-commissioning.web.cern.ch/schedule/LHC-long-term.htm, [Online; accessed 18-December-2021], 2021 (cit. on p. 181).

Glossary of acronyms

BSM	Beyond (the) Standard Model	11, 60, 73, 104, 169, 180
CR	Control Region	125, 126
CSC	Cathode Strip Chamber	26, 28
DNN	Deep Neural Network	58
DQMD	Data Quality Monitoring Display	39
DR	Diagram Removal	77, 84, 124, 127, 132, 140
DS	Diagram Subtraction	77, 84, 124, 127, 132, 140
ECAL	Electromagnetic Calorimeter	24, 25
EFT	Effective Field Theory	11, 12, 72, 76, 77, 95, 96, 119, 169, 170, 171, 173, 174, 175, 176, 178, 180
EM	Electromagnetic	3, 4, 24, 25, 45, 47, 48, 50, 54
EW	Electroweak	3, 76, 171, 179
FCAL	Forward Calorimeter	24, 25
FSR	Final State Radiation	75, 95, 127, 129, 140
GSC	Global Sequential Calibration	54, 56, 57
HCAL	Hadronic Calorimeter	24, 25
HLT	High Level Trigger	30, 31, 33, 34

IBL	Insertable *b* Layer	22, 23
IBU	Iterative Bayesian Unfolding	101, 104, 105, 111
ID	Inner Detector	21, 22, 24, 30, 32, 43, 44, 48, 50, 51, 60, 122
IP	Interaction Point	19, 20, 31
IR	Infrared	65, 66
ISR	Initial State Radiation	74, 95, 127, 129, 140, 150, 156, 185
JER	Jet Energy Resolution	56, 57, 122, 132, 140
JES	Jet Energy Scale	54, 55, 56, 57, 122, 132, 133, 139, 140, 141, 143, 165, 167
JSF	Jet Scale Factor	79, 83, 133, 134, 135, 136, 137, 139, 140, 141, 142, 143, 144, 166, 167, 181
JVT	Jet Vertex Tagger	57, 122, 140
LAR	Liquid Argon (calorimeter)	24, 25, 54
LCW	Local Cell Weighting	45
LO	Leading Order	9, 65, 75, 78, 180
MC	Monte-Carlo	61, 66, 68, 73, 74, 75, 78, 80, 92, 93, 94, 103, 104, 107, 111, 113, 114, 116, 117, 118, 120, 121, 122, 123, 124, 125, 126, 129, 131, 134, 135, 136, 140, 146, 147, 149, 150, 153, 161, 162, 163, 164, 166, 171, 180, 185, 189, 190, 191, 192
MDT	Monitored Drift Tube	26, 27, 28, 29, 32, 38, 44, 50
ME	Matrix Element	61, 65, 66, 75, 160
MPI	Multiple Parton Interactions	63, 68

MS	Muon Spectrometer	26, 28, 32, 44, 50, 51
NDF	Number of Degrees of Freedom	114, 115, 150
NLO	Next-to-Leading Order	9, 65, 66, 74, 75, 76, 78, 86, 93, 147, 148, 150, 151, 152, 153, 154, 155, 156, 157, 159, 160, 161, 162, 163, 164, 171, 179, 180, 185, 186, 187, 188, 189, 190, 191, 192
NNLL	Next-to-Next-to-Leading Logarithm	9, 73, 75, 76, 144, 148, 150, 171
NNLO	Next-to-Next-to-Leading Order	9, 65, 73, 75, 76, 124, 144, 147, 148, 150, 151, 153, 154, 155, 161, 162, 163, 164, 170, 171, 172, 174, 179, 180, 185, 186, 189, 190, 191, 192
OHP	Online Histogram Presenter	39
PDF	Parton Distribution Function	64, 74, 75, 76, 78, 131, 140, 142, 144, 148, 171, 172
PS	Parton Shower	62, 66, 67, 75, 76, 93, 150, 151, 152, 156, 157, 159, 161, 162, 163, 164, 179, 180, 185, 187, 188, 189, 190, 191, 192
PU	Pileup	62
QCD	Quantum Chromodynamics	5, 9, 51, 62, 65, 67, 68, 71, 73, 76, 78, 80, 84, 126, 180
QED	Quantum Electrodynamics	49
QFT	Quantum Field Theory	3, 61
RC	Re-clustered (jet)	59, 83, 86, 92, 122
RMS	Root Mean Squared	50, 121, 134, 136

ROI	Region Of Interest	31, 32, 33, 34, 35, 36
RPC	Resistive Plate Chamber	26, 28, 29, 31, 32, 36, 38, 40, 44
SCT	Semiconductor Tracker	21, 23, 43
SM	Standard Model	3, 4, 5, 6, 9, 10, 11, 12, 60, 64, 65, 72, 73, 76, 77, 91, 95, 104, 119, 147, 154, 155, 156, 157, 159, 161, 162, 163, 164, 165, 169, 170, 171, 173, 174, 175, 178, 185, 186, 187, 188, 189, 190, 191, 192
SMEFT	Standard Model Effective Field Theory	11
SR	Signal Region	125
TDAQ	Trigger and Data Acquisition	30, 31
TGC	Thin Gap Chamber	26, 28, 31, 32, 38, 44
TRT	Transition Radiation Tracker	21, 23, 27
UE	Underlying Event	62, 63, 68
UV	Ultraviolet	65

List of figures

List of tables